ANALYTICAL METHODS TO INTERPRET GROUND DEFORMATIONS DUE TO SOFT GROUND TUNNELING

by

Federico Pinto

Ingeniero Civil (1997)

National University of Cordoba

SUBMITTED TO THE DEPARTMENT OF
CIVIL AND ENVIRONMENTAL ENGINEERING
IN PARTIAL FULFILLMENT OF THE REQUIREMENTS FOR THE DEGREE OF
MASTER OF SCIENCE IN CIVIL AND ENVIRONMENTAL ENGINEERING

at the

MASSACHUSETTS INSTITUTE OF TECHNOLOGY

September 1999
[February 2000]

Signature of Author.....
Department of Civil and Environmental Engineering
September 30, 1999

Certified by.....
Andrew J. Whittle
Associate Professor of Civil and Environmental Engineering
Thesis Supervisor

Accepted by.....
Daniele Veneziano
Professor of Civil and Environmental Engineering
Chairman, Departmental Graduate Committee

ANALYTICAL METHODS TO INTERPRET GROUND DEFORMATIONS DUE TO SOFT GROUND TUNNELING

by

Federico Pinto

Submitted to the Department of Civil and Environmental Engineering on September 30, 1999, in partial fulfillment of the requirements for the degree of Master of Science in Civil and Environmental Engineering

ABSTRACT

This thesis studies the application of simplified analytical models for predicting ground deformations caused by tunneling. The analytical models are principally based on the assumption of linear elastic ground mass response. Complete solutions are presented for ground movements in a 2-D half-plane due to prescribed deformation modes at the circular tunnel cavity wall. Preliminary 3-D solutions are also presented for the case of a tunnel heading with a uniform rate of ground convergence. The results show that approximate models based on point ground losses and distortions provide a good approximation to solutions from analyses that model the exact tunnel geometry. Further analyses show how deformations around a rectangular tunnel drift can be modeled by a series of line sinks. Deformations occurring close to the tunnel cavity are influenced by soil plasticity. The thesis proposes a simple correction factor that should be applied to measurements of cavity convergence in order to estimate far-field elastic ground movements. An alternative approach, proposed by Sagaseta (1988), assumes an average dilation rate due to plastic behavior in the soil mass. This average dilation model produces significant differences in the predicted far-field deformation pattern.

The proposed analyses have been validated using data from published case studies of tunnels constructed using different techniques and soil properties. A simple procedure is proposed for estimating the three model input parameters based on surface settlement and inclinometer data. Three of the examples show encouraging agreement with the proposed analysis. However, data from a fourth project, a deep NATM tunnel in stiff London Clay, is not consistent with either the proposed elastic or average dilation models. The proposed analysis is now available for comparison with monitoring data from the on-going Tren Urbano project in San Juan.

Thesis Supervisor: Prof. Andrew J. Whittle
Title: Associate Professor of Civil and Environmental Engineering

ACKNOWLEDGEMENTS

I would like to thank Prof. Andrew J. Whittle for his kind support, continuous positive feedback and the energy that he dedicated towards the completion of this thesis. His insight lead me through this new and challenging experience. I would also like to thank the Tren Urbano team at MIT; Dr. John T. Germaine, Yun Kim, Guoping Zang, and Yo-Ming Hsieh, who continuously provided new ideas and insightful comments towards my work. The interaction amongst the team has made this experience very enjoyable. I would like to acknowledge the economic support provided by Tren Urbano through a contract between MIT and the KKZ/CMA Joint Venture responsible for design-build of Section 7 in Rio Piedras. The economic support provided by Fulbright/CONICOR during the summer is also gratefully acknowledged.

Acknowledgements also go out to:
Prof. Carlos A. Prato, who encouraged me to pursue graduate studies in Civil Engineering and was instrumental in nourishing my interest for research.
Prof. Hai S. Yu, who contributed to this thesis during his stay at MIT.
The faculty of the Mechanics and Materials group at MIT.

Last but not least, I would like to thank my family, who has been the main source of my strength and inspiration during this challenging year. My fellow students and friends from the Geotech group at MIT; Jorge Gonzalez, Martin Nussbaumer, Alexis Liakos, Dominic Assimaki, George Kokossalakis, Christoph Haas, Attasit 'Pong' Korchaiyapruk, Dimitrios Konstantakos, Sanjay Pahuja, Catalina Marulanda, Kurt Sjoblom, Laurent Levy, Lana Aref and Kortney Adams. Their friendship is a treasure that I will carry with me forever.

to my family

TABLE OF CONTENTS

LIST OF FIGURES

NOTATION

Chapter 1

V_f	Deformed volume of tunnel
V_0	Initial volume of tunnel
V_L	Ground loss volume
u_y^{max}	Maximum surface settlement
R	Tunnel radius
H	Depth to centerline of tunnel
x_I	Inflection point of Gaussian curve
K_0	Coefficient of earth pressures at rest
x,	Horizontal coordinate
y	Vertical coordinate

Chapter 2

R	Tunnel radius
σ'_{v0}	In-situ vertical effective stress
K_0	Coefficient of earth pressures at rest
σ'_{h0}	In-situ horizontal effective stress
σ'	Effective stress
σ	Total stress
u_w	In-situ pore pressures
p_0	In-situ average total stress
q_0	In-situ deviatoric stress
M	One dimensional elastic modulus
λ	Elastic constant
u_x	Horizontal displacement
u_y	Vertical displacement
x	Horizontal coordinate

y	Vertical coordinate
ν	Poisson ratio
G	Elastic shear modulus
u_r	Radial displacement
r	Radial distance from tunnel centerline
σ_r	Radial stress
σ_θ	Hoop stress
A, B, C, D	Integration constants
u_ε	Uniform radial convergence at the tunnel wall
ε	Uniform radial displacement parameter
θ	Angular coordinate
$\tau_{r\theta}$	Shear stress
F	Airy's stress function
ϕ	Radial variation of Airy's stress function
n	Coefficient
Q_1, Q_2, q_1, q_2	Auxiliary functions
u_δ	Distortion displacement
δ	Ovalization parameter
u_δ^*	Apparent distortion displacement
ρ	Relative distortion
r_u	Pore pressure ratio
ρ^*	Apparent relative distortion
p_I	Internal pressure inside tunnel
r_p	Internal pressure ratio
OCR	Overconsolidation ratio

Chapter 3

R	Tunnel radius
H	Depth to centerline of tunnel

K_0	Coefficient of earth pressures at rest
ν	Poisson ratio
ϕ, ψ	Goursat Functions
G	Elastic shear modulus
u_z	Complex displacement vector
z	Complex coordinate vector
κ	Elastic constant
u_x	Horizontal displacement
i	Imaginary constant
u_y	Vertical displacement
$\underline{x}$	Horizontal coordinate
y	Vertical coordinate
ζ	Mapped complex coordinate
α	Embedment ratio parameter
i	Subscript
a_i, b_i, c_i, d_I	Laurent series coefficients
k	Arbitrary index for Laurent series coefficient
σ	Mapped coordinate at the surface
θ	Mapped angular coordinate
A_k	Fourier expansion coefficient
u_ε	Uniform radial convergence at the tunnel wall
ε	Error norm
u_y^∞	Surface vertical displacement in the far field
u_x^∞	Surface horizontal displacement in the far field
L	Integration interval to define error norm
Δu_y	Vertical translation
β	Angular coordinate in the z plane
u_δ	Distortion displacement
τ_{xy}	Shear tractions
r	Radial coordinate from tunnel centerline

V_L	Ground loss volume
F	Airy's stress function
$\mathfrak{T}_{xy}$	Fourier transform of the corrective shear tractions at the surface
ω	Auxiliary variable
Q_1, Q_2, q_1, q_2	Auxiliary functions
W_1	Volume expansion at the tunnel springline
W_2	Volume contraction at the tunnel crown
δ	Distortion parameter
y_c	Vertical coordinate of the center of the circular area where heaving occurs
R_c	Radius of circular area where heaving occurs
Ω	Area of settlement trough
r_u	Pore pressure ratio
r_p	Internal pressure ratio
OCR	Overconsolidation ratio
u_y^0	Vertical surface settlement above the crown
u_x^{max}	Maximum horizontal displacement
x_h	Location of maximum horizontal displacement at the surface
$u_x^{(y=0)}$	Horizontal displacement at the surface

Chapter 4

K_0	Coefficient of earth pressures at rest
H	Depth to centerline of tunnel
V_L	Volume of ground loss
x	Horizontal coordinate
y	Vertical coordinate
u_x	Horizontal displacement
u_y	Vertical displacement
f, g	Functions that govern the spatial distribution of displacements due to a cavity contraction

Γ_x, Γ_y	Green functions due to a cavity contraction
X, Y	Vertical and horizontal coordinates of the point cavity
s	Parametric coordinate
$e(s)$	Local thickness of the cavity
a, b, c, d	Geometric coordinates of the drift
κ	Elastic constant
B	Width of rectangular drift
D	Height of rectangular drift
R_{eq}	Equivalent radius of the drift

Chapter 5

K_0	Coefficient of earth pressures at rest
ψ	Dilation angle
R_p	Radius of the plastic zone
u_ε^e	Equivalent elastic displacement at the tunnel wall
u_ε^y	Critical yield displacement at the tunnel wall
R	Tunnel radius
$N_{\phi'}$	Flow factor
ϕ'	Drained friction angle
Y	Mohr-Coulomb parameter that depends on cohesion
c'	Drained cohesion intercept
G	Pre-yield average shear modulus
p'_0	In-situ effective stress
u_ε^p	Plastic displacement at the tunnel wall
T	Function of the internal pressure
β	Coefficient that depends on the dilation angle
V_L	Ground loss volume
OCR	Overconsolidation ratio
RF	Reduction factor
x	Horizontal coordinate

y	Vertical coordinate
u_x	Horizontal displacement
u_y	Vertical displacement
α	Dilation parameter
u_ε	Uniform convergence displacement
H	Depth to centerline of tunnel
u_δ	Distortion displacement

Appendix I

F	Airy's stress function
x	Horizontal coordinate
y	Vertical coordinate
z	Complex coordinate vector
ϕ, ψ, χ	Goursat Functions
G	Elastic shear modulus
u_x	Horizontal displacement
u_y	Vertical displacement
u_z	Complex displacement vector
i	Imaginary constant
κ	Elastic constant
σ_x	Total normal stress in the horizontal direction
σ_y	Total normal stress in the vertical direction
τ_{xy}	Shear stress
Σ	Integral of tractions along tunnel wall
t_x	Traction along tunnel wall in the horizontal direction
t_y	Traction along tunnel wall in the vertical direction
s	Parametric coordinate along tunnel boundary
C	Integration constant
ζ	Mapped complex coordinate
H	Depth to centerline of tunnel

α	Embedment ratio parameter
R	Tunnel radius
i	Subscript
a_i, b_i, c_i, d_I	Laurent series coefficients
σ	Mapped coordinate at the surface
θ	Mapped angular coordinate
k	Arbitrary index for Laurent series coefficient
A_k	Fourier expansion coefficient

Appendix III

x	Horizontal coordinate
y	Vertical coordinate
F	Airy's stress function
$\mathfrak{F}$	Fourier transform of Airy's stress function
$\mathfrak{S}_y$	Fourier transform of the normal stresses at the surface
$\mathfrak{T}_{xy}$	Fourier transform of the shear stresses at the surface
ω	Auxiliary variable
δ	Auxiliary parameter
A, B, C, D	Integration constant

Appendix IV

K_0	Coefficient of earth pressures at rest
σ'_r	Effective radial stress
σ'_θ	Effective hoop stress
r	Radial coordinate from the center of the cavity
p'_i	Effective pressure inside cavity
p'_0	In situ effective stress
R	Radius of the cavity

u_r	Radial displacement
M	One dimensional elastic modulus
λ	Elastic constant
A, B, C, D, J	Integration constants
ν	Poisson ratio
G	Pre-yield average shear modulus
$N_{\phi'}$	Flow factor
ϕ'	Drained friction angle
Y	*Cohesion ratio*
c'	Drained cohesion intercept
R_p	Radius of the plastic zone
T	Function of the internal pressure
ε_r^p	Plastic radial strain
ε_r^p	Plastic hoop strain
β	Coefficient that depends on the dilation angle
ψ	Dilation angle
u_ε^p	Plastic displacement at the tunnel wall
u_ε^y	Critical yield displacement at the tunnel wall

1. Introduction

The steadily growing demand of modern society for public transportation systems in congested urban areas has encouraged innovations in underground construction techniques. Due to the fact that soft ground conditions are found in many of these urban areas, soft-ground excavation techniques have experienced a particularly remarkable advance. In the past fifty years the number of soft-ground tunnels has steadily increased, primarily due to the technological advance in tunnel machinery, grouting techniques and groundwater flow control. It is believed that this trend will continue to grow in the future since underground construction provides a solution for the need of space in densely populated urban areas. The technological advance has made possible the successful excavation of tunnels in a wide range of soils, under different groundwater conditions (Peck, 1969).

Section 7 of the Tren Urbano alignment in San Juan de PR is being constructed underground over a total length of 1.5 km trough the town of Río Piedras (extending from Villa Nevarez to Hato Rey). The tunnel passes trough deep alluvial deposits of interbedded stiff clays and sandy clays, referred to as the Hato Rey fromation (often referred to as 'old alluvium'). Three construction methods are being used in order to excavate the tunnel; i) New Austrian Tunneling Method (NATM), for the alignment south of Calle Georgetti ; ii) stacked drift construction to support the excavation of the main cavern of the Río Piedras station using a series of 15 drifts; and iii) twin bored tunnels excavated by means of a Earth Pressure Balance (EPB) Tunneling Boring Machine (TBM) from the Río Piedras station towards the University of PR (UPR) station. The entire underground alignment is built underneath existing buildings (mainly masonry structures) and other facilities sensitive to ground deformations. Hence, ground deformations produced by the excavation activities are of great concern.

Ground deformations arise due to the fact that the initial state of stresses is altered by the excavation, generating a new state of equilibrium and mobilizing the shear strength of the soil in the near field around the excavated cavity. This strength mobilization leads to deformations at the excavation face, which cause the volume of the excavated soil, V_0, to be larger than the volume occupied by the tunnel, V_f. This difference between the excavated volume and the

volume occupied by the tunnel is called "ground loss", $V_L = V_f - V_0$, and is often expressed as a ground loss ratio, $V_L = (V_f - V_0)/ V_0 \cdot 100$ %. As the ground loss is a function of the amount of deformations at the tunnel face, its value is inextricably linked to the construction method. Hence, the prediction of ground deformations has to somehow take into account the effects of the construction method.

The methods of modeling ground deformations due to tunneling, range in complexity; from purely empirical results (e.g., Peck, 1969) to complex non-linear 3-D finite element analyses (e.g., Lee and Rowe, 1990).

Empirical methods

Empirical methods have the obvious advantage that they fit a certain amount of case studies and are relatively simple to use. Peck (1969) proposed an analysis method for estimating ground deformations induced by tunneling based on data (mainly from the Chicago Subway) from 18 tunnels excavated in cohesive and granular soils by means of shields or hand mined. Although the method has no theoretical basis, it has been widely adopted in engineering practice. Many case studies have been analyzed by this approach in the past 30 years (e.g., Attewell and Farmer, 1974; Oteo and Sagaseta, 1996, Bowers et al., 1996). Peck's approach characterizes the distribution of surface settlements using a Gaussian distribution curve (Figure 1.1). There are two parameters that define a particular curve; i) the surface settlement above the crown, u_y^{max}, and ii) the inflection point x_i. These parameters were obtained for several case studies by means of matching Gaussian curves to measured surface settlements. By then correlating these parameters with geometric characteristics for each tunnel, design charts were developed for predicting ground displacements due to tunneling. The settlement at the inflection point (for the Gaussian distribution curve) coresponds to $0.61 \cdot u_y^{max}$ (Figure 1.1). Hence, the inflection point was defined as the abscissa at which the observed settlement is 0.61 times the maximum. The inflection point, normalized by the tunnel radius[1], R, was then correlated with the embedment depth ratio, $H / 2 \cdot R$, to form a chart such as Figure 1.2, where the dotted lines delineate different

soil types. Since Peck's original work, more data has been included in such charts (e.g., Oteo and Sagaseta, 1996). This method, also assumes that the over-excavated volume $V = V_f - V_0$ (i.e., ground loss) had the same magnitude than the volume of the settlement trough (i.e., the area enclosed by the original and deformed ground surface). However, it will be shown in this work (also Verruijt and Booker, 1996), that the over-excavated volume coincides with the volume of the settlement trough only if the material is incompressible[2] (e.g., undrained behavior of clays). Once the inflection point and the volume of ground loss per unit length, V, are known, the maximum displacement at the surface can be evaluated by matching the volume of ground loss with the area of the settlement trough. The volume of ground loss in this approach is left unknown and is calculated by means of assuming empirical values for u_y^{max}. This method has the disadvantage that it cannot take into account complex construction activities (e.g. compensation grouting) and produces only one displacement pattern that can only be scaled by means of the inflection point, x_i. Another disadvantage is that it does not predict either vertical or horizontal displacements within the soil mass[3]. However, this method has been able to mach many case studies since the practitioner has the option of shifting the width of the trough by means of the inflection point as needed in order to match each particular case.

Finite Element Models

Finite Element models provide the most general framework for analyses of ground deformation due to tunneling. Different soil models can be incorporated in the analysis (e.g., Oettl et al., 1998), thus improving the modeling of real soil behavior. 3-D Construction activities and tunnel geometries can also be included in the analysis (e.g., Lee and Rowe, 1992). FEM models can also analyze staged construction, such as NATM (e.g., Dasari et al., 1996), EPB tunnel-soil-tunnel interactions (Bernat et al., 1999) and ground treatment, such as compensation grouting (e.g., Kovacevic et al., 1996). In order to perform such analyses the soil properties at the site (stiffness, strength, permeability, etc.) must be obtained by means of a comprehensive

---

[1] It will be shown in this work that the parameter that normalizes the spatial coordinates (i.e., x and y) is the depth to centerline, H, rather than the tunnel radius, R. If R is used in order to normalize x and y, the R/H ratio effect needs to be taken into account separately.

[2] If the behavior is drained, the volume at the surface could be either larger or smaller, depending on Poisson ratio and dilation angle.

[3] Attewell and Farmer (1974) extended this method in order to predict displacements within the soil mass.

laboratory-testing program, which sometimes is not readily available. Ground water conditions (hydrostatic, steady state or transient seepage, etc.) also need to be included in the analysis, which requires sophisticated site investigation (e.g., piezometers and observation wells). The construction sequences—sometimes very complex or not known in advance—also influence on the model predictions. One advantage of these methods is that they are 'complete' in the sense that it is possible to estimate all the input parameters. Another advantage is that, by means of FEM, it is possible to model details of the tunneling process. However, the set up of the model is very time-consuming and, in many cases, the actual 3-D problem must be analyzed by 2-D approaches in order to simplify the model. Model predictions are also highly dependent on the constitutive model assumed in order to approximate the real soil behavior.

Analytical models

These methods make gross approximations to the real soil behavior but otherwise fulfill all other axioms of continuum mechanics. Analytical methods can predict ground displacements throughout the soil mass with a very few input parameters. Moreover, the input parameters needed for the analysis are relatively simple to estimate, for which these methods are very useful in preliminary design. Most of these methods are readily extendable to 3-D and can predict both vertical and horizontal displacements throughout the soil mass. Another advantage is that they provide a framework for studying complex construction procedures, such as the stacked drift construction of the Río Piedras cavern by direct superposition of solutions. Grouting activities can also be taken into account by assuming cavity expansions, rather than contractions. In situ K_0 conditions, soil-lining interaction and construction procedure effects can also be conceptually taken into account by shifting the relative contribution of basic deforming modes at the tunnel wall. However, one major drawback of these methods is that they can not model the soil-structure interaction of pre-existing structures at the surface, which in some cases may lead to large differences in ground deformations due to local yielding effects. These models may also miss some features associated with complex soil behavior.

Sagaseta (1987) proposed simplified analytical expressions for evaluating short-term ground displacements around tunnels in clays. His solution considered a point cavity contraction (which

represented concentrated ground loss at the tunnel axis) from an initial isotropic state of stresses (i.e., $K_0 = 1$) in an elastic half-plane (Figure 1.3). The settlement trough, evaluated by means of this solution, has a similar shape as the Gaussian distribution curve proposed by Peck (1969). However, the resulting settlement trough is wider than the empirical distribution proposed by Peck (see Schmidt, 1988). Verruijt and Booker (1996) extended the method for arbitrary Poisson ratios and included a second deformation mode of the tunnel wall corresponding to an elastic cavity distortion from an anisotropic initial state of stresses (i.e., $K_0 \neq 1$). It was found that the deformation at the tunnel wall has a significant impact on the displacement distribution at the surface and inside the ground. The distortion mode reduces the width of the settlement trough due to the isotropic compression alone. Thus, by combining both deformation modes, different displacement patterns can be modeled. The aforementioned methods do not explicitly consider the geometry of the tunnel wall in the analysis. In that sense, they are regarded as "point solutions". Verruijt (1997) presented a more refined solution method by explicitly considering the presence of the tunnel wall. His published results are limited to the isotropic case. Other approaches have been pursued by Sagaseta (1999), who modified the point solutions in order to account for dilation due to the drained shearing. The effect of the dilation is to reduce the width of the settlement trough for cavity contraction[4]. In practice, however, dilation is only likely to occur in the near field aaround the tunnel (where soil yields). Thus, the selection of a single dilation parameter represents a practical limitation of this approach.

Longanathan and Poulos (1998) proposed an empirical extension of the analytical solutions[5] proposed by Verruijt and Booker (1996) neglecting the distortion component due to $K_0 \neq 1$. Their analysis recognizes that settlement troughs are generally wider than experimental measurements and assumes that Verruijt's solution accounted for a uniform convergence at the tunnel wall[6]. Hence, the solution was modified by arbitrary functions in order to match a set of case studies and account for non-uniform displacements at the tunnel wall (larger at the crown and smaller at the invert). Although based on correct concepts, this method has no theoretical justification and

[4] Dilation has the opposite effect if a cavity expansion is considered

[5] Their appproach ignores the distortion component as they argue that this does not occur in the short-term. This is actually unrealistic since, as it will be shown in this work, distortion will occur whenever K_0 is not unity.

[6] It will be shown in this work that Verruijt's expressions include a vertical translation component, which is responsible for the displacement at the tunnel crown being larger than the one in correspondence to the invert.

can only predict one fixed displacement field. This limitation is of particular concern while comparing inclinometer readings with measured data, since outward movements (likely to occur when $K_0 < 1$) at the tunnel springline cannot be modeled. However, this method seems to match several case studies for a wide range of soil types.

Thesis Goals

This thesis focuses on the modeling of ground deformations by analytical methods derived from continuum mechanics. Throughout this thesis, the available solutions are re-derived and studied while some original solutions are proposed. Modeling considerations for different construction procedures (e.g., NATM vs. TBM), ground conditions (e.g., normally consolidated vs. overconsolidated), soil structure interaction (e.g., pre-cast lining vs. shotcrete), and ground treatment (e.g., grout injection) are discussed. Effects of plasticity, proximity of tunnel heading (i.e., 3-D effects) and tunnel geometry (e.g., circular vs. square) are also studied in the framework of the analytical models. This thesis proposes a simple method for interpreting model input parameters from in-situ monitoring data in order to assess the practical applicability of the analytical models.

1.1. Thesis Outline

Chapter 2 shows the derivation of the elastic solution for the displacement field due to a tunnel in an infinite elastic plane. The solution is subdivided into two basic deformation modes, and the relative contribution of each mode is defined in terms of K_0 and soil-structure interaction effects.

Chapter 3 studies the effect of a stress-free surface by considering the aforementioned basic deformation modes separately. The exact solution for the isotropic deformation mode is re-derived and an exact solution for the anisotropic (distortion) deformation mode is presented following Verruijt's (1997) approach. The approximate solutions for both deformation modes are also re-derived and compared with the exact ones. Ground displacement patterns obtained by these solutions are studied and discussed.

Chapter 4 discusses the influence of the tunnel geometry by considering a rectangular drift. An elastic solution for this problem is presented and compared with results from equivalent circular tunnel solutions.

Chapter 5 addresses the influence of soil plasticity. Closed-form analytical solutions by Yu and Rowe (1998) for the case of an isotropic cavity unloading problem in an infinite plane are re-arranged in order to account for a cavity contraction problem. The author proposes a simple method for relating convergence measurements at the tunnel wall to the proposed elastic solutions that control far field deformations. Anisotropy of initial stresses and stress-free surface effects are also discussed.

Experimental verifications of model predictions are given in Chapter 6 using a series of four case studies. In each case, model input parameters are derived using a standard procedure for interpreting field monitoring data. The procedure is summarized in the form of a series of design charts.

Chapter 7 shows the effects of the proximity of the tunnel heading. Elastic solutions for a spherical cavity unloading and contraction in an infinite and semi-infinite half space are re-derived and studied. A closed form solution for the displacement field of a semi-infinite tunnel in a half-space is obtained in order to assess the 3-D effects near the tunnel heading.

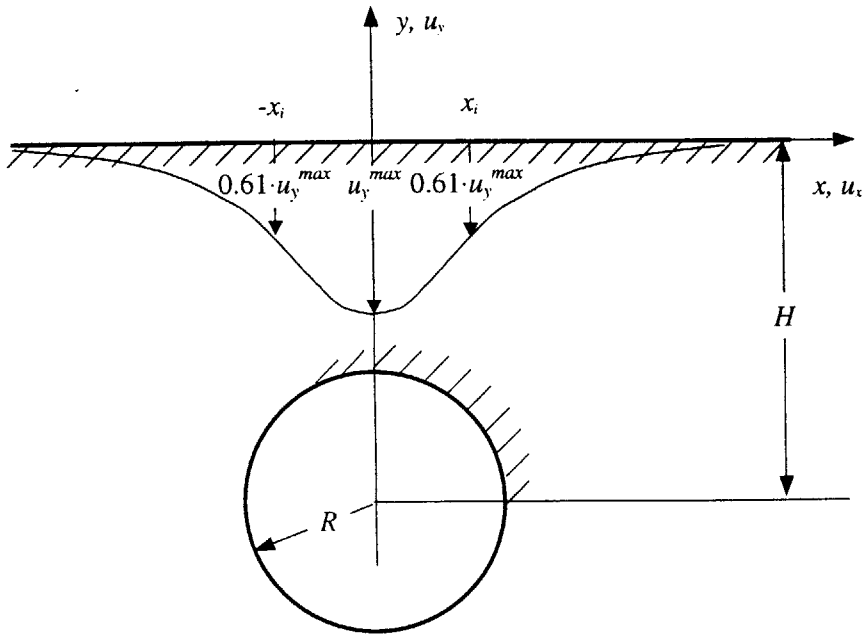

Figure 1.1. Surface settlements predicted by Peck's empirical approach

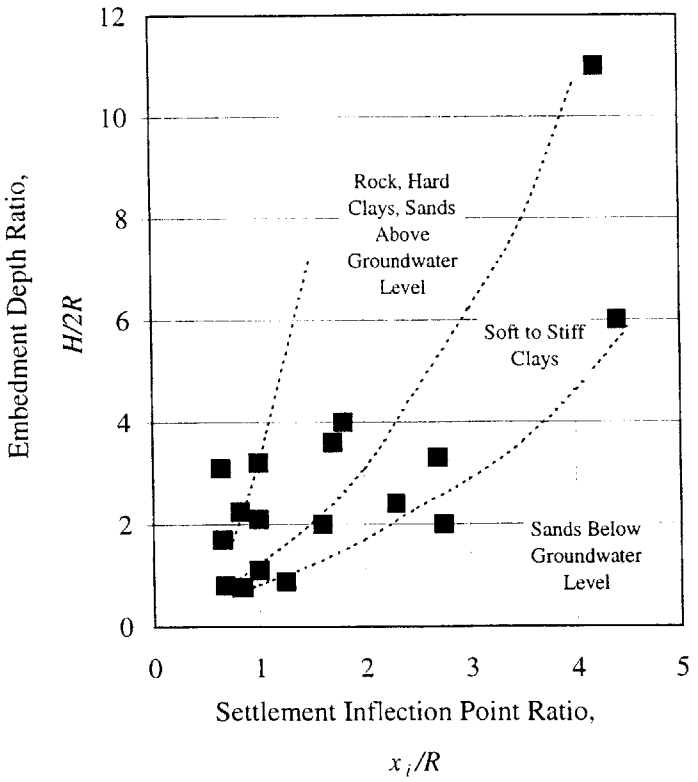

Figure 1.2. Inflection point[7] as a function of soil type and embedment ratios *H/2R*

[7]Inflection point, x_I, defined as offset where $u_y = 0.61 \cdot u_y^{max}$

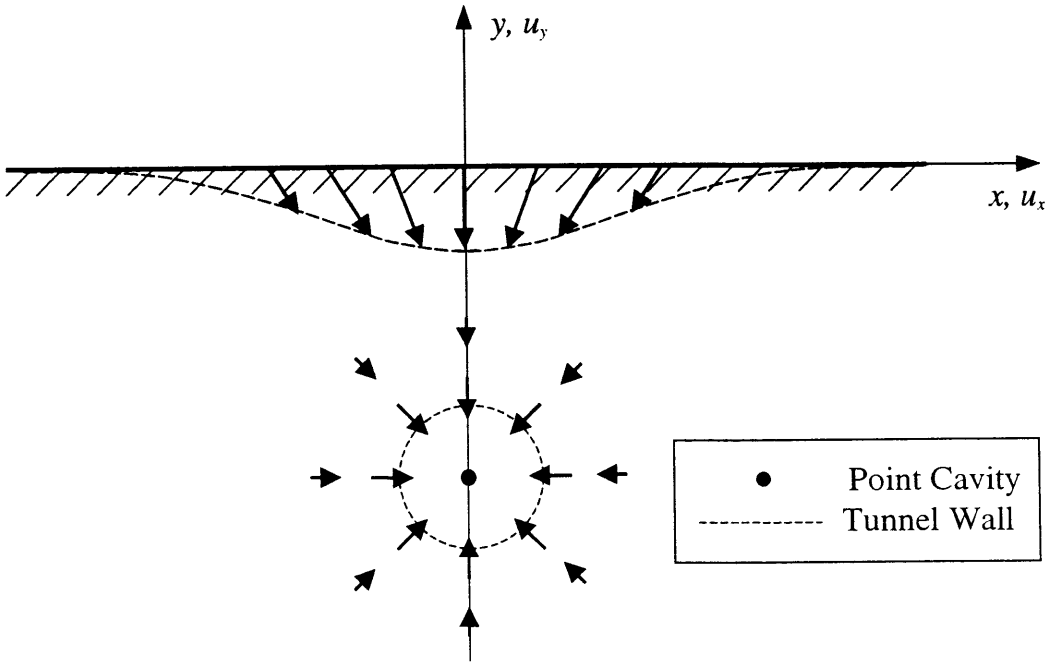

Figure 1.3. Point cavity contraction, after Sagaseta (1986)

2. 2-D Deformation Analyses for a Deep Circular Tunnel in an Infinite Elastic Soil

This chapter reviews theoretical solutions for displacement fields around an unlined cylindrical hole of radius R, in an infinite elastic medium. The analyses simulate the case of a deep tunnel in a soil medium with initial geostatic stresses characterized by an average vertical overburden stress, σ'_{vo}, and an earth pressure coefficient, $K_0=\sigma'_{ho}/\sigma'_{v0}$, where σ'_{ho} and σ'_{v0} are the effective stresses defined by Terzaghi (i.e., $\sigma'=\sigma-u_w$, where u_w are the in-situ pore pressures). The stress state can be decomposed into two components; i) uniform hydrostatic compression, p_0, and ii) uniform pure distortion, q_0, as;

$$p_0 = \sigma'_{v0}\cdot\frac{(1+K_0)}{2}+u_w \qquad \{2\text{-}1a\}$$

$$q_0 = \sigma'_{v0}\cdot\frac{(1-K_0)}{2} \qquad \{2\text{-}1b\}$$

Figure 2.1 illustrates the problem representation, superimposing solution for the isotropic compression and pure distortion stresses. This thesis assumes stresses are positive in tension. This problem was first solved by Kirsch (1898) for a thin plate (plane stress) with a pre-existing hole subjected to tensile stresses and is a classical solution in the theory of elasticity. The solutions show that displacements are unbounded (i.e., do not vanish at infinity), around a pre-existing tunnel/cavity. However, in tunneling problems, it is the displacements due to the creation of the cavity within a pre-stressed medium that are of concern. Hence, the displacements due to the pre-stressed infinite space need to be subtracted from those corresponding to the infinite space with a hole at the origin. The following sections describe the derivation of these solutions.

2.1. Uniform hydrostatic compression

The displacements corresponding to the pre-existing state of stresses in an infinite plane without the cavity (i.e., prior to tunneling) are found by the elastic constitutive relations (assuming small strains and plane strain conditions) as follows:

$$\begin{Bmatrix} M & \lambda \\ \lambda & M \end{Bmatrix} \cdot \begin{Bmatrix} \dfrac{\partial u_x}{\partial x} \\ \dfrac{\partial u_y}{\partial y} \end{Bmatrix} = \begin{Bmatrix} -p_0 \\ -p_0 \end{Bmatrix} \qquad \{2\text{-}2\}$$

where λ and M are elastic constants related to the shear modulus, G, and Poisson ratio ,ν, as follows:

$$M = \frac{2 \cdot G \cdot (1-\nu)}{1-2 \cdot \nu} \qquad \{2\text{-}3a\}$$

$$\lambda = \frac{2 \cdot \nu \cdot G}{1-2 \cdot \nu} \qquad \{2\text{-}3b\}$$

After solving equation {2-2} and integrating, the displacements can be expressed as follows:

$$u_x = -\frac{p_0 \cdot (1-2 \cdot \nu)}{2 \cdot G} \cdot x \qquad \{2\text{-}4a\}$$

$$u_y = -\frac{p_0 \cdot (1-2 \cdot \nu)}{2 \cdot G} \cdot y \qquad \{2\text{-}4b\}$$

which can be expressed in polar coordinates as follows:

$$u_r = -\frac{p_0 \cdot (1-2\nu)}{2 \cdot G} \cdot r \qquad \{2\text{-}5\}$$

The next step is to introduce a cylindrical hole of radius, R (at the origin). Given the fact that the boundary conditions at infinity and at the tunnel wall do not depend on the angular coordinate, θ (Figure 2.1), the problem is one-dimensional and can be solved using the radial distance from the origin, r. The equilibrium condition in the radial direction can be written in cylindrical coordinates:

$$\frac{\partial \sigma_r}{\partial r} + \frac{\sigma_r - \sigma_\theta}{r} = 0 \qquad \{2\text{-}6\}$$

The elastic constitutive equations become:

$$\sigma_r = M \cdot \frac{\partial u_r}{\partial r} + \lambda \cdot \frac{u_r}{r} \qquad \{2\text{-}7a\}$$

$$\sigma_\theta = M \cdot \frac{u_r}{r} + \lambda \cdot \frac{\partial u_r}{\partial r} \qquad \{2\text{-}7b\}$$

Replacing {2-7} in {2-6} and rearranging, the following ordinary differential equation (ODE) is found:

$$\frac{\partial^2 u_r}{\partial r^2} + \frac{1}{r} \cdot \frac{\partial u_r}{\partial r} - \frac{u_r}{r^2} = 0 \qquad \{2\text{-}8\}$$

The general solution for equation {2-8} is given by:

$$u_r = A \cdot r + \frac{B}{r} \qquad \{2\text{-}9\}$$

where A and B are integration constants, which are evaluated by imposing the following boundary conditions:

In the far field:

$$\sigma_r\big|_{r\to\infty} = -p_0 \qquad \{2\text{-}10a\}$$

In tunnel wall:

$$\sigma_r\big|_{r=R} = 0 \qquad \{2\text{-}10b\}$$

Hence, the radial displacements are given by:

$$u_r = -\frac{p_0}{2\cdot G}\cdot\left[(1-2\cdot\nu)\cdot r + \frac{R^2}{r}\right] \qquad \{2\text{-}11\}$$

Subtracting the displacements due to the pre existing state of stresses (equation {2-5}), the final expression for radial displacements around a cavity in an infinite, pre-stressed plane is obtained:

$$u_r = -\frac{p_0\cdot R^2}{2\cdot G\cdot r} \qquad \{2\text{-}12\}$$

which can be expressed in Cartesian coordinates as follows:

$$u_x = -\frac{p_0\cdot R^2}{2\cdot G}\cdot\frac{x}{x^2+y^2} \qquad \{2\text{-}13a\}$$

$$u_y = -\frac{p_0\cdot R^2}{2\cdot G}\cdot\frac{y}{x^2+y^2} \qquad \{2\text{-}13b\}$$

The radial displacement at the tunnel wall is defined as the radial convergence (u_ε):

$$u_\varepsilon = -\frac{p_0 \cdot R}{2 \cdot G} \qquad \{2\text{-}14\}$$

The radial convergence is defined positive when the tunnel expands and negative when it contracts. Introducing the radial convergence in {2-13}, the displacements can be expressed as:

$$u_x(x, y) = u_\varepsilon \cdot \frac{x \cdot R}{x^2 + y^2} \qquad \{2\text{-}15a\}$$

$$u_y(x, y) = u_\varepsilon \cdot \frac{y \cdot R}{x^2 + y^2} \qquad \{2\text{-}15b\}$$

In principle, u_ε can be evaluated by solving equation {2-14}. However, in practice, u_ε is regarded as an input parameter, regardless of its origin and is commonly related to the amount of "ground loss" at the tunnel heading. Similar expressions were given by Verruijt et al. (1996), who re-write the convergence parameter as a fraction of the tunnel radius, and refer to this ratio as the "uniform radial displacement parameter", ε.

$$\varepsilon = -\frac{u_\varepsilon}{R} \qquad \{2\text{-}16\}$$

As can be seen, this definition implies that ε is positive for a uniform contraction at the tunnel wall, while it is negative for a uniform expansion. This is slightly inconvenient, since it is a standard solid mechanics definition that a contracting volume is negative, while an expansion is positive. Throughout this work, expansions will be treated as positive, while contractions will be negative.

2.2. Pure Distortion

The displacements corresponding to the initial state of stresses in the infinite plane without the tunnel are found by the elastic constitutive relations as before (equation {2-2}):

$$\begin{Bmatrix} M & \lambda \\ \lambda & M \end{Bmatrix} \cdot \begin{Bmatrix} \frac{\partial u_x}{\partial x} \\ \frac{\partial u_y}{\partial y} \end{Bmatrix} = \begin{Bmatrix} q_0 \\ -q_0 \end{Bmatrix} \qquad \{2\text{-}17\}$$

After solving {2-17} and integrating, the displacements are found to be:

$$u_x = \frac{q_0}{2 \cdot G} \cdot x \qquad \{2\text{-}18a\}$$

$$u_y = -\frac{q_0}{2 \cdot G} \cdot y \qquad \{2\text{-}18b\}$$

Figure 2.2 shows the Mohr circle representation of the far field stresses around the tunnel based on the cylindrical coordinate system shown in Figure 2.1. It can readily be seen that the far field stresses can be expressed as follows:

$$\sigma_r = q_0 \cdot cos(2 \cdot \theta) \qquad \{2\text{-}19a\}$$

$$\sigma_\theta = -q_0 \cdot cos(2 \cdot \theta) \qquad \{2\text{-}19b\}$$

$$\tau_{r\theta} = -q_0 \cdot sin(2 \cdot \theta) \qquad \{2\text{-}19c\}$$

The stresses are related to Airy's stress function as follows:

$$\sigma_r = \frac{1}{r}\cdot\frac{\partial F}{\partial r} + \frac{1}{r^2}\cdot\frac{\partial^2 F}{\partial \theta^2} \qquad \{2\text{-}20a\}$$

$$\sigma_\theta = \frac{\partial^2 F}{\partial r^2} \qquad \{2\text{-}20b\}$$

$$\tau_{r\theta} = -\frac{\partial}{\partial r}\left(\frac{1}{r}\cdot\frac{\partial F}{\partial \theta}\right) \qquad \{2\text{-}20c\}$$

Equations {2-20} and {2-19} suggest that Airy's stress function can be expressed as:

$$F(r,\theta) = \phi(r)\cdot\cos(2\cdot\theta) \qquad \{2\text{-}21\}$$

which can be regarded as a result of the method of separation of variables with only one Fourier expansion term in the angular coordinate (θ). Hence, the compatibility equation in terms of Airy's stress function can be expressed as follows:

$$\left(\frac{\partial}{\partial r^2} + \frac{1}{r}\cdot\frac{\partial}{\partial r} - \frac{4}{r^2}\right)\cdot\left(\frac{\partial \phi}{\partial r^2} + \frac{1}{r}\cdot\frac{\partial \phi}{\partial r} - \frac{4\cdot\phi}{r^2}\right) = 0 \qquad \{2\text{-}22\}$$

In order to solve the PDE, the following assumption is made:

$$\phi(r) = r^n \qquad \{2\text{-}23\}$$

where n is a coefficient obtained by replacing {2-23} in {2-22}, which yields:

$$n\cdot r^{n-4}\cdot\left(n^3 - 4\cdot n^2 - 4\cdot n + 16\right) = 0 \qquad \{2\text{-}24\}$$

Solving for n yields:

$$n = \begin{Bmatrix} -2 \\ 0 \\ 2 \\ 4 \end{Bmatrix} \qquad \{2\text{-}25\}$$

Hence, the general solution of the ODE can be expressed as:

$$\phi(r) = \frac{A}{r^2} + B + C \cdot r^2 + D \cdot r^4 \qquad \{2\text{-}26\}$$

where A, B, C, D, are integration constants, which are found by imposing the stress boundary conditions at infinity, given by {2-19}, and the stress-free condition[1] at the tunnel wall. In order to impose the boundary conditions, the stresses are evaluated by means of {2-20}:

$$\sigma_r = -2 \cdot \left(\frac{3 \cdot A}{r^4} + \frac{2 \cdot B}{r^2} + C \right) \cdot \cos(2 \cdot \theta) \qquad \{2\text{-}27a\}$$

$$\sigma_\theta = 2 \cdot \left(\frac{3 \cdot A}{r^4} + C + 6 \cdot D \cdot r^2 \right) \cdot \cos(2 \cdot \theta) \qquad \{2\text{-}27b\}$$

$$\tau_{r\theta} = 2 \cdot \left(-\frac{3 \cdot A}{r^4} - \frac{B}{r^2} + C + 3 \cdot D \cdot r^2 \right) \cdot \sin(2 \cdot \theta) \qquad \{2\text{-}27c\}$$

These expressions reduce in the far field to:

$$\sigma_r\big|_{r \to \infty} = -2 \cdot C \cdot \cos(2 \cdot \theta) \qquad \{2\text{-}28a\}$$

[1] Assuming there is no pressure inside the cavity.

$$\sigma_\theta\big|_{r\to\infty} = 2\cdot(C+6\cdot D\cdot\infty)\cdot\cos(2\cdot\theta) \qquad \{2\text{-}28b\}$$

$$\tau_{r\theta}\big|_{r\to\infty} = 2\cdot(C+3\cdot D\cdot\infty)\cdot\sin(2\cdot\theta) \qquad \{2\text{-}28c\}$$

Comparing {2-28} with {2-19}, the integration constants C and D are found to be:

$$C = -\frac{q_0}{2} \qquad \{2\text{-}29a\}$$

$$D = 0 \qquad \{2\text{-}29b\}$$

The stresses at the tunnel wall are:

$$\sigma_r = -2\cdot\left(\frac{3\cdot A}{R^4}+\frac{2\cdot B}{R^2}-\frac{q_0}{2}\right)\cdot\cos(2\cdot\theta) \qquad \{2\text{-}30a\}$$

$$\sigma_\theta = 2\cdot\left(\frac{3\cdot A}{R^4}-\frac{q_0}{2}\right)\cdot\cos(2\cdot\theta) \qquad \{2\text{-}30b\}$$

$$\tau_{r\theta} = 2\cdot\left(-\frac{3\cdot A}{R^4}-\frac{B}{R^2}-\frac{q_0}{2}\right)\cdot\sin(2\cdot\theta) \qquad \{2\text{-}30c\}$$

Since no lining is assumed, the radial (σ_r) and shear ($\tau_{r\theta}$) stresses at the tunnel wall must vanish. This condition is fulfilled provided that:

$$A = -\frac{q_0\cdot R^4}{2} \qquad \{2\text{-}31a\}$$

$$B = q_0\cdot R^2 \qquad \{2\text{-}31b\}$$

Hence, Airy's stress function is given by the following expression;

$$F(r,\theta) = q_0 \cdot \left(-\frac{R^4}{2 \cdot r^2} + R^2 - \frac{r^2}{2} \right) \cdot \cos(2 \cdot \theta) \qquad \{2\text{-}32\}$$

or in Cartesian coordinates:

$$F(x,y) = q_0 \cdot \left(-\frac{R^4}{2 \cdot (x^2 + y^2)} + R^2 - \frac{x^2 + y^2}{2} \right) \cdot \left(\frac{2 \cdot x^2}{x^2 + y^2} - 1 \right) \qquad \{2\text{-}33\}$$

In order to evaluate the displacements, the following expressions derived from the theory of elasticity are used (e.g.; Boresi and Chong, 1987):

$$u_x = \frac{1}{2 \cdot G} \cdot \left[(1 - \nu) \cdot q_1 - \frac{\partial F}{\partial x} \right] \qquad \{2\text{-}34a\}$$

$$u_y = \frac{1}{2 \cdot G} \cdot \left[(1 - \nu) \cdot q_2 - \frac{\partial F}{\partial y} \right] \qquad \{2\text{-}34b\}$$

where:

$$q_1 + i \cdot q_2 = \int (Q_1 + i \cdot Q_2) \cdot dz \qquad \{2\text{-}35\}$$

$$Q_1 = \nabla^2 F \qquad \{2\text{-}36\}$$

$$z = x + i \cdot y \qquad \{2\text{-}37\}$$

and Q_2 is the harmonic conjugate of Q_1, i.e. they fulfill the Cauchy-Goursat condition, given by the following expression:

$$\frac{\partial Q_1}{\partial x} = \frac{\partial Q_2}{\partial y} ; \frac{\partial Q_1}{\partial y} = -\frac{\partial Q_2}{\partial x} \qquad \{2\text{-}38\}$$

For this problem, Q_1 is found to be:

$$Q_1 = -\frac{4 \cdot R^2 \cdot q_0}{x^2 + y^2} \cdot \left(\frac{2 \cdot x^2}{x^2 + y^2} - 1 \right) \qquad \{2\text{-}39\}$$

The harmonic conjugate, evaluated by means of the Cauchy-Goursat conditions is:

$$Q_2 = 8 \cdot R^2 \cdot q_0 \cdot \frac{x \cdot y}{\left(x^2 + y^2\right)^2} \qquad \{2\text{-}40\}$$

Hence $Q_1 + i \cdot Q_2$ is given by:

$$Q_1 + i \cdot Q_2 = -\frac{4 \cdot R^2 \cdot q_0}{z^2} \qquad \{2\text{-}41\}$$

Replacing {2-41} in {2-35} and evaluating the integral produces:

$$q_1 + i \cdot q_2 = \frac{4 \cdot R^2 \cdot q_0}{z} \qquad \{2\text{-}42\}$$

After separating real and imaginary components, the following expressions are found:

$$q_1 = 4 \cdot R^2 q_0 \cdot \frac{x}{x^2 + y^2} \qquad \{2\text{-}43a\}$$

$$q_2 = -4 \cdot R^2 q_0 \cdot \frac{y}{x^2 + y^2} \qquad \{2\text{-}43b\}$$

Finally, the spatial derivatives of the Airy stress function are needed to calculate the displacement components (equation {2-34}).

$$\frac{\partial F}{\partial x} = -q_0 \cdot x \cdot \frac{\left(x^2+y^2\right)^2 + R^2 \cdot \left(x^2 - 3 \cdot y^2\right)}{\left(x^2+y^2\right)^3} \cdot \left(x^2+y^2-R^2\right) \qquad \{2\text{-}44a\}$$

$$\frac{\partial F}{\partial y} = q_0 \cdot y \cdot \frac{\left(x^2+y^2\right)^2 + R^2 \cdot \left(y^2 - 3 \cdot x^2\right)}{\left(x^2+y^2\right)^3} \cdot \left(x^2+y^2-R^2\right) \qquad \{2\text{-}44b\}$$

Hence, replacing {2-43} and {2-44} in {2-34}, the displacement field can be expressed as:

$$u_x(x,y) = \frac{q_0}{G} \cdot \frac{x}{x^2+y^2} \cdot \left\{ 2 \cdot (1-\nu) \cdot R^2 + \frac{\left(x^2+y^2\right)^2 + R^2 \cdot \left(x^2 - 3 \cdot y^2\right)}{2 \cdot \left(x^2+y^2\right)^2} \cdot \left(x^2+y^2-R^2\right) \right\} \qquad \{2\text{-}45a\}$$

$$u_y(x,y) = -\frac{q_0}{G} \cdot \frac{y}{x^2+y^2} \cdot \left\{ 2 \cdot (1-\nu) \cdot R^2 + \frac{\left(x^2+y^2\right)^2 + R^2 \cdot \left(y^2 - 3 \cdot x^2\right)}{2 \cdot \left(x^2+y^2\right)^2} \cdot \left(x^2+y^2-R^2\right) \right\} \qquad \{2\text{-}45b\}$$

Subtracting the displacements due to the pre-existing state of stresses (equations {2-18}), the final expression for the displacements due to a hole in an elastic infinite pre-stressed plane can be written:

$$u_x(x,y) = \frac{q_0}{G} \cdot \frac{x}{x^2+y^2} \cdot \left\{ 2 \cdot (1-\nu) \cdot R^2 + \frac{\left(x^2+y^2\right)^2 + R^2 \cdot \left(x^2 - 3 \cdot y^2\right)}{2 \cdot \left(x^2+y^2\right)^2} \cdot \left(x^2+y^2-R^2\right) - \frac{\left(x^2+y^2\right)}{2} \right\} \qquad \{2\text{-}46a\}$$

$$u_y(x,y) = -\frac{q_0}{G} \cdot \frac{y}{x^2+y^2} \cdot \left\{ 2 \cdot (1-\nu) \cdot R^2 + \frac{\left(x^2+y^2\right)^2 + R^2 \cdot \left(y^2 - 3 \cdot x^2\right)}{2 \cdot \left(x^2+y^2\right)^2} \cdot \left(x^2+y^2-R^2\right) - \frac{\left(x^2+y^2\right)}{2} \right\} \qquad \{2\text{-}46b\}$$

The maximum horizontal displacement at the tunnel boundary is defined as the distortion, u_δ:

$$u_\delta = \frac{q_0 \cdot R}{2 \cdot G} \cdot (3 - 4 \cdot \nu) \qquad \{2\text{-}47\}$$

Although u_δ can be estimated from known values of G and ν, it is standard practice in ground deformation analysis to assume (or measure) a value of u_δ, regardless of its origin. Nevertheless, equation {2-47} gives an insight on the influence of the mechanical properties of the soil (K_0 = 1-2q_0/σ'_{vo}, G, and ν) on the expected distortion at the tunnel wall.

Displacements within the surrounding soil can be written as functions of u_δ as follows:

$$u_x(x,y) = u_\delta \cdot \frac{R}{3-4\cdot\nu} \cdot x \cdot \frac{(3-4\cdot\nu)\cdot(x^2+y^2)^2 - (3\cdot y^2 - x^2)\cdot(x^2+y^2-R^2)}{(x^2+y^2)^3} \qquad \{2\text{-}48a\}$$

$$u_y(x,y) = -u_\delta \cdot \frac{R}{3-4\cdot\nu} \cdot y \cdot \frac{(3-4\cdot\nu)\cdot(x^2+y^2)^2 - (3\cdot x^2 - y^2)\cdot(x^2+y^2-R^2)}{(x^2+y^2)^3} \qquad \{2\text{-}48b\}$$

In the far field [i.e., neglecting $O(R/r)^3$], these expressions reduce to:

$$u_x(x,y) = \frac{4\cdot(1-\nu)}{3-4\cdot\nu} \cdot u_\delta \cdot R \cdot \frac{x \cdot \left(x^2 - \frac{\nu}{1-\nu}\cdot y^2\right)}{(x^2+y^2)^2} \qquad \{2\text{-}49a\}$$

$$u_y(x,y) = \frac{4\cdot(1-\nu)}{3-4\cdot\nu} \cdot u_\delta \cdot R \cdot \frac{y \cdot \left(\frac{\nu}{1-\nu}\cdot x^2 - y^2\right)}{(x^2+y^2)^2} \qquad \{2\text{-}49b\}$$

Similar expressions were presented by Verruijt and Booker (1996). These authors expressed the distortion as a fraction of the radius by means of the so called "ovalization parameter" (δ) as follows:

$$\delta = \frac{u^*_\delta}{R} \qquad \{2\text{-}50\}$$

where u^*_δ is the apparent distortion parameter (i.e., the maximum horizontal displacement at the tunnel wall evaluated by equation {2-49}, expression that is only accurate for the far field). The apparent distortion parameter can be related to the true distortion parameter (equation {2-47}) as follows:

$$u^*_\delta = \frac{4 \cdot (1-\nu)}{3-4 \cdot \nu} \cdot u_\delta \qquad \{2\text{-}51\}$$

Hence, the apparent distortion is always larger than the true distortion by 33-100 %. This is important when comparing elastic solutions with published data, since most of the former are based on the apparent distortion parameter, leading to larger and unrealistic distortions at the tunnel wall. This is of particular concern while analyzing undrained behavior ($\nu = 0.5$), since for this case there is 100% difference between the apparent and the true distortion.

It is interesting to note that the absolute displacement vectors at the tunnel have a constant magnitude, u_δ, and re-oriented at $-\theta$ (for points with initial orientation $+\theta$) as shown in Figure 2.3.

2.3. Relative Distortion

The relative distortion of the tunnel can be defined as the ratio of the wall distortion to uniform convergence as follows:

$$\rho = -\frac{u_\delta}{u_\varepsilon} \qquad \{2\text{-}52\}$$

where u_ε and u_δ are given by equations {2-14} and {2-47} respectively. For the case of a deep tunnel in infinite elastic soil subject to a K_0 initial state of stresses and zero pore pressures u_w;

$$\rho = \frac{1 - K_0}{1 + K_0 + 2 \cdot r_u} \cdot (3 - 4 \cdot \nu) \qquad \{2\text{-}53\}$$

where $r_u = u_w/\sigma'_{v0}$ is the pore pressure ratio. Figure 2.4 shows the influence of K_0, r_u, and ν on the relative distortion. It can be seen that increasing Poisson and pore pressure ratios leads to lower relative distortions. Higher K_0 values also produce lower relative distortions. Negative values of ρ are possible for $K_0 > 1$ (e.g., $OCR > 4$). However, these solutions do not consider the effects of the ground surface and stress gradient.

As mentioned before, Sagaseta (1998) defined the apparent relative distortion, ρ^*, as the ratio of the maximum horizontal displacement at the tunnel wall due to distortion as evaluated by means of the far field approximation and the displacement at the tunnel wall due to uniform convergence:

$$\rho^* = \rho \cdot \frac{4 \cdot (1 - \nu)}{3 - 4 \cdot \nu} \qquad \{2\text{-}54\}$$

where it can be seen that ρ^* is always larger (33-100%) than ρ. Sagaseta studied the undrained deformations by considering $\nu = 0.5$. Hence, the reported relative distortion values are 100% higher than the true relative distortion presented here.

2.4. Influence of Internal Pressure Inside Tunnel

In many cases there is a certain amount of internal pressure inside the tunnel. In the undrained case, and if the tunnel is excavated by a TBM, the pressure arises as a result of grouting being injected in the gap between the lining and the excavated cavity, which is standard practice. In the drained case, the pressure arises from soil-structure interaction with the lining, which is much stiffer when compressed as a ring than when distorted. Hence, this pressure can be assumed to be approximately uniform around the tunnel wall. The influence of this internal pressure, p_i, is to reduce the amount of displacement due to the isotropic compression component as follows:

$$u_x(x,y) = -\frac{(p_0 - p_i)\cdot R^2}{2\cdot G}\cdot\frac{x}{x^2+y^2} \qquad \{2\text{-}55a\}$$

$$u_y(x,y) = -\frac{(p_0 - p_i)\cdot R^2}{2\cdot G}\cdot\frac{y}{x^2+y^2} \qquad \{2\text{-}55b\}$$

As the interior pressure is assumed to be uniformly distributed at the tunnel face, it has no effect on displacements due to pure distortion. Hence, the relative distortion for the general case of $p_I \neq 0$ is given by:

$$\rho = \frac{1-K_0}{1+K_0+2\cdot r_u}\cdot\frac{3-4\cdot\nu}{1-r_p} \qquad \{2.56\}$$

where $r_p = p_i/p_o$ is the internal pressure ratio. Figure 2.5 shows the effect of the internal pressure ratio on the relative distortion, where it can be seen that high values of r_p increase very significantly the relative distortion. Normally consolidated deposits (i.e., $K_0 \approx 0.6$) with $r_p = 0.80$, $\nu = 0.33$, and $r_u = 1$[2] would have relative distortion $\rho \approx 1$ while overconsolidated deposits (e.g., $OCR \approx 10$, $K_0 \approx 1.5$) would have $\rho \approx -1$.

[2] Ground water conditions hydrostatic with ground water table at the surface.

In this work ρ will be considered large when larger than unity and low when less than 0.5. Hence, it can be said that it is a general trend that normally consolidated deposits have large relative distortions, while overconsolidated deposits have low relative distortions (even negative).

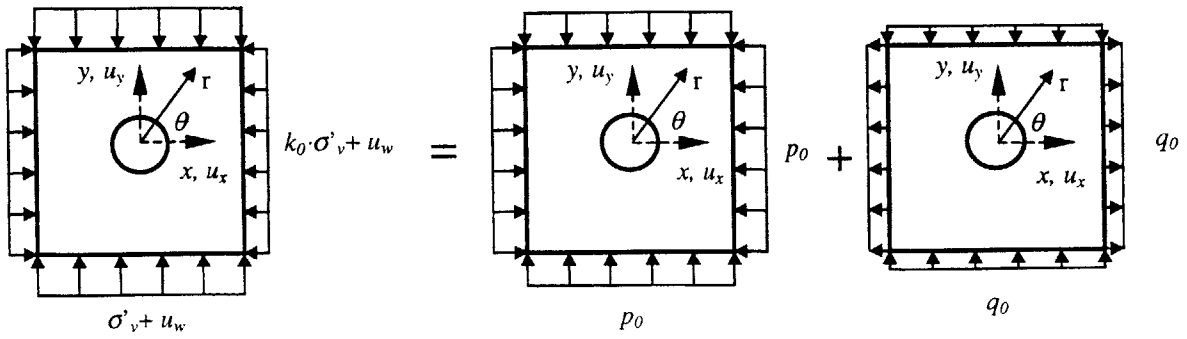

Figure 2.1. Initial state of stresses

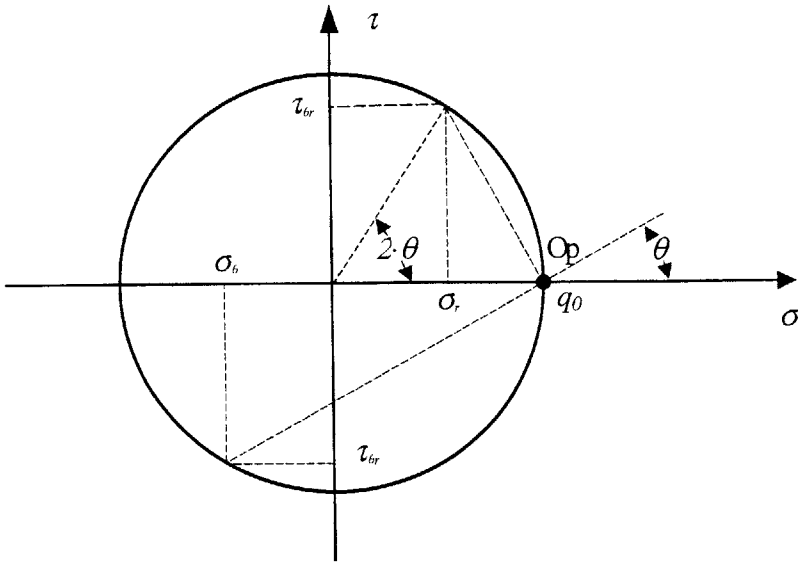

Figure 2.2. Boundary conditions at infinity

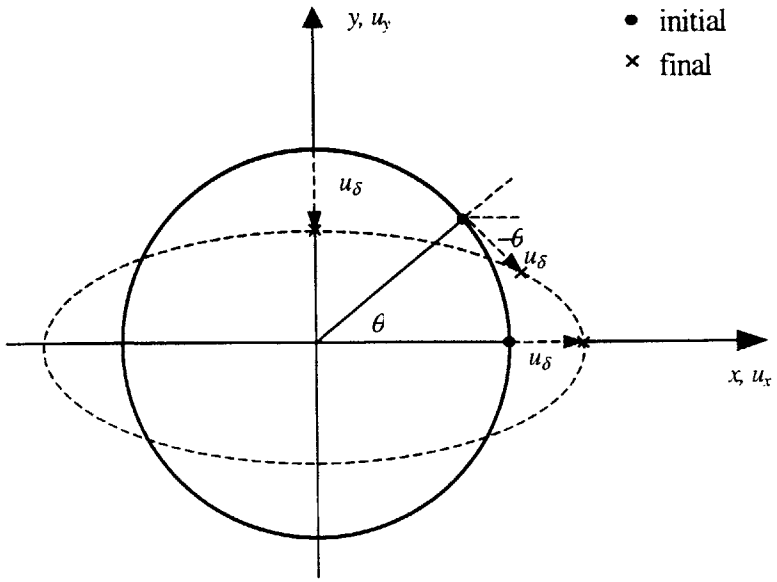

Figure 2.3. Displacements pattern at the tunnel wall

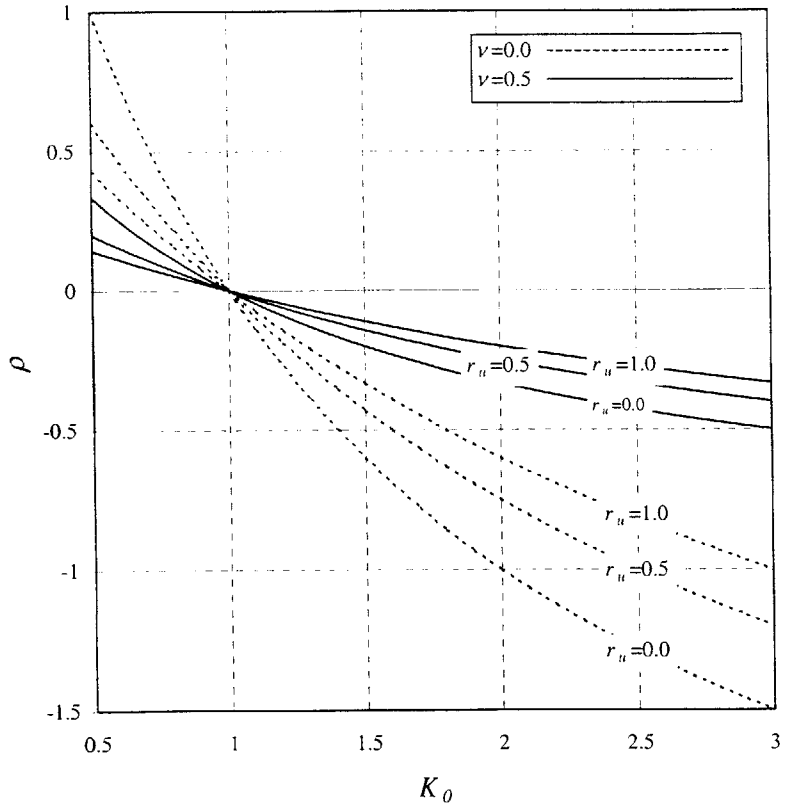

Figure 2.4. Effect of ground state on relative distortion

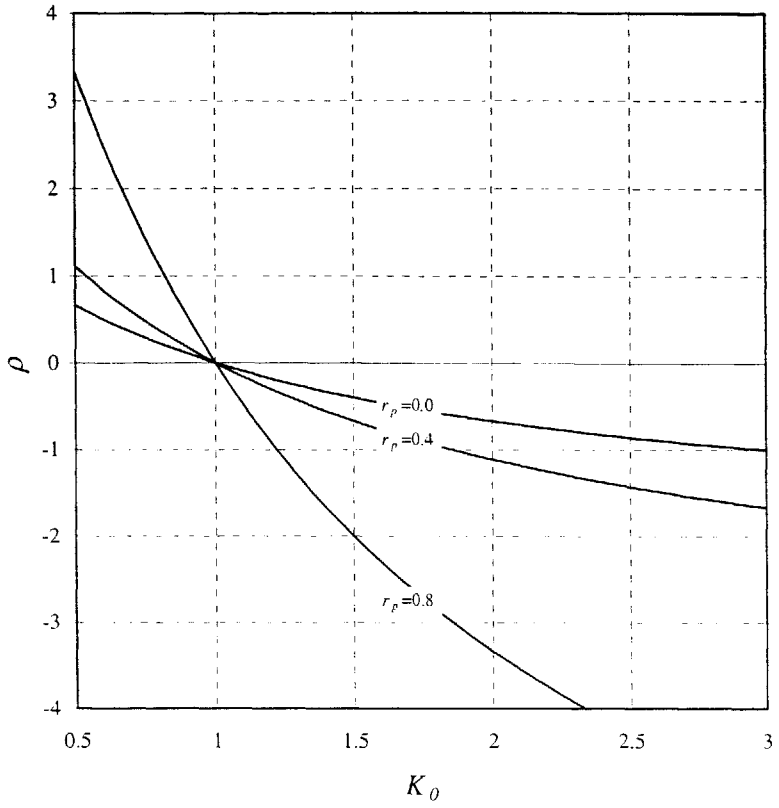

Figure 2.5. Effect of internal pressure on relative distortion for $r_u = 0$, $\nu = 0.25$

3. 2-D Deformation Analyses for a Circular Tunnel in an Elastic Half-Plane

When the tunnel is relatively shallow, the pattern of ground deformations is strongly influenced by proximity to the stress-free ground surface. This chapter considers the problem defined in Figure 4.1 of a multiply connected elastic region, bounded by a horizontal line (ground surface) at which the stresses are zero and a circle (unlined tunnel wall) at which loading takes place in the form of prescribed displacements. The tunnel has radius, R, and is embedded at depth, H, from the ground surface. The displacement boundary condition at the tunnel wall can be subdivided into three basic mode shapes (after Sagaseta, 1999), i) uniform convergence (ground loss); ii) pure distortion (ovalization); and iii) vertical translation (downward movement), as shown in Figure 3.2.

3.1. Background

Mindlin (1939) first studied a similar problem but imposing a stress-free boundary condition at the tunnel wall and considering the gradient of vertical stresses with depth. The problem was solved using bipolar coordinates for three particular cases: i) an initial hydrostatic pressure (i.e., $K_0 = 1$); ii) initial state of stress with no horizontal deformation [i.e., $K_0 = \nu/(1-\nu)$]; and iii) zero horizontal stresses (i.e., $K_0 = 0$). Mindlin then analyzed the distribution of the azimuthal stresses along the tunnel wall.

Sagaseta (1987) proposed an approximate solution method for this problem for the case of a uniform radial convergence (ground loss) at the tunnel wall. His analysis solved the deformations at the ground surface for the case of an incompressible material ($\nu = 0.5$, i.e., corresponding to undrained conditions of a low permeability soil), assuming that the tunnel could be represented by a point/line sink.

Verruijt and Booker (1996), following Sagaseta's approach gave an approximate solution for this problem for the case when the displacements at the wall are a combination of a uniform convergence and a distortion. This solution was reported for arbitrary Poisson ratio (i.e., corresponding to drained or undrained conditions in the surrounding soil).

Verruijt (1997) subsequently solved the problem for an arbitrary displacement boundary condition defined at the tunnel wall using functions of complex variables. To date, however, results have only been presented for the case of a uniform convergence at the tunnel wall. The following Sections re-derive and extend these "exact analyses" (i.e., exact tunnel geometry) proposed by Verruijt (1997), and the approximate results using the singularity (point line/sink) approach of Sagaseta (1987), and Verruijt and Booker (1996).

3.2. Exact Solutions

As mentioned in the above paragraph, the exact solution for the problem discussed in this chapter was obtained by Verruijt (1997) using the complex formulation of planar elasticity. In this formulation, the solution is expressed in terms of two functions (ϕ and ψ) called "Goursat functions", which are found by imposing the boundary conditions (Appendix I). The displacements are related to these functions as follows:

$$2 \cdot G \cdot u_z(z) = \kappa \cdot \phi(z) - z \cdot \overline{\frac{d\phi}{dz}} - \overline{\psi(z)} \qquad \{3\text{-}1\}$$

where G is the elastic shear modulus, i the imaginary constant, ϕ and ψ the Goursat functions, the overscript "$\overline{\ }$" stands for complex conjugate and:

$$u_z = u_x + i \cdot u_y \qquad \{3\text{-}2\}$$

$$z = x + i \cdot y \qquad \{3\text{-}3\}$$

$$\kappa = 3 - 4 \cdot \nu \qquad \{3\text{-}4\}$$

The domain in the z-space is mapped onto an annular region in the ζ-space by the following transformation:

$$\zeta(z)=\frac{i\cdot z\cdot\left(1+\alpha^2\right)-H\cdot\left(1-\alpha^2\right)}{i\cdot z\cdot\left(1+\alpha^2\right)+H\cdot\left(1-\alpha^2\right)} \qquad \{3\text{-}5\}$$

where H is the depth to centerline and α is given by:

$$\alpha=\frac{H}{R}-\sqrt{\left(\frac{H}{R}\right)^2-1} \qquad \{3\text{-}6\}$$

where R is the tunnel radius (Figure 3.3). It can readily be seen that H can spatially normalize the solution and that the key parameter is the embedment to radius ratio, R/H. The horizontal boundary given by y=0 in the z-space is mapped onto a circle of unit radius in the ζ-space and the circular tunnel boundary given by $\left(x^2\right)+\left(H+y\right)^2-R^2=0$ at the z-space onto a circle of radius α in the ζ-space.

As the Goursat functions are analytic, they can be expanded in Laurent series as follows:

$$\phi(\zeta)=a_0+\sum_{k=1}^{\infty}a_k\cdot\zeta^k+\sum_{k=1}^{\infty}b_k\cdot\zeta^{-k} \qquad \{3\text{-}7a\}$$

$$\psi(\zeta)=c_0+\sum_{k=1}^{\infty}c_k\cdot\zeta^k+\sum_{k=1}^{\infty}d_k\cdot\zeta^{-k} \qquad \{3\text{-}7b\}$$

where the coefficients a_k, b_k, c_k, and d_k are found by imposing the boundary conditions at both boundaries. These coefficients are calculated by means of recursive relations derived from the boundary conditions. Only the value of a_0 remains undetermined, but it is obtained as the value that makes the coefficients of the expansions vanish for large k (a requirement for convergence). This is done by means of taking advantage of the linearity of the recursive relations. Hence, two tentative values of a_0 are used to calculate an approximate value of a_∞ and the value that makes a_∞= 0 is found by linear interpolation. Further details are given in Appendix I.

In order to obtain the recursive relations, the displacement boundary condition needs to be expanded in Fourier series as follows:

$$2 \cdot G \cdot (1 - \alpha \cdot \sigma) \cdot u_z(\sigma) = \sum_{k=-\infty}^{\infty} A_k \cdot \sigma^k \qquad \{3\text{-}8\}$$

where $\alpha \cdot \sigma = \alpha \cdot e^{i \cdot \theta}$ represent the mapped coordinate ζ at the tunnel boundary. The coefficients A_k are obtained as follows:

$$A_k = \frac{1}{2 \cdot \pi} \cdot \int_0^{2 \cdot \pi} 2 \cdot G \cdot (1 - \alpha \cdot \sigma) \cdot u_z(\sigma) \cdot \sigma^{-k} \cdot d\theta \qquad \{3\text{-}9\}$$

Once the values of these coefficients are known, they are replaced in the recursive relations in order to calculate the Laurent expansion coefficients. Thus, the Goursat functions and their derivatives are calculated and the solution for the problem can be obtained.

3.2.1. Uniform Convergence

Verruijt (1997) gives full details of the uniform convergence solution. The coefficients in equation {3-9} are given by:

$$\left.\begin{aligned} A_k &= 0 && \forall k < 0 \\ A_0 &= 2 \cdot i \cdot G \cdot u_\varepsilon \cdot \alpha \\ A_1 &= -2 \cdot i \cdot G \cdot u_\varepsilon \\ A_k &= 0 && \forall k > 1 \end{aligned}\right\} \qquad \{3\text{-}10\}$$

where u_ε is the radial convergence at the tunnel wall, defined positive as shown in Figure 3.4. This definition is consistent with the convention adopted in Section 2.1.

The vertical displacements do not vanish at infinity for this solution. Instead they converge to a finite value. This means that a rigid body motion must be subtracted in order to obtain physically

meaningful far field conditions. Verruijt (1997) discusses this peculiar result, which is a consequence of the half plane being unrestrained[1].

A simple computer program has been written (Appendix II) in order to implement this solution. The number of terms needed for the evaluation of the Goursat functions is determined by a convergence criterion. The criterion is based on the following error norm:

$$\varepsilon = \sqrt{\frac{1}{L}\cdot\int_{L}\left[\left(u_x - u^{\infty}{}_x\right)^2 + \left(u_y - u^{\infty}{}_y\right)^2\right]\cdot dx}\Bigg|_{y=0,\ L\to\infty} \qquad \{3\text{-}11\}$$

where $u_y{}^{\infty}$ and $u_x{}^{\infty}$ are the ground surface displacement components in the far field ($x \rightarrow \infty$). The length, L, is taken as $8{\cdot}H$, $u^{\infty}{}_x$ and $u^{\infty}{}_y$ are evaluated with k = 150. The criterion consist of selecting the minimum value of k that makes $\varepsilon < 10^{-8}$, which is the round-off error used in the numerical evaluation of $u^{\infty}{}_x$ and $u^{\infty}{}_y$. Results for different *R/H* ratios are shown in Figure 3.5. It can be seen that the series converge faster for lower *R/H* ratios (i.e., deep tunnels), being the absolute minimum number of terms needed dictated by the Fourier representation of the displacement boundary conditions (which in this case is 2). The convergence rate appears to be independent of the Poisson ratio.

The vertical translation is shown in Figure 3.6 as a function of the tunnel raidus to depth ratio (*R/H*). In this figure, Δu_y are the corrective vertical rigid body displacement (equal to the vertical translation of the tunnel) and u_ε is the convergence at the tunnel wall (Figure 3.4). The results highlight the importance of Poisson ratio in controlling the vertical translation. The higher the Poisson ratio the smaller the translation correction.

This result is explained by the fact that the spring constants (i.e., stresses due to a unit displacement) at the tunnel wall are more uniform for higher Poisson ratios as can be seen in

[1] The author has also verified that if a uniform vertical displacement boundary condition is applied at the tunnel wall, the solution is a rigid body motion. Hence, after correcting the displacements at infinity, the solution is zero, which is again a consequence of the half plane being unrestrained. Hence, the complex function solution cannot separate the influence of the uniform convergence from the vertical translation deformation modes (Figure 3.2).

Figure 3-7 (Verruijt, 1997). The ratio $\Delta u_y/u_\varepsilon > 1$ means that the vertical displacement at the tunnel invert is negative (i.e., downward movement), while the vertical displacement at the crown exceeds the assumed uniform convergence u_ε by more than 100%. This situation can only takes place for shallow tunnels (R/H>0.65) and Poisson ratios lower than 0.2, approximately.
Figure 3.8 illustrates the combined effects of uniform convergence and vertical translation predicted for selected R/H and ν parameters for an assumed uniform convergence of u_ε/R = 0.4. The effects of vertical translation become minor for deep tunnels (R/H = 0.2) in incompressible soils. Figure 3.9 and 3.10 illustrate typical predictions of the horizontal and vertical ground displacements (u_x, u_y) for a tunnel with R/H = 0.5 and ν = 0.25.

3.2.2. Pure Distortion

Chapter 2 showed that an anisotropic initial state of stresses (i.e., $K_0 \neq 1$) in an infinite elastic plane can be represented by the superposition of solutions for hydrostatic compression and a pure distortion. The displacements at the tunnel wall, given by the elastic solution (equation {2-48}) due to the pure distortion in an infinite plane are:

$$u_x(\beta) = u_\delta \cdot cos(\beta) \qquad \{3\text{-}12a\}$$

$$u_y(\beta) = u_\delta \cdot sin(-\beta) \qquad \{3\text{-}12b\}$$

where u_δ is the distortion parameter, which can be obtained from equation {2-47} or taken as an input parameter, regardless of its origin and β is defined in Figure 3.11. The deformation mode, defined by u_δ is defined positive as indicated in Figure 3.11. These displacements are imposed as a boundary condition at the tunnel wall in order to obtain the exact ground displacements in correspondence with this deformation mode.

In order to expand {3-12} into a Fourier series, as required by the exact solution, the displacements need to be expressed complex form. Hence, replacing equation {3-12} in {3-9} and integrating yields:

$$u_z(\beta) = u_\delta \cdot e^{-i\cdot\beta} \qquad \{3\text{-}13\}$$

The $e^{-i\cdot\beta}$ factor can be found by considering the complex vector decomposition in Figure 3.12, where it can be readily seen that:

$$R \cdot e^{i\cdot\beta} = z + i \cdot H \qquad \{3\text{-}14\}$$

Hence,

$$e^{i\cdot\beta} = \frac{z + i \cdot H}{R} \qquad \{3\text{-}15\}$$

Finally;

$$u_z(\beta) = u_\delta \cdot \frac{R}{z(\beta) + i \cdot H} \qquad \{3\text{-}16\}$$

After mapping in the ζ-plane by means of {3-5}, expression {3-16} becomes:

$$u_z(\sigma) = u_\delta \cdot i \cdot \frac{1 - \alpha \cdot \sigma}{\sigma - \alpha} \qquad \{3\text{-}17\}$$

where $\alpha\cdot\sigma = \alpha\cdot e^{i\cdot\theta}$ represent the mapped coordinate ζ at the tunnel boundary and α is given by equation {3-6}. Hence, the Fourier coefficients are found as follows:

$$A_k = \frac{1}{2\cdot\pi}\cdot\int_0^{2\cdot\pi} 2\cdot G\cdot\frac{(1-\alpha\cdot\sigma)^2}{\sigma-\alpha}\cdot u_\delta\cdot i\cdot\sigma^{-k}\cdot d\theta \qquad \{3\text{-}18\}$$

After evaluating the integral expression, the Fourier coefficients can be expressed as follows:

$$\left.\begin{aligned} A_k &= 2\cdot G\cdot u_\delta\cdot i\cdot\left[\alpha^{-(k+1)}\cdot(1-\alpha^2)^2\right] && \forall k<0 \\ A_0 &= 2\cdot G\cdot u_\delta\cdot i\cdot\alpha\cdot(\alpha^2-2) && \\ A_1 &= 2\cdot G\cdot u_\delta\cdot i\cdot\alpha^2 && \\ A_k &= 0 && \forall k>1 \end{aligned}\right\} \qquad \{3\text{-}19\}$$

where $\alpha < 1$.

At this point, it is important to remark that α has been defined as indicated in {3-6}, which is slightly different from the original definition proposed by Verruijt (1997), and allows the square root term to be either positive or negative in sign. This general definition would produce exactly the same kind of conformal transformation, regardless of the sign. However, the convergence of the Fourier series terms, given by equation {3-19}, is only assured if α is less than unity, which is fulfilled by the definition expressed in equation {3-6}. The series converges in a few terms as can be seen in Figure 3.13. The number of terms needed for the evaluation of the Goursat functions is determined by the same convergence criterion used for the uniform convergence problem. Results for different *R/H* ratios are shown in Figure 3.14. As for the case of a uniform convergence boundary condition, the series converges faster for lower *R/H* ratios (i.e., deep tunnels), being the absolute minimum number of terms needed dictated by the Fourier representation of the displacement boundary conditions (which in this case is 2). As before, Poisson ratio does not significantly affect the convergence rate.

Once again, the far field vertical displacements do not vanish and a rigid body vertical translation correction is required (as in Section 3.1). The magnitude of this rigid body translation is smaller than that obtained in Section 4.1 for the uniform convergence boundary condition. Figure 3.15 summarizes the correction as a function of *R/H* ratio and ν. A significant influence of the Poisson

ratio is again observed, with larger corrections occurring for higher Poisson ratios, in contrast to the uniform convergence case.

Figure 3.16 illustrates the combined effects of pure distortion and vertical translation predicted for selected R/H and ν parameters for an assumed radial distortion $u_\delta/R = 0.4$. Figures 3.17 and 3.18 illustrate typical predictions of the horizontal and vertical ground displacements (u_x, u_y) for a tunnel with $R/H = 0.5$ and $\nu = 0.25$.

3.3. Approximate Solutions

Sagaseta (1987) proposed an approximate method for estimating the ground displacements by representing the ground loss due to a line sink in an incompressible medium (i.e., $\nu = 0.5$) at shallow depth. The solution method, outlined in Figure 3.19, uses the fundamental solutions for a line sink (ground loss due to tunnel) in a full space. The stress-free ground surface is obtained by superimposing solutions for i) an image sink, which cancels out the normal stress at the surface, and ii) applying corrective surface shear tractions, τ_{xy} (in order to balance the stress component that was not cancelled by the virtual image). This procedure is illustrated in Figure 3.19.

3.3.1. Uniform Convergence

This solution was first obtained by Sagaseta (1987) for the case of a contracting cavity in an incompressible medium (i.e., $\nu = 0.5$) at shallow depth. This problem is often called "ground loss" due to the fact that there is an amount of volume that is lost in the contraction, or "point sink" due to its similarity with the fluid dynamics problem. The solution obtained is exact provided the contracting cavity collapses to a point (i.e., the problem domain is a half plane without a hole). In that sense, the solution is regarded as a "point solution". This solution has found application in several geotechnical problems, yet its most remarkable contribution has been in the analysis of ground deformations due to tunneling. Verruijt et al. (1996), following Sagaseta's method, extended the solution for a general value of Poisson ratio.

Sagaseta obtained the displacement field due to the point sink and its image by starting from the incompressibility condition and assuming that the direction of the displacement vectors was radial from the point sink (i.e., a one-dimensional problem). The solution, thus obtained, is independent of the constitutive model of the material, provided that it is incompressible. Nevertheless, the solution is the same as the one discussed in Section 2.1. which considers the displacements field due to a hole in an infinite pre-stressed medium subjected to isotropic compression. Hence, both conceptual approaches are valid for the solution: i) the isotropic compression due to a hole in an infinite pre-stressed medium and, ii) a contracting cavity.

The displacement field due to the line sink is given by:

$$u_x(x,y) = u_\varepsilon \cdot \frac{x \cdot R}{x^2 + (y+H)^2} \qquad \{3\text{-}20a\}$$

$$u_y(x,y) = u_\varepsilon \cdot \frac{(y+H) \cdot R}{x^2 + (y+H)^2} \qquad \{3\text{-}20b\}$$

where u_ε is the radial convergence at the tunnel boundary ($r = R$). Equations {3-20} can also be expressed in terms of the ground loss volume (V_L), which is related to the radial convergence as follows:

$$u_\varepsilon = \frac{V_L}{2 \cdot \pi \cdot R} \qquad \{3\text{-}21\}$$

The displacements field due to the negative mirror image (located at $y = H$, Figure 3.19) is:

$$u_x(x,y) = -u_\varepsilon \cdot \frac{x \cdot R}{x^2 + (y-H)^2} \qquad \{3\text{-}22a\}$$

$$u_y(x,y) = -u_\varepsilon \cdot \frac{(y-H)\cdot R}{x^2+(y-H)^2} \qquad \{3\text{-}22b\}$$

By adding equations {3-20} and {3-22} both the horizontal displacements and normal stresses at the surface vanish. However, it should be noticed that the displacement field, resulting from the addition of {3-20} and {3-22}, would be exact only for the case of a cavity which collapses into a point (since each solution does not consider the presence of the cavity created by the other).

The unbalanced shear stresses, τ_{xy}, at the surface are calculated by the following classical expression derived from theory of elasticity:

$$\tau_{xy} = G \cdot \left[\frac{\partial u_y}{\partial x} + \frac{\partial u_x}{\partial y} \right] \qquad \{3\text{-}23\}$$

Replacing equations {3-20} and {3-22} into {3-23} yields:

$$\tau_{xy}(x) = -8 \cdot G \cdot u_\varepsilon \cdot R \cdot H \cdot \frac{x}{\left(x^2+H^2\right)^2} \qquad \{3\text{-}24\}$$

Hence, in order to balance the shear stresses at the surface, a stress boundary condition opposite to {85} has to be applied at the surface. In order to evaluate the displacement field due to these stresses, Airy's stress function (F) needs to be obtained by the following expression (Appendix III):

$$F(x,y) = \frac{i}{2\cdot\pi} \cdot \int_{-\infty}^{\infty} \Im_{xy}(\omega) \cdot \frac{y}{\omega} \cdot e^{|\omega|\cdot y} \cdot e^{i\cdot\omega\cdot x} \cdot d\omega \qquad \{3\text{-}25\}$$

where $\Im_{xy}(\omega)$ stands for the Fourier transform of the shear stress boundary condition, given by:

$$\Im_{xy}(\omega) = \int_{-\infty}^{\infty} 8 \cdot G \cdot u_\varepsilon \cdot R \cdot H \cdot \frac{x}{\left(x^2 + H^2\right)^2} \cdot e^{-i \cdot \omega \cdot x} \cdot dx \qquad \{3\text{-}26\}$$

Equation {3-25} is the exact solution for the stress Function of a half plane (i.e., without a hole) subjected to shear stresses at the surface (i.e., it is only exact if the cavity collapses into a point).

After the evaluation of the integral, equation {3-26} becomes:

$$\Im_{xy}(\omega) = -4 \cdot \pi \cdot \omega \cdot i \cdot G \cdot u_\varepsilon \cdot R \cdot e^{-|\omega| \cdot H} \qquad \{3\text{-}27\}$$

Hence, replacing equation {3-27} in {3-25} and evaluating the integral yields:

$$F(x,y) = 4 \cdot G \cdot u_\varepsilon \cdot R \cdot y \cdot \frac{H - y}{x^2 + (y - H)^2} \qquad \{3\text{-}28\}$$

In order to evaluate the displacements, equations {2-34} to {2-38} are used. For this problem, Q_1 is given by:

$$Q_1(x,y) = 8 \cdot G \cdot u_\varepsilon \cdot R \cdot \frac{(y - H)^2 - x^2}{\left((y - H)^2 + x^2\right)^2} \qquad \{3\text{-}29\}$$

and the harmonic conjugate Q_2 by[2]:

$$Q_2(x,y) = 16 \cdot G \cdot u_\varepsilon \cdot R \cdot x \cdot \frac{(y - H)}{\left((y - H)^2 + x^2\right)^2} \qquad \{3\text{-}30\}$$

---

[2] i.e., $Q_2 = -\int \frac{\partial Q_1}{\partial y} \cdot dx$

$$Q_1 + i \cdot Q_2 = -8 \cdot G \cdot u_\varepsilon \cdot \frac{R}{(z - i \cdot H)^2} \qquad \{3\text{-}31\}$$

Replacing {3-31} in {2-35} and evaluating the integral yields:

$$q_1 + i \cdot q_2 = \frac{8 \cdot G \cdot u_\varepsilon \cdot R}{z - i \cdot H} \qquad \{3\text{-}32\}$$

After separating real and imaginary components of {3-32} the following expressions are found:

$$q_1 = 8 \cdot G \cdot u_\varepsilon \cdot R \cdot \frac{x}{x^2 + (y - H)^2} \qquad \{3\text{-}33a\}$$

$$q_2 = -8 \cdot G \cdot u_\varepsilon \cdot R \cdot \frac{(y - H)}{x^2 + (y - H)^2} \qquad \{3\text{-}33b\}$$

Differentiation of the Airy stress function (equation {3-28}) with respect to the spatial coordinates:

$$\frac{\partial F}{\partial x} = 8 \cdot G \cdot u_\varepsilon \cdot R \cdot y \cdot x \cdot \frac{y - H}{\left(x^2 + (y - H)^2\right)^2} \qquad \{3\text{-}34a\}$$

$$\frac{\partial F}{\partial y} = -4 \cdot G \cdot u_\varepsilon \cdot R \cdot \frac{2 \cdot (y - H) \cdot x^2 + H \cdot \left[x^2 - (y - H)^2\right]}{\left(x^2 + (y - H)^2\right)^2} \qquad \{3\text{-}34b\}$$

Replacing equations {3-33} and {3-34} in {2-34} leads to the displacement field due to the corrective shear stresses at the surface:

$$u_x(x,y) = 4 \cdot u_\varepsilon \cdot R \cdot \left\{ \frac{(1-\nu)\cdot x}{x^2+(y-H)^2} - \frac{(y-H)\cdot x \cdot y}{\left[x^2+(y-H)^2\right]^2} \right\} \qquad \{3\text{-}35a\}$$

$$u_y(x,y) = 2 \cdot u_\varepsilon \cdot R \cdot \left\{ \frac{2\cdot(y-H)\cdot x^2 + H\cdot\left[x^2-(y-H)^2\right]}{\left[x^2+(y-H)^2\right]^2} - \frac{2\cdot(1-\nu)\cdot(y-H)}{x^2+(y-H)^2} \right\} \qquad \{3\text{-}35b\}$$

The final solution is found by adding equations {3-20}, {3-22}, and {3-35}. Verruijt et al. (1996) obtained the same solution by using a positive mirror image.

With this approach, a uniform vertical translation at the tunnel wall is also obtained, primarily due to the negative mirror image. The vertical translation is defined as the vertical displacement at the springline, Δu_y, the resulting expression is:

$$\frac{\Delta u_y}{u_\varepsilon} = 4 \cdot \frac{R}{H} \cdot \frac{8\cdot(1-\nu) - (1-2\cdot\nu)\cdot\left(\frac{R}{H}\right)^2}{\left[4+\left(\frac{R}{H}\right)^2\right]^2} \qquad \{3\text{-}36\}$$

This result is in remarkably close agreement with the exact solution (Section 3.2.1.), as can be seen in Figure 3.20.

Figure 3.21 summarizes deformations of the tunnel wall for different Poisson ratios and radius to depth ratios. It can be seen that the deformed shapes are very similar to results presented previously in Figure 3.8 using exact modeling of the tunnel cavity. The approximate solution generates slightly higher displacements at the tunnel crown as can be seen in Figure 3.22, which corresponds to the case of a shallow tunnel. Figure 3.23 and 3.24 illustrate typical predictions of the horizontal and vertical ground displacements (u_x, u_y) for a tunnel with R/H = 0.5 and ν = 0.25. It can be seen that the results are similar to those presented previously in Figures 3.9 and 3.10 using exact modeling of the tunnel cavity.

It is important to notice the singular nature of this solution. If the tunnel radius tends to zero, but keeping the amount of ground loss volume (given by equation {3-21}) finite, the displacement field remains finite.

3.3.2. Pure Distortion

This solution was first obtained by Verruijt et al. (1996) using the same approach as Sagaseta (1987) for the line sink. In this case, the fundamental solution used is the one corresponding to the distortion of a circular hole in an infinite plane, derived in Section 2.2. Verruijt and Booker (1996) used the far-field approximation for the fundamental displacement solutions, which simplifies the mathematical expressions. In this work, the exact solutions are used for the distortion of the unlined tunnel and its mirror image, while the far field approximation is used in order to correct the shear tractions at the surface.

The displacement field due to the distortion of the unlined tunnel at depth H (equations {2-48}) is given by (full space solution):

$$u_x(x,y)=u_\delta\cdot\frac{R}{3-4\cdot\nu}\cdot x\cdot\frac{(3-4\cdot\nu)\cdot\left[x^2+(y+H)^2\right]^2-\left[3\cdot(y+H)^2-x^2\right]\cdot\left[x^2+(y+H)^2-R^2\right]}{\left[x^2+(y+H)^2\right]^3} \qquad \{3\text{-}37a\}$$

$$u_y(x,y)=-u_\delta\cdot\frac{R}{3-4\cdot\nu}\cdot(y+H)\cdot\frac{(3-4\cdot\nu)\cdot\left[x^2+(y+H)^2\right]^2-\left[3\cdot x^2-(y+H)^2\right]\cdot\left[x^2+(y+H)^2-R^2\right]}{\left[x^2+(y+H)^2\right]^3} \qquad \{3\text{-}37b\}$$

where u_δ is the distortion parameter. Assuming small displacements (i.e., $u_\delta/R \ll 1$) the distortion parameter can be related to the volume of the expansion at the tunnel springline (Figure 3.25) as follows:

$$W_1 = u_\delta \cdot R \qquad \{3\text{-}38\}$$

This volume W_1 is equal in magnitude and opposite in sign to the volume of the contraction at the tunnel crown and invert (W_2, Figure 3.25, assuming small displacements).

Following the method of Sagaseta (1987), the displacement field due to the negative mirror image is:

$$u_x(x,y) = -u_\delta \cdot \frac{R}{3-4\cdot\nu} \cdot x \cdot \frac{(3-4\cdot\nu)\cdot\left[x^2+(y-H)^2\right]^2 - \left[3\cdot(y-H)^2 - x^2\right]\cdot\left[x^2+(y-H)^2-R^2\right]}{\left[x^2+(y-H)^2\right]^3} \qquad \{3\text{-}39a\}$$

$$u_y(x,y) = u_\delta \cdot \frac{R}{3-4\cdot\nu} \cdot (y-H) \cdot \frac{(3-4\cdot\nu)\cdot\left[x^2+(y-H)^2\right]^2 - \left[3\cdot x^2 - (y-H)^2\right]\cdot\left[x^2+(y-H)^2-R^2\right]}{\left[x^2+(y-H)^2\right]^3} \qquad \{3\text{-}39b\}$$

By adding {3-37} and {3-39}, the horizontal displacements and the normal stresses cancel out at the surface ($y = 0$). It should be noticed that this direct superposition of the solutions neglects the influence of the holes. Hence, the superposition is only exact for the case of an infinitesimal tunnel.

The unbalanced tractions at the ground surface are calculated by replacing the equations {3-37} and {3-39} into {3-23}:

$$\tau_{xy} = \frac{16\cdot u_\delta \cdot H \cdot R \cdot G \cdot x}{3-4\cdot\nu} \cdot \frac{\left(x^2-H^2\right)\cdot\left[2\cdot\left(x^2+H^2\right)-3\cdot R^2\right]}{\left(x^2+H^2\right)^4} \qquad \{3\text{-}40\}$$

Assuming that $H^2 >> R^2$, equation {3-40} reduces to:

$$\tau_{xy} = -\frac{32 \cdot u_\delta \cdot H \cdot R \cdot G \cdot x}{3-4 \cdot \nu} \cdot \frac{x^2 - H^2}{\left(x^2 + H^2\right)^3} \qquad \{3\text{-}41\}$$

Hence, in order to balance the shear stresses at the surface, a stress boundary condition opposite to {3-41} must be introduced at the surface. The displacements are evaluated by means of expressions {2-34} to {2-37}, for which Airy's stress function needs to be evaluated as outlined above (equation {3-25}).

The Fourier transform for the shear stress boundary condition at the surface for this case is:

$$\mathfrak{T}_{xy}(\omega) = \int_{-\infty}^{\infty} \frac{32 \cdot u_\delta \cdot H \cdot R \cdot G \cdot x}{3-4 \cdot \nu} \cdot \frac{x^2 - H^2}{\left(x^2 + H^2\right)^3} \cdot e^{-i \cdot \omega \cdot x} \cdot dx \qquad \{3\text{-}42\}$$

After the evaluation of the integral expression, equation {3-42} becomes:

$$\mathfrak{T}_{xy}(\omega) = \frac{8 \cdot u_\delta \cdot R \cdot G}{3-4 \cdot \nu} \cdot \pi \cdot i \cdot \omega \cdot e^{-|\omega| \cdot H} \cdot \left(|\omega| \cdot H - 1\right) \qquad \{3\text{-}43\}$$

Hence, replacing {3-43} in {3-25} and evaluating the integral, the Airy stress function is obtained as:

$$F(x,y) = \frac{8 \cdot u\delta \cdot R \cdot G}{3-4 \cdot \nu} \cdot \frac{H \cdot x^2 - (y-H) \cdot \left[(y-H)^2 + H \cdot (y-H) + x^2\right]}{\left[x^2 + (y-H)^2\right]^2} \qquad \{3\text{-}44\}$$

The displacements are obtained using the derivatives of the Airy stress function and harmonic functions Q_1 and Q_2, as indicated in {2-34}. For this problem, Q_1 is given by:

$$Q_1 = -\frac{16 \cdot u\delta \cdot R \cdot G}{3-4 \cdot \nu} \cdot \frac{H^4 + x^4 - y^4 + 2 \cdot H \cdot y \cdot \left(y^2 - H^2\right) + 6 \cdot x^2 \cdot H \cdot (y - H)}{\left[x^2 + (y-H)^2\right]^3} \qquad \{3\text{-}45a\}$$

Its harmonic conjugate Q_2 by:

$$Q_2 = \frac{32 \cdot u\delta \cdot R \cdot G}{3-4 \cdot \nu} \cdot x \cdot \frac{2 \cdot H \cdot \left(H^2 - x^2\right) - 3 \cdot y \cdot H^2 + y \cdot \left(x^2 + y^2\right)}{\left[x^2 + (y-H)^2\right]^3} \qquad \{3\text{-}45b\}$$

and the sum, $Q_1 + i \cdot Q_2$:

$$Q_1 + i \cdot Q_2 = -\frac{16 \cdot u\delta \cdot R \cdot G}{3-4 \cdot \nu} \cdot \frac{z + i \cdot H}{(z - i \cdot H)^3} \qquad \{3\text{-}46\}$$

Replacing equation {3-46} in {2-35} and evaluating the integral we obtain:

$$q_1 + i \cdot q_2 = \frac{16 \cdot u\delta \cdot R \cdot G}{3-4 \cdot \nu} \cdot \left[\frac{1}{z - i \cdot H} + \frac{i \cdot H}{(z - i \cdot H)^2}\right] \qquad \{3\text{-}47\}$$

After separating real and imaginary components of {3-47}, q_1 and q_2 are found as:

$$q_1 = \frac{16 \cdot u\delta \cdot R \cdot G}{3-4 \cdot \nu} \cdot \left\{x \cdot \frac{x^2 + y^2 - H^2}{\left[x^2 + (y-H)^2\right]^2}\right\} \qquad \{3\text{-}48a\}$$

$$q_2 = \frac{16 \cdot u\delta \cdot R \cdot G}{3-4 \cdot \nu} \cdot \left\{\frac{x^2 \cdot (2 \cdot H - y) - y \cdot (y-H)^2}{\left[x^2 + (y-H)^2\right]^2}\right\} \qquad \{3\text{-}48b\}$$

Differentiation of the Airy stress function (equation {3-44}) with respect to the spatial coordinates yields:

$$\frac{\partial F}{\partial x} = \frac{16 \cdot u\delta \cdot R \cdot G}{3-4 \cdot \nu} \cdot x \cdot y \cdot \frac{y \cdot \left(x^2 + y^2\right) + 2 \cdot H \cdot \left(H^2 - x^2\right) - 3 \cdot y \cdot H^2}{\left[x^2 + (y-H)^2\right]^3} \qquad \{3\text{-}49a\}$$

$$\frac{\partial F}{\partial y} = \frac{16 \cdot u\delta \cdot R \cdot G}{3-4 \cdot \nu} \cdot \frac{(y-H) \cdot \left\{H \cdot y \cdot (y-H)^2 - x^2 \cdot \left[\left(x^2 + y^2\right) + H \cdot (y+H)\right]\right\}}{\left[x^2 + (y-H)^2\right]^3} \qquad \{3\text{-}49b\}$$

Replacing equations {3-49} and {3-49} in {2-34} produces the displacement field due to the corrective shear stresses at the surface:

$$u_x = \frac{8 \cdot u_\delta \cdot R}{3-4 \cdot \nu} \cdot \left\{ x \cdot \frac{x^2 + y^2 - H^2}{\left[x^2 + (y-H)^2\right]^2} \cdot (1-\nu) - x \cdot y \cdot \frac{y \cdot \left(x^2 + y^2\right) + 2 \cdot H \cdot \left(H^2 - x^2\right) - 3 \cdot y \cdot H^2}{\left[x^2 + (y-H)^2\right]^3} \right\} \qquad \{3\text{-}50a\}$$

$$u_y = \frac{8 \cdot u_\delta \cdot R}{3-4 \cdot \nu} \cdot \left\{ \begin{array}{l} \dfrac{x^2 \cdot (2 \cdot H - y) - y \cdot (y-H)^2}{\left[x^2 + (y-H)^2\right]^2} \cdot (1-\nu) - \ldots \\ \ldots - \dfrac{(y-H) \cdot \left\{H \cdot y \cdot (y-H)^2 - x^2 \cdot \left[\left(x^2 + y^2\right) + H \cdot (y+H)\right]\right\}}{\left[x^2 + (y-H)^2\right]^3} \end{array} \right\} \qquad \{3\text{-}50b\}$$

The final solution is found by adding equations {3-37}, {3-39}, and {3-50}. Verruijt and Booker (1996) obtained similar expressions by using a positive mirror image. However, Verruijt et al. used the far field approximation for the image and its mirror image and defined a relative ovalization parameter (δ) which is related to the distortion parameter (u_δ) as follows:

$$\delta = \frac{u_\delta}{R} \frac{4 \cdot (1-\nu)}{3-4 \cdot \nu} \qquad \{3\text{-}51\}$$

With this approach, a uniform vertical translation at the tunnel wall is also obtained (primarily due to the negative mirror image). The vertical translation, Δu_y, is defined as the vertical displacement at the springline, the resulting expression is:

$$\frac{\Delta u_y}{u_\delta} = \frac{2}{3-4\cdot\nu}\cdot\frac{R}{H}\cdot\frac{(1-8\cdot\nu)\cdot\left(\frac{R}{H}\right)^4+(11-8\cdot\nu)\cdot 4\cdot\left(\frac{R}{H}\right)^2-32}{\left[4+\left(\frac{R}{H}\right)^2\right]^3} \qquad \{3\text{-}52\}$$

which is again in close agreement with the solution for the exact geometry as shown in Figure 3.26 except for very shallow tunnels with $R/H > 0.75$ and $\nu = 0.5$.

Deformed tunnel walls for different Poisson ratios and R/H ratios are shown in Figure 3.27. It can be seen that the deformed shapes in correspondence to the approximate solution are in good agreement with the ones in correspondence to the exact tunnel geometry (Figure 3.17), especially for the case of deep tunnels. The approximate solution generates higher displacements at the tunnel crown, as can be seen in Figure 3.28 for the case of a shallow tunnel. Typical ground deformation patterns are shown in Figures 3.29 and 3.30. These patterns will be discussed in a subsequent chapter.

It is important to notice the singular nature of this solution. If the tunnel radius tends to zero, but keeping the amount of contracting volume at the sides of the tunnel (given by equation {3-38}) finite, the displacement field remains finite.

3.4. Comparison of Displacement Solutions for Shallow Tunnels

The previous Sections 3.2 and 3.3 have presented two sets of analytical solutions for shallow tunnels, the first modeling the exact circular tunnel geometry (with radius R) and the second assuming that the problem can be approximated by point/line solutions. This Section compares results from both exact and approximate solutions in order to assess whether the simpler approximate solutions can be applied in order to model ground displacements around tunnels.

3.4.1. Uniform Convergence Mode

Figures 3.32 to 3.49 summarize comparisons of ground displacements around a shallow circular tunnel for selected embedment (*R/H*) and Poisson ratios (ν). In all cases, the vertical displacements are symmetric with respect to the *y*-axis, while horizontal displacements are anti-symmetric. The ground displacements distribution—but not their magnitude—evaluated by means of the approximate solution do not depend on the *R/H* ratio, since the displacement field is given by a function of the dimensionless coordinates *x/H* and *y/H* multiplied by *R/H*.

3.4.1.1. Horizontal Displacements

A uniform contraction (i.e. negative u_ε) along the tunnel wall, plus the corresponding vertical translation, causes horizontal ground movements towards the tunnel. The horizontal displacements at the surface are given by:

$$\frac{u_x}{u_\varepsilon} = 4 \cdot (1-\nu) \cdot \frac{R}{H} \cdot \frac{\frac{x}{H}}{\left(\frac{x}{H}\right)^2 + 1} \qquad \{3\text{-}53\}$$

This equation implies a maximum inward displacement at $x = \pm H$, independent of the Poisson ratio. The maximum horizontal displacement, evaluated by the approximate solution, is given by:

$$\frac{u_x|_{\max}}{u_\varepsilon} = \pm 2 \cdot \frac{R}{H} \cdot (1-\nu) \qquad \{3\text{-}54\}$$

Increasing the Poisson ratio has the effect of a faster attenuation of the horizontal displacements with distance, thus reducing the horizontal displacements at the surface.

Similar horizontal displacement patterns are given by both the exact and simplified solutions. However, the approximate solution, predicts slightly higher horizontal displacements (up to

20%) than the exact solution for the case of shallow tunnels (i.e. R/H = 0.7), especially at points near the surface.

3.4.1.2. Vertical Displacements

A uniform contraction along the tunnel wall, plus the corresponding vertical translation, leads to downward displacements everywhere, except in an approximately circular region with a center at $y = y_c$ and radius R_c where:

$$\frac{y_c}{H} = -\frac{2\cdot(1-\nu)+1+\sqrt{1+4\cdot(1-\nu)^2}}{4\cdot(1-\nu)} \qquad \{3\text{-}55a\}$$

$$\frac{R_c}{H} = \frac{\sqrt{1+4\cdot(1-\nu)^2}-(1-2\cdot\nu)}{2\cdot(1-\nu)} \qquad \{3\text{-}56b\}$$

These equations have been derived by means of the approximate solution, hence the R/H ratio has no effects. However, both exact and approximate solutions show the same zone of heaving, defined by equations {3-55}. Increasing the Poisson ratio has the following effects:

- The heaving zone is increased, since the vertical translation decreases (Figure 11).
- There is a larger attenuation of displacements with distance, leading to smaller vertical displacements at the surface.

There is a critical radius to embedment ratio (function of Poisson ratio) for which the heaving zone lies inside the region occupied by the tunnel. Hence, if the R/H ratio exceeds this critical ratio, there is no heaving associated with the contraction of the tunnel. The critical R/H ratio is given by:

$$\left.\frac{R}{H}\right|_{crit} = \frac{(2\cdot\nu - 1) + \sqrt{1 + 4\cdot(1-\nu)^2}}{2\cdot(1-\nu)} \qquad \{3\text{-}57\}$$

Equation {3-57} is plotted in Figure 3.31, where it can be seen that for realistic tunnel embedment (i.e., $R/H<0.7$) there is always a heaving zone for $\nu > 0.1$.

The vertical displacements at the surface are given by:

$$\frac{u_y}{u_\varepsilon} = 4\cdot(1-\nu)\cdot\frac{R}{H}\cdot\frac{1}{\left(\frac{x}{H}\right)^2 + 1} \qquad \{3\text{-}58\}$$

The maximum surface displacement occurs at:

$$\frac{u_y|_{max}}{u_\varepsilon} = 4\cdot\frac{R}{H}\cdot(1-\nu) \qquad \{3\text{-}59\}$$

Hence, the maximum vertical displacement is two times larger than the maximum horizontal displacements. This is also observed in the results obtained by the exact solution.

The area (Ω) enclosed by the original surface and the deformed settlement trough can be evaluated using the approximate solutions, assuming only vertical displacements contribute to this area, given by:

$$\Omega = 4\cdot\pi\cdot u_\varepsilon\cdot R\cdot(1-\nu) \qquad \{3\text{-}60\}$$

Equation {3-60}, together with {3-21}, indicate that the amount of ground loss at the surface (Ω) is equal or bigger than the amount of ground loss at the tunnel wall (V). For the undrained case (i.e. $\nu = 0.5$), $\Omega = V$, while for $\nu = 0$, $\Omega = 2\cdot V$. This was pointed out previously by Verruijt and Booker (1996).

Similar vertical displacement patterns are given by both the exact and simplified solutions. However, the approximate solution, predicts higher vertical displacements (up to 50% at the surface) than the exact solution for the case of shallow tunnels (i.e. R/H = 0.7), especially at points near the surface. This difference is reduced with increasing Poisson ratios.

3.4.2. Pure Distortion Mode

Figures 3-50 to 3.67 summarize approximate and exact predictions of ground displacements for the pure distortion of the tunnel wall at the same selected R/H and ν parameters. As for the previous case, vertical displacements are symmetric with respect to the y-axis, while horizontal displacements are anti-symmetric. In this case, the ground displacements evaluated by means of the approximate solution do depend on the R/H ratio since the displacement field is given by a function of the dimensionless coordinates x/H, y/H, and R/H, multiplied by R/H.
However, if the far field approximations are used (following Verruijt and Booker., 1996), this dependence is lost, since the displacement field is given by a function of the dimensionless coordinates x/H and y/H, multiplied by R/H.

3.4.2.1. Horizontal Displacements

A positive distortion at the tunnel wall leads to:

- Inward movements in an approximately triangular zone bounded by a horizontal line from (x = 0, y = 0) to ($x = \pm H$, y = 0) approximately, and a line from (x = 0, y = 0) to a point at the y axis which depends on the R/H and Poisson ratios. This point is near the crown for ν = 0.5, and is moved upwards with decreasing Poisson ratios. Increasing R/H ratios have the same effect.
- Inward movements occur in an approximately parabolic area underneath the tunnel invert. The vertex of the parabola is located at the y axis at a certain distance from the tunnel invert wich decreases with increasing Poisson ratio. This distance is approximately equal to R for ν = 0.25, and is approximately zero for ν = 0.50. The distance between the vertex of the

parabola and the tunnel invert increases with increasing *R/H* ratio. The parabola tends to open with increasing Poisson ratio, hence leading to a larger area of inward movements.

- Outward movements at the entire ground, with the exception of the areas mentioned above. Horizontal displacements attenuate less with distance with increasing Poisson ratios.

The surface displacements distribution, evaluated by the approximate solution, do not depend on *R/H* or *ν*. However, the magnitude of the displacements do depend on the embedment and Poisson's ratios. The surface displacements, evaluated by the approximate solution, are given by:

$$\frac{u_x(x)}{u_\delta} = 2 \cdot \frac{R}{H} \cdot \frac{4 \cdot (1-\nu)}{3-4 \cdot \nu} \cdot \frac{\left(\frac{x}{H}\right)^2 - 1}{\left[\left(\frac{x}{H}\right)^2 + 1\right]^2} \qquad \{3\text{-}61\}$$

The maximum horizontal displacement at the surface is then obtained as:

$$\frac{u_x}{u_\delta} = \pm \frac{R}{H} \cdot \frac{2 \cdot (1-\nu)}{3-4 \cdot \nu} \qquad \{3\text{-}62\}$$

occuring at the point:

$$\frac{x}{H} = \pm 1 \mp \sqrt{2} \qquad \{3\text{-}63\}$$

Hence, the maximum inward movement at the tunnel surface (at $x/H = \pm 0.4142$) is equal in magnitude and opposite in sign to the maximum outward movement (at $x/H = \pm 2.4142$).
However, the exact solution does not show this symmetry of maximum-minimum values. To the contrary, for very shallow tunnels (i.e. $R/H = 0.7$), the exact solution predicts that the maximum inward movemert is close to zero, thus leading to a zone of almost no horizontal displacements at the surface.

Nevertheless, similar horizontal displacement patterns are given by both the exact and simplified solutions. The approximate solution, predicts higher horizontal displacements than the exact solution for the case of shallow tunnels (i.e. $R/H = 0.7$), especially at points near the surface. This difference is increased with increasing Poisson ratios, especially for very shallow tunnels.

3.4.2.2. Vertical Displacements

A positive distortion at the tunnel wall leads to:

- Downward displacements in an approximately rectangular area delimited by two horizontal segments from ($x = -H$, $y = 0,-1$) to ($x=0$, $y=0,-1$) and two vertical segments from ($x = 0,-1$, $y = -1$) to ($x = 0,-1$, $y = 0$). Increasing Poisson ratios tend to distort this rectangular area, and increase the downward movement zone.
- Upward displacements at the entire ground, with the exception of the above mentioned rectangular area.

The surface displacement distribution, evaluated by the approximate solution, does not depend on the R/H and Poisson ratio. However, the magnitude of the displacements do depend on the R/H and Poisson ratio. The surface displacements, evaluated by the approximate solution, are given by:

$$\frac{u_v(x)}{u_\delta} = 2 \cdot \frac{R}{H} \cdot \frac{4 \cdot (1-\nu)}{3-4 \cdot \nu} \cdot \frac{\left[\left(\frac{x}{H}\right)^4 - 1\right] + \frac{1}{4 \cdot (1-\nu)} \cdot \left(\frac{R}{H}\right)^2 \cdot \left[1 - 3 \cdot \left(\frac{x}{H}\right)^2\right]}{\left[\left(\frac{x}{H}\right)^2 + 1\right]^3} \qquad \{3\text{-}64\}$$

where it can readily be seen that the R/H and Poisson ratios do affect the distribution of displacements at the surface. However, if the far field approximation is assumed, the displacements at the surface are given by:

$$\frac{u_y(x)}{u_\delta} = 2 \cdot \frac{R}{H} \cdot \frac{4 \cdot (1-\nu)}{3-4 \cdot \nu} \cdot \frac{\left(\frac{x}{H}\right)^2 - 1}{\left[\left(\frac{x}{H}\right)^2 + 1\right]^2} \qquad \{3\text{-}65\}$$

where it can be seen that the *R/H* and Poisson ratios do not affect the distribution of displacements at the surface. This expression is also given by Verruijt and Booker (1996).

Equation {3-65} generates a minimum value (i.e. a maximum surface settlement) at x=0, given by:

$$\frac{u_y|_{min}}{u_\delta} = -2 \cdot \frac{R}{H} \cdot \frac{4 \cdot (1-\nu)}{3-4 \cdot \nu} \cdot \left[1 - \frac{1}{4 \cdot (1-\nu)} \cdot \left(\frac{R}{H}\right)^2\right] \qquad \{3\text{-}66\}$$

If the far field approximation is used, equation {3-66} can be simplified as follows:

$$\frac{u_y|_{min}}{u_\delta} = -2 \cdot \frac{R}{H} \cdot \frac{4 \cdot (1-\nu)}{3-4 \cdot \nu} \qquad \{3\text{-}67\}$$

Conversely, there is also a maximum value (i.e. a maximum surface heave) at:

$$\frac{x}{H} = \pm \sqrt{1 + \frac{3}{4 \cdot (1-\nu)} \cdot \left(\frac{R}{H}\right)^2 + \sqrt{4 + 9 \cdot \left(\frac{1}{2 \cdot \sqrt{1-\nu}} \cdot \frac{R}{H}\right)^4}} \qquad \{3\text{-}68\}$$

If the far field approximation is used, equation {3-68} can be simplified to:

$$\frac{x}{H} = \pm \sqrt{3} \qquad \{3\text{-}69\}$$

The maximum value of the vertical displacement is given by:

$$\frac{u_u|_{max}}{u_\delta} = \frac{R}{H}\cdot\frac{32\cdot(1-\nu)^2}{3-4\cdot\nu}\cdot\ldots$$
$$\ldots\cdot\frac{\left[\left(\frac{R}{H}\right)^2+8\cdot(1-\nu)\right]^2+8\cdot\left(\frac{R}{H}\right)^4+\left[3\cdot\left(\frac{R}{H}\right)^2-8\cdot(1-\nu)\right]\cdot\sqrt{64\cdot(1-\nu)^2+9\cdot\left(\frac{R}{H}\right)^4}}{\left[3\cdot\left(\frac{R}{H}\right)^2+8\cdot(1-\nu)+\sqrt{64\cdot(1-\nu)^2+9\cdot\left(\frac{R}{H}\right)^4}\right]^3} \qquad \{3\text{-}70\}$$

which can be simplified by using the far field approximation as follows:

$$\frac{u_u|_{max}}{u_\delta} = \frac{R}{H}\cdot\frac{1-\nu}{3-4\cdot\nu} \qquad \{3\text{-}71\}$$

By comparing equations {3-71} and {3-67}, it can be seen that the maximum heaving is approximately (since the expressions correspond to the far field approximation of the approximate solution) one half of the maximum settlement.

Similar vertical displacement patterns are given by both the exact and simplified solutions. The approximate solution, predicts higher vertical displacements than the exact solution for the case of shallow tunnels (i.e. R/H = 0.7), especially at points near the surface. This difference is increased with increasing Poisson ratios, especially for very shallow tunnels.

3.4.3. Conclusions

Both exact and approximate solutions give similar ground displacement patterns due to both uniform convergence and pure distortion modes. For very shallow tunnels (i.e., $R/H > 0.45$) the magnitudes of the ground displacements evaluated by means of the approximate solution differ from the ones corresponding to the exact modeling of the tunnel geometry. Nevertheless, for deep tunnels (i.e., $R/H < 0.45$), the difference is negligible for practical purposes.

In order to model ground displacements due to very shallow cavities (such as the Río Piedras Station in the Tren Urbano), the complex variable solution can be used in order to obtain more realistic results. However, for deep cavities (such as grouting activities and the Twin Bored Tunnels of the Tren Urbano) point solutions should be used, since they are much simpler and the results do not differ (for practical purposes) from the ones corresponding to the exact modeling of the tunnel geometry.

3.5. Relative Distortion

This Section considers the ground displacement patterns due to a combination of a uniform convergence and distortion (and the associated vertical translation). The relative amount of distortion and uniform convergence is given by the relative distortion parameter, ρ, defined in equation {2-53}. If the surface effect and the gradient of stresses with depth are neglected[3], elastic theory indicates that this parameter is a function of K_0, Poisson's ratio, the pore pressure ratio, r_u, and the inner pressure ratio r_p.

The inner pressure arises due to the compression of the lining (in the drained and undrained case) and/or injection pressure of the grouting in the tail void (undrained case). The pressure is assumed to be uniform, since the lining is much stiffer when compressed isotropically due to the ring effect, which is controlled by the axial stiffness, in contrast to the distortion, which is controlled by the bending stiffness. The sign of the relative distortion parameter, as evaluated by means of elasticity theory, is controlled mainly by the K_0 value (ρ negative for $K_0 > 1$). Hence, it would be expected that only highly overconsolidated deposits (i.e., $OCR > 4$) would show negative ρ values.

Figures 3.68 to 3.85 show the normalized ground displacements for R/H = 0.2-0.7, ρ = -0.5, 0.5 and 1.0, and ν = 0.25. It can be seen that the difference between the results obtained by means of the exact and approximate solutions is small. However, the difference increases for very shallow tunnels, especially in the region above the tunnel springline, as discussed in Section 3.4.

[3] Sagaseta (1999), using Verruijt's (1996) solution for the case of a shallow tunnel in an isotropically pre-stressed elastic half plane, has shown that a distortion component also arises from the stress free surface effect. This is explained by the fact that the spring constants along the shallow tunnel wall are non-uniform.

Increasing the relative distortion has the following effects:

- The vertical displacements at the surface have a faster attenuation with distance, hence leading to a narrower width of the settlement trough (i.e., u_y at the surface vs. x). This effect is stronger at low relative distortions.
- The magnitude of the vertical displacement at $x = 0$, $y = 0$ is increased.
- The horizontal displacements at the surface have a faster attenuation, producing a narrower horizontal displacement trough. This effect is much more noticeable at low relative distortions.
- The magnitude of the horizontal displacements at the surface are slightly reduced for negative ρ and increased for $\rho > 0$.
- The ground vertical displacement patterns change dramatically in the region of $\rho < 0$ (e.g., Figure 3.69 vs. Figure 3.71), whereas there is a less dramatic change on the region of $\rho > 0$ (e.g., Figure 3.71 vs. Figure 3.73).
- The ground horizontal displacement patterns change dramatically. If a contraction at the tunnel wall is considered (i.e., negative u_ε), the inward movements near the sides of the tunnel are decreased, leading to a lateral expansion zone for $\rho > 0.8$ (e.g., Figure 3.71 vs. Figure 3.73).

3.5.1. Effects of Relative Distortion on Surface Displacements

This Section studies the effects of ρ, ν, and R/H on the surface displacements. In order to present results in simple equations, the approximate solutions will be used. Nevertheless, it has been show in previous Sections that both exact and approximate solutions show similar results for deep tunnels (i.e., $R/H < 0.7$). However, if a more refined evaluation of ground displacements is needed, the exact solutions can be used.

The effects of relative distortion on the surface displacements will be studied by means of examining its influence on the following:

- General features
- Vertical displacement at x=0 (u_y^0)
- Maximum horizontal displacement (u_x^{max})
- Width of the settlement trough

3.5.1.1. General Features

The surface displacements are given by:

$$\frac{u_x}{u_\varepsilon} = 4\cdot(1-\nu)\cdot\frac{R}{H}\cdot\frac{x}{H}\cdot\frac{\frac{-2\cdot\rho}{3-4\cdot\nu}\cdot\left[\left(\frac{x}{H}\right)^2-1\right]+\left[\left(\frac{x}{H}\right)^2+1\right]^2}{\left[\left(\frac{x}{H}\right)^2+1\right]^3} \qquad \{3\text{-}72a\}$$

$$\frac{u_y}{u_\varepsilon} = 4\cdot(1-\nu)\cdot\frac{R}{H}\cdot\frac{\frac{-2\cdot\rho}{3-4\cdot\nu}\cdot\left\{\left[\left(\frac{x}{H}\right)^4-1\right]-\frac{1}{4\cdot(1-\nu)}\cdot\left[3\cdot\left(\frac{x}{H}\right)^2-1\right]\cdot\left(\frac{R}{H}\right)^2\right\}+\left[\left(\frac{x}{H}\right)^2+1\right]^2}{\left[\left(\frac{x}{H}\right)^2+1\right]^3} \qquad \{3\text{-}72b\}$$

From these equations it can be noticed that:

- Poisson ratio affects both the magnitude [due to the term $4\cdot(1-\nu)$] and distribution of vertical and horizontal displacements [due to the term $(3-4\cdot\nu)$ for the case of the horizontal displacements and due to both $(3-4\cdot\nu)$ and $4\cdot(1-\nu)$ terms for the vertical displacements].
- The *R/H* ratio affects the magnitude and distribution of vertical displacements. However it only affects the magnitude of horizontal displacements, but not their distribution. The horizontal displacements are linear in *R/H*.

It should be noticed that in order to balance the shear stresses at the surface for the pure distortion case, the far field approximation has been used for the point and its mirror image. This involves the approximation that, at the surface, the term $(r/R)^3$ has a negligible influence. If the far field approximation is used for the point and its mirror image, equation {3-72b} becomes:

$$\frac{u_y}{u_\varepsilon} = 4\cdot(1-\nu)\cdot\frac{R}{H}\cdot\frac{\frac{-2\cdot\rho}{3-4\cdot\nu}\cdot\left[\left(\frac{x}{H}\right)^2-1\right]+\left[\left(\frac{x}{H}\right)^2+1\right]}{\left[\left(\frac{x}{H}\right)^2+1\right]^2} \qquad \{3\text{-}73\}$$

It can readily be noticed that if the far field approximation is used for the point and its mirror image, the *R/H* ratio does not affect the distribution of the vertical displacements. It can also be noticed that the vertical and horizontal displacements at the surface are related as follows:

$$u_x = \frac{x}{H}\cdot u_y \qquad \{3\text{-}74\}$$

Hence, in the region where $-H < x < H$, the vertical displacements are larger than the horizontal displacements, and the horizontal displacements are larger than the vertical displacements elsewhere.

3.5.1.2. Vertical Displacement at $x = 0$

The vertical displacement at $x = 0$,u_y^0, is given by:

$$\frac{u_y^{\,0}}{u_\varepsilon} = \frac{4\cdot(1-\nu)}{3-4\cdot\nu}\cdot\frac{R}{H}\cdot\left\{2\cdot\rho\cdot\left[1-\frac{1}{4\cdot(1-\nu)}\cdot\left(\frac{R}{H}\right)^2\right]+3-4\cdot\nu\right\} \qquad \{3\text{-}75\}$$

If the far field approximation is used for the point and its mirror image, u_y^0 can be expressed as follows:

$$\frac{u_y^{\ 0}}{u_\varepsilon} = \frac{4\cdot(1-\nu)}{3-4\cdot\nu}\cdot\frac{R}{H}\cdot\{2\cdot\rho+3-4\cdot\nu\} \qquad \{3\text{-}76\}$$

Figures 3.86 to 3.87 show the effects of ν, ρ and R/H in u_y^0 using both approximate and far field solutions. It can be seen that increasing ν reduce the vertical displacement u_y^0, while increasing R/H and ρ has the effect of increasing the vertical displacement u_y^0. The results obtained by means of the far field approximation are very close to those given by the approximate solution, especially at low embedment ratios, R/H.

3.5.1.3. Maximum Horizontal Displacement

The absolute maximum horizontal displacement occurs at:

$$\frac{x_h}{H} = \pm\sqrt{\frac{\sqrt{32\cdot\rho^2+9-8\cdot(3-2\cdot\nu)}-6\cdot\rho}{3-4\cdot\nu-2\cdot\rho}} \qquad \{3\text{-}77\}$$

From which it can be seen that x_h is a function of the relative distortion and the Poisson ratio. Figure 3.88 shows the influence of relative distortion ρ on the location of maximum horizontal displacement. It can be seen that an increase in the relative distortion has the effect of decreasing the location of the maximum horizontal displacement. For $\rho = 0$, $x_h/H = 1$. The value of x_h/H increases for $\rho < 0$ and higher Poisson ratios, and decreases for positive values of ρ and smaller Poisson ratios. For very large relative distortions, the location of the maximum horizontal displacements tends to a constant value, which is independent of Poisson ratio and is given by {3-63}.

Figure 3.89 shows the value of the absolute maximum displacement, u_x^{max}/u_ε, for different ρ and ν values, where advantage has been taken of the fact that the horizontal displacements are linear in R/H. It can be seen that the absolute maximum horizontal displacement increases with increasing absolute values of relative distortion. Poisson ratio has a strong influence, being the absolute maximum horizontal displacement larger for lower Poisson ratios.

3.5.1.4. Width of the Settlement Trough

Equation {3-72b} shows that the width of the settlement trough is affected by ν, ρ and R/H. However, if the far field (equation {3-73}) approximation is used, R/H does not affect the settlement trough shape. Hence, it can be expected very little influence of R/H on the width of the settlement trough.

Vertical displacement distributions for different R/H ratios are shown in Figure 3-90, where it can be seen that R/H has indeed very little influence for positive relative distortions. Figure 3-91 shows the vertical displacement distribution for different Poisson ratios, from where it can be seen that Poisson ratio does affect the surface settlement distribution. Increasing the Poisson ratio has the effect of decreasing the width of the settlement trough. Figure 3-92 shows the vertical displacement distribution for different relative distortion parameters. In these curves, ρ has a very strong influence on the width of the settlement trough, producing a narrower trough at higher ρ ratios. It can also be seen that the maximum vertical displacement does not occur at x=0 for negative ρ values.

Figure 3.93 shows horizontal displacement distributions for different Poisson ratios, from where it can be seen that ν has a strong influence at the far field (i.e., $|x/H| > 1$). Increasing Poisson ratios leads to a larger attenuation of the horizontal displacements with distance. However, its influence is negligible in the near field. Figure 3.94 shows horizontal displacement distributions for different relative distortions, from where it can be seen that ρ has a strong influence. Increasing relative distortion leads to a faster attenuation of the horizontal displacements with distance. However, if only positive relative distortions are considered, its influence is negligible at the near field.

3.5.2. Effects of Relative Distortion on Horizontal Displacements on a Vertical Line Inside the Ground

This Section considers the effects of the parameters ρ, ν, and R/H on the horizontal displacements along a reference vertical line at $x=2 \cdot R$. The vertical line could represent an inclinometer installed near the tunnel.

Figure 3.95 shows the influence of R/H ratio on the normalized horizontal displacements, $u_x/u_x^{(y=0)}$, where $u_x^{(y=0)}$ is the horizontal displacement at the surface. It can be seen that deeper tunnels ($R/H = 0.2$) show more pronounced inward movements at the springline elevation. It can also be seen that the far field approximation shows slightly different results, especially at the tunnel springline.

Figure 3.96 shows the influence of Poisson ratio, where it can be seen its variation strongly affects the magnitude of the horizontal displacements, especially at the tunnel springline. As for the previous case, the far field approximation shows slightly different results, especially at the tunnel springline.

Figure 3.97 shows the influence of ρ, where it can be seen that it has a strong influence on the horizontal displacement distribution. The horizontal displacement at the tunnel springline and at the surface have opposite signs for high relative distortions ($\rho = 1$). The far field approximation over-estimates the horizontal displacement at the springline for $\rho < 0$ and under-predicts it for $\rho > 0$.

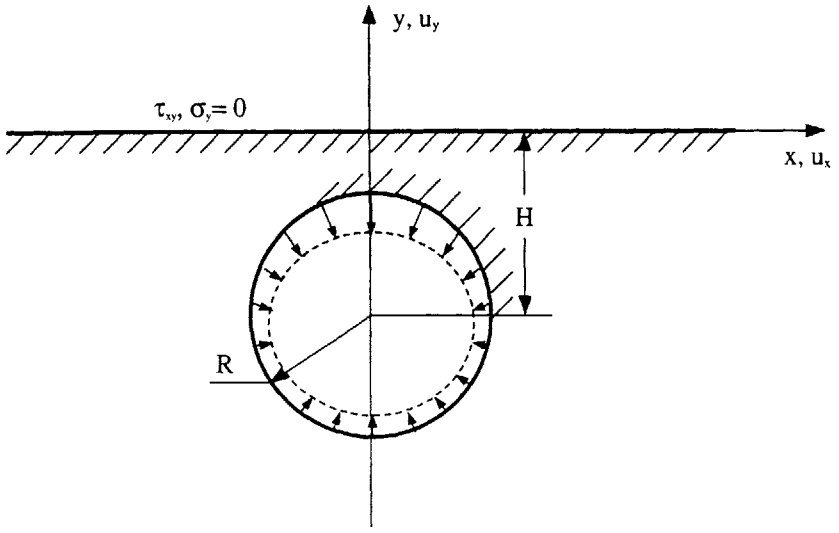

Figure 3.1. Problem outline

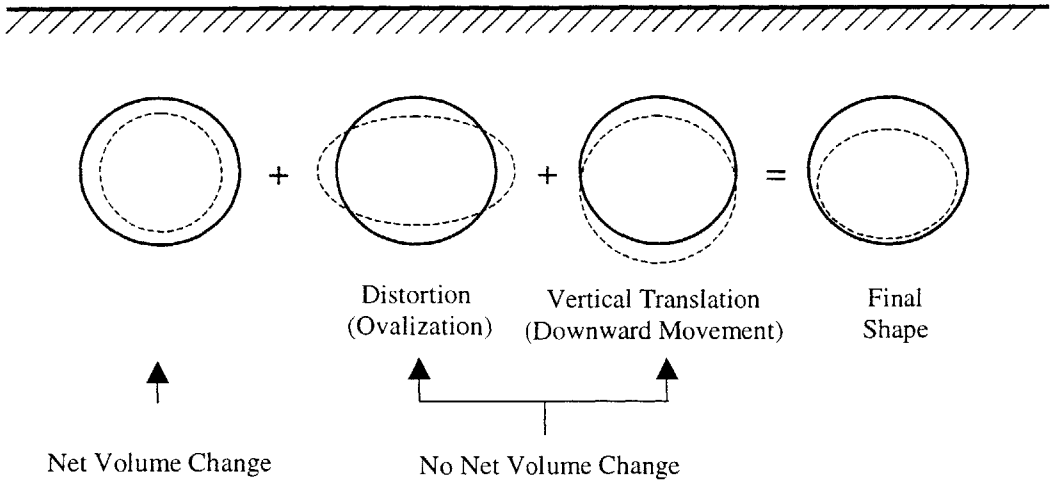

Figure 3.2. Basic deforming modes for tunnel wall (after Sagaseta, 1999)

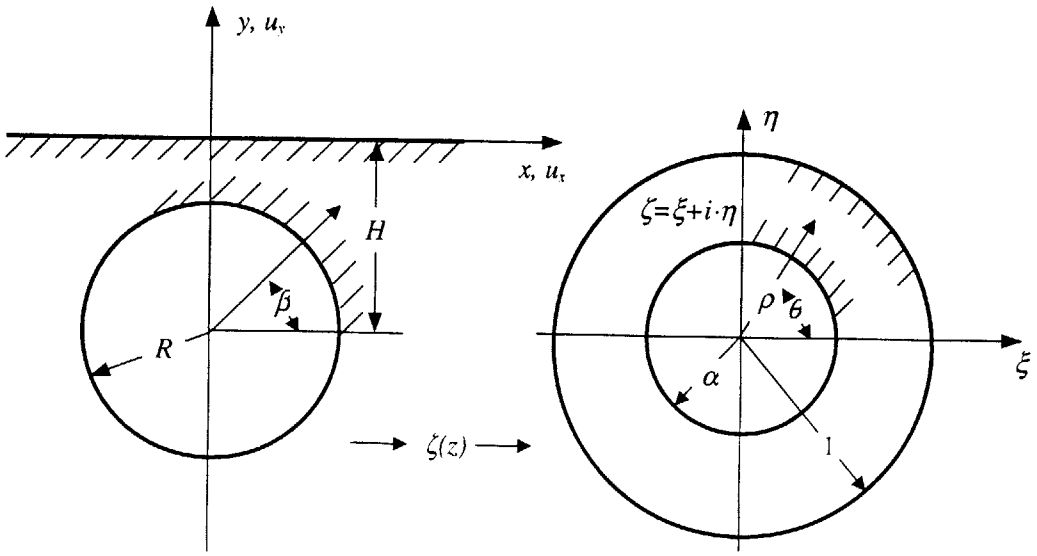

Figure 3.3. Conformal mapping (after Verruijt, 1997)

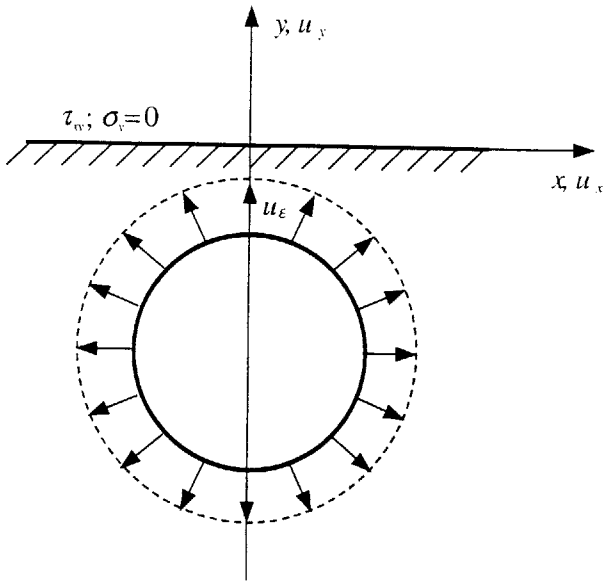

Figure 3.4. Uniform Convergence, definition of u_ε

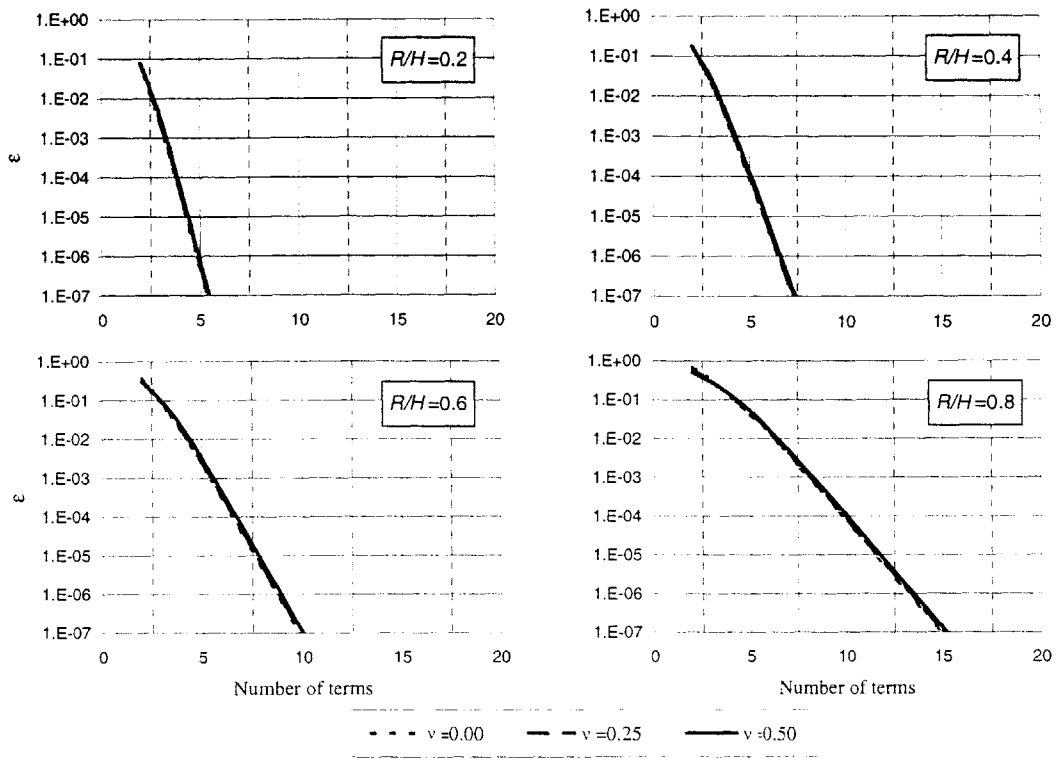

Figure 3.5. Number of series terms needed for accurate evaluation of the Goursat functions

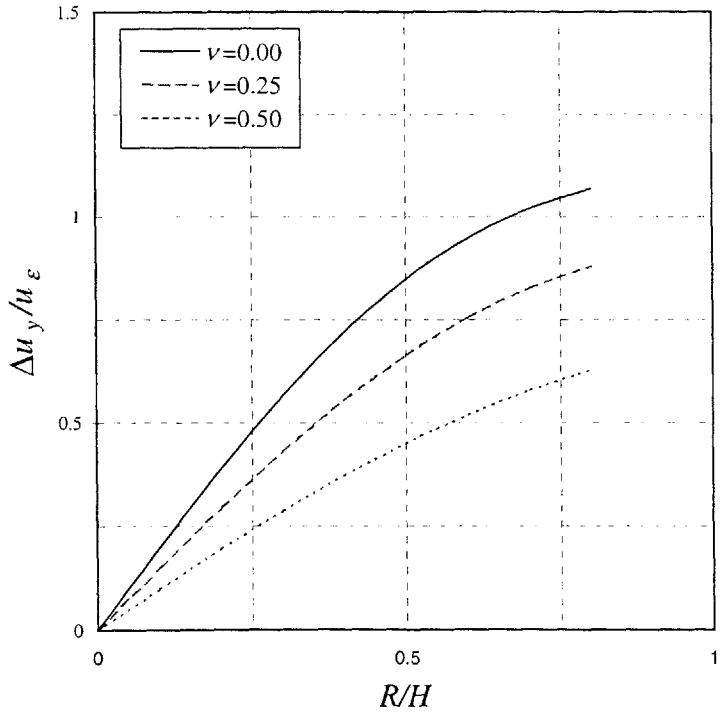

Figure 3.6. Corrections for analytic solutions using functions of complex variables

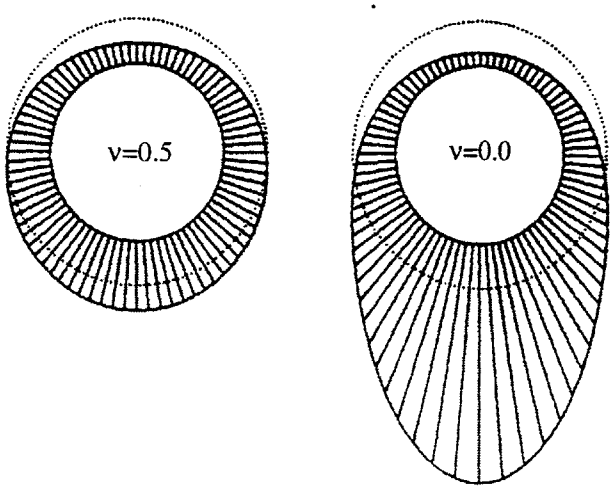

Figure 3.7. Springs constants along tunnel wall, $R/H = 0.5$ (Verruijt, 1997)

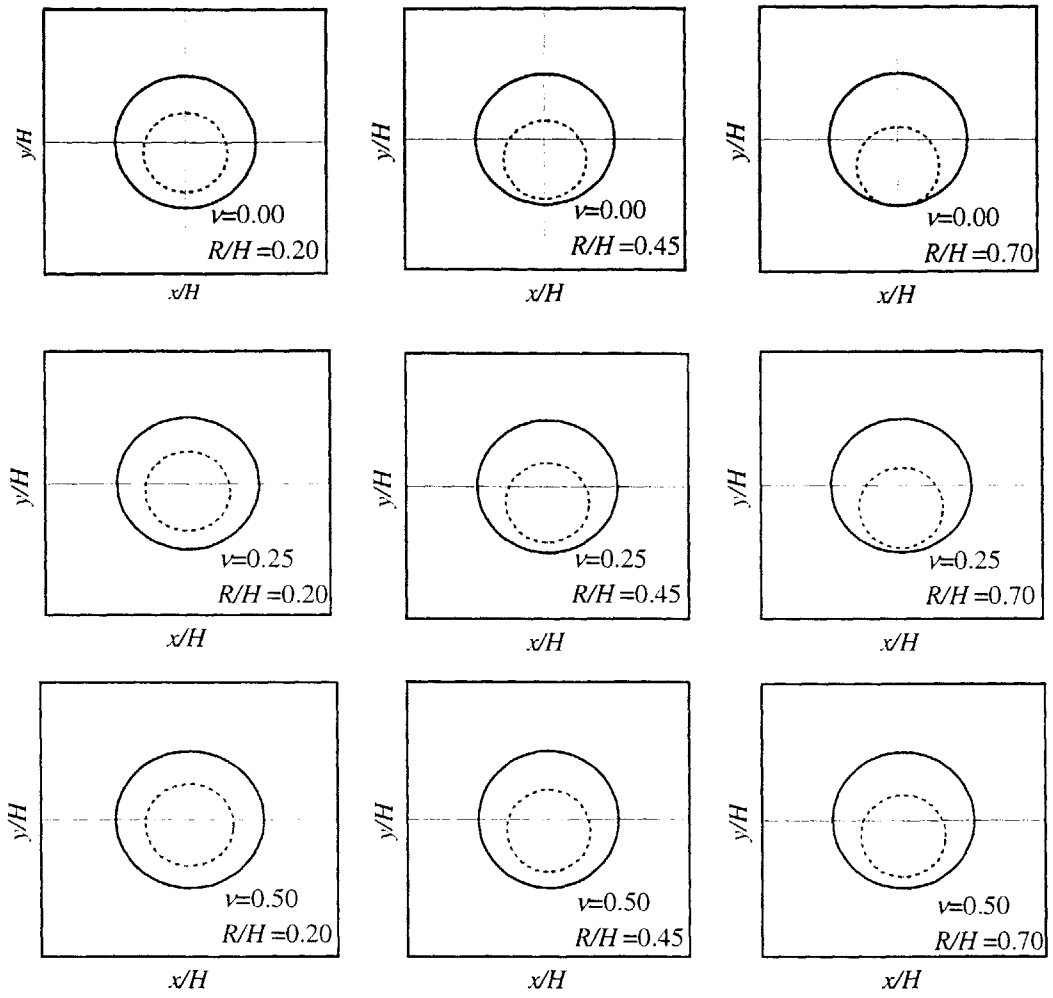

Figure 3.8. Tunnel wall deformations for conbined uniform convergence and vertical translation, $u_\varepsilon/R = 0.4$

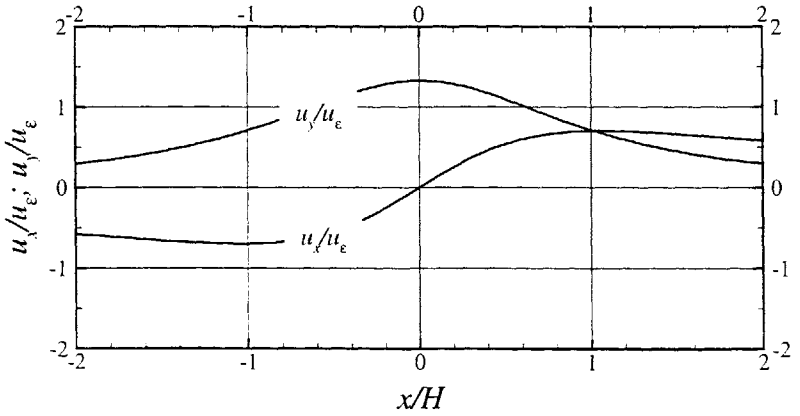

Figure 3.9. Surface displacements for uniform convergence, $R/H = 0.5$, $\nu = 0.25$

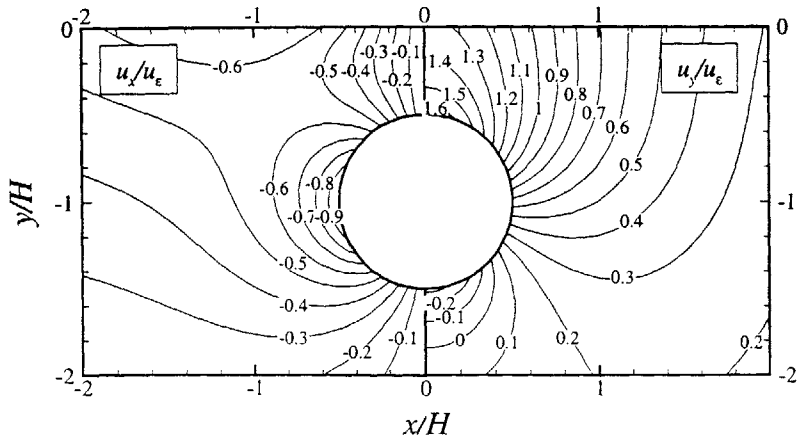

Figure 3.10. Normalized ground displacements, $R/H = 0.5$, $\nu = 0.25$

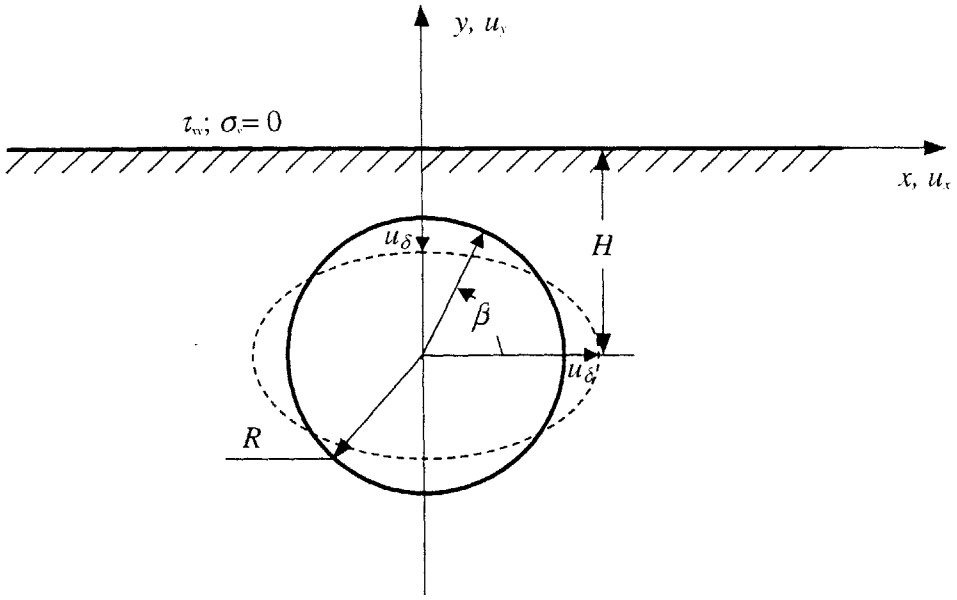

Figure 3.11. Convention for tunnel distortion

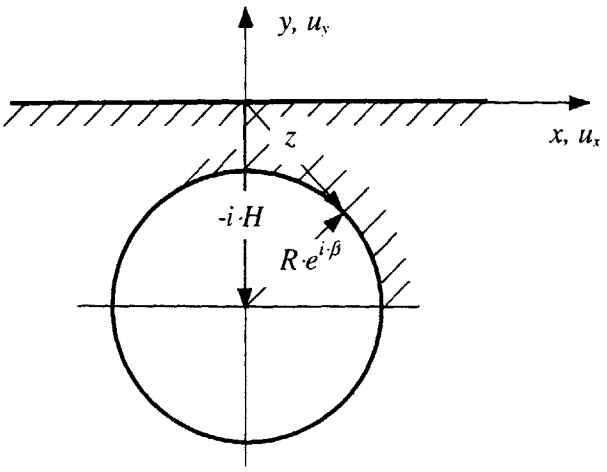

Figure 3.12. Complex vector decomposition

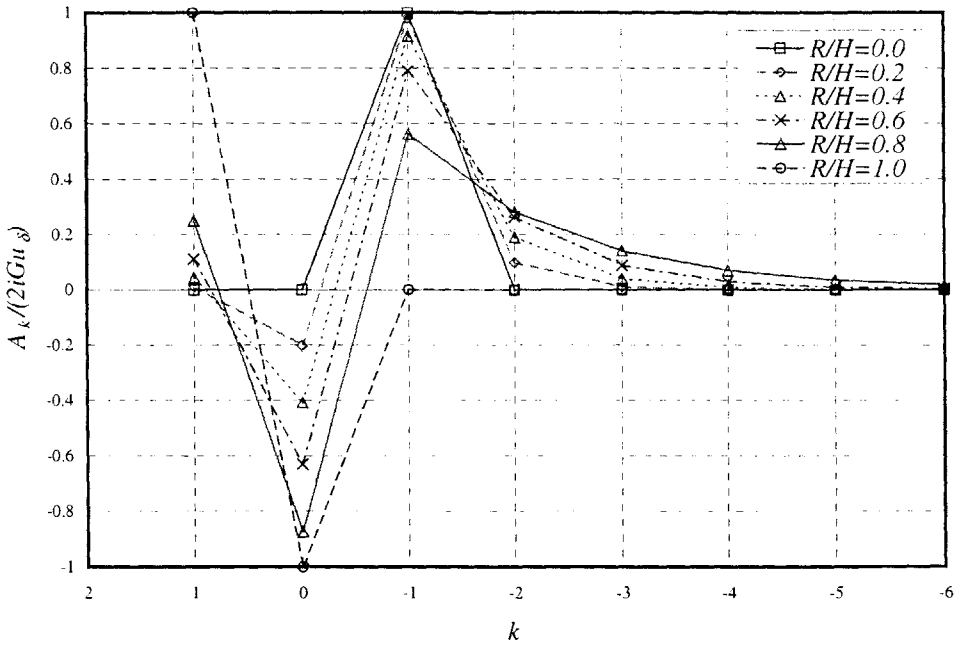

Figure 3.13. Fourier coefficients (equation {3-19})

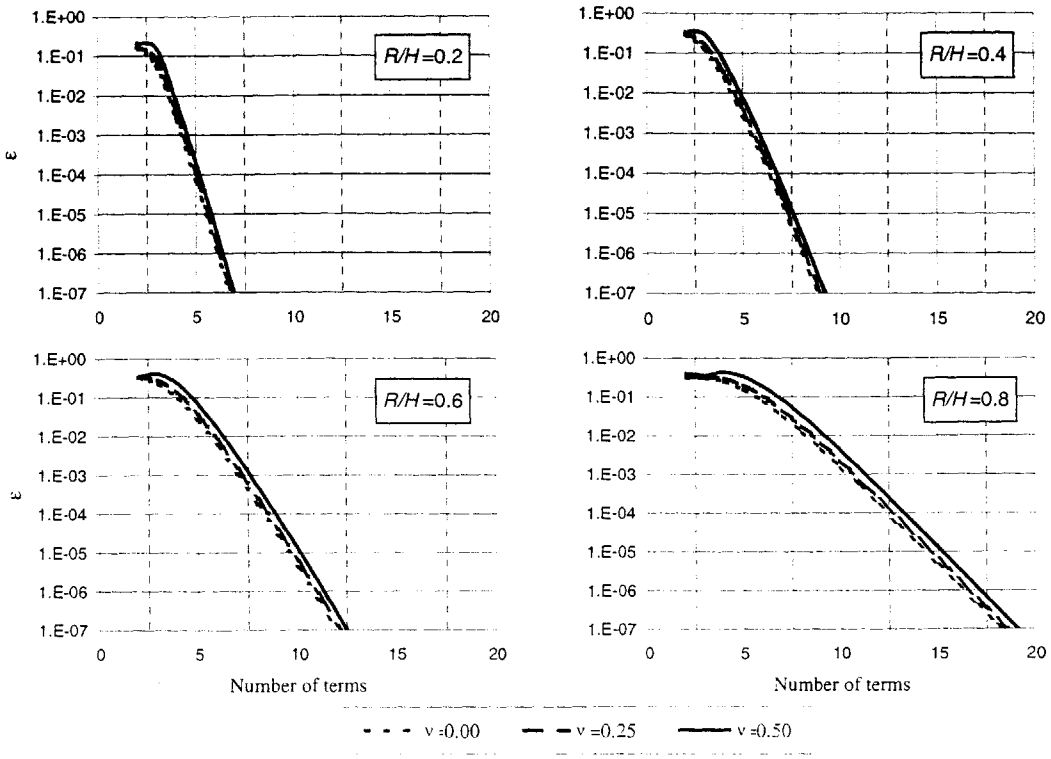

Figure 3.14. Number of terms needed for evaluation of the Goursat functions

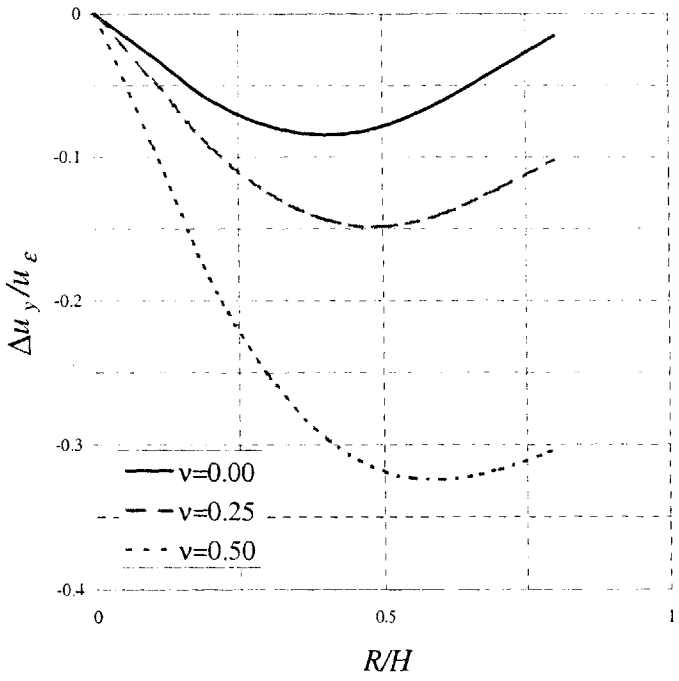

Figure 3.15. Vertical translation correction for tunnel wall radial distortion case

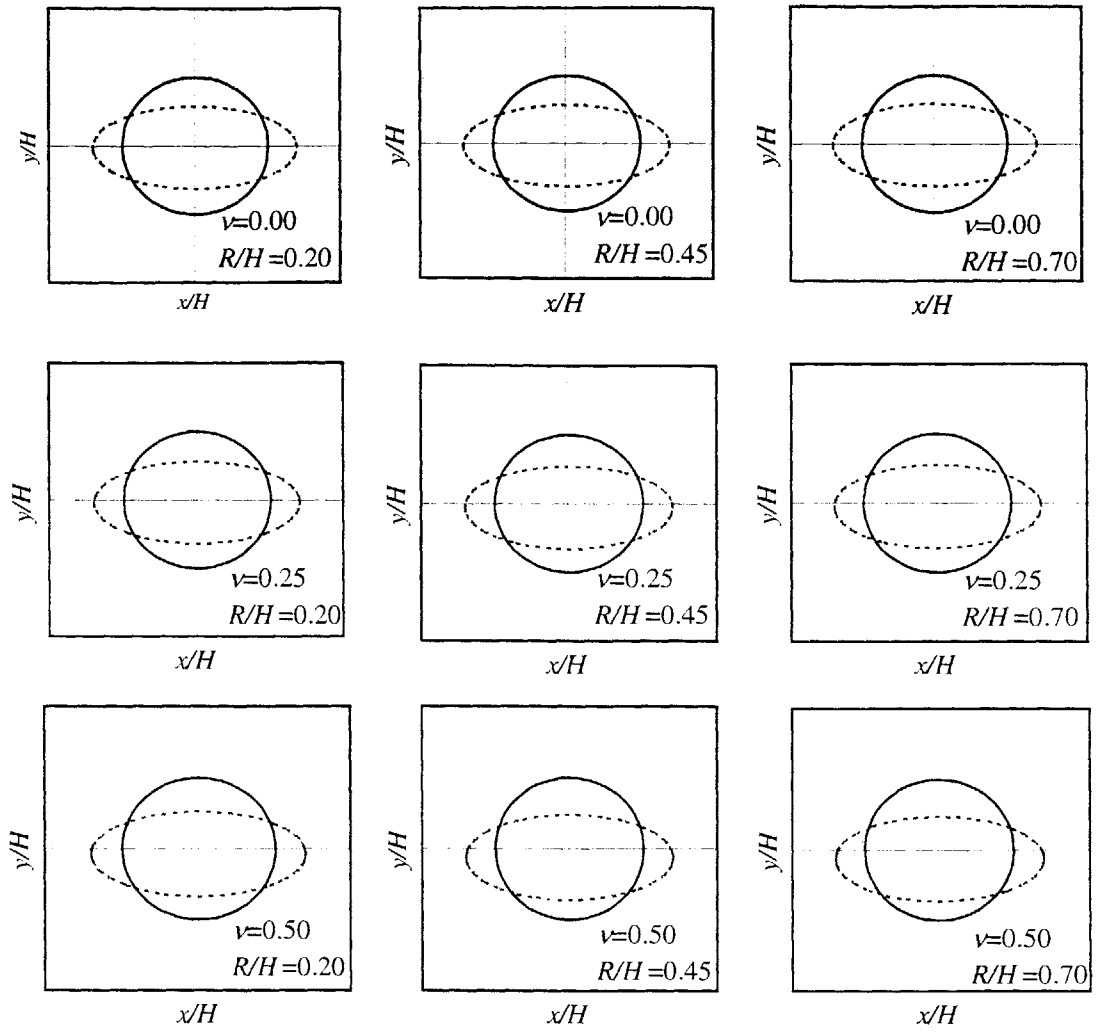

Figure 3.16. Tunnel wall deformations for combined pure distortion and vertical translation, $u_\delta/R = 0.4$

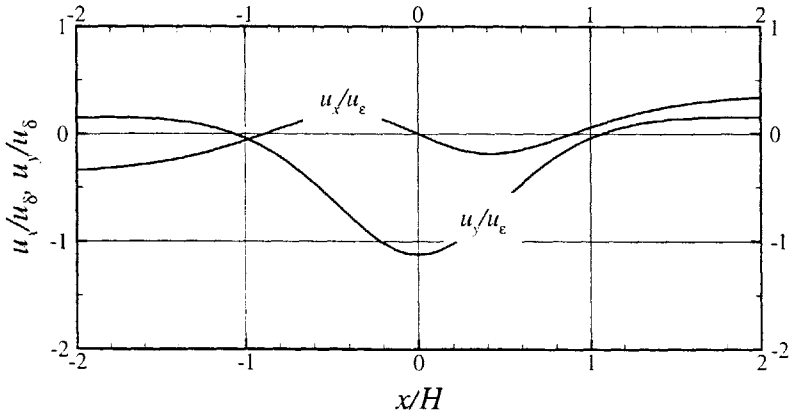

Figure 3.17. Surface displacements, $R/H = 0.5$, $\nu = 0.25$

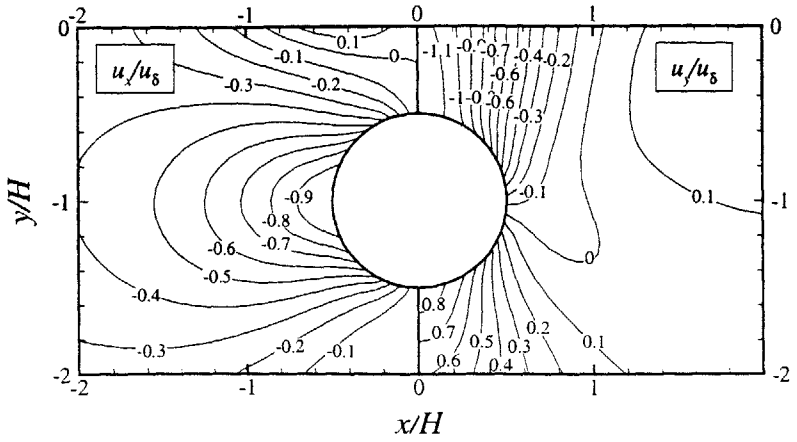

Figure 3.18. Ground deformations, $R/H = 0.5$, $\nu = 0.25$

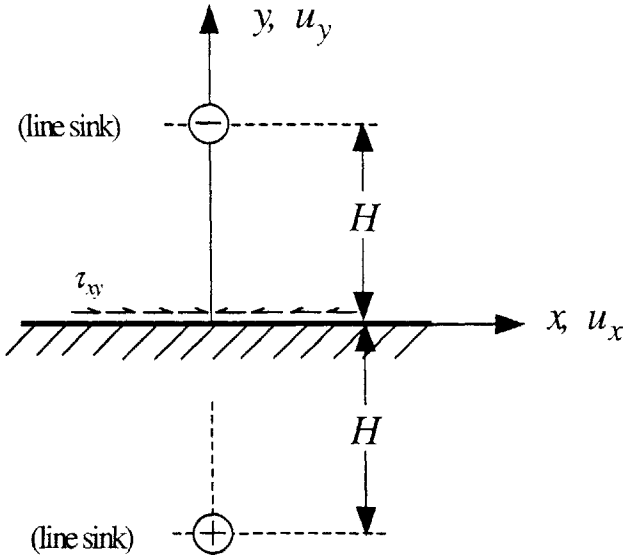

Figure 3.19. Outline of solution method proposed by Sagaseta (1987)

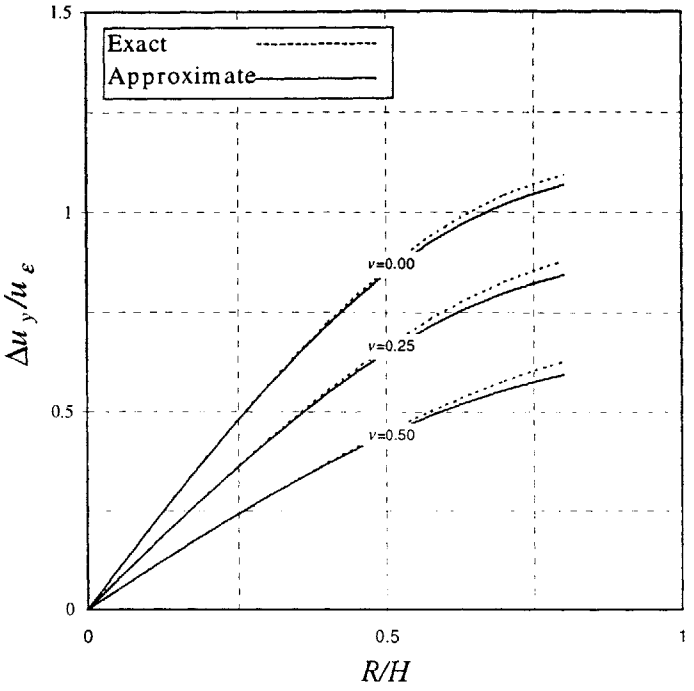

Figure 3.20. Vertical translation of tunnel springline for approximate solution for uniform convergence mode

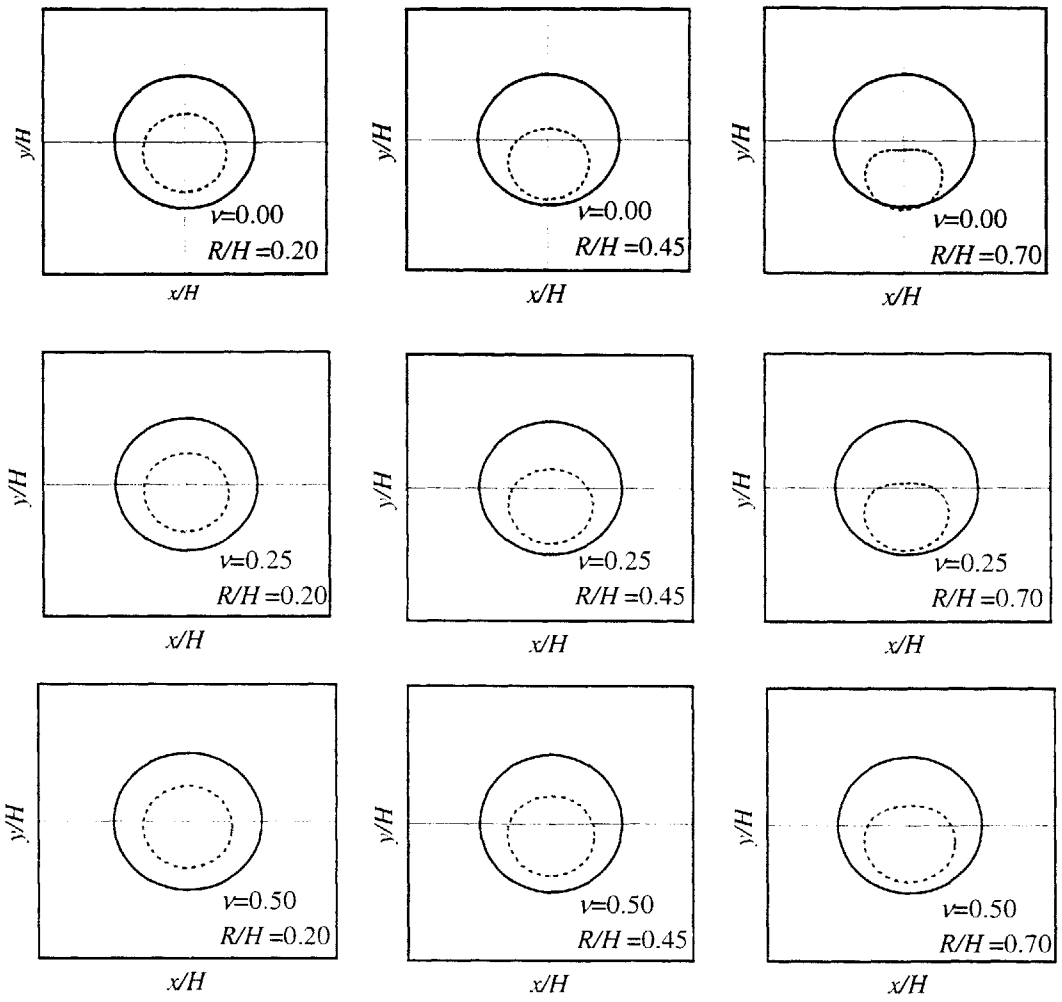

Figure 3.21. Deformations of tunnel wall due to uniform convergence mode with u_c/R = -0.4 by approximate method

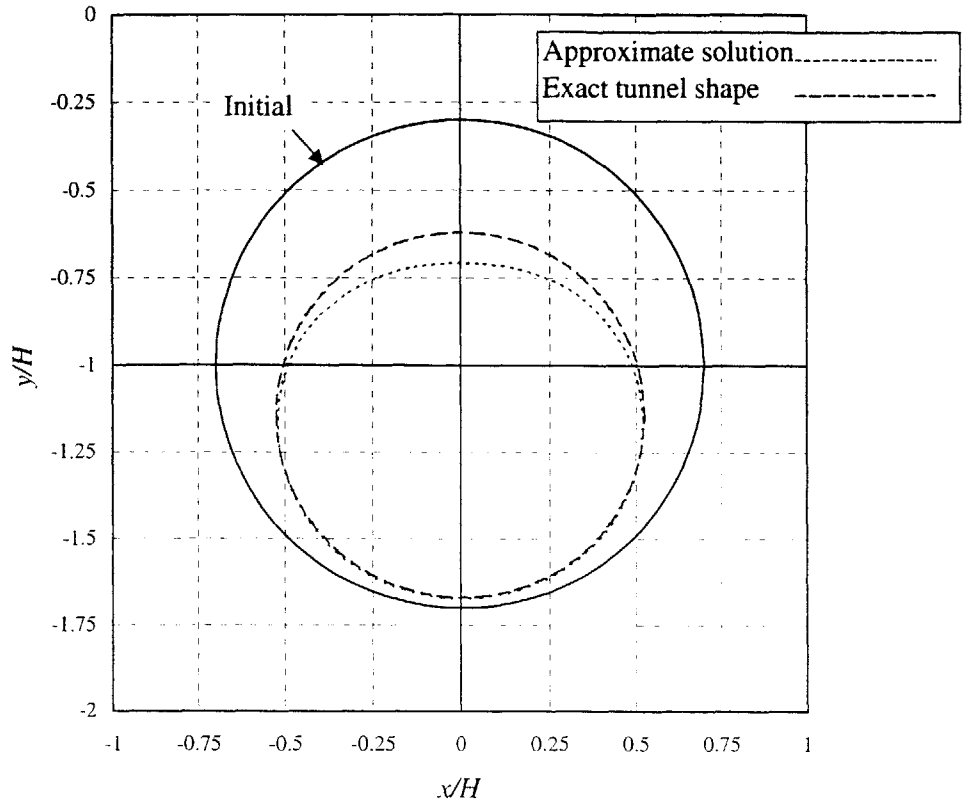

Figure 3.22. Effects of approximation of tunnel shape on deformed tunnel wall with u_ε/R = -0.4, R/H = 0.7, ν = 0.25

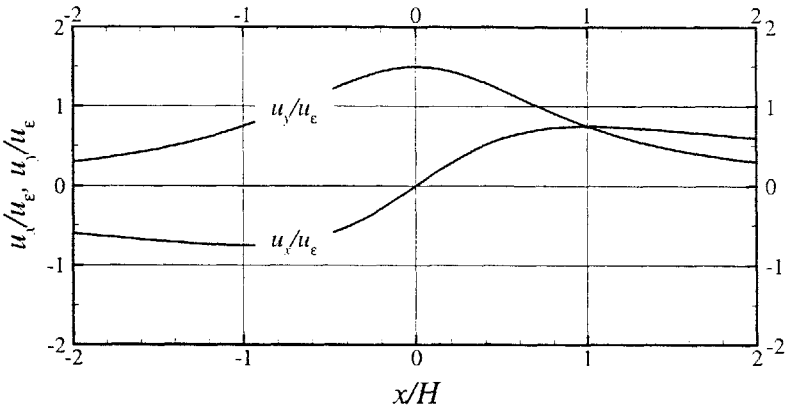

Figure 3.23. Normalized surface displacements. R/H = 0.5, ν = 0.25

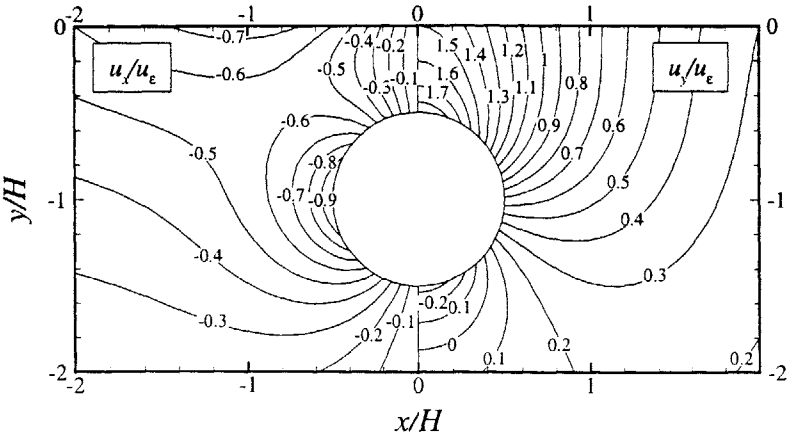

Figure 3.24. Normalized ground displacements. $R/H = 0.5$, $\nu = 0.25$

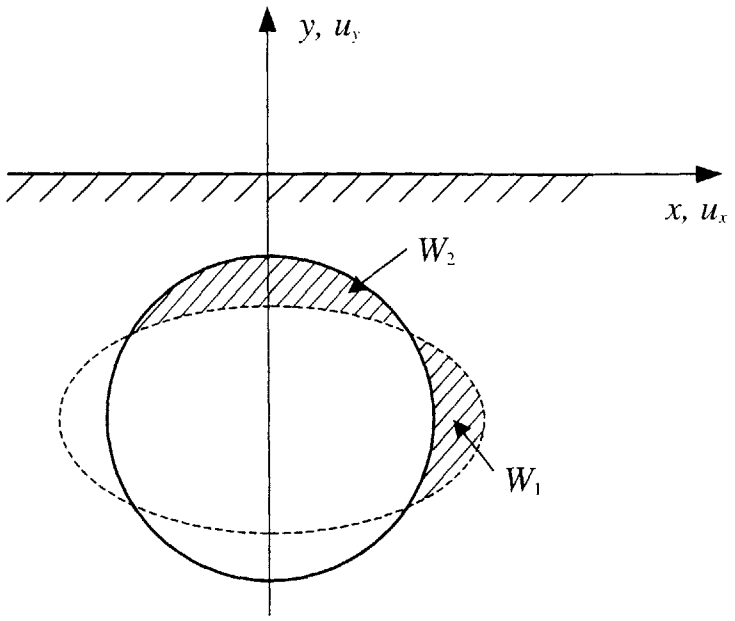

Figure 3.25. Volume of expansion due to pure distortion

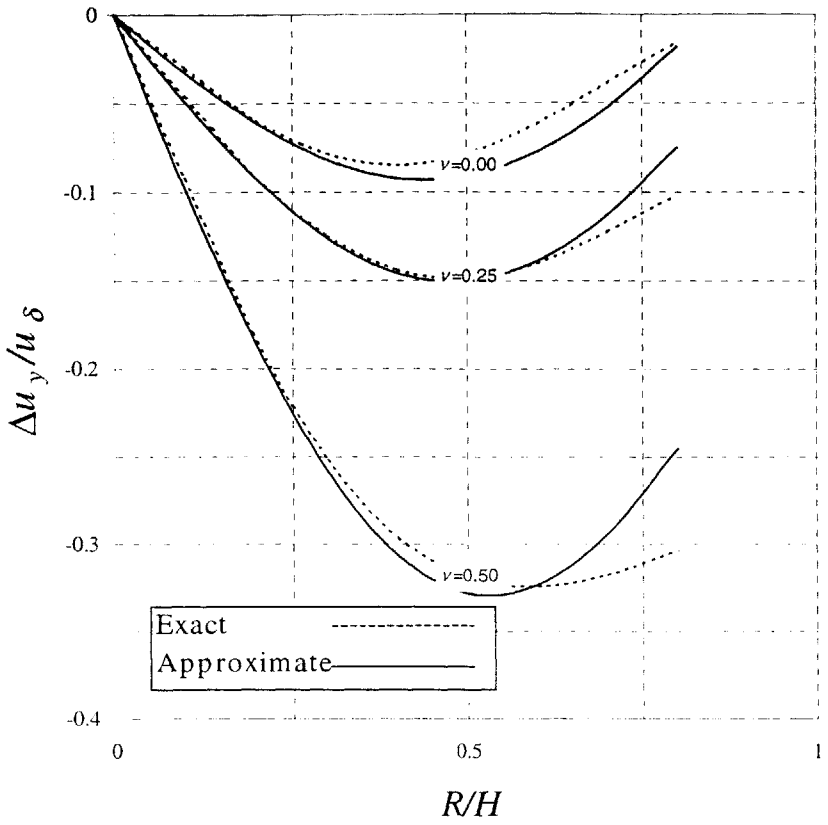

Figure 3.26. Vertical translation of tunnel springline from approximate solution for pure distortion mode

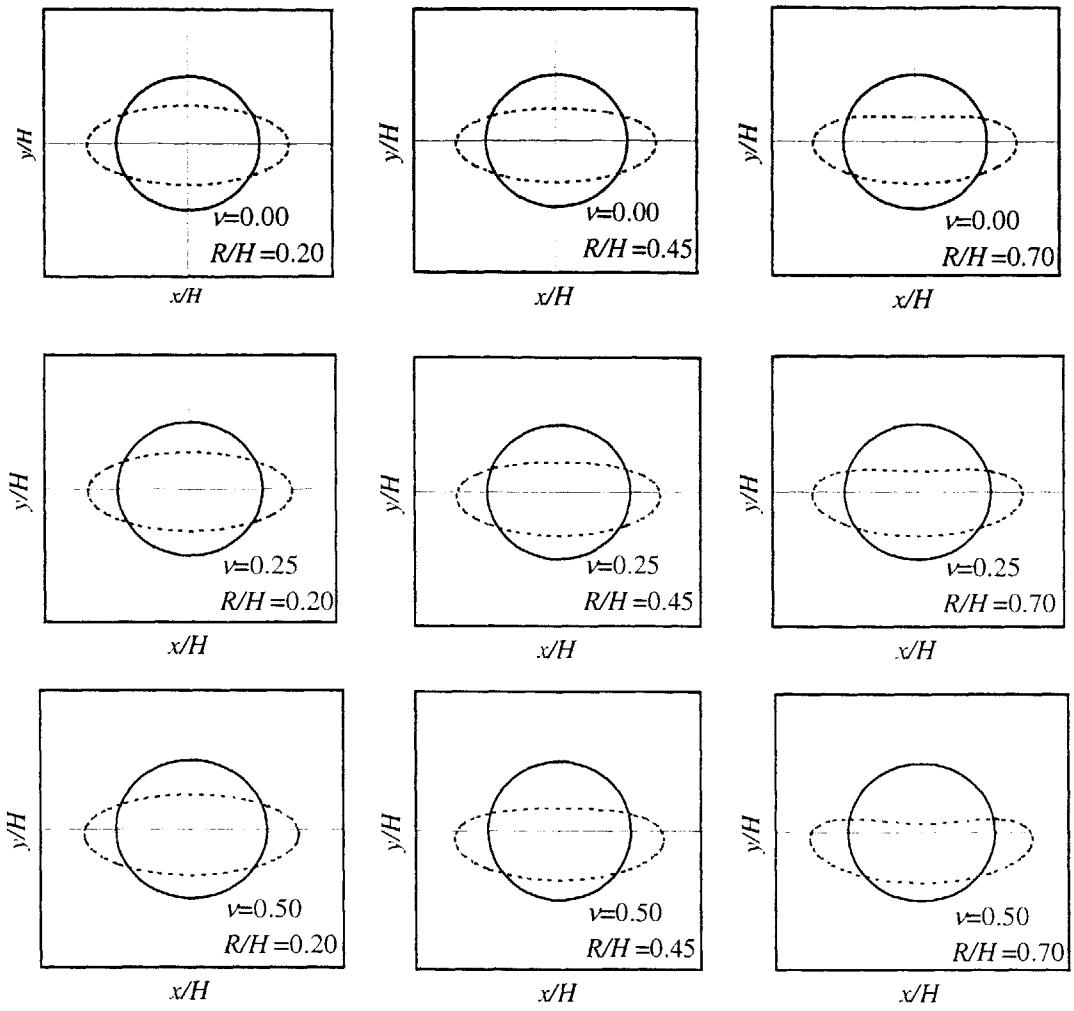

Figure 3.27. Deformations of tunnel wall due to pure distortion with $u_\delta/R = 0.4$ by approximate method

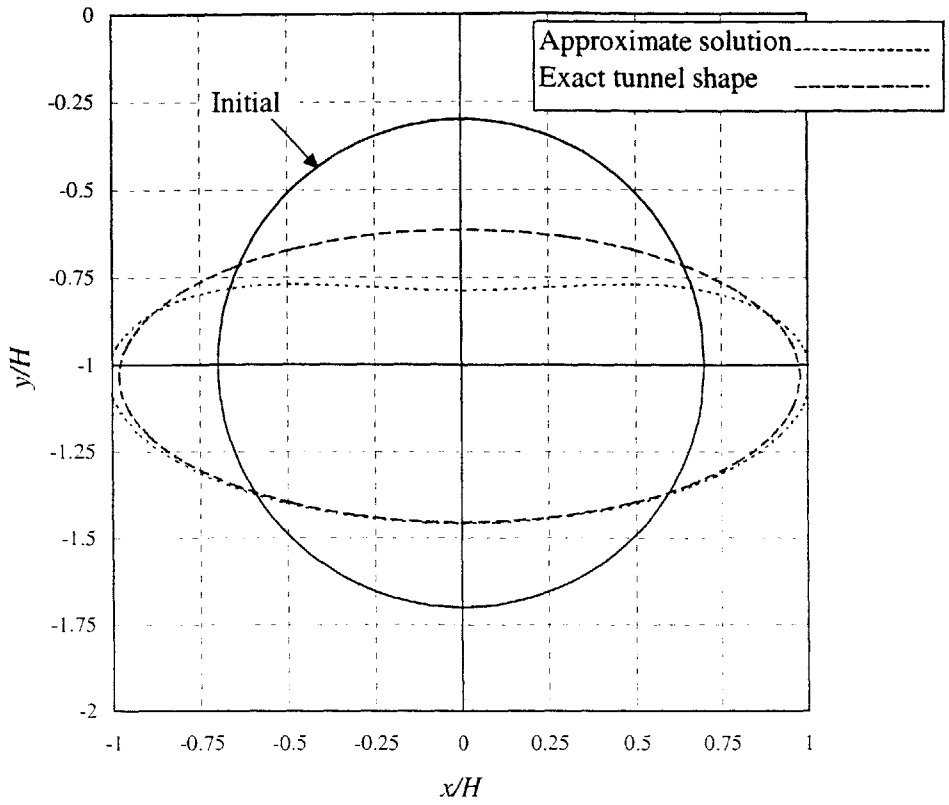

Figure 3.28. Effect of approximation of tunnel shape on deformed tunnel wall for $u_\varepsilon/R = -0.4$, $R/H = 0.7$, $\nu = 0.25$

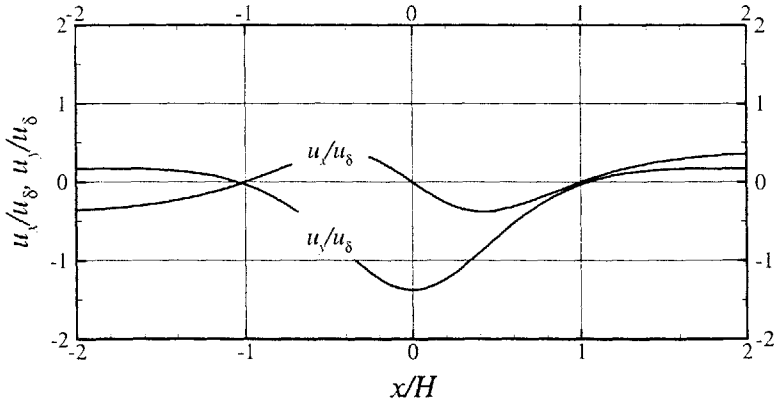

Figure 3.29. Normalized surface displacements for pure distortion mode. Approximate solution for $R/H = 0.5$, $\nu = 0.25$

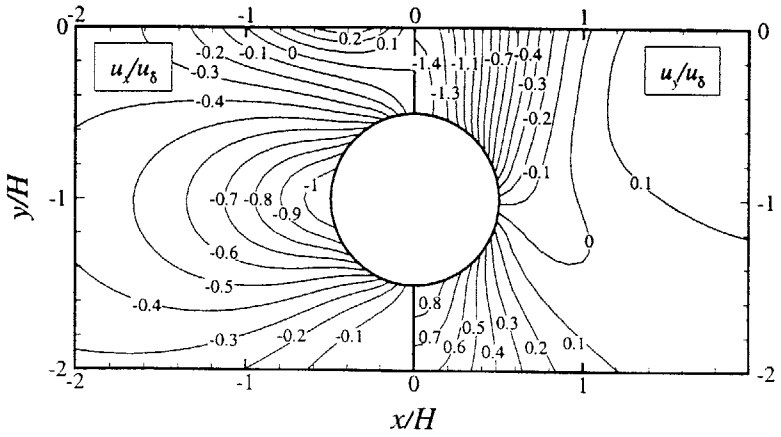

Figure 3.30. Normalized ground displacements for pure distortion mode. Approximate solution for $R/H = 0.5$, $\nu = 0.25$

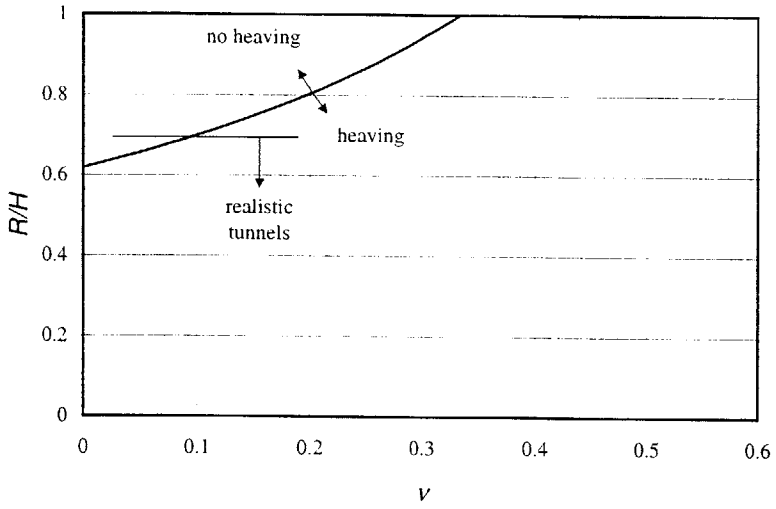

Figure 3.31. Critical *R/H* ratio vs. Poisson ratio

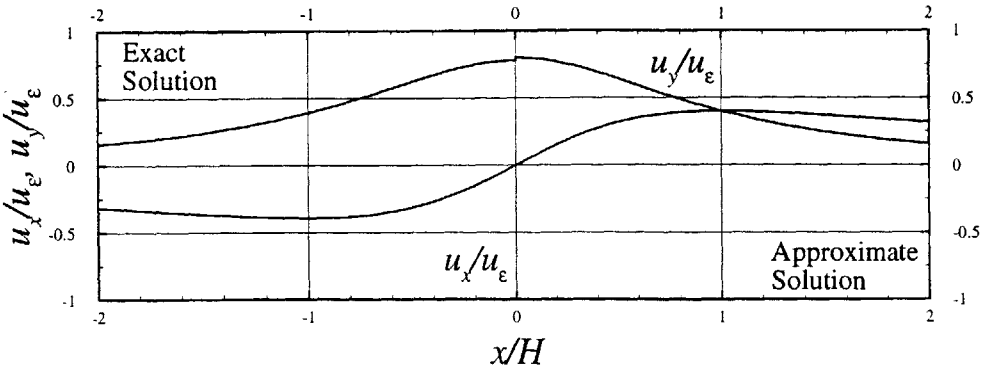

Figure 3.32. Surface displacements due to uniform convergence mode, $R/H = 0.20$, $\nu = 0.00$

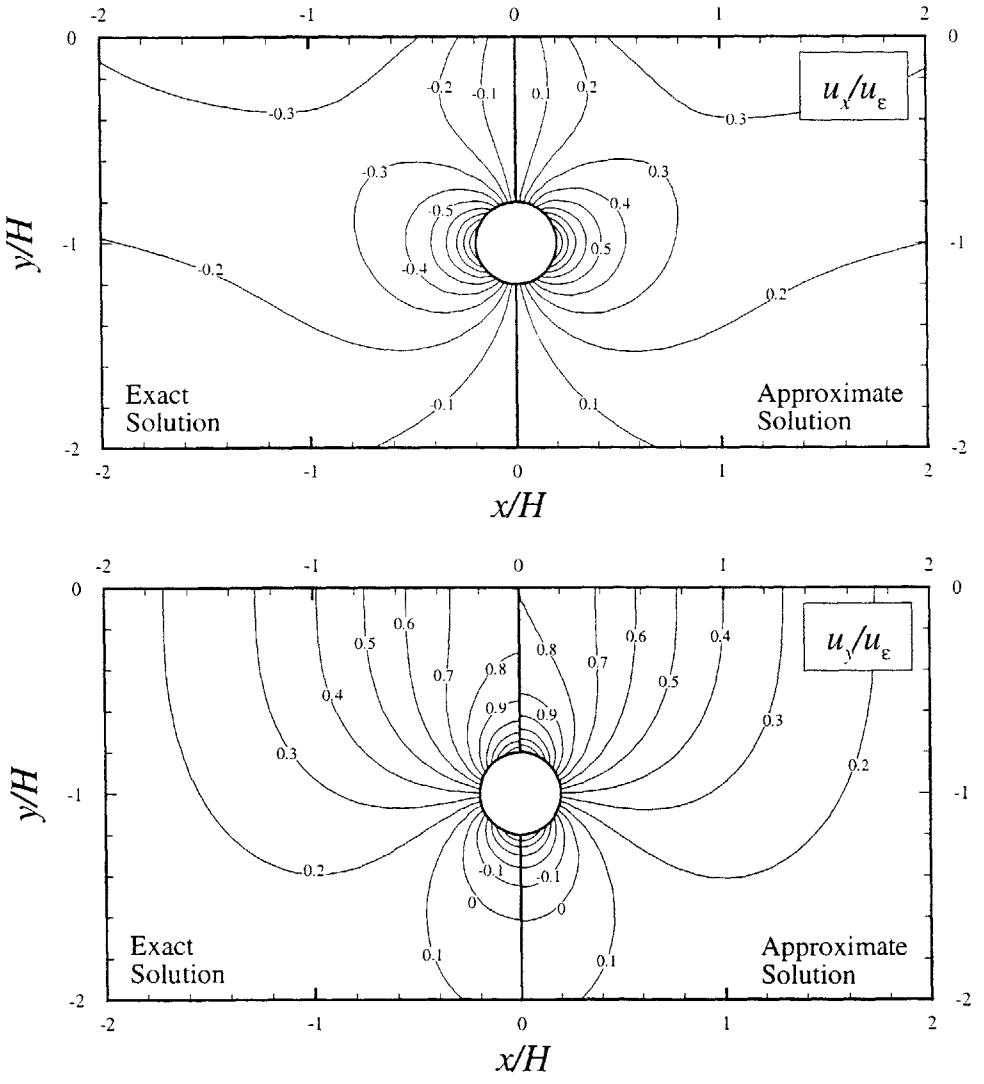

Figure 3.33. Ground displacements due to uniform convergence mode, $R/H = 0.20$, $\nu = 0.00$

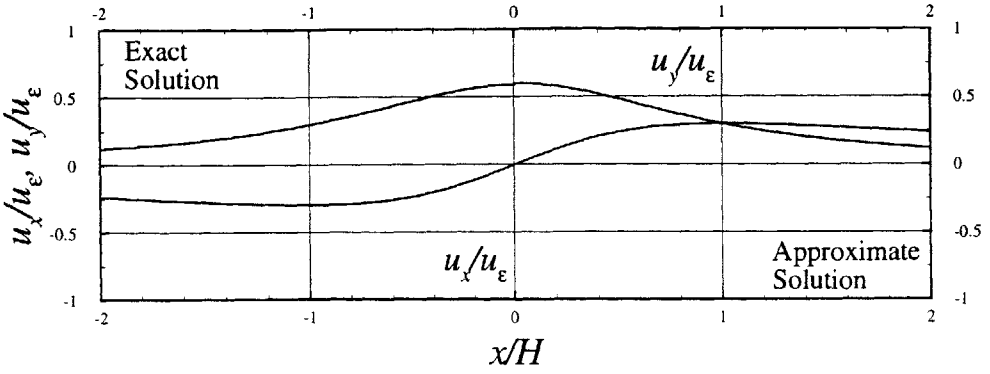

Figure 3.34. Surface displacements due to uniform convergence mode, $R/H = 0.20$, $\nu = 0.25$

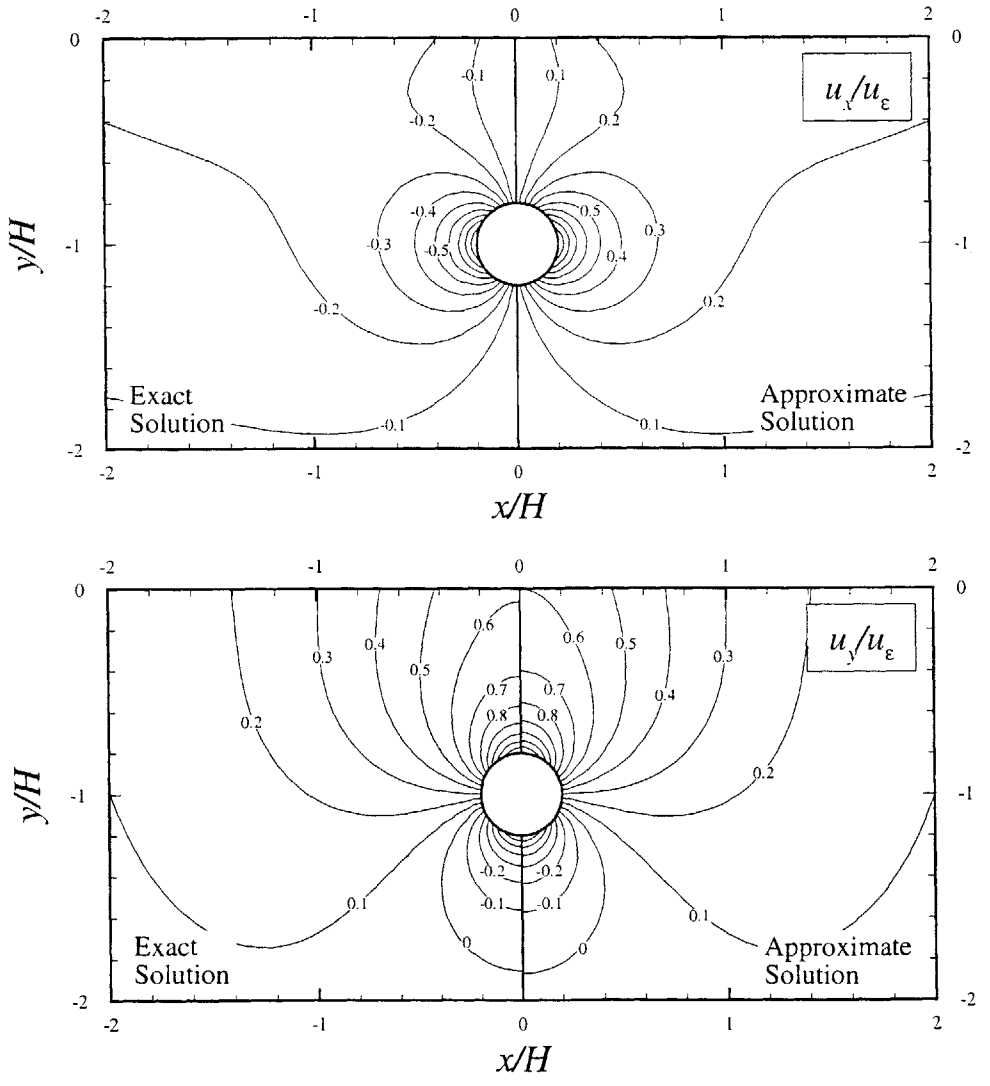

Figure 3.35. Ground displacements due to uniform convergence mode, $R/H = 0.20$, $\nu = 0.25$

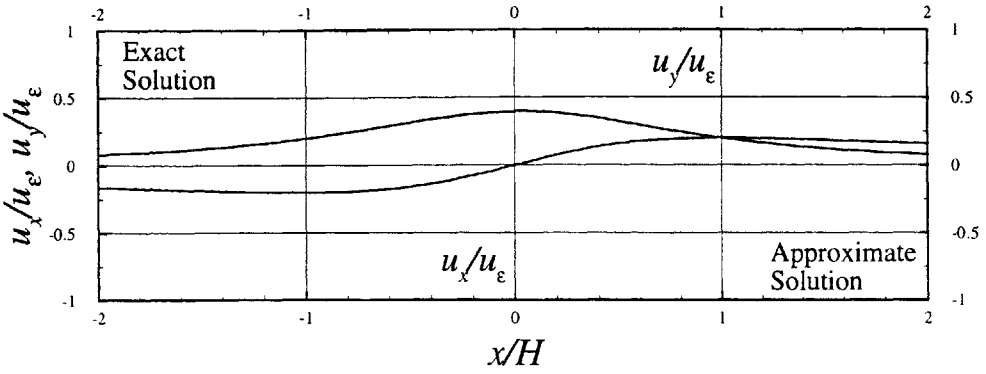

Figure 3.36. Surface displacements due to uniform convergence mode, R/H = 0.20, ν = 0.50

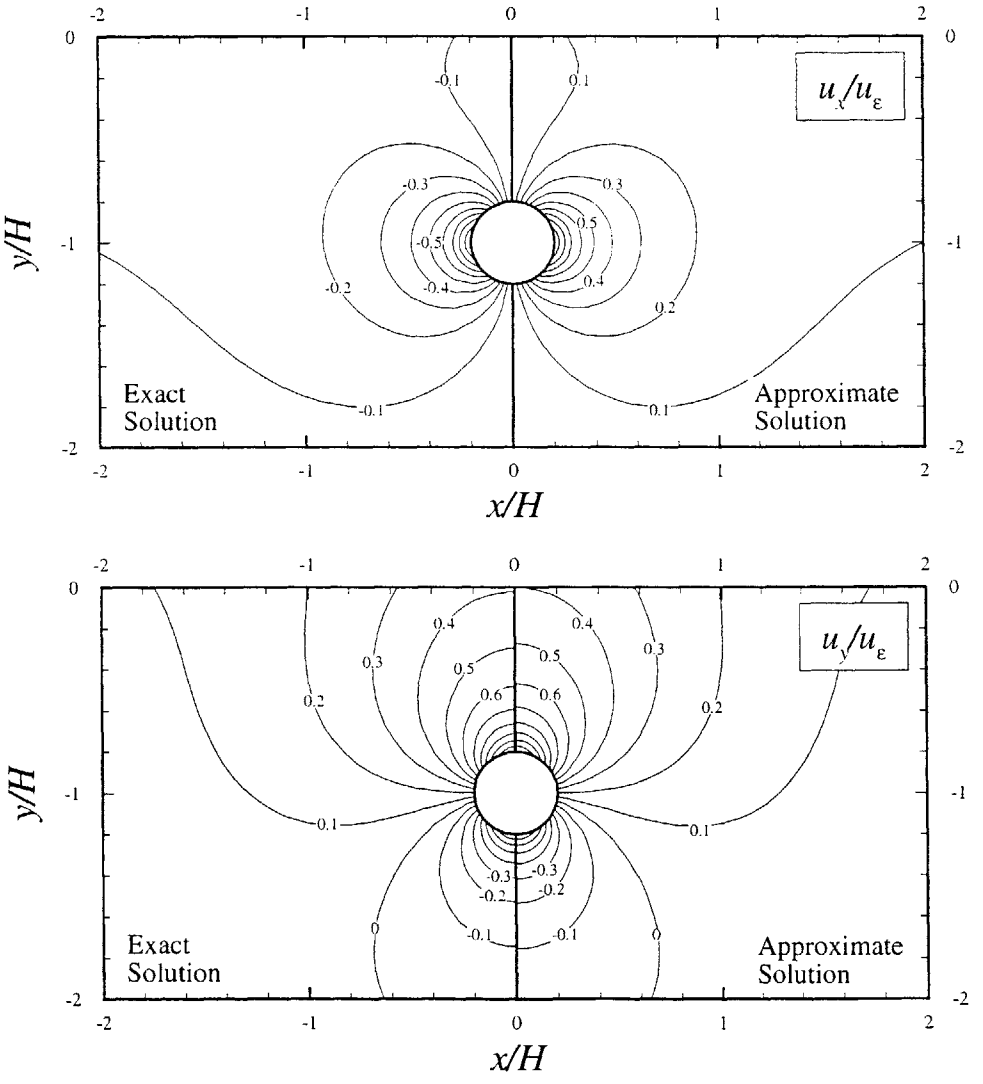

Figure 3.37. Ground displacements due to uniform convergence mode, R/H = 0.20, ν = 0.50

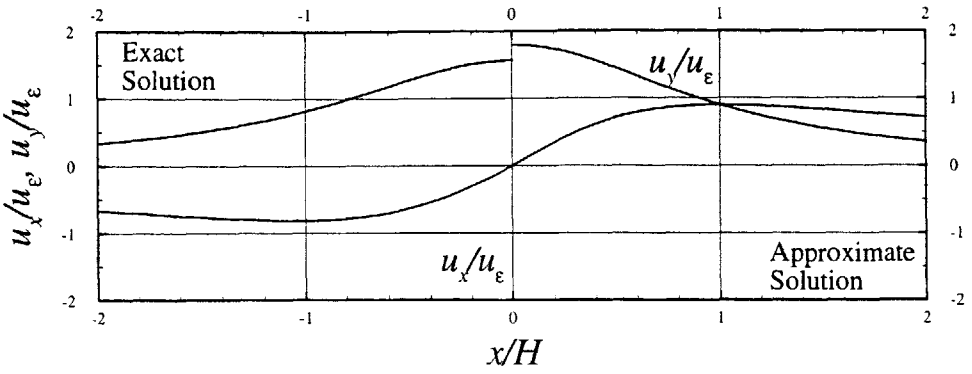

Figure 3.38. Surface displacements due to uniform convergence mode, $R/H = 0.45$, $\nu = 0.00$

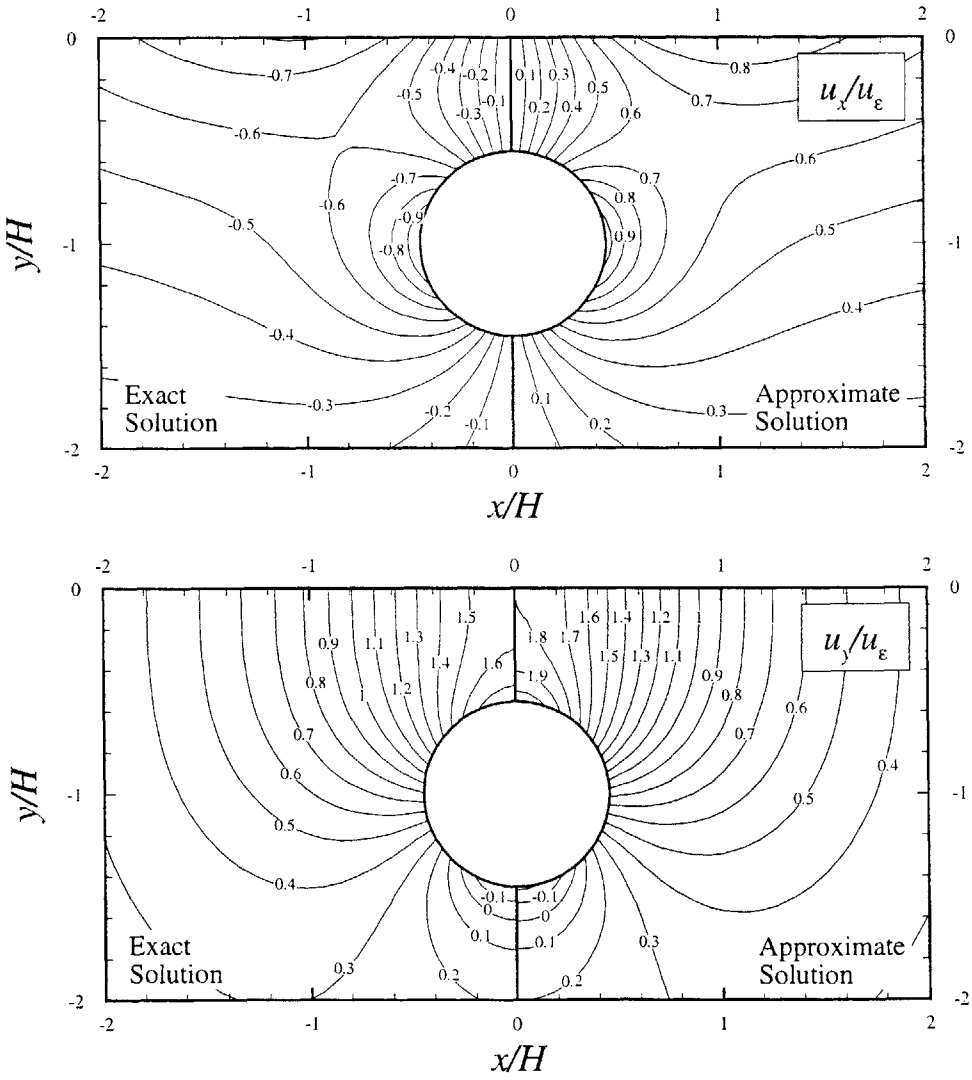

Figure 3.39. Ground displacements due to uniform convergence mode, $R/H = 0.45$, $\nu = 0.00$

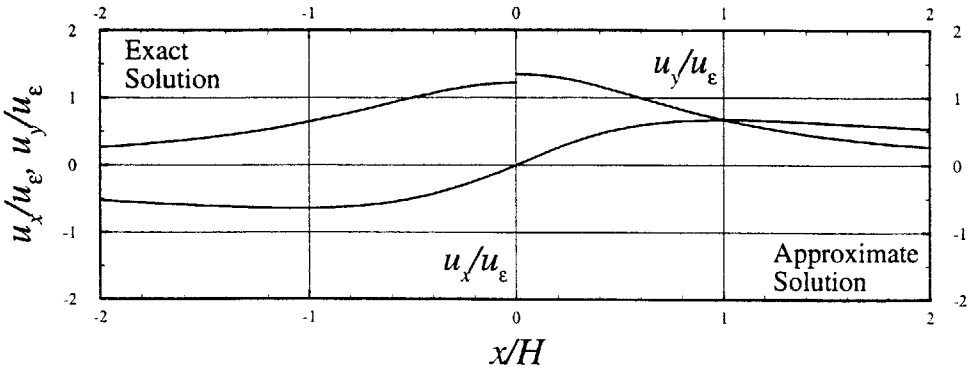

Figure 3.40. Surface displacements due to uniform convergence mode, $R/H = 0.45$, $\nu = 0.25$

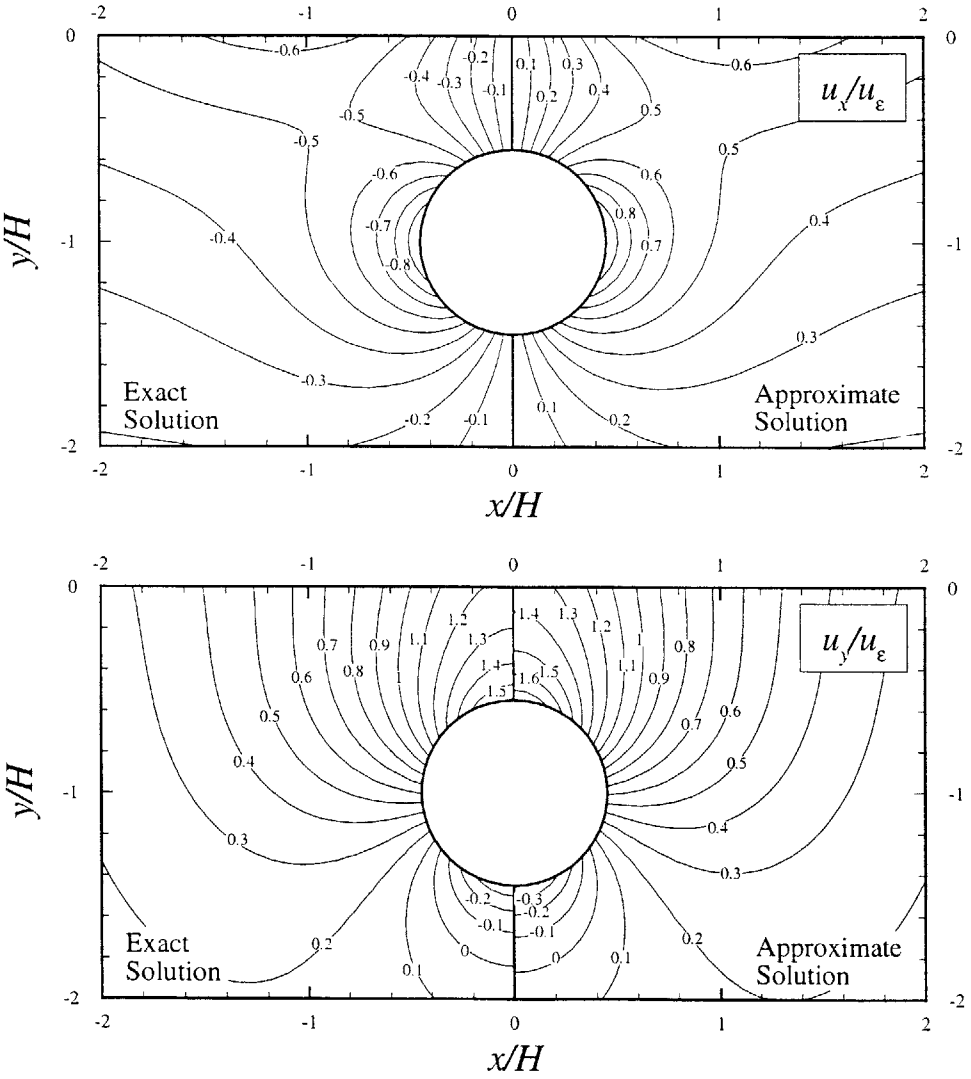

Figure 3.41. Ground displacements due to uniform convergence mode, $R/H = 0.45$, $\nu = 0.25$

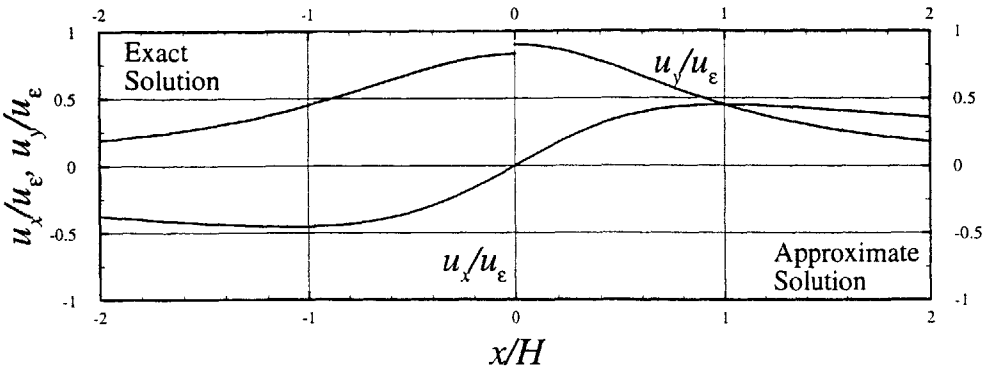

Figure 3.42. Surface displacements due to uniform convergence mode, $R/H = 0.45$, $\nu = 0.50$

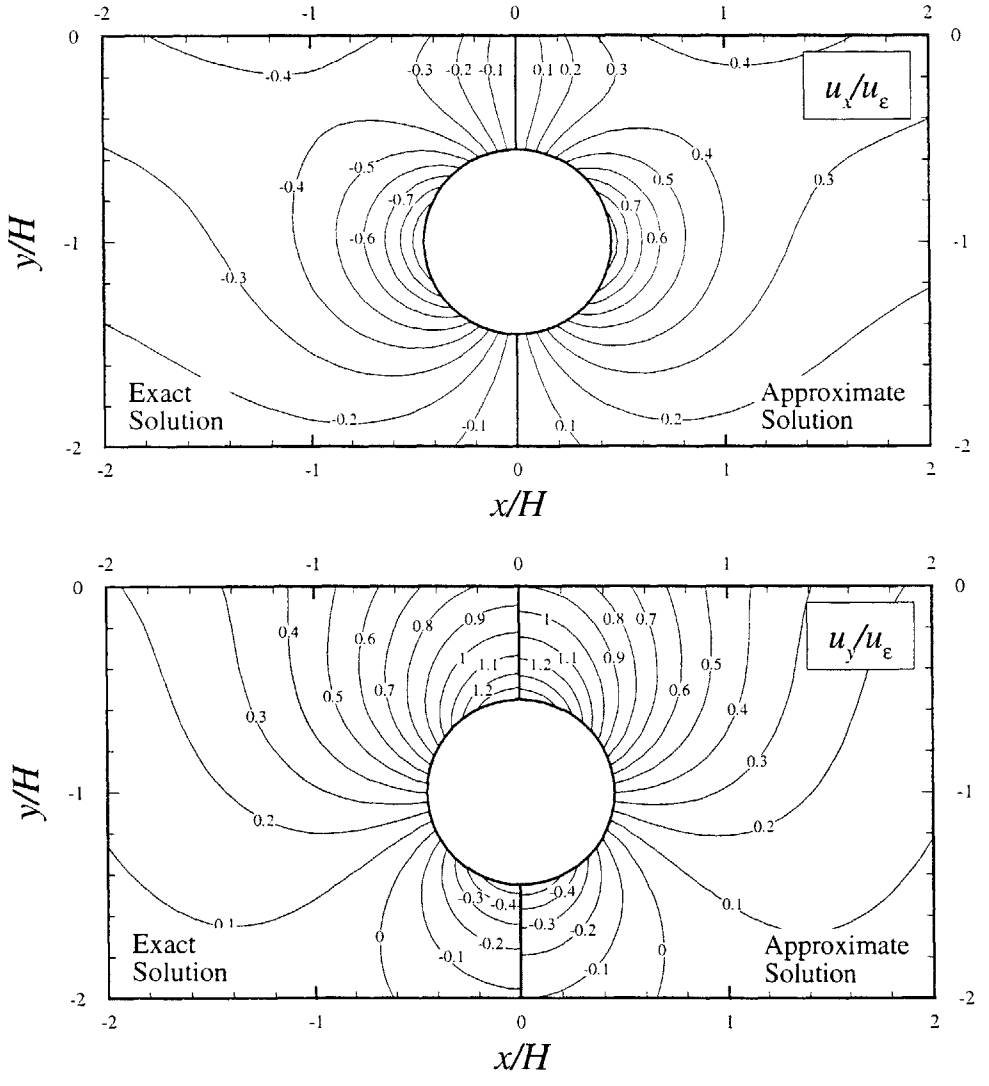

Figure 3.43. Ground displacements due to uniform convergence mode, $R/H = 0.45$, $\nu = 0.50$

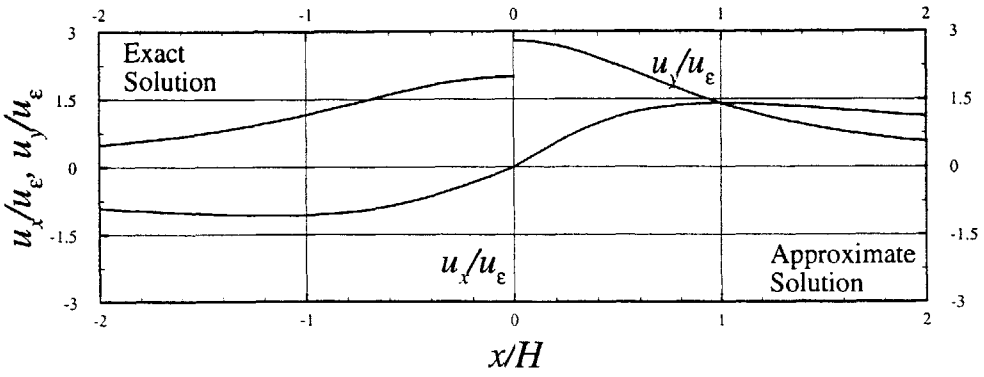

Figure 3.44. Surface displacements due to uniform convergence mode, $R/H = 0.70$, $\nu = 0.00$

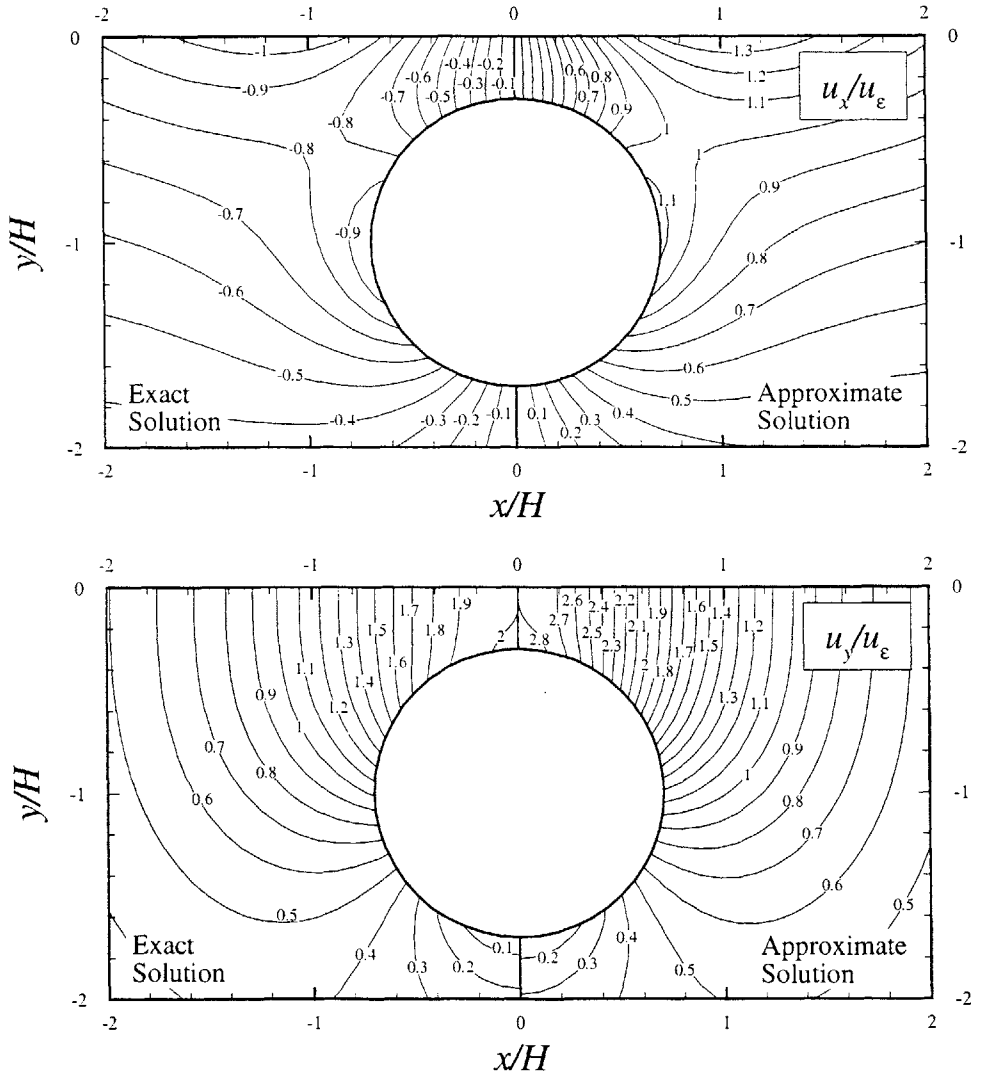

Figure 3.45. Ground displacements due to uniform convergence mode, $R/H = 0.70$, $\nu = 0.00$

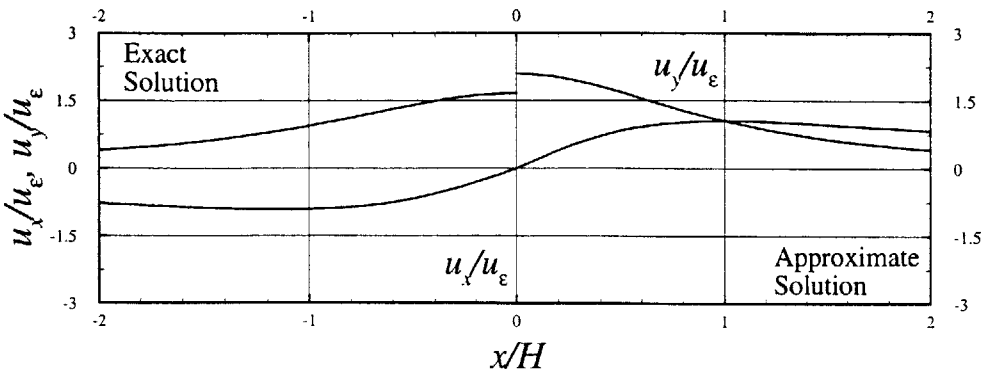

Figure 3.46. Surface displacements due to uniform convergence mode, $R/H = 0.70$, $\nu = 0.25$

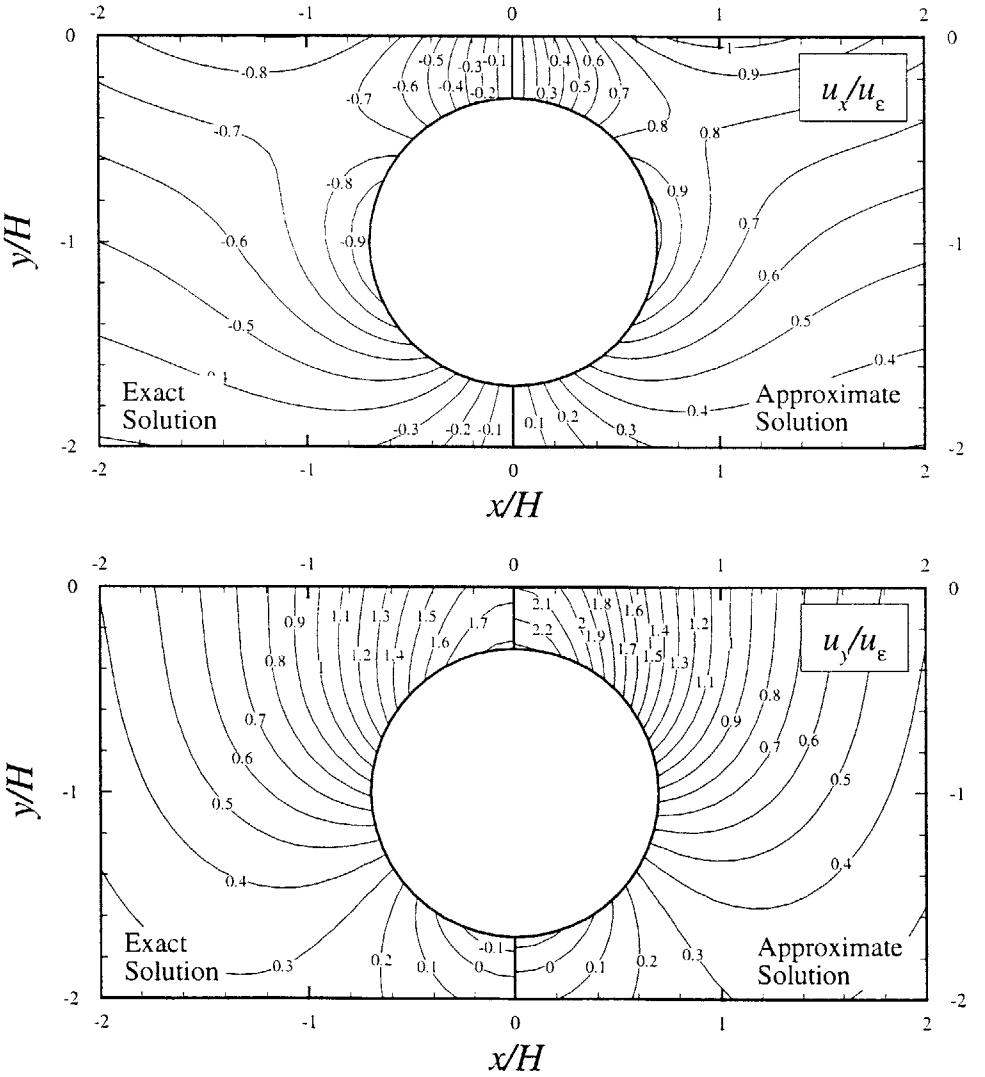

Figure 3.47. Ground displacements due to uniform convergence mode, $R/H = 0.70$, $\nu = 0.25$

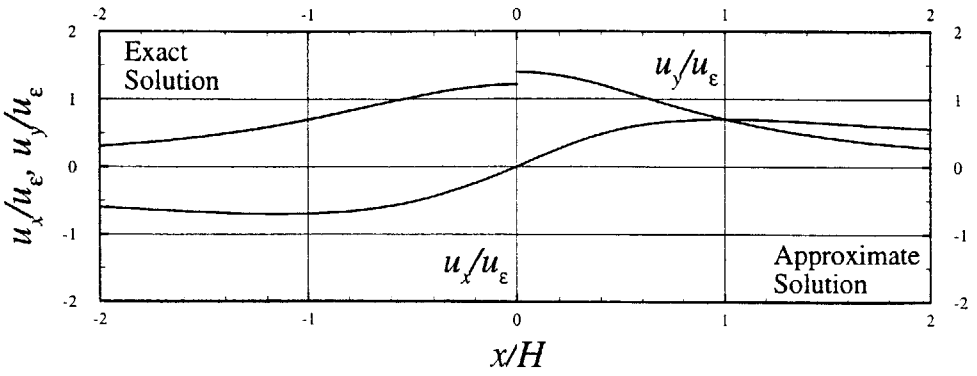

Figure 3.48. Surface displacements due to uniform convergence mode, $R/H = 0.70$, $\nu = 0.50$

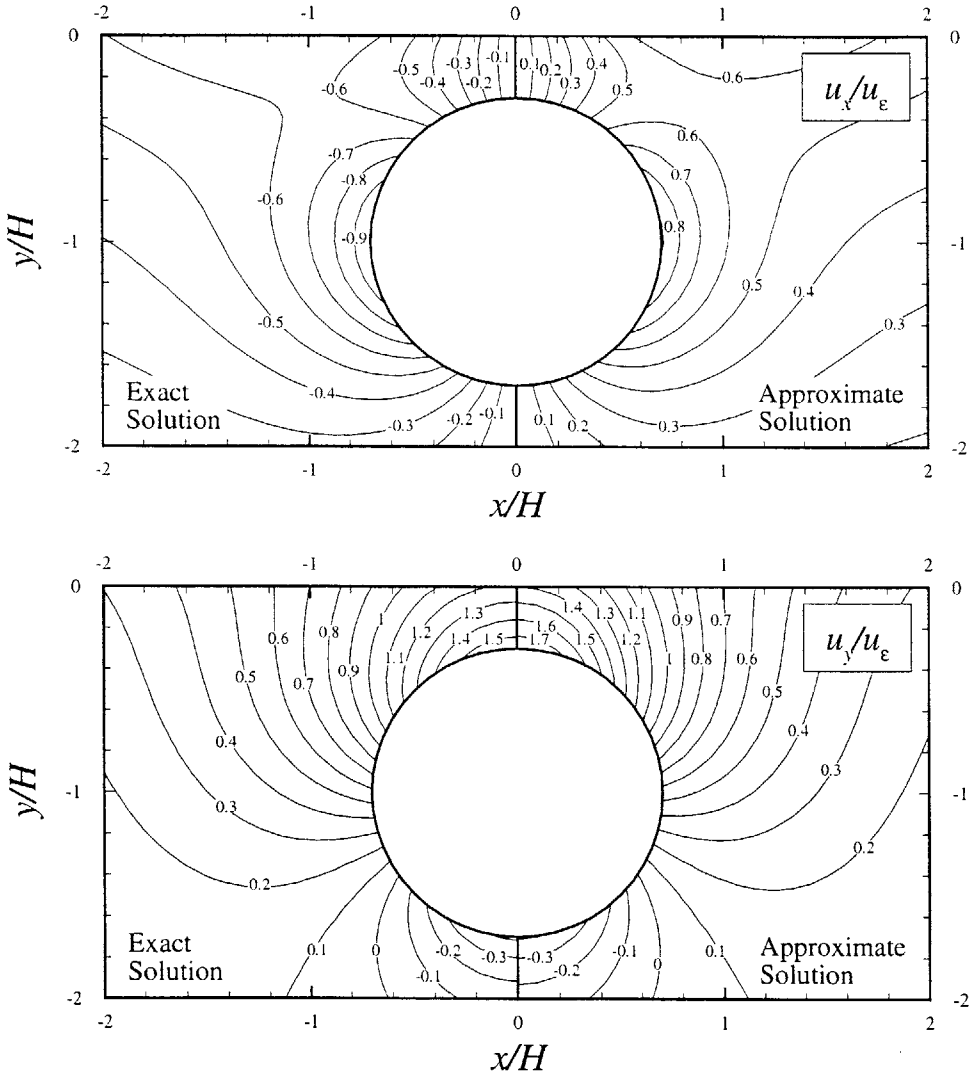

Figure 3.49. Ground displacements due to uniform convergence mode, $R/H = 0.70$, $\nu = 0.50$

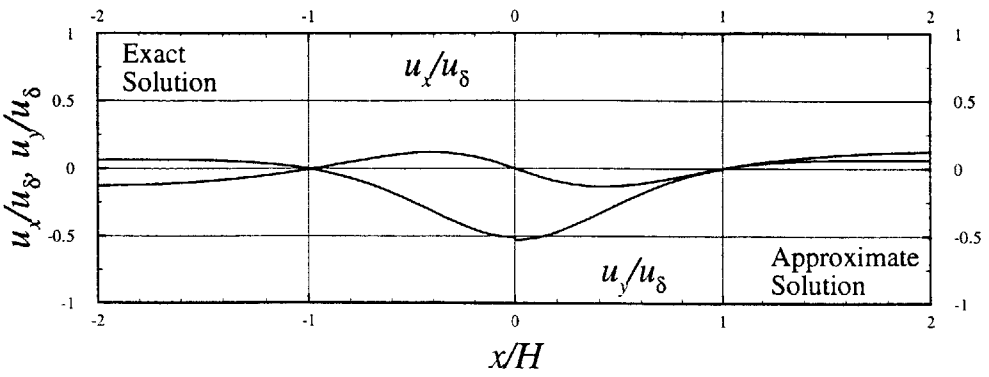

Figure 3.50. Surface displacements due to pure distortion mode, $R/H = 0.20$, $\nu = 0.00$

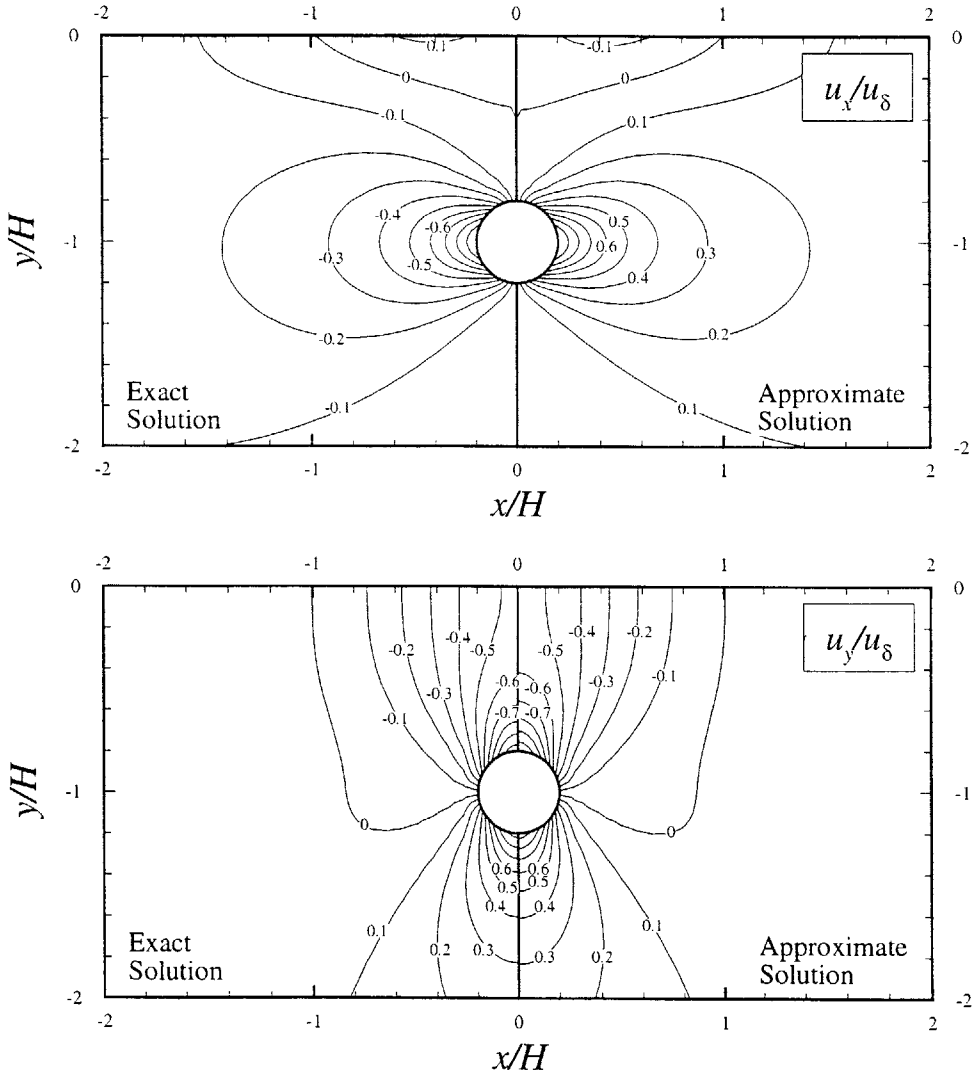

Figure 3.51. Ground displacements due to pure distortion mode, $R/H = 0.20$, $\nu = 0.00$

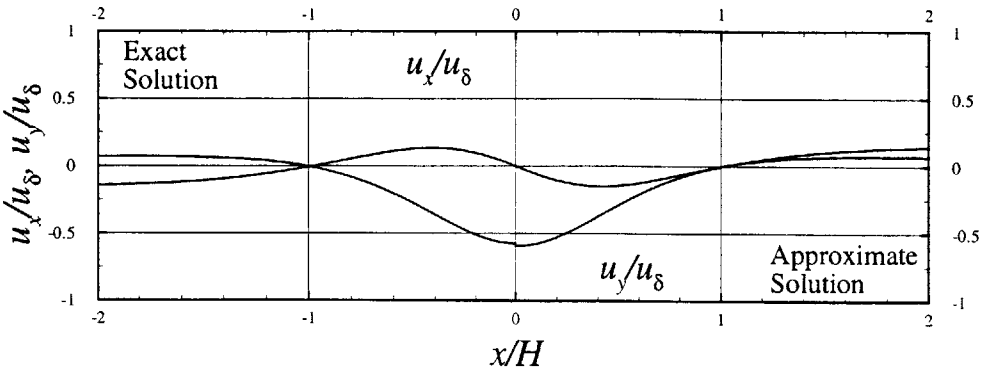

Figure 3.52. Surface displacements due to pure distortion mode, $R/H = 0.20$, $\nu = 0.25$

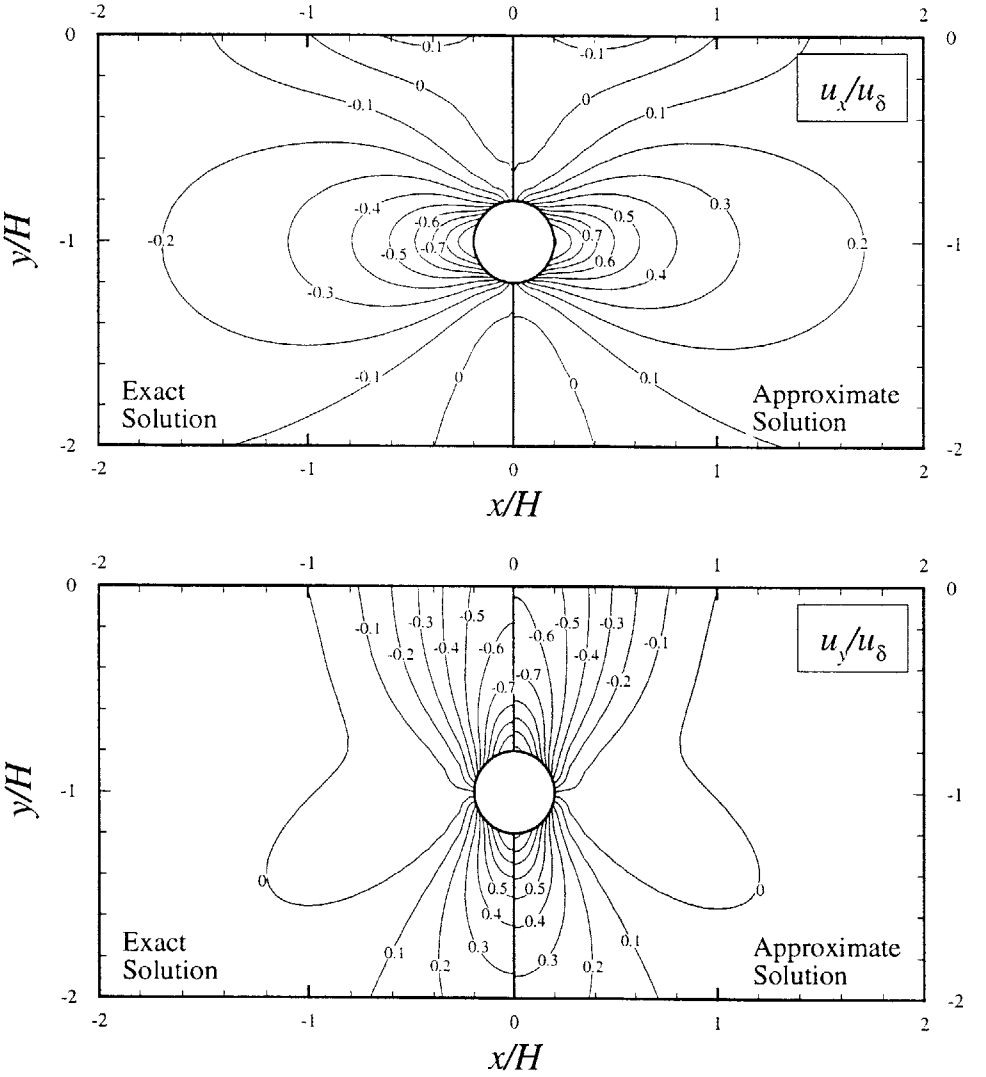

Figure 3.53. Ground displacements due to pure distortion mode, $R/H = 0.20$, $\nu = 0.25$

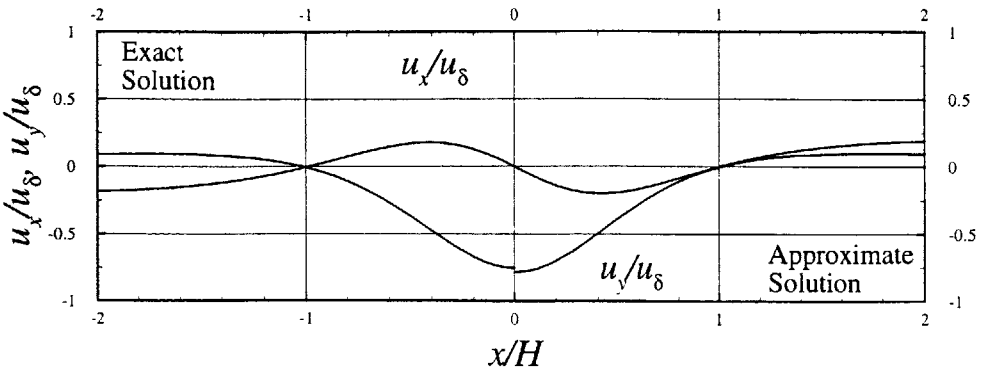

Figure 3.54. Surface displacements due to pure distortion mode, $R/H = 0.20$, $\nu = 0.50$

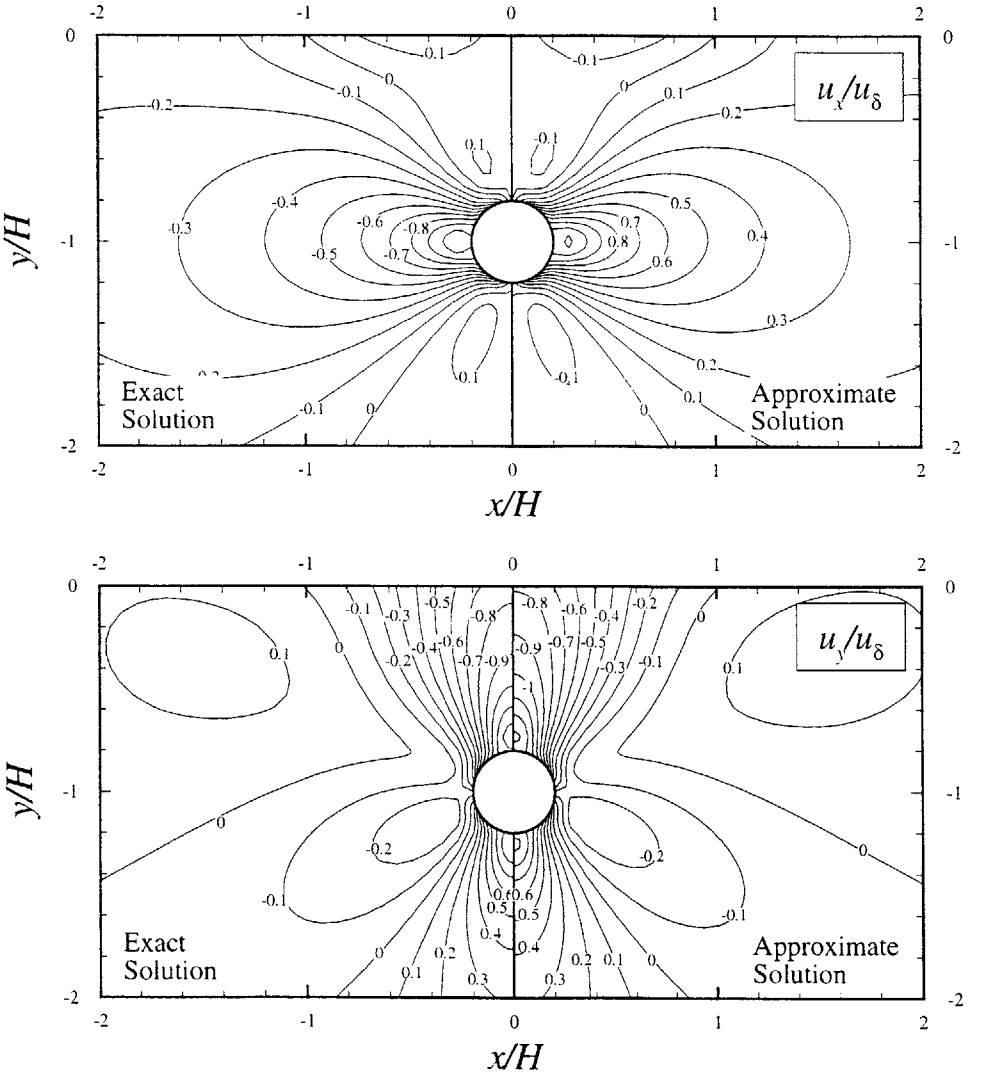

Figure 3.55. Ground displacements due to pure distortion mode, $R/H = 0.20$, $\nu = 0.50$

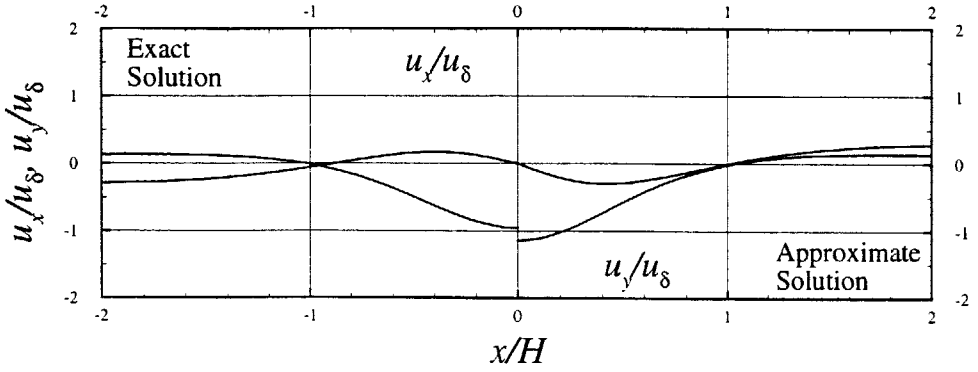

Figure 3.56. Surface displacements due to pure distortion mode, R/H = 0.45, ν = 0.00

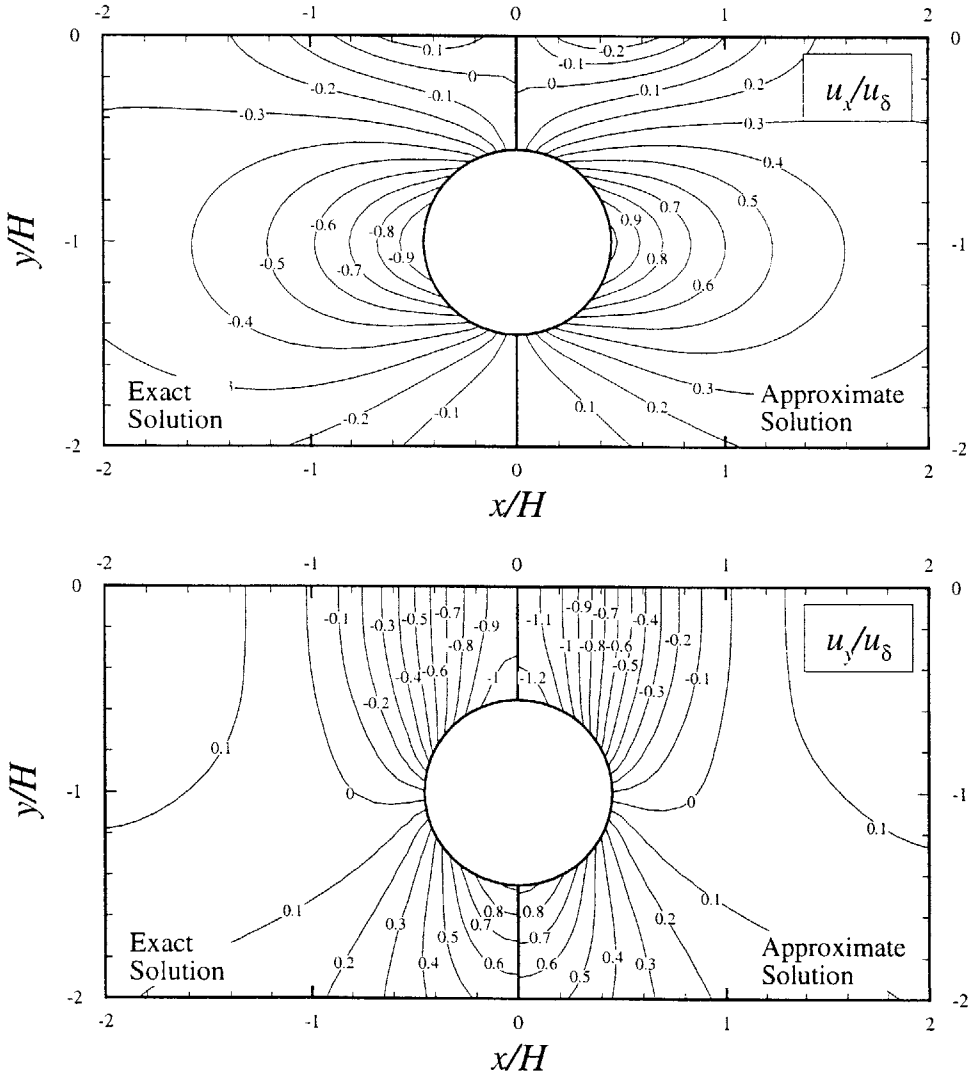

Figure 3.57. Ground displacements due to pure distortion mode, R/H = 0.45, ν = 0.00

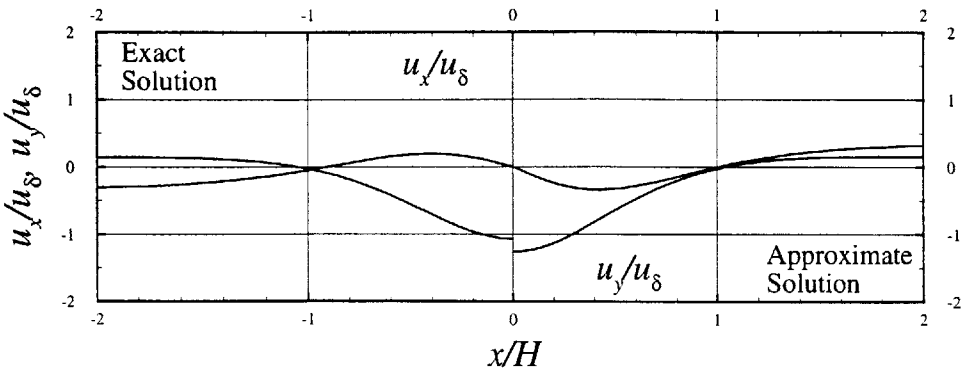

Figure 3.58. Surface displacements due to pure distortion mode, $R/H = 0.45$, $\nu = 0.25$

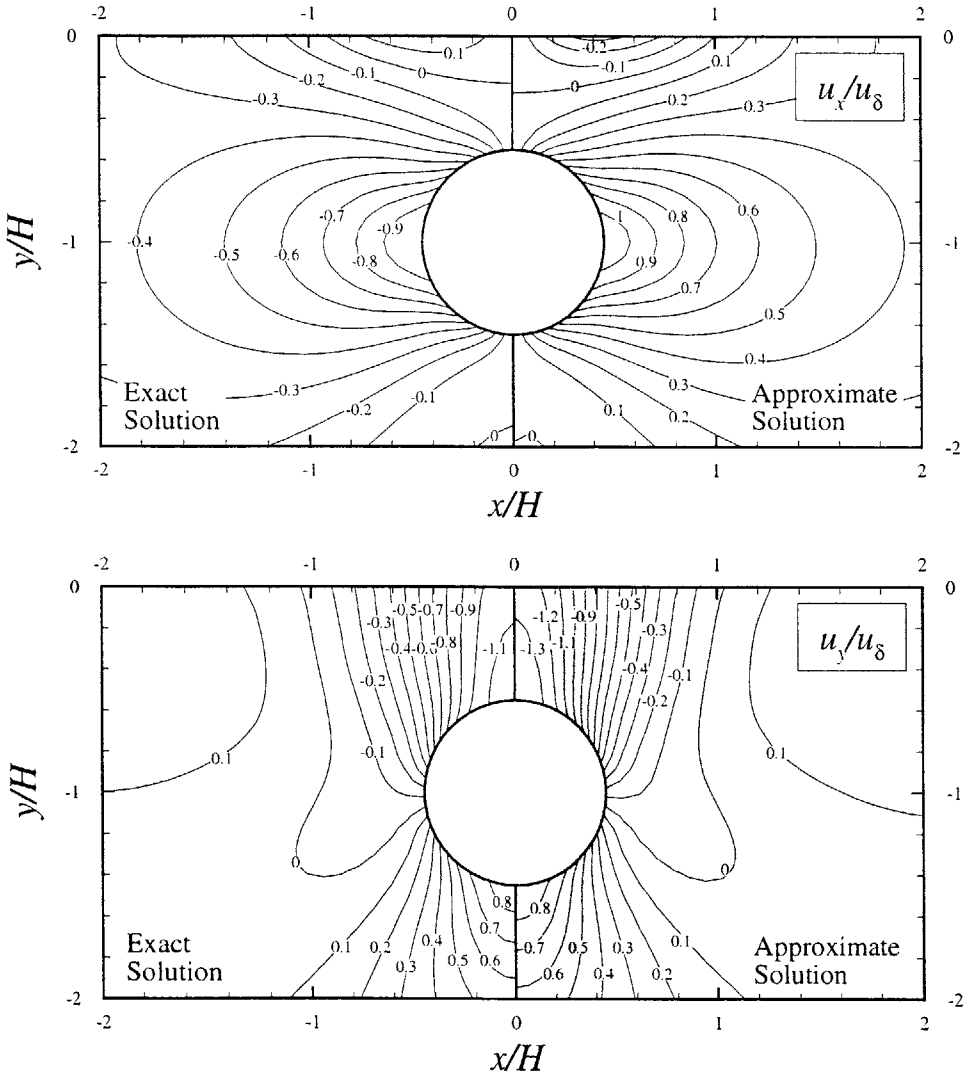

Figure 3.59. Ground displacements due to pure distortion mode, $R/H = 0.45$, $\nu = 0.25$

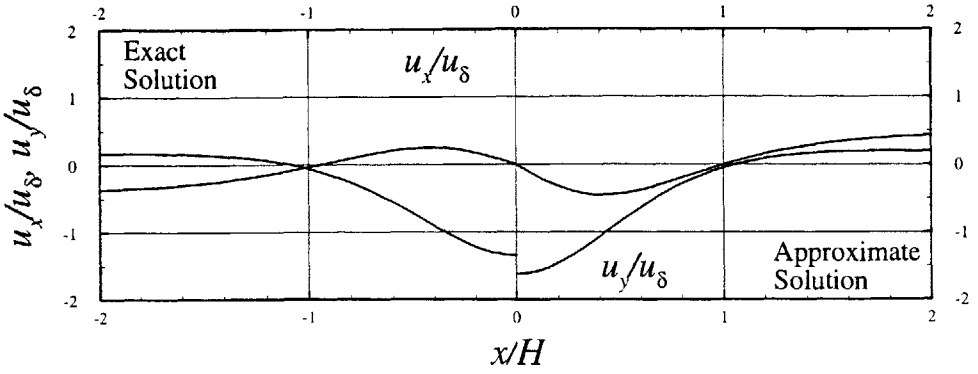

Figure 3.60. Surface displacements due to pure distortion mode, $R/H = 0.45$, $\nu = 0.50$

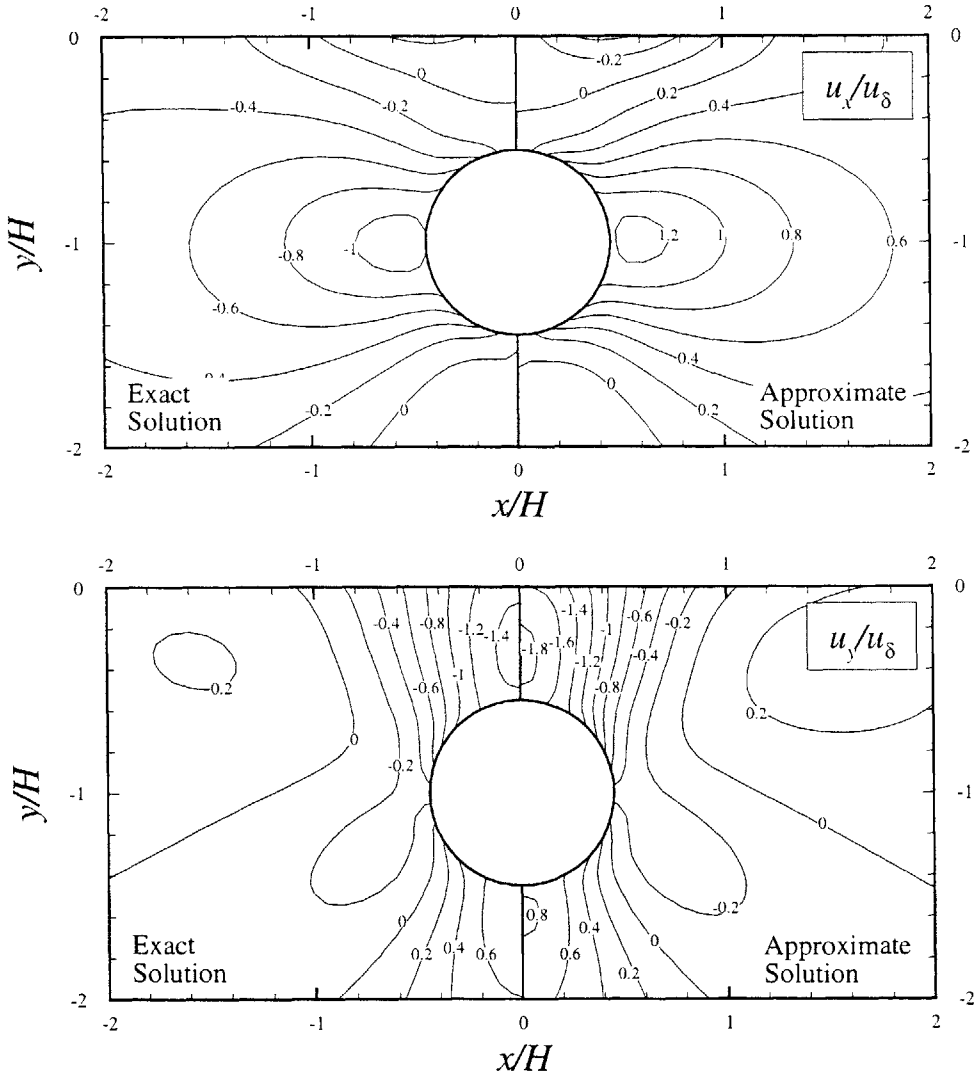

Figure 3.61. Ground displacements due to pure distortion mode, $R/H = 0.45$, $\nu = 0.50$

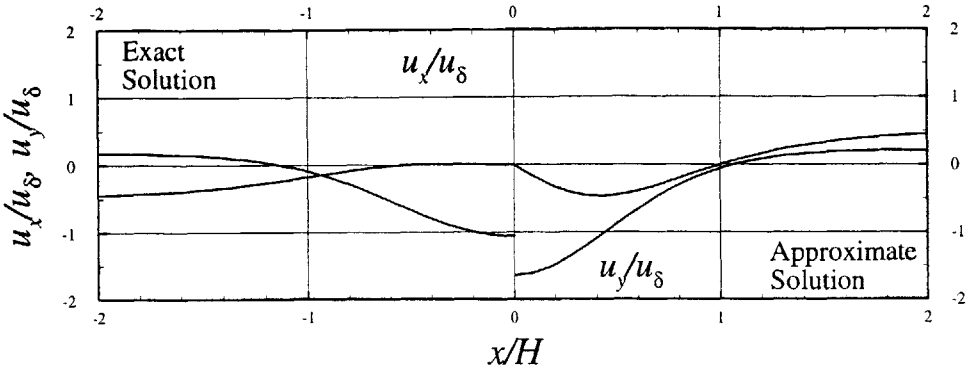

Figure 3.62. Surface displacements due to pure distortion mode, $R/H = 0.70$, $\nu = 0.00$

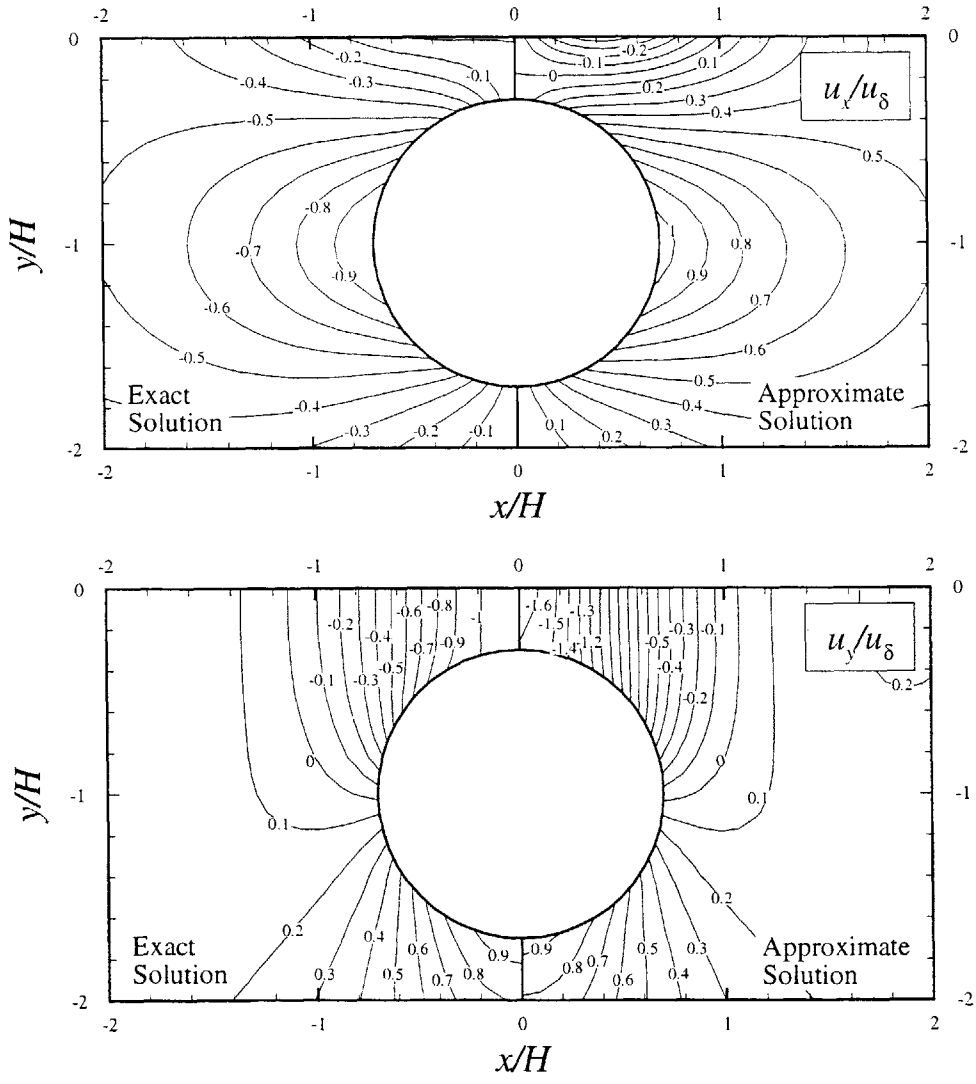

Figure 3.63. Ground displacements due to pure distortion mode, $R/H = 0.70$, $\nu = 0.00$

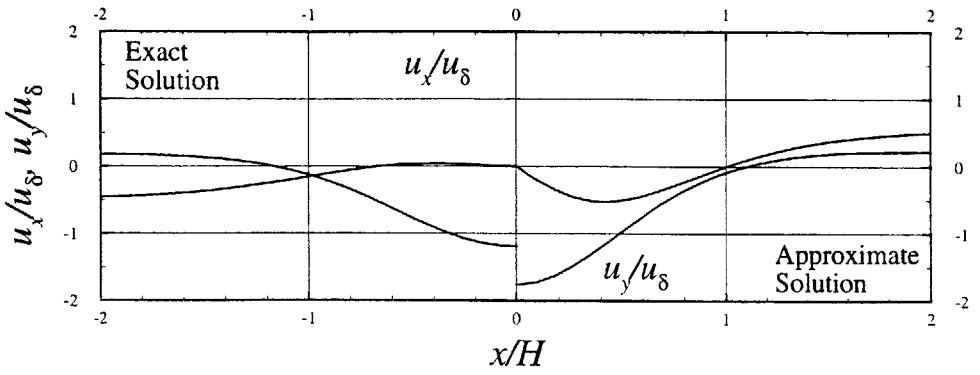

Figure 3.64. Surface displacements due to pure distortion mode, $R/H = 0.70$, $\nu = 0.25$

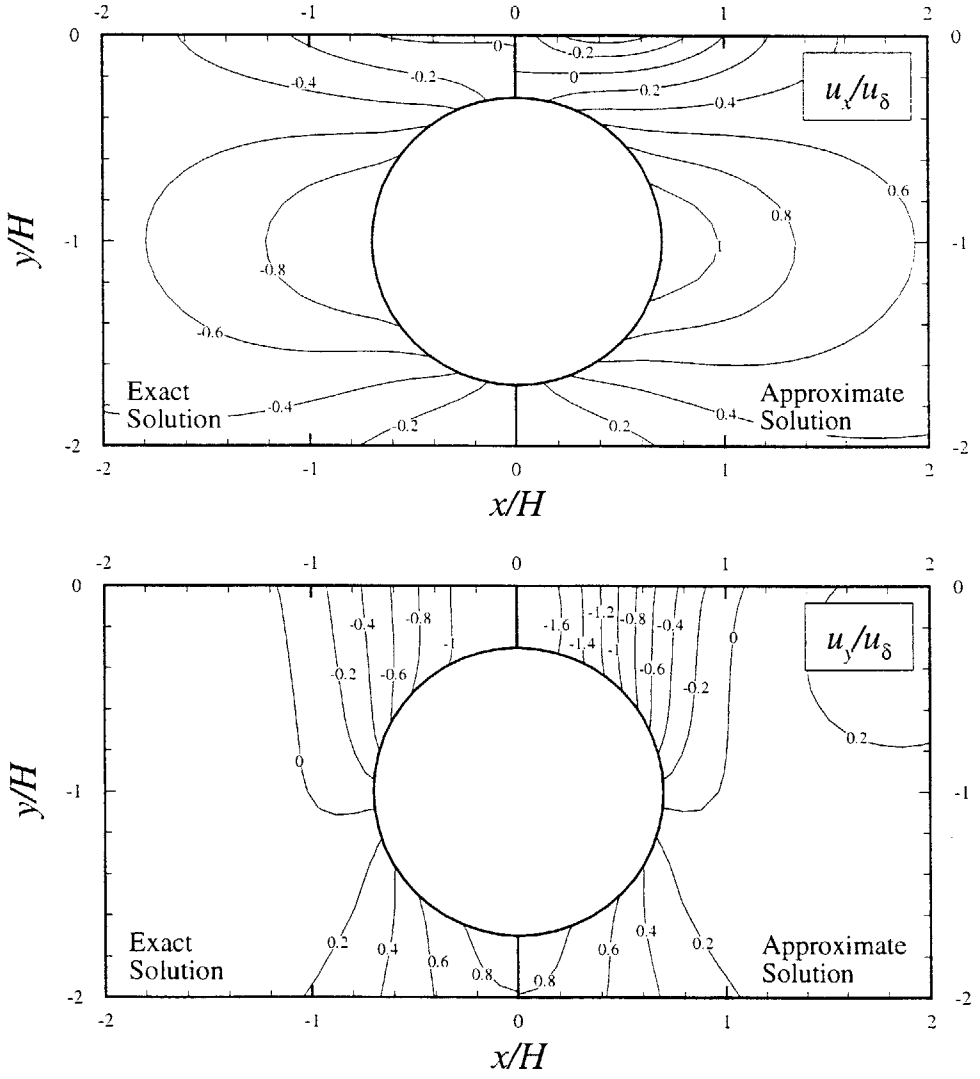

Figure 3.65. Ground displacements due to pure distortion mode, $R/H = 0.70$, $\nu = 0.25$

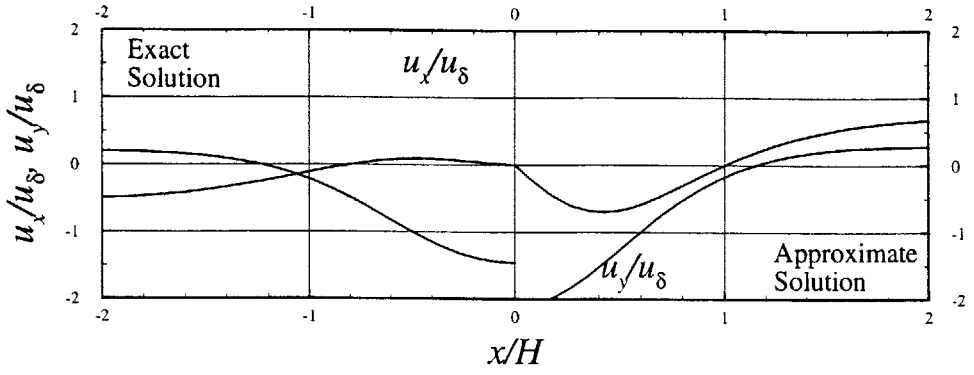

Figure 3.66. Surface displacements due to pure distortion mode, $R/H = 0.70$, $\nu = 0.50$

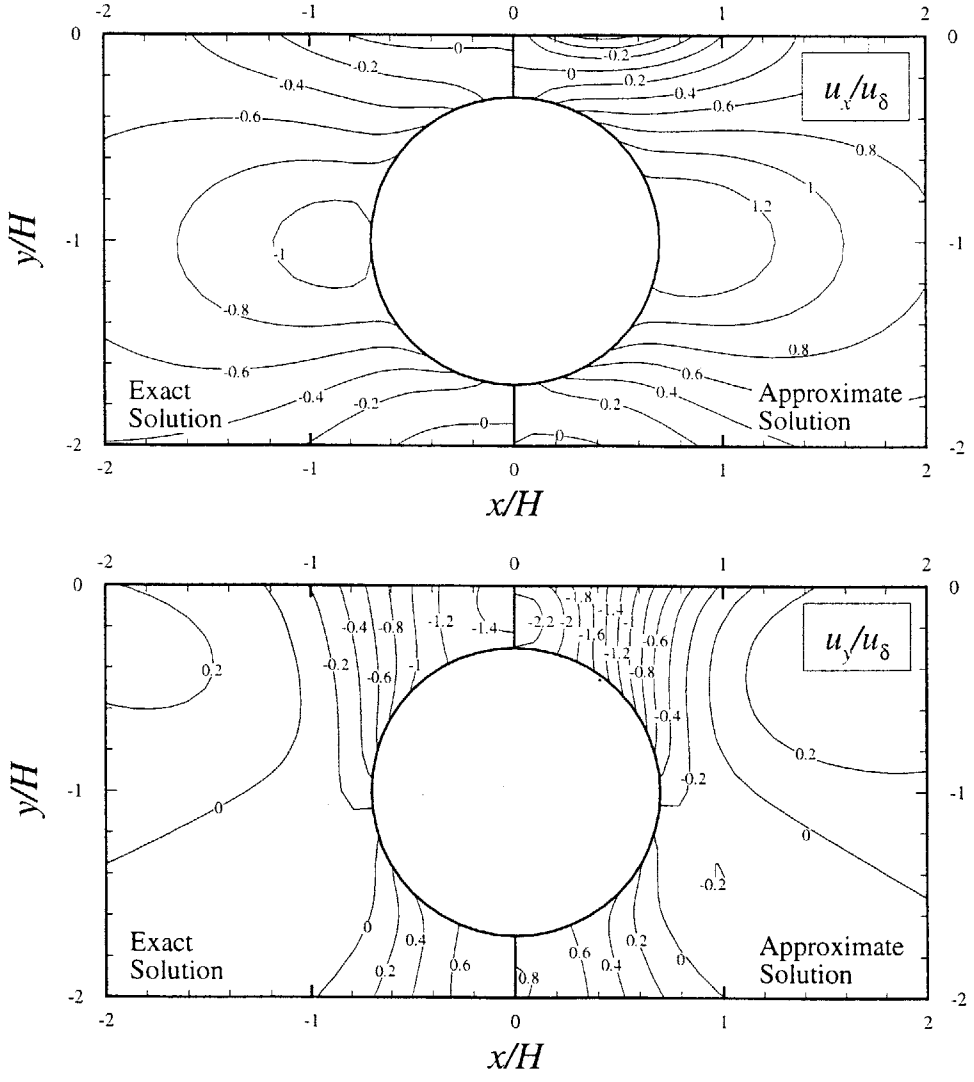

Figure 3.67. Ground displacements due to pure distortion mode, $R/H = 0.70$, $\nu = 0.50$

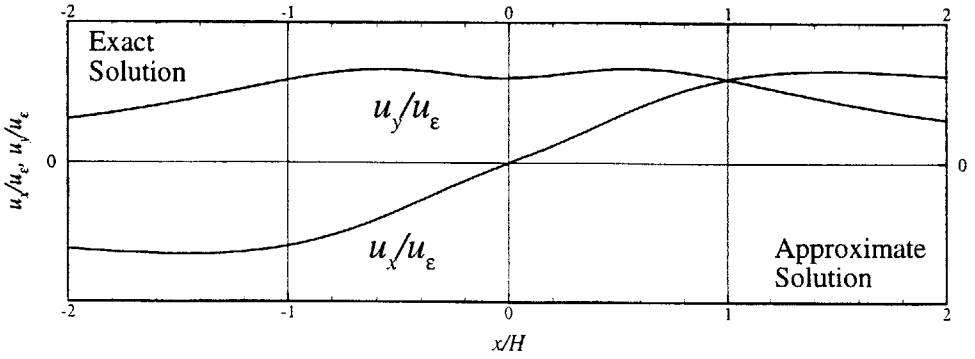

Figure 3.68. Surface displacements, R/H = 0.20, ρ = -0.5, ν = 0.25

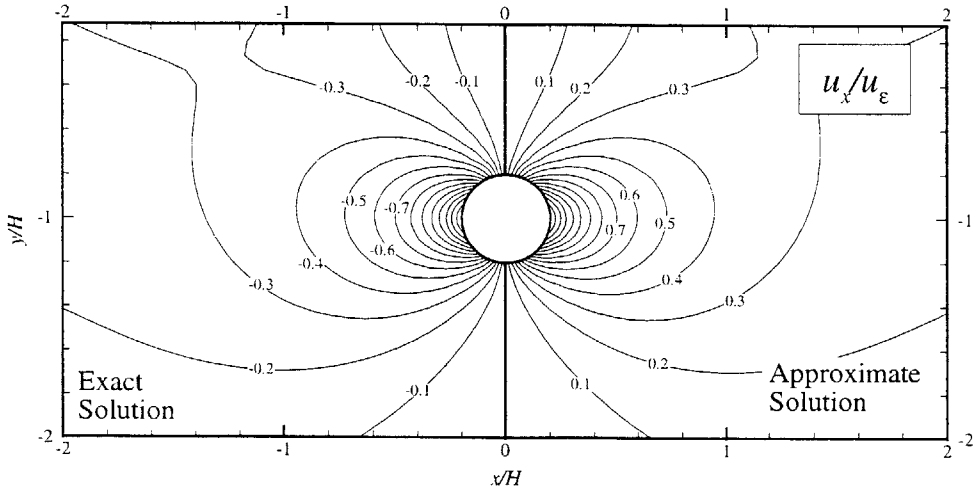

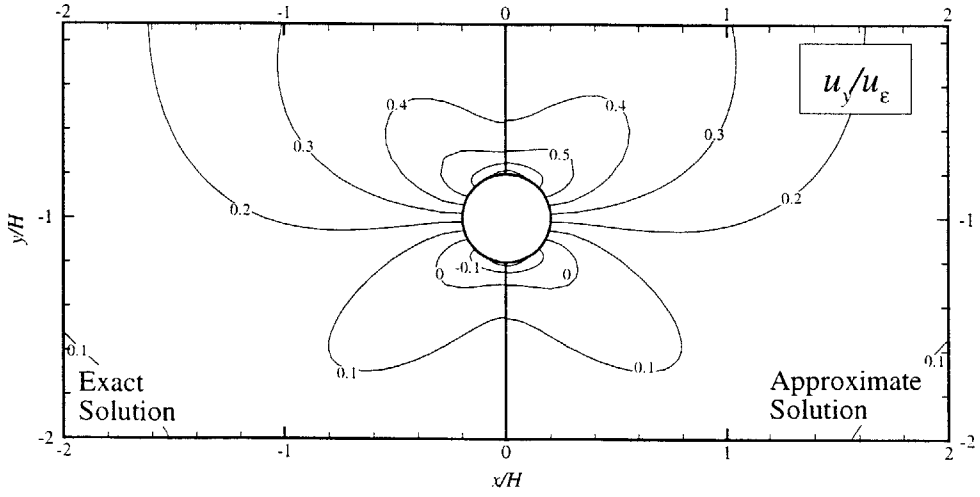

Figure 3.69. Ground displacements, R/H = 0.20, ρ = -0.5, ν = 0.25

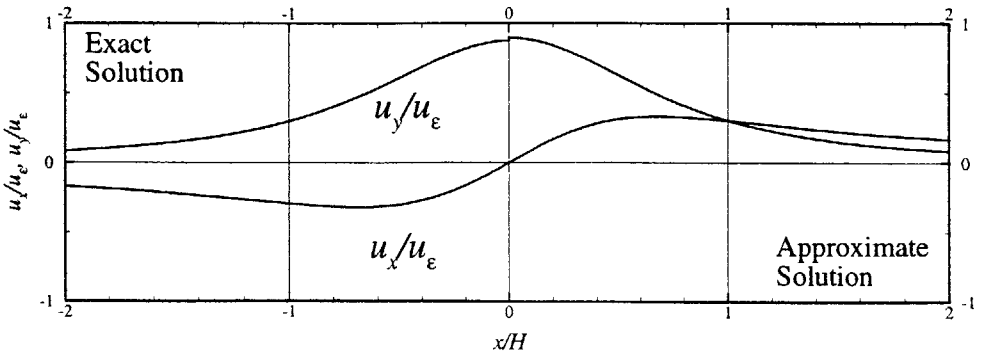

Figure 3.70. Surface displacements, $R/H = 0.20$, $\rho = 0.5$, $\nu = 0.25$

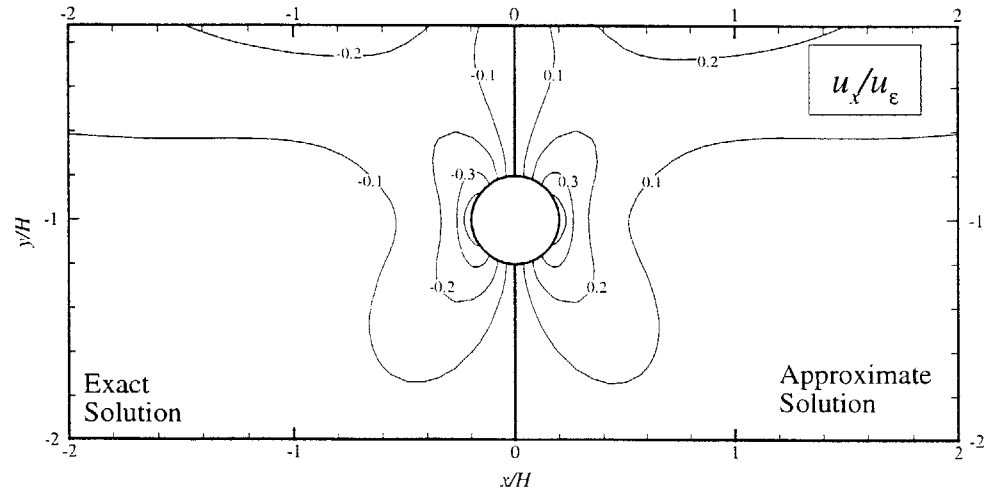

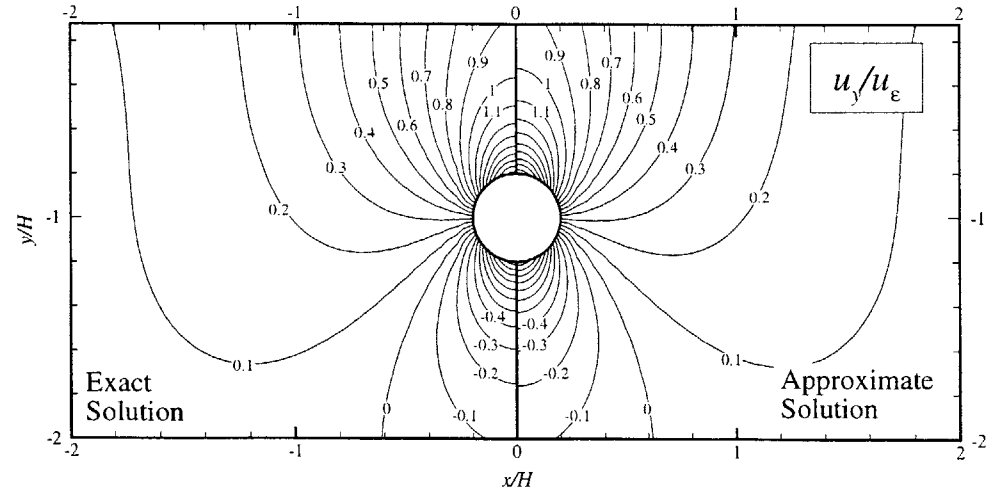

Figure 3.71. Ground displacements, $R/H = 0.20$, $\rho = 0.5$, $\nu = 0.25$

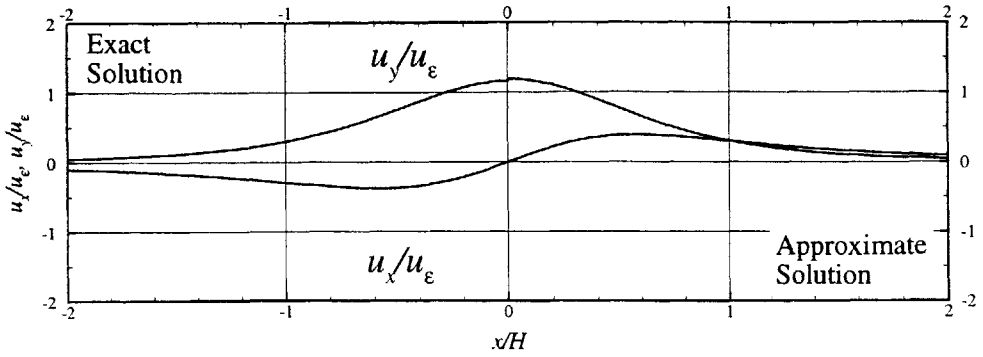

Figure 3.72. Surface displacements, $R/H = 0.20$, $\rho = 1$, $\nu = 0.25$

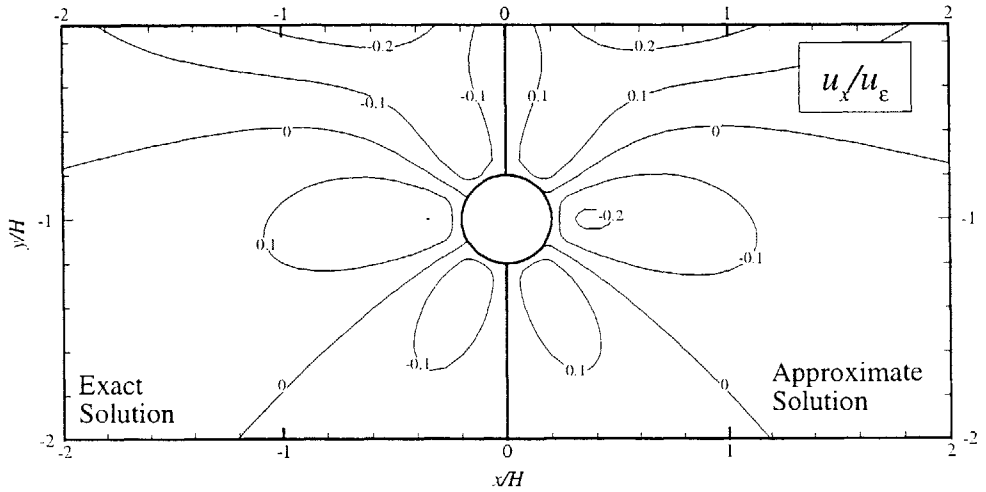

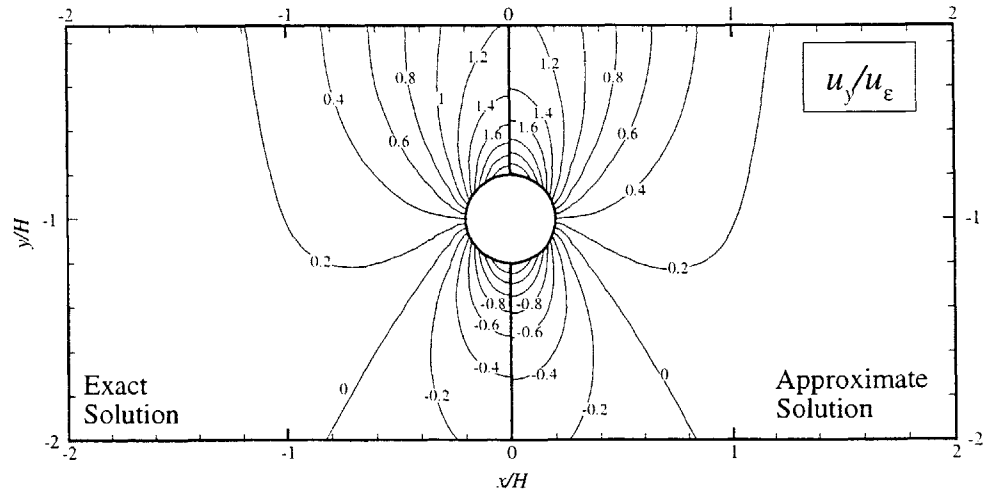

Figure 3.73. Ground displacements, $R/H = 0.20$, $\rho = 1$, $\nu = 0.25$

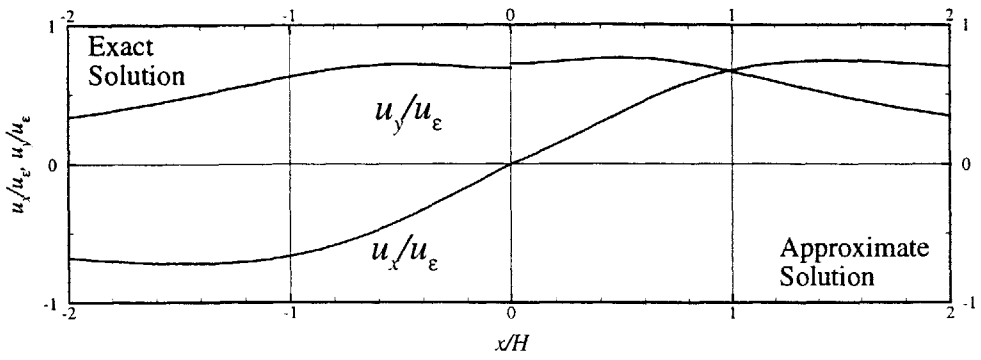

Figure 3.74. Surface displacements, R/H = 0.45, ρ = -0.5, ν = 0.25

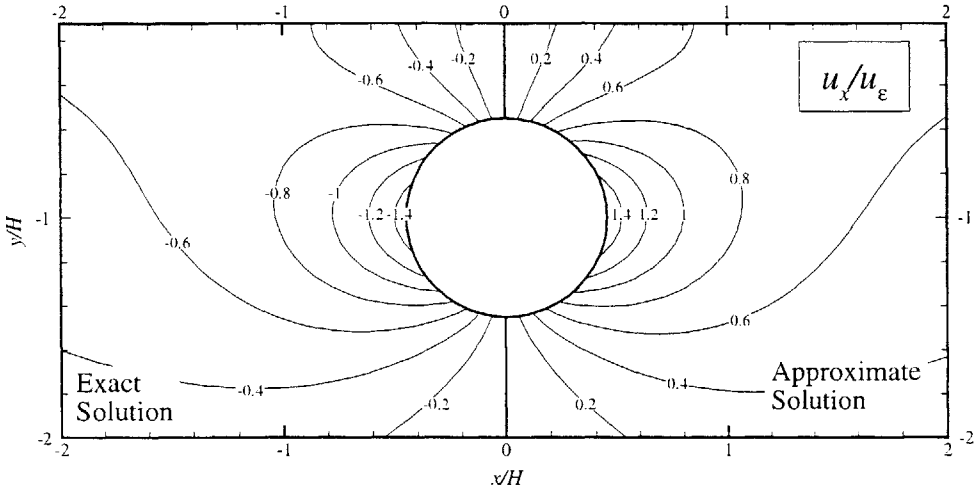

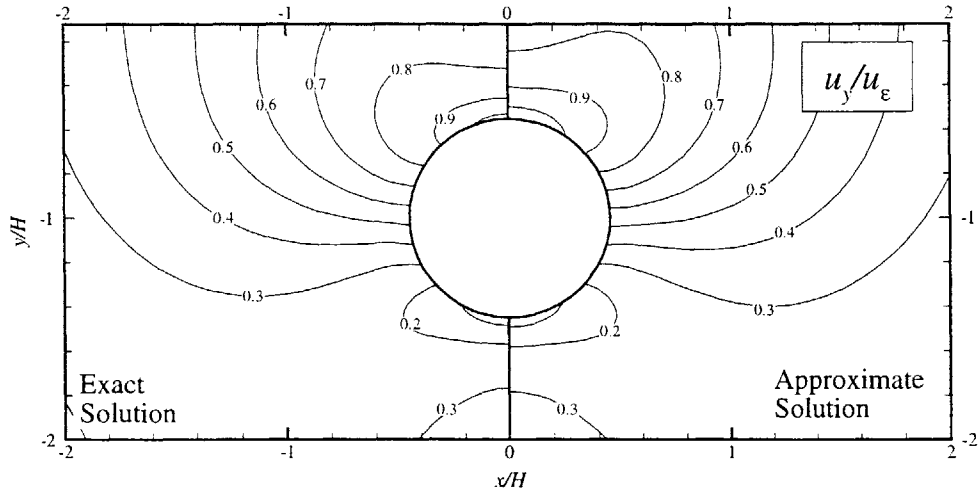

Figure 3.75. Ground displacements, R/H = 0.45, ρ = -0.5, ν = 0.25

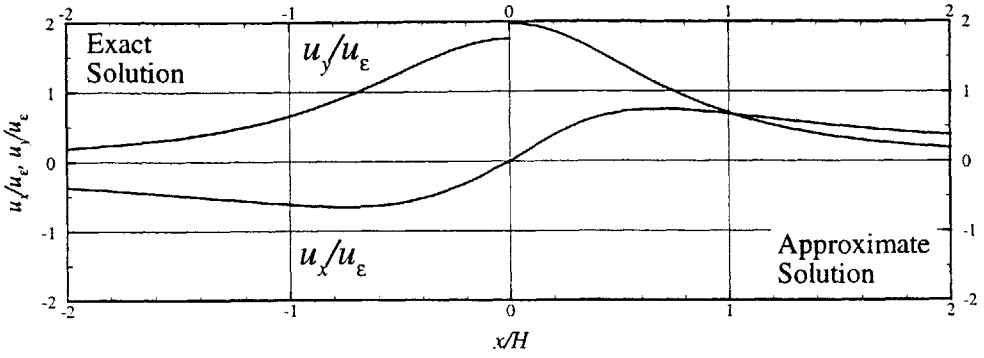

Figure 3.76. Surface displacements, R/H = 0.45, ρ = 0.5, ν = 0.25

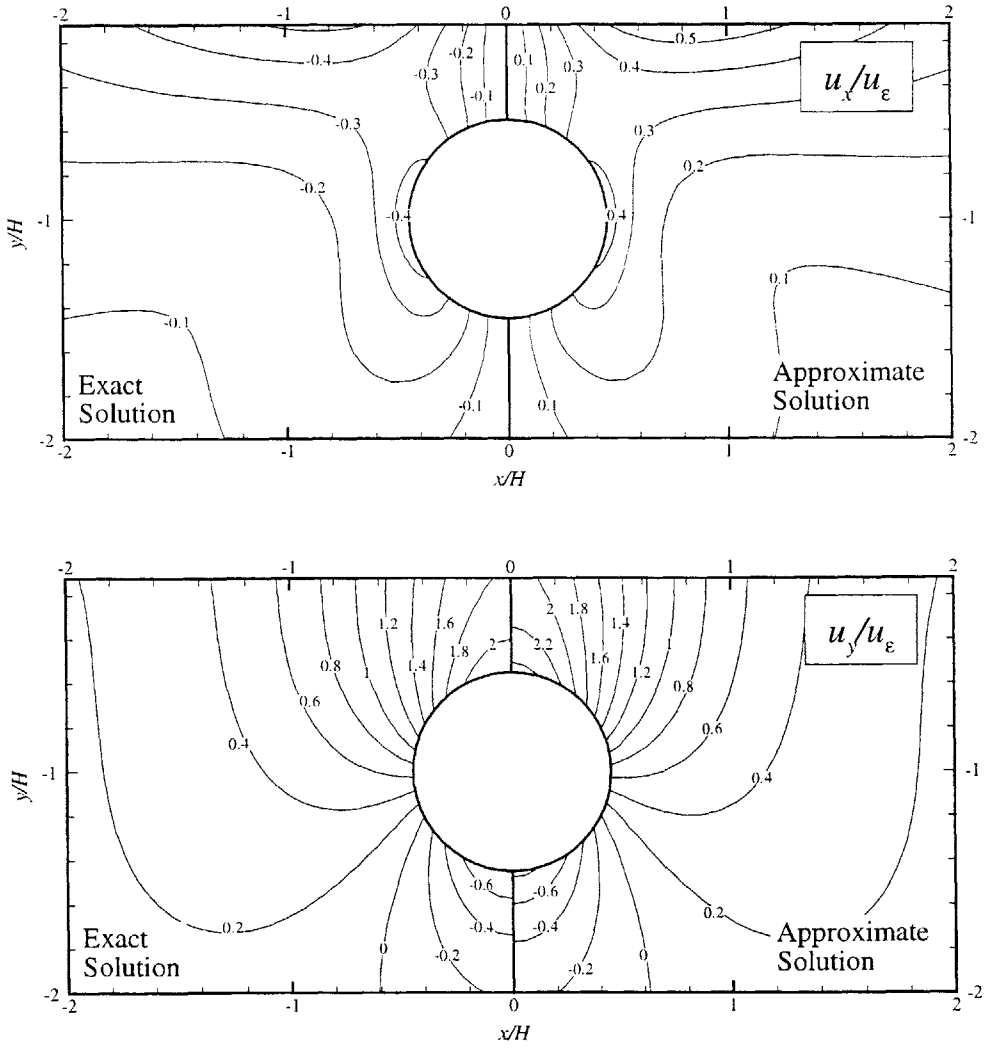

Figure 3.77. Ground displacements, R/H = 0.45, ρ = 0.5, ν = 0.25

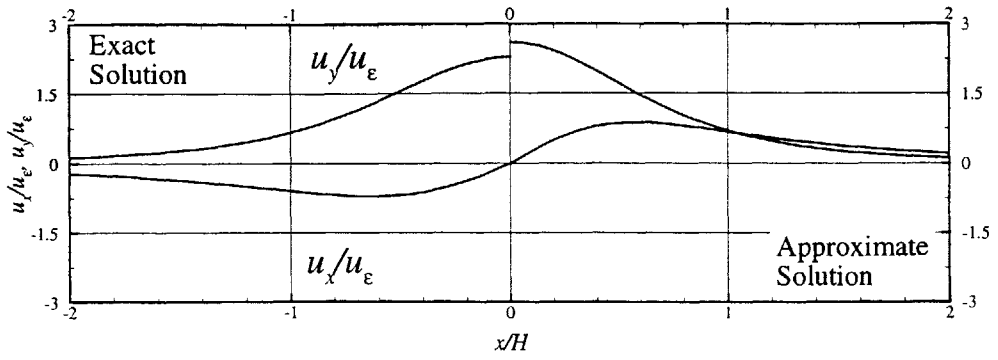

Figure 3.78. Surface displacements, $R/H = 0.45$, $\rho = 1$, $\nu = 0.25$

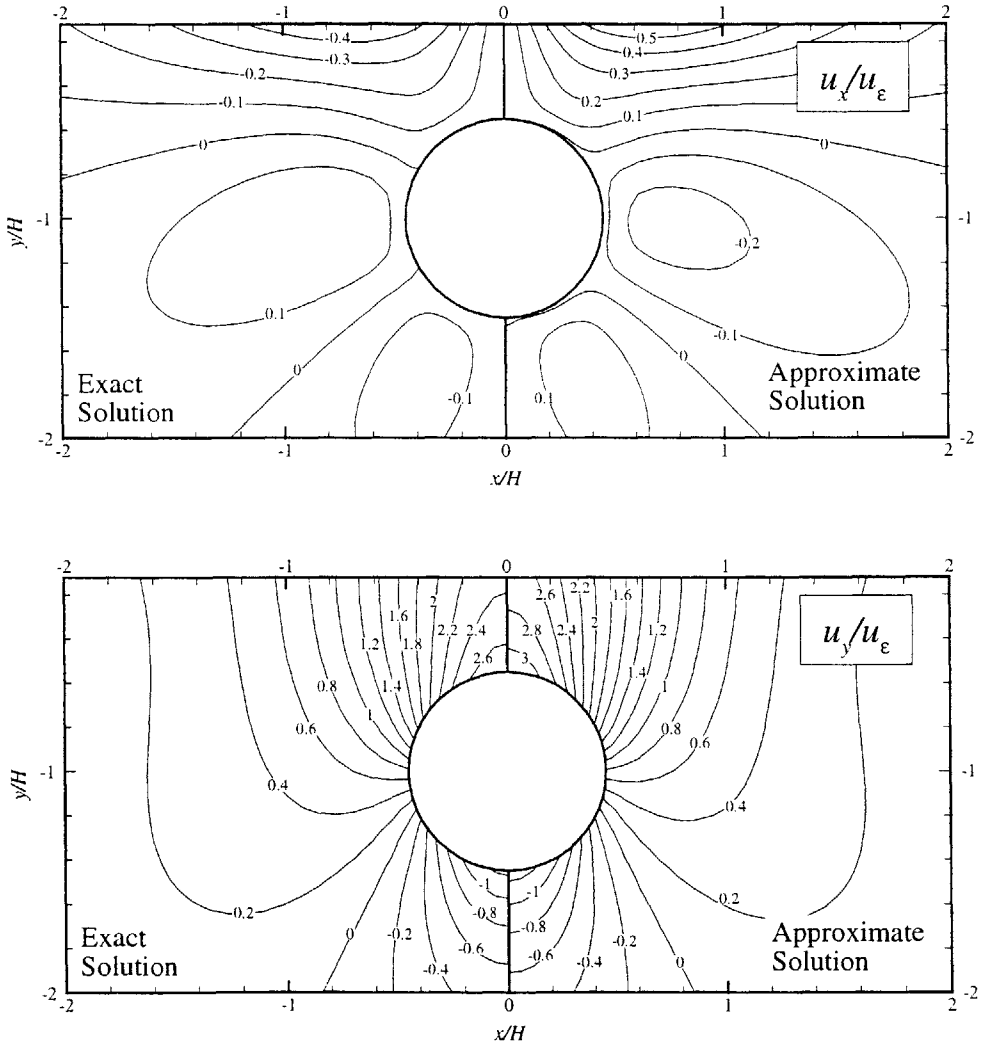

Figure 3.79. Ground displacements, $R/H = 0.45$, $\rho = 1$, $\nu = 0.25$

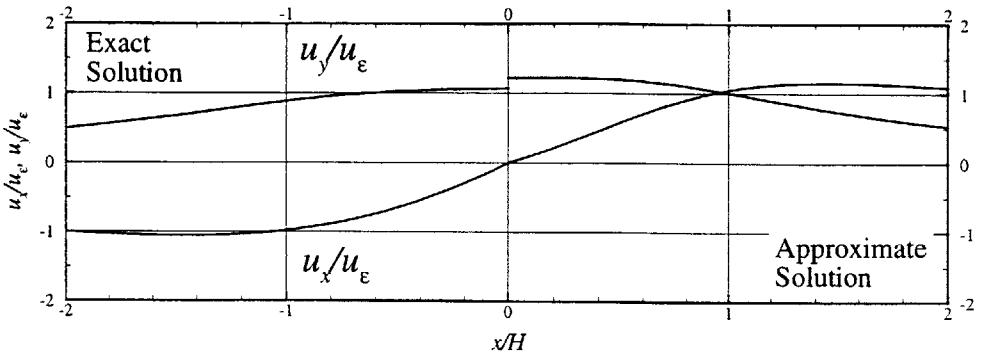

Figure 3.80. Surface displacements, R/H = 0.70, ρ = -0.5, ν = 0.25

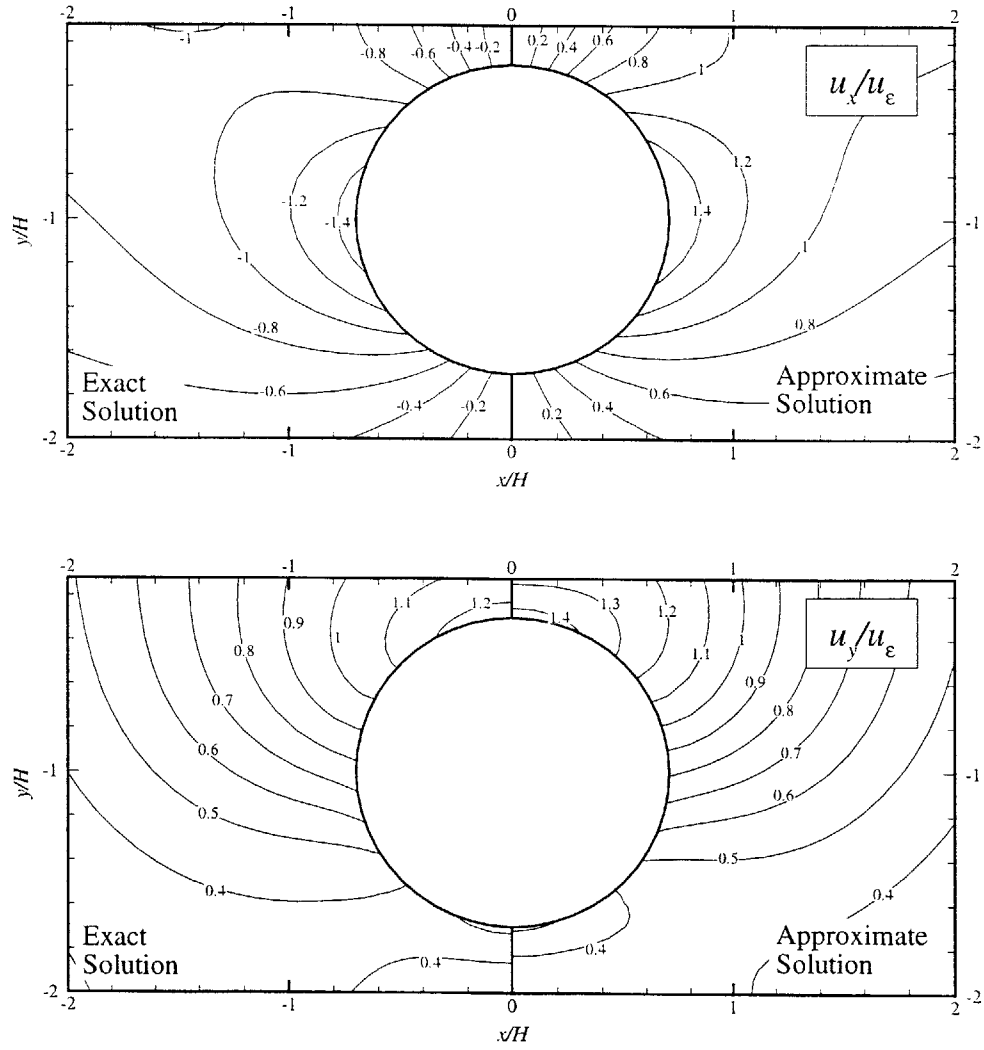

Figure 3.81. Ground displacements, R/H = 0.70, ρ = -0.5, ν = 0.25

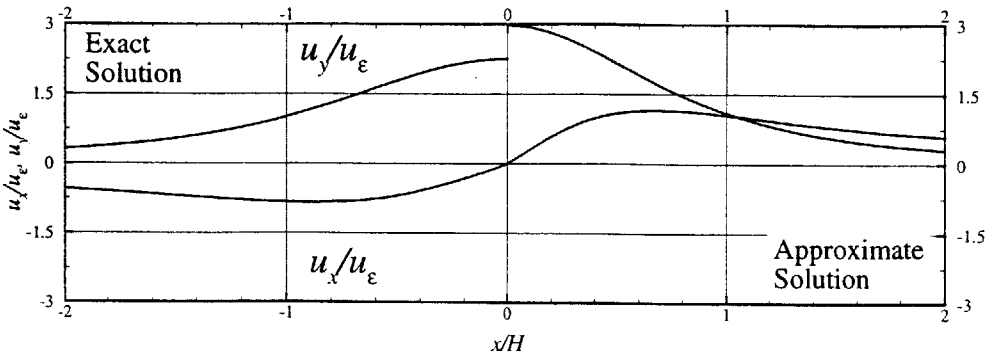

Figure 3.82. Surface displacements, $R/H = 0.70$, $\rho = 0.5$, $\nu = 0.25$

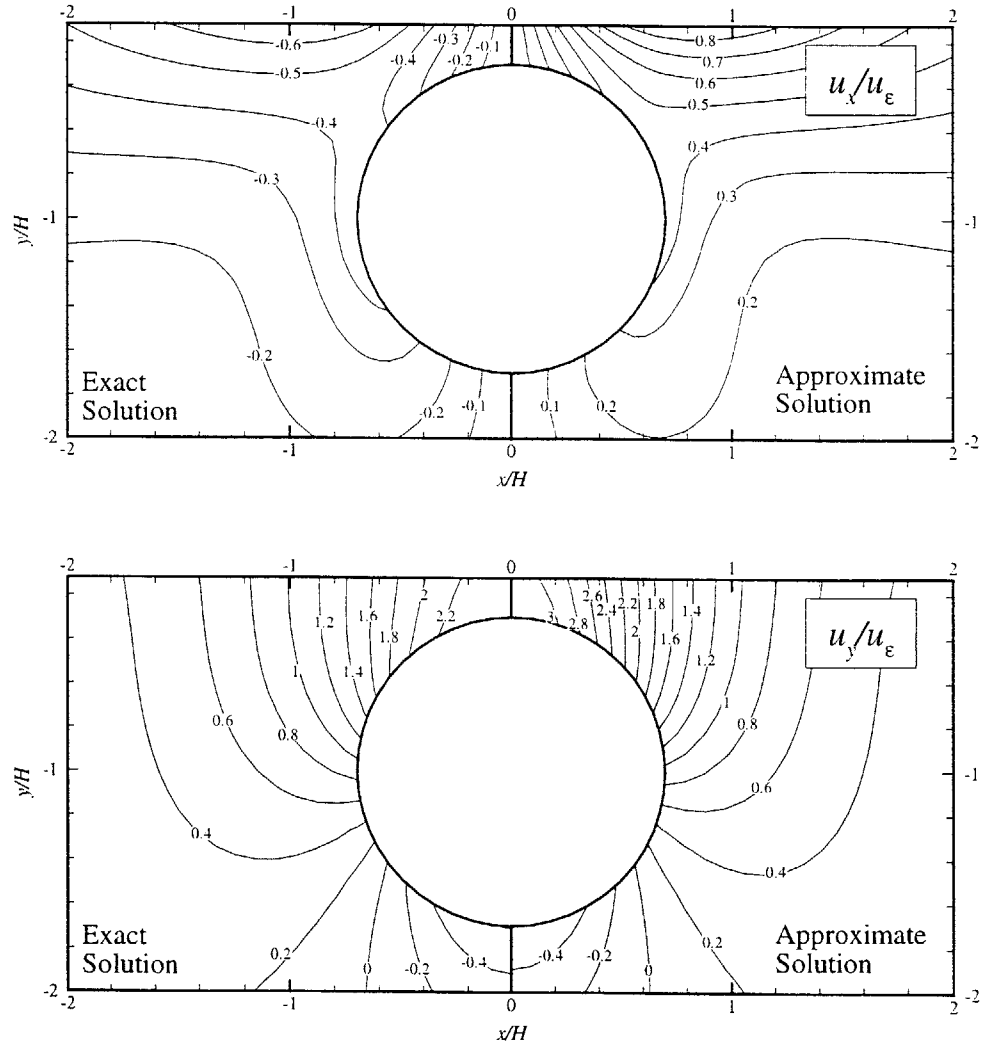

Figure 3.83. Ground displacements, $R/H = 0.70$, $\rho = 0.5$, $\nu = 0.25$

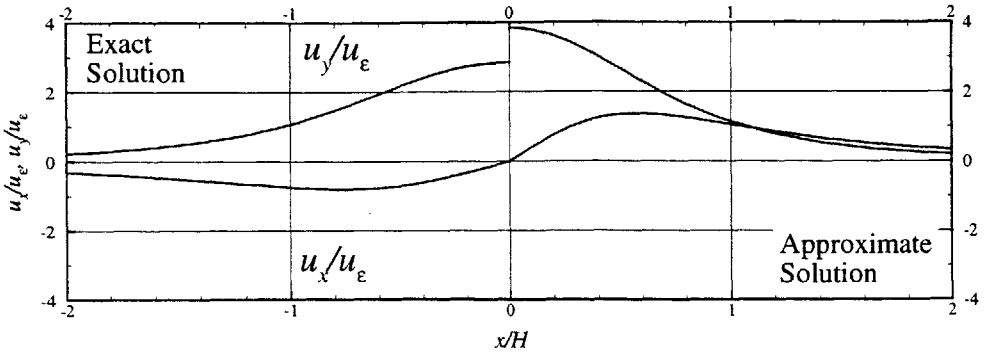

Figure 3.84. Surface displacements, $R/H = 0.70$, $\rho = 1$, $\nu = 0.25$

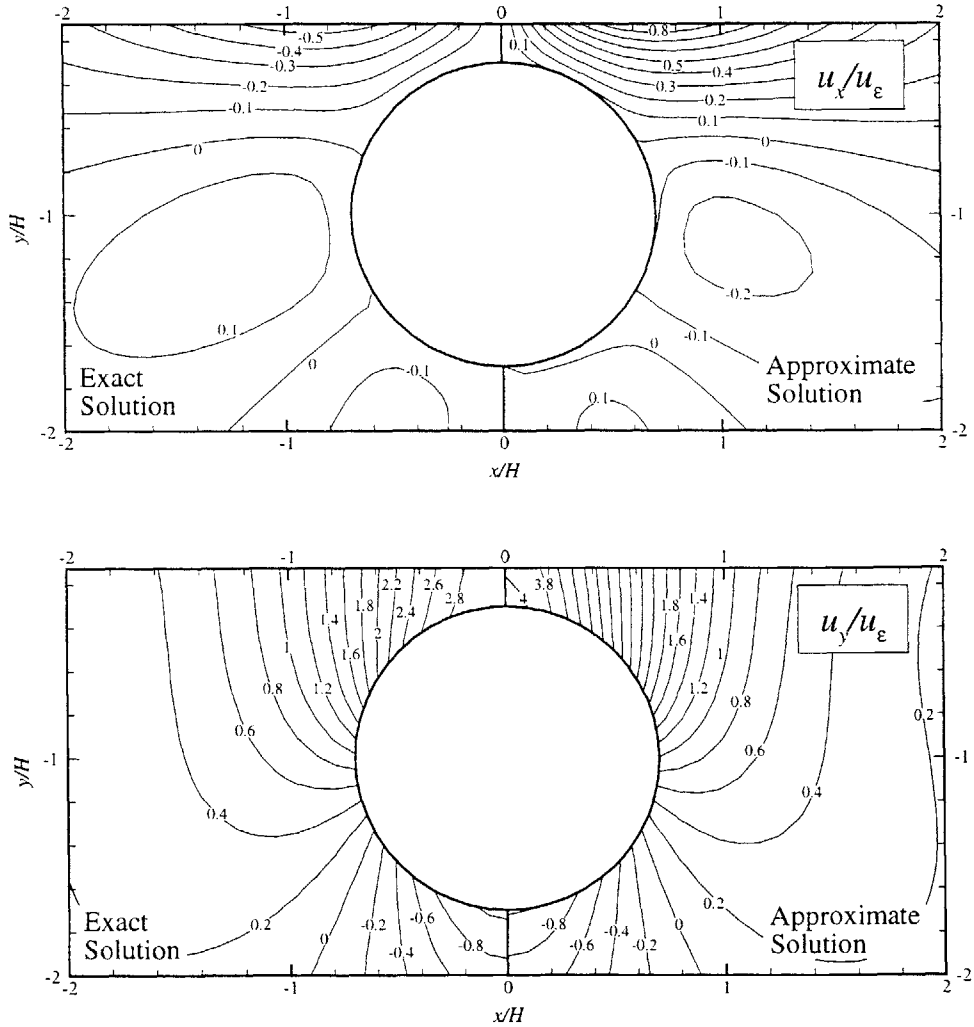

Figure 3.85. Ground displacements, $R/H = 0.70$, $\rho = 1$, $\nu = 0.25$

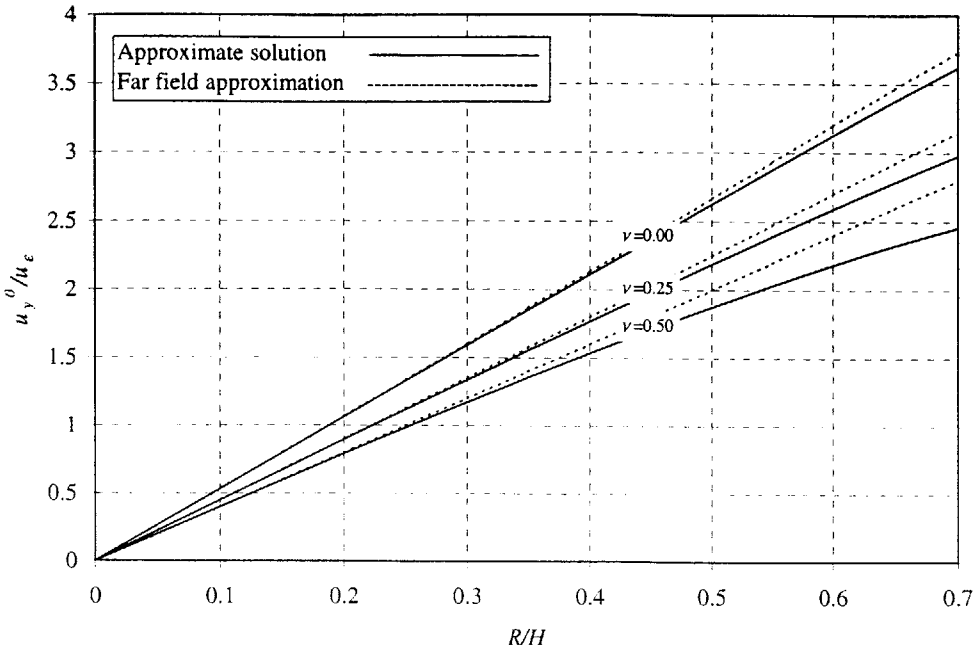

Figure 3.86. Influence of ν on the normalized surface vertical displacement at x = 0, $\rho = 0.5$

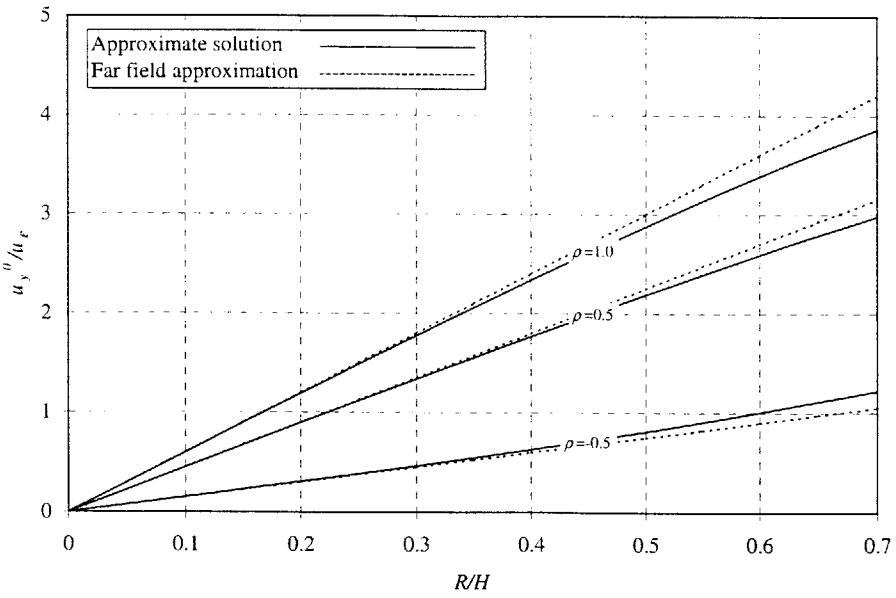

Figure 3.87. Influence of ρ on the normalized surface vertical displacement at x = 0, $\nu = 0.25$

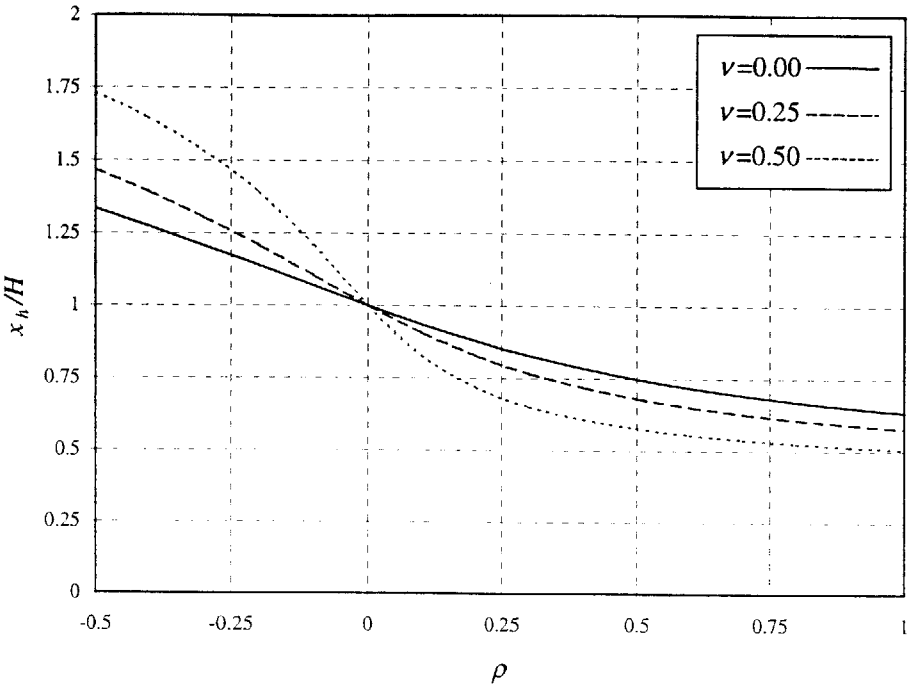

Figure 3.88. Influence of relative distortion ρ on the location of maximum horizontal displacement, x_h

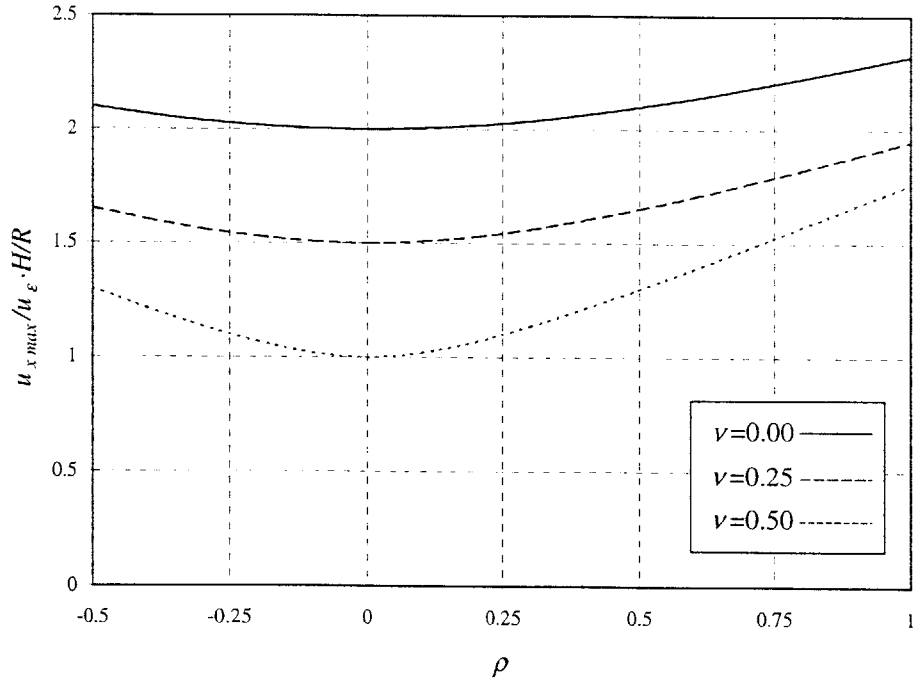

Figure 3.89. Influence of relative distortion on the normalized maximum horizontal displacement

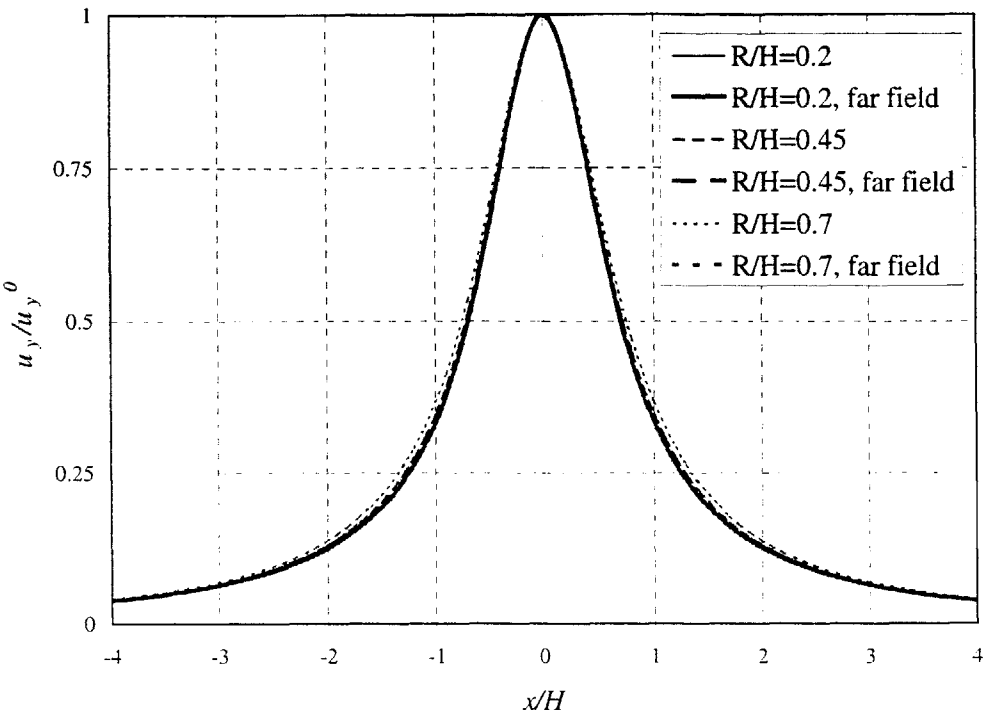

Figure 3.90. Influence of embedment ratio, *R/H*, on the surface settlement distribution. $\rho = 0.5$; $\nu = 0.25$

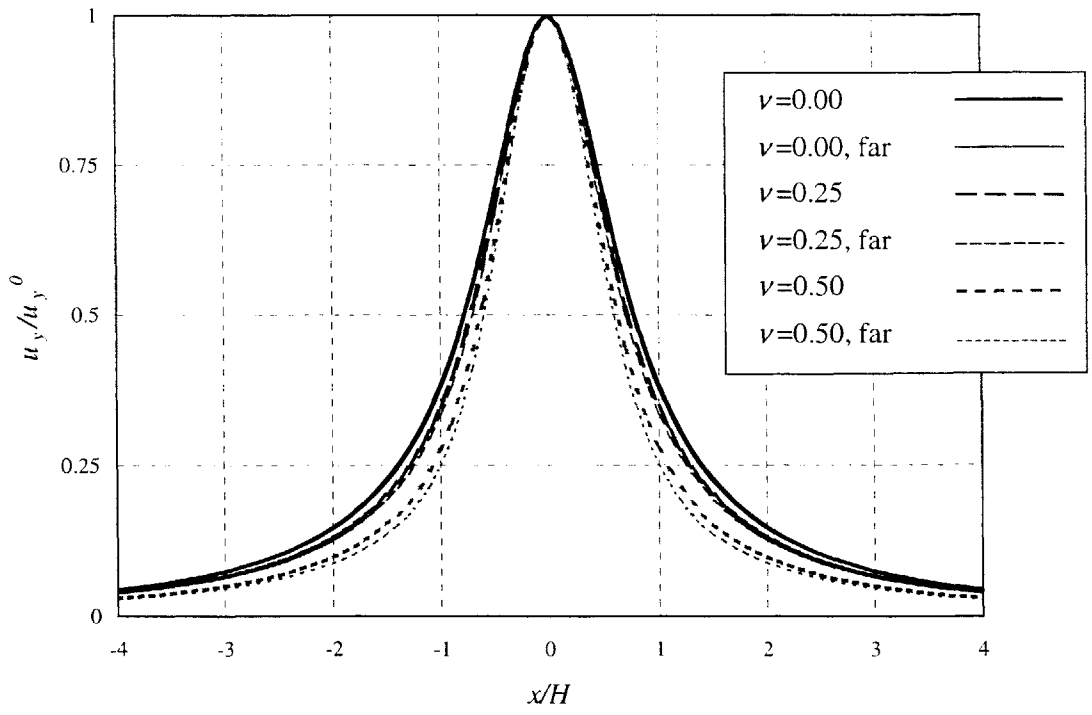

Figure 3.91. Influence of Poisson ratio, ν, on the surface settlement distribution. $\rho = 1$; *R/H* = 0.45

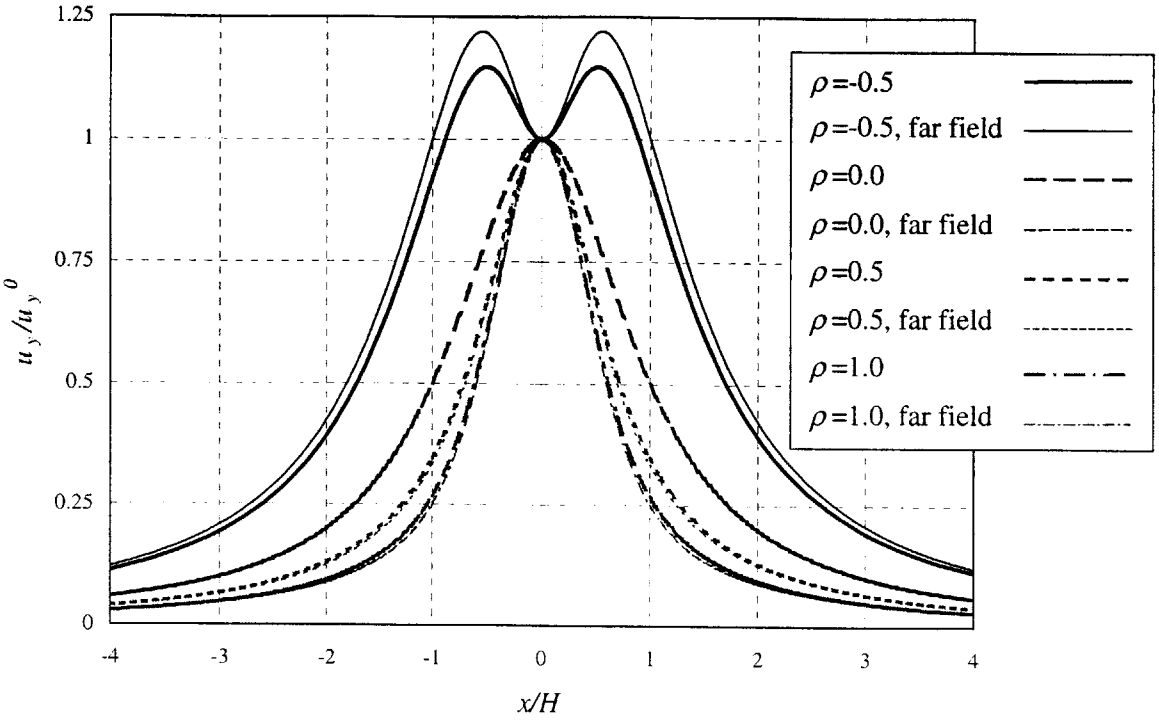

Figure 3.92. Influence of relative distortion, ρ, on the surface settlement distribution for $\nu = 0.25$; $R/H = 0.45$

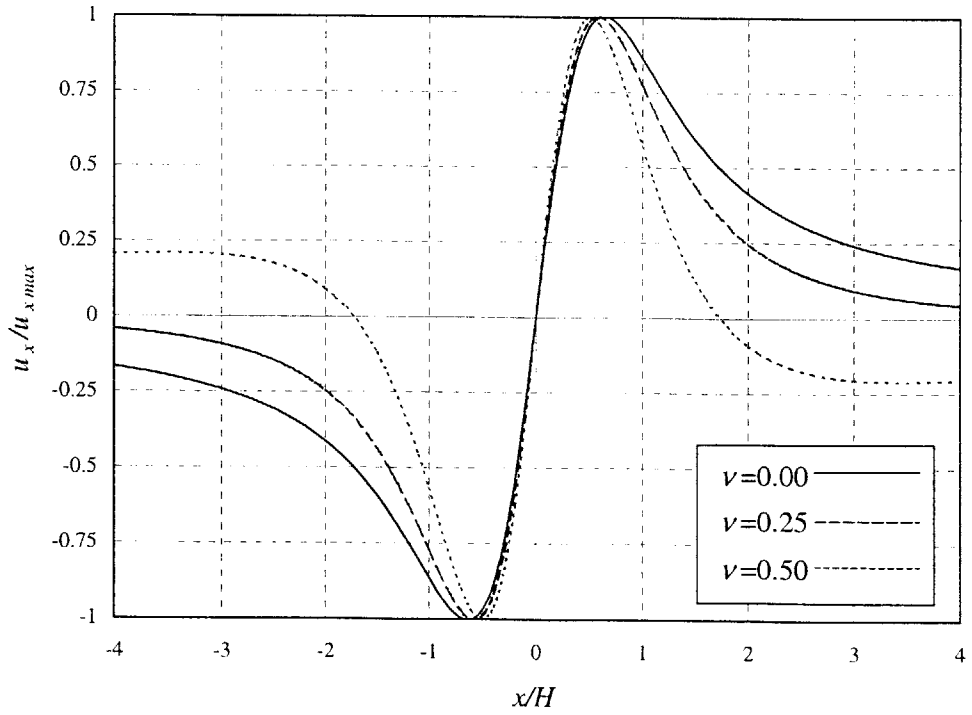

Figure 3.93. Horizontal displacement distribution, $\rho = 1.0$

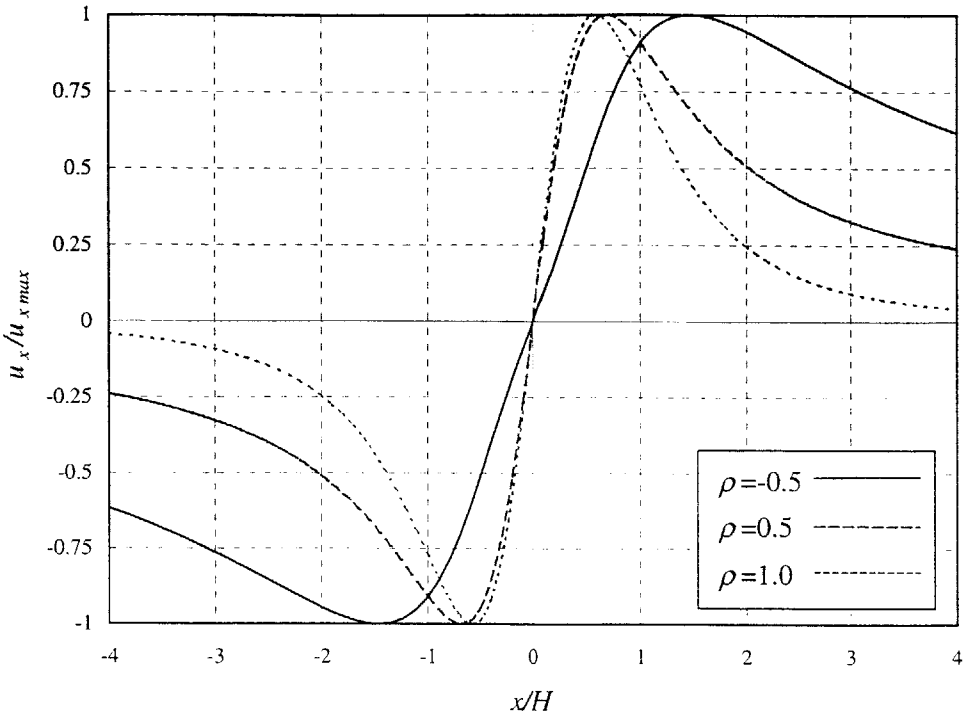

Figure 3.94. Horizontal displacement distribution, $\nu = 0.25$

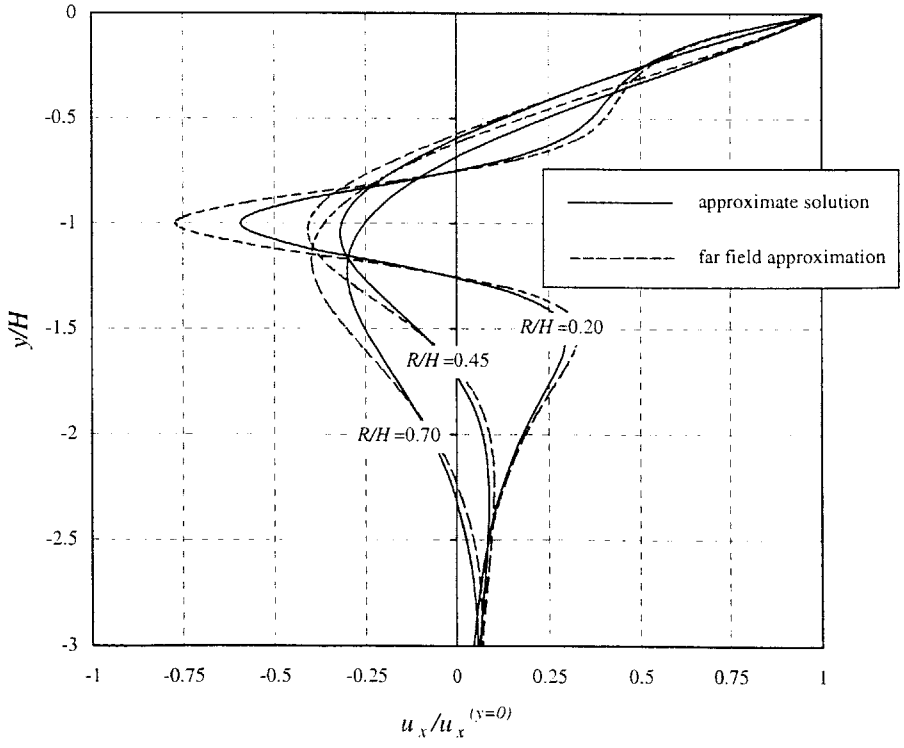

Figure 3.95. Horizontal displacements at $x = 2 \cdot R$, $\rho = 1$, $\nu = 0.25$

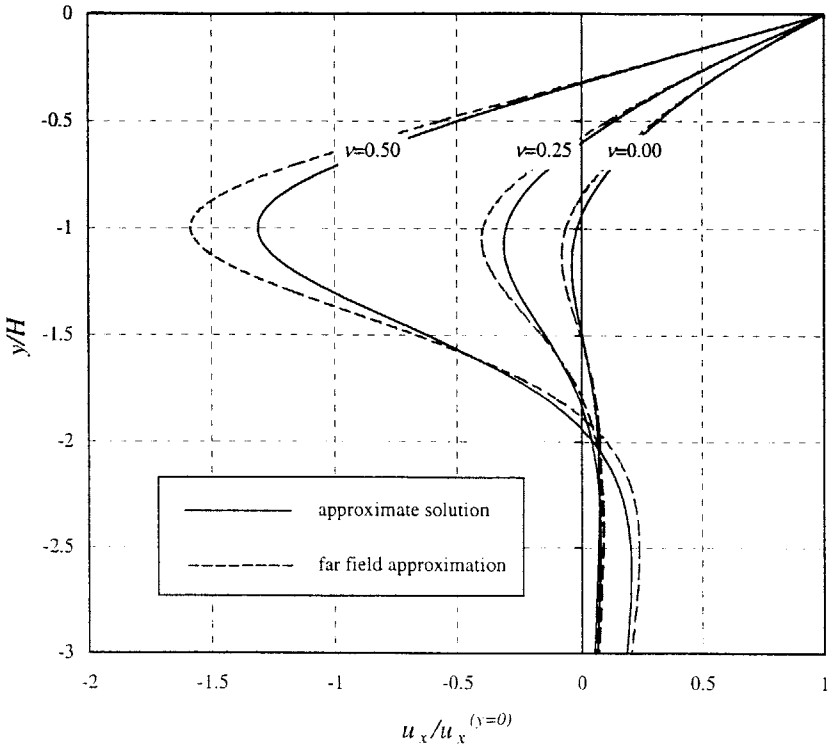

Figure 3.96. Horizontal displacements at $x = 2 \cdot R$, $\rho = 1$, $R/H = 0.5$

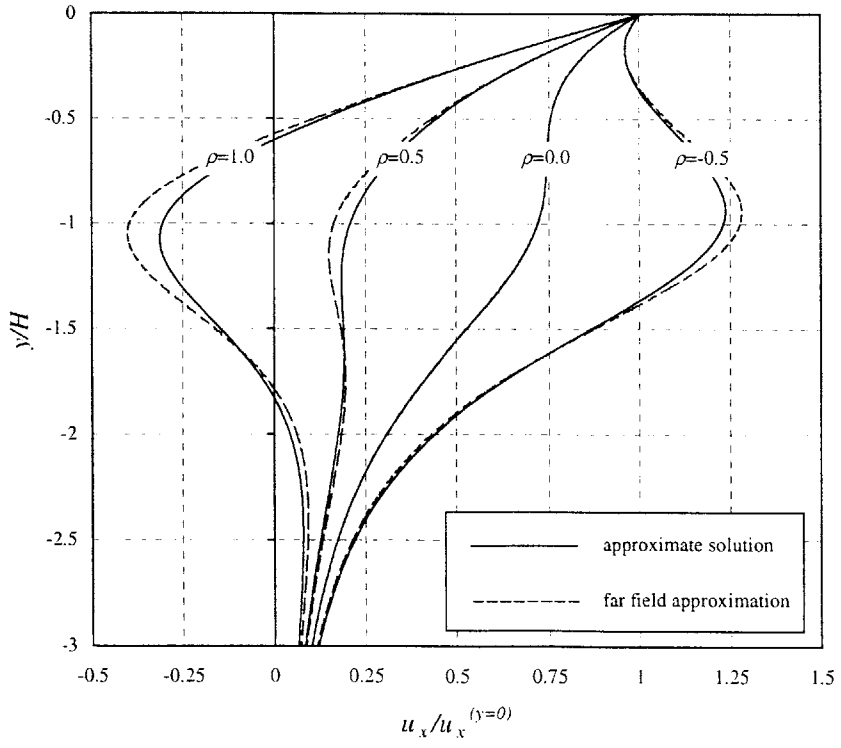

Figure 3.97. Horizontal displacements at $x = 2 \cdot R$, $\nu = 0.25$, $R/H = 0.5$

4. Influence of Tunnel Geometry. Rectangular Drift

This Chapter investigates the effects of tunnel geometry on the ground displacement field by analyzing the behavior of a rectangular tunnel in an elastic half-plane. This analysis method considers the displacement field due to an arbitrarily shaped cavity that collapses into a line (similar to the approximate model proposed by Sagaseta, 1987). The solution is obtained by means of integrating the Green functions (defined as the displacement functions due to a unit volume cavity contraction/expansion) over the line to which the cavity collapses. It should be noticed that this is an exact approach, since the Green functions are exact in the differential level (i.e., infinitesimal cavity contraction). However, its application for ground deformation analysis due to a deforming rectangular drift is approximate. The geometry of the drift is exactly represented, but the displacement field is constrained by the Green functions.

The displacement field due to an equivalent distortion could also be modeled by assuming that the net volume change is zero, i.e., superimposing a cavity contraction and an expansion. However, this seriously under-predicts the effects of the distortion component, since the obtained solution will not be singular (Sections 3.3.1 and 3.3.2) in the sense that if the distance between the cavities is reduced to zero (i.e., a point solution), but keeping the volume expansion/contraction finite, the displacement field vanishes at the far field. Hence, in order to take into account the distortion effect—due to $K_0 \neq 1$—the point solution for the pure distortion case (given in Section 3.3.2) should be used.

4.1. Green Functions due to a Cavity Contraction/Expansion in an Elastic Half-Plane

The analytical expressions describing the distribution of displacements due to a contracting/expanding cavity embedded at depth H in an elastic half-plane can be written as (see Section 3.3.1):

$$u_x(x,y) = \frac{V}{2 \cdot \pi} \cdot f(x,y,H) \qquad \{4\text{-}1a\}$$

$$u_y(x,y)=\frac{V}{2\cdot\pi}\cdot g(x,y,H) \qquad \{4\text{-}1b\}$$

where V is the ground loss volume and $f(x,y,H)$, $g(x,y,H)$ are continuous functions given by the following equations:

$$f(x,y,H)=\left\{\begin{array}{l}\dfrac{x}{x^2+(y+H)^2}-\dfrac{x}{x^2+(y-H)^2}+\ldots\\ \ldots+4\cdot\left[\dfrac{(1-\nu)\cdot x}{x^2+(y-H)^2}-\dfrac{(y-H)\cdot x\cdot y}{\left[x^2+(y-H)^2\right]^2}\right]\end{array}\right\} \qquad \{4.2a\}$$

$$g(x,y,H)=\left\{\begin{array}{l}\dfrac{(y+H)}{x^2+(y+H)^2}-\dfrac{(y-H)}{x^2+(y-H)^2}+..\\ ..+2\cdot\left[\dfrac{2\cdot(y-H)\cdot x^2+H\cdot\left[x^2-(y-H)^2\right]}{\left[x^2+(y-H)^2\right]^2}-\dfrac{2\cdot(1-\nu)\cdot(y-H)}{x^2+(y-H)^2}\right]\end{array}\right\} \qquad \{4.2b\}$$

If the cavity has an arbitrary position (X, Y), equations {4-1} become:

$$u_x(x,y,X,Y)=\frac{V}{2\cdot\pi}\cdot f(x-X,y,-Y) \qquad \{4\text{-}3a\}$$

$$u_y(x,y,X,Y)=\frac{V}{2\cdot\pi}\cdot g(x-X,y,-Y) \qquad \{4\text{-}3b\}$$

Hence, the Green functions, Γ_x and Γ_y are:

$$\Gamma_x(x,y,X,Y)=\frac{1}{2\cdot\pi}\cdot f(x-X,y,-Y) \qquad \{4\text{-}4a\}$$

$$\Gamma_y(x,y,X,Y)=\frac{1}{2\cdot\pi}\cdot g(x-X,y,-Y) \qquad \{4\text{-}4b\}$$

where f and g are given in equations {4-2}. The displacement field due to an arbitrary shaped cavity contraction can be obtained by integrating the Green functions over the line to which the cavity collapses, as illustrated in Figure 4.1. The displacements due to the contraction are given by equations {4-5}.

$$u_x(x,y)=\int_{s^i}^{s^f}\Gamma_x\{x,y,X(s),Y(s)\}\cdot e(s)\cdot\sqrt{\left(\frac{\partial X}{\partial s}\right)^2+\left(\frac{\partial Y}{\partial s}\right)^2}\cdot ds \qquad \{4\text{-}5a\}$$

$$u_y(x,y)=\int_{s^i}^{s^f}\Gamma_y\{x,y,X(s),Y(s)\}\cdot e(s)\cdot\sqrt{\left(\frac{\partial X}{\partial s}\right)^2+\left(\frac{\partial Y}{\partial s}\right)^2}\cdot ds \qquad \{4\text{-}5b\}$$

where s is a parametric coordinate (i.e., s^i=0 and s^f=1), $X(s)$ and $Y(s)$ describe the geometry of the line, and $e(s)$ is the local thickness of the cavity. Hence, equation {4-5} is the general solution of the distributed ground loss problem for a given cavity geometry, i.e., given $e(s)$, $X(s)$, and $Y(s)$.

4.2. Uniformly Distributed Ground Loss Along a Rectangular Line

The problem is outlined in Figure 4.2, where it can be seen that u_ε is defined for this case as the half-thickness of the cavity. For the sake of convenience, this problem is subdivided into four sub-problems corresponding to the two horizontal segments (indicated as 1 and 2 in Figure 4.2) and two vertical segments (indicated as 3 and 4 in Figure 4.2)

The functions that define the cavity geometry [i.e., $e(s)$, $X(s)$, and $Y(s)$] for each segment are summarized in Tables 4.1 and 4.2 for the horizontal and vertical segments, respectively. Once these functions are established, the displacement field due to the ground loss distributed over the segment in consideration is found by means of equations {4-5}. Results are summarized in Tables 4.1 and 4.2 for the horizontal and vertical segments, respectively. The parameters that appear in the aforementioned equations are defined as follows:

$$a_1 = y + H - \frac{D}{2} \qquad \{4\text{-}6a\}$$

$$b_1 = y - H - \frac{D}{2} \qquad \{4\text{-}6b\}$$

$$c = x + \frac{B}{2} \qquad \{4\text{-}6c\}$$

$$d = x - \frac{B}{2} \qquad \{4\text{-}6e\}$$

$$a_2 = y + H + \frac{D}{2} \qquad \{4\text{-}6f\}$$

$$b_2 = y - H + \frac{D}{2} \qquad \{4\text{-}6g\}$$

$$\kappa = 3 - 4 \cdot \nu \qquad \{4\text{-}6h\}$$

The final solution for the rectangular drift is found by adding the contribution of each individual segment.

4.3. Comparison of Displacement Solutions

Figures 4.3 to 4.12 summarize the comparison between displacement fields for the uniformly distributed ground loss along a rectangular drift (Section 4.2) versus an equivalent point/line sink solutions (i.e., having the same total volume of ground loss) located at the center of the drift, for different embedment, *D/2H*, and aspect ratios, *B/D*. It can be seen that both solutions show quite similar results in the far field, especially for deep (i.e., $D/2H < 0.45$) square tunnels (i.e., $B/D = 1$). However, the difference increases for the case of shallow (i.e., $D/2H = 0.7$) and rectangular

tunnels (i.e., $B/D \neq 1$). It can also be seen that the distributed ground loss solution provides a more correct representation of the displacement singularities at the corners of the drift.

Figures 4.13 and 4.14 show comparisons between the settlement troughs predicted by distributed ground loss and point/line sink solutions for different embedment, $D/2H$, and aspect ratios, B/D, respectively. It can be seen in Figure 4.13 that the shallow tunnels (i.e., $D/2H < 0.45$) produce very similar shapes of the settlement trough to the equivalent point/line solutions (which produce a settlement trough shape independent of the embedment ratio when plotted against the normalized coordinate x/H). It can also be seen that the distributed ground loss solution predicts wider settlement troughs for shallow tunnels. Figure 4.15 shows that the aspect ratio, B/D, modifies the width of the settlement trough predicted by the point/line sink solutions. The distributed ground loss solution predicts narrower troughs for $B/D < 1$ and wider for $B/D > 1$. However, if nearly square tunnels are considered (i.e., $B/D \approx 1$), the trough shape can be fairly well approximated by point solutions.

Figures 4.15 and 4.16 show comparisons between the horizontal displacements at $x = 2 \cdot R_{eq}$ (where R_{eq} is the equivalent radius of the drift, $R_{eq} = \sqrt{B \cdot D / \pi}$) predicted by distributed ground loss and point/line sink solutions for different embedment, $D/2H$, and aspect ratios, B/D, respectively. Figure 4.15 shows that the point/line sink solution predicts very similar results to the distributed ground loss solution, regardless of the embedment ratio, $D/2H$. The difference between both solutions is about 3% at the tunnel springline. It can be seen in Figure 4.16 that the distributed ground loss solution predicts higher horizontal displacements than the point/line sink solutions at the tunnel springline for $B/D > 1$ and lower for $B/D<1$. The difference ranges from –20% for $B/D = 0.5$ to +10% for $B/D = 2$.

4.4. Conclusions

This Chapter has shown that the influence of the tunnel drift geometry is confined to a region very close to the tunnel wall. As plastic behavior is very likely to take place in the region where both solutions show considerable differences (i.e., near the tunnel, Chapter 5), either solution

would lack accuracy in that region. Hence, point solutions can be used in order to model the far field distribution of ground movements around a rectangular drift. This conclusion can be extended for geometries other than rectangular.

In order to model a stacked drift construction, as the Rio Piedras cavern in the Tren Urbano Poject, point/line sink and distortion solutions can be used in order to model the displacement field associated with each individual drift. The displacements produced after excavation of the core material (i.e., the soil inside the cavern) can be modeled either by point/line solutions (or functions of complex variables if the cavern is very shallow) considering the stacked drift as an equivalent circular tunnel.

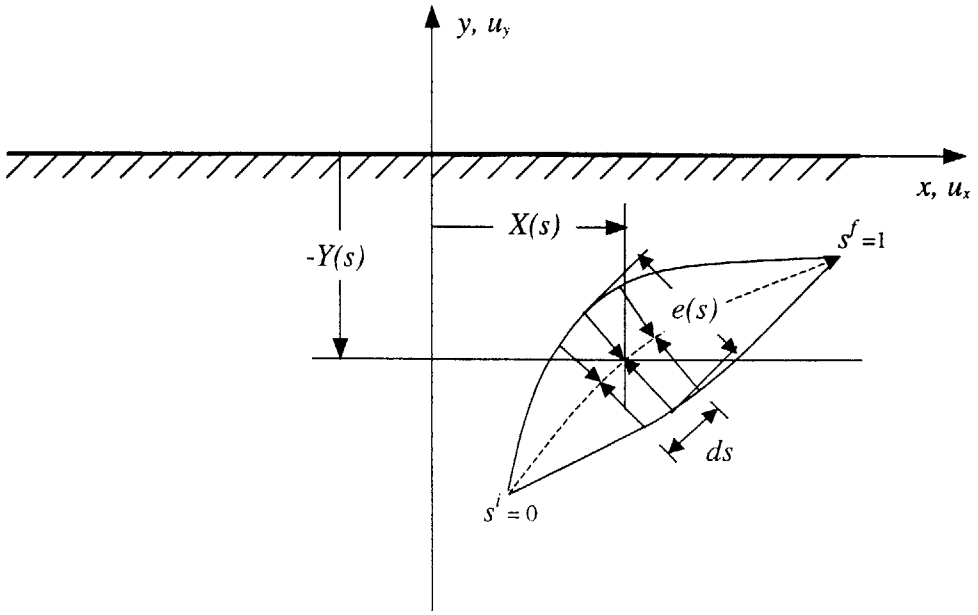

Figure 4.1. Arbitrary cavity contraction

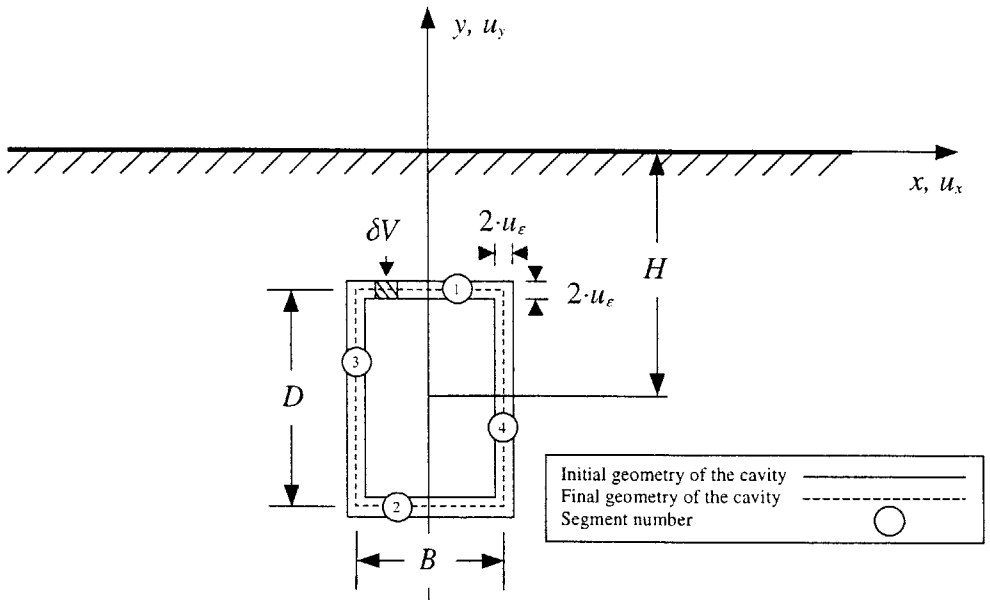

Figure 4.2. Modeling of distributed ground loss along rectangular drift

Seg. No.	$X(s)$	Y(s)	$e(s)$	Displacements
1	$B\cdot\left(s-\frac{1}{2}\right)$	$-H+\frac{D}{2}$	u_ε	$u_x(x,y)=\frac{u_\varepsilon}{2\cdot\pi}\cdot\left\{ln\left[\left(\frac{c^2+b_1^{\,2}}{d^2+b_1^{\,2}}\right)^{\kappa}\cdot\frac{c^2+a_1^{\,2}}{d^2+a_1^{\,2}}\right]-\frac{8\cdot B\cdot b_1\cdot y\cdot x}{\left(d^2+b_1^{\,2}\right)\cdot\left(c^2+b_1^{\,2}\right)}\right\}$ $u_y(x,y)=\frac{u_\varepsilon}{\pi}\cdot\left\{tan^{-1}\left(\frac{c}{a_1}\right)-tan^{-1}\left(\frac{d}{a_1}\right)+\left[tan^{-1}\left(\frac{d}{b_1}\right)-tan^{-1}\left(\frac{c}{b_1}\right)\right]\cdot\kappa+\frac{2\cdot y\cdot B\cdot\left(c\cdot d-b_1^{\,2}\right)}{\left(d^2+b_1^{\,2}\right)\cdot\left(c^2+b_1^{\,2}\right)}\right\}$
2	$B\cdot\left(s-\frac{1}{2}\right)$	$-H-\frac{D}{2}$	u_ε	$u_x(x,y)=\frac{u_\varepsilon}{2\cdot\pi}\cdot\left\{ln\left[\left(\frac{c^2+b_2^{\,2}}{d^2+b_2^{\,2}}\right)^{\kappa}\cdot\frac{c^2+a_2^{\,2}}{d^2+a_2^{\,2}}\right]-\frac{8\cdot B\cdot b_2\cdot y\cdot x}{\left(d^2+b_2^{\,2}\right)\cdot\left(c^2+b_2^{\,2}\right)}\right\}$ $u_y(x,y)=\frac{u_\varepsilon}{\pi}\cdot\left\{tan^{-1}\left(\frac{c}{a_2}\right)-tan^{-1}\left(\frac{d}{a_2}\right)+\left[tan^{-1}\left(\frac{d}{b_2}\right)-tan^{-1}\left(\frac{c}{b_2}\right)\right]\cdot\kappa+\frac{2\cdot y\cdot B\cdot\left(c\cdot d-b_2^{\,2}\right)}{\left(d^2+b_2^{\,2}\right)\cdot\left(c^2+b_2^{\,2}\right)}\right\}$

Table 4.1. Displacement solutions due to horizontal segments

Seg. No.	$X(s)$	$Y(s)$	$e(s)$	Displacements
3	$-\frac{B}{2}$	$-H+D\cdot\left(s-\frac{1}{2}\right)$	u_ε	$u_x(x,y)=\frac{u_\varepsilon^{\,v}}{\pi}\left\{\begin{array}{l}\left[\tan^{-1}\left(\frac{b_1}{c}\right)-\tan^{-1}\left(\frac{b_2}{c}\right)\right]\cdot\kappa+\tan^{-1}\left(\frac{a_2}{c}\right)-\tan^{-1}\left(\frac{a_1}{c}\right)+\ldots\\ \ldots+\frac{2\cdot c\cdot y}{c^2+y^2}\cdot\left[\frac{y^2-b_1^{\,2}}{c^2+b_1^{\,2}}-\frac{y^2-b_2^{\,2}}{c^2+b_2^{\,2}}\right]\end{array}\right\}$ $u_y(x,y)=\frac{u_\varepsilon^{\,v}}{2\cdot\pi}\cdot\left\{\begin{array}{l}ln\left[\frac{c^2+a_2^{\,2}}{c^2+a_1^{\,2}}\cdot\left(\frac{c^2+b_2^{\,2}}{c^2+b_1^{\,2}}\right)^{\kappa}\right]+\ldots\\ \ldots+\frac{4\cdot y}{c^2+y^2}\cdot\left[\frac{\left(c^2-y\cdot b_2\right)\cdot\left(y-b_2\right)}{c^2+b_2^{\,2}}-\frac{\left(c^2-y\cdot b_1\right)\cdot\left(y-b_1\right)}{c^2+b_1^{\,2}}\right]\end{array}\right\}$
4	$\frac{B}{2}$	$-H+D\cdot\left(s-\frac{1}{2}\right)$	u_ε	$u_x(x,y)=\frac{u_\varepsilon}{\pi}\left\{\begin{array}{l}\left[\tan^{-1}\left(\frac{b_1}{d}\right)-\tan^{-1}\left(\frac{b_2}{d}\right)\right]\cdot\kappa+\tan^{-1}\left(\frac{a_2}{d}\right)-\ldots\\ \ldots-\tan^{-1}\left(\frac{a_1}{d}\right)+\frac{2\cdot d\cdot y}{d^2+y^2}\cdot\left[\frac{y^2-b_1^{\,2}}{d^2+b_1^{\,2}}-\frac{y^2-b_2^{\,2}}{d^2+b_2^{\,2}}\right]\end{array}\right\}$ $u_y(x,y)=\frac{u_\varepsilon}{2\cdot\pi}\cdot\left\{\begin{array}{l}ln\left[\frac{d^2+a_2^{\,2}}{d^2+a_1^{\,2}}\cdot\left(\frac{d^2+b_2^{\,2}}{d^2+b_1^{\,2}}\right)^{\kappa}\right]+\ldots\\ \ldots+\frac{4\cdot y}{d^2+y^2}\cdot\left[\frac{\left(d^2-y\cdot b_2\right)\cdot\left(y-b_2\right)}{d^2+b_2^{\,2}}-\frac{\left(d^2-y\cdot b_1\right)\cdot\left(y-b_1\right)}{d^2+b_1^{\,2}}\right]\end{array}\right\}$

Table 4.2. Displacement solutions due to vertical segments

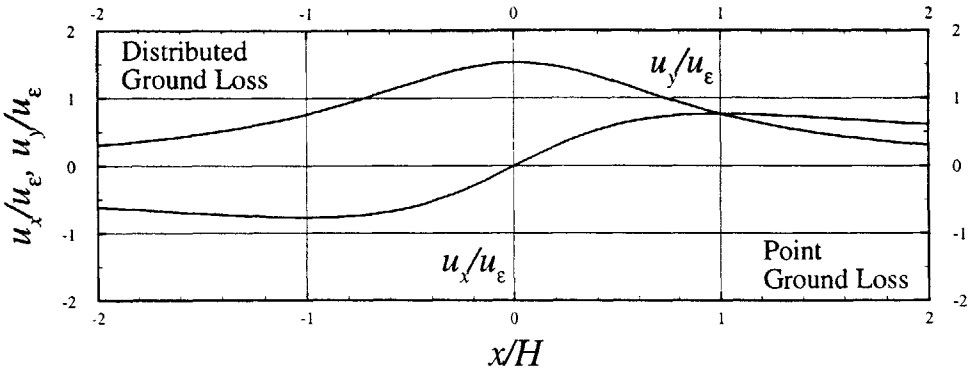

Figure 4.3. Surface displacements due to uniformly distributed ground loss along rectangular tunnel for D/B = 1, $D/2H$=0.2, and ν=0.25

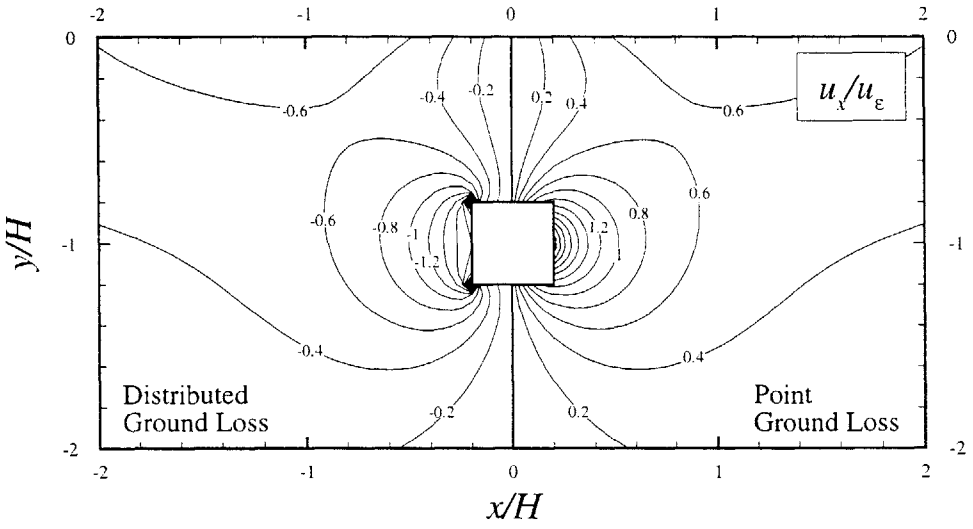

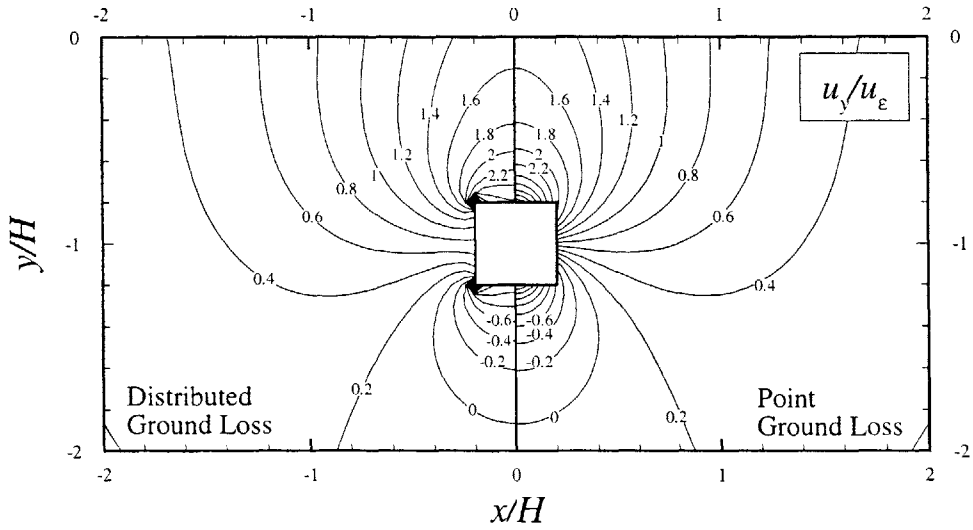

Figure 4.4. Ground displacements due to uniformly distributed ground loss along rectangular tunnel for D/B = 1, $D/2H$=0.2, and ν=0.25

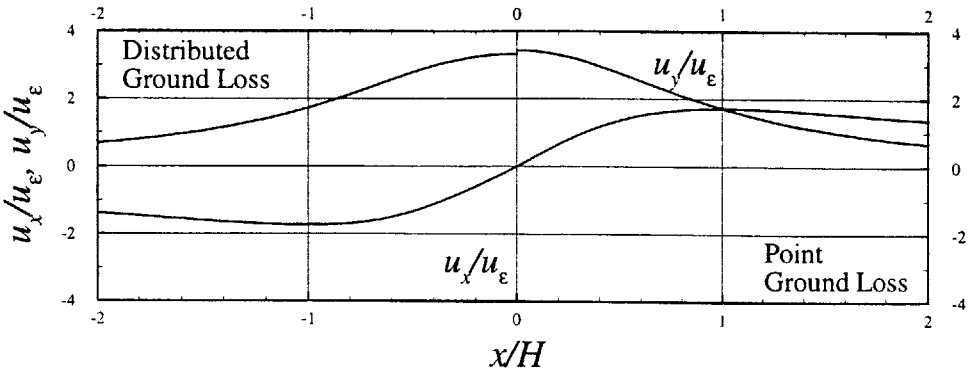

Figure 4.5. Surface displacements due to uniformly distributed ground loss along rectangular tunnel for D/B = 1, $D/2H$=0.45, and ν = 0.25

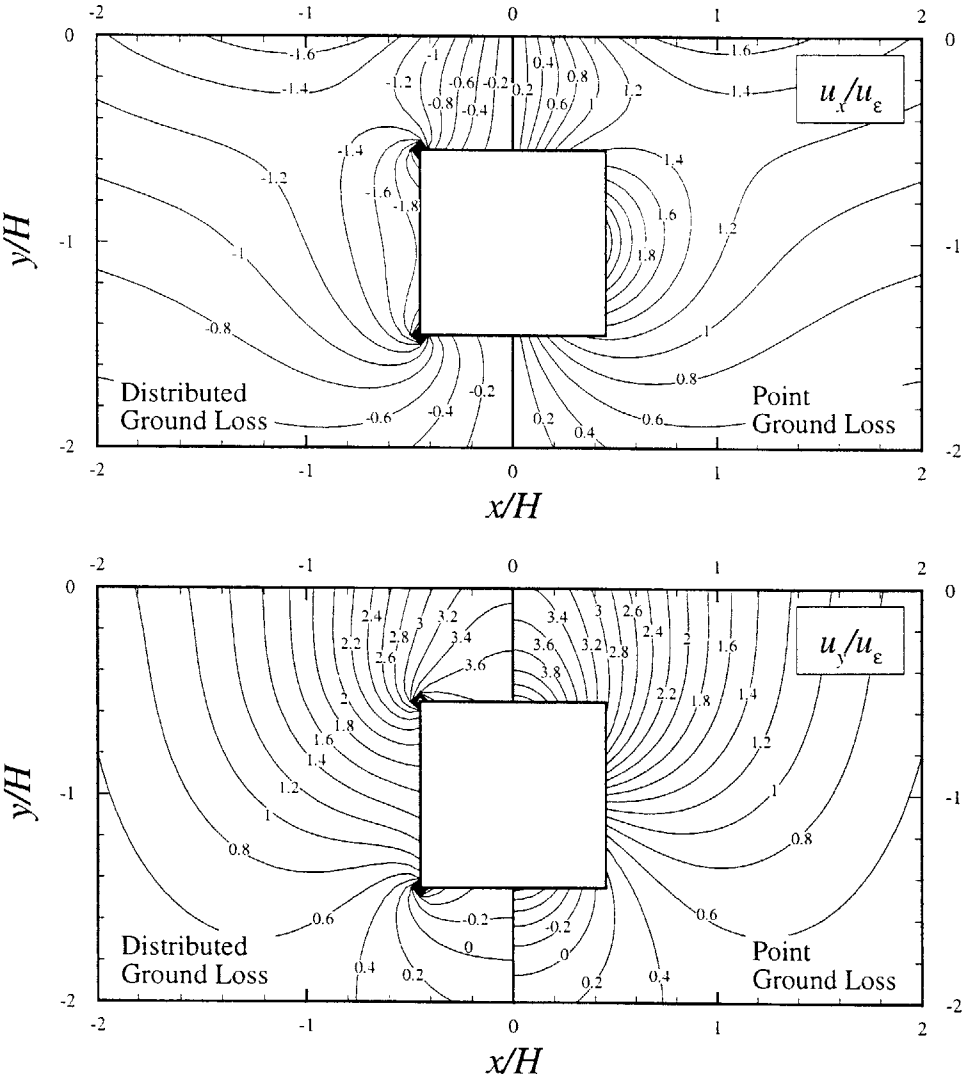

Figure 4.6. Ground displacements due to uniformly distributed ground loss along rectangular tunnel for D/B = 1, $D/2H$=0.4, and ν = 0.25

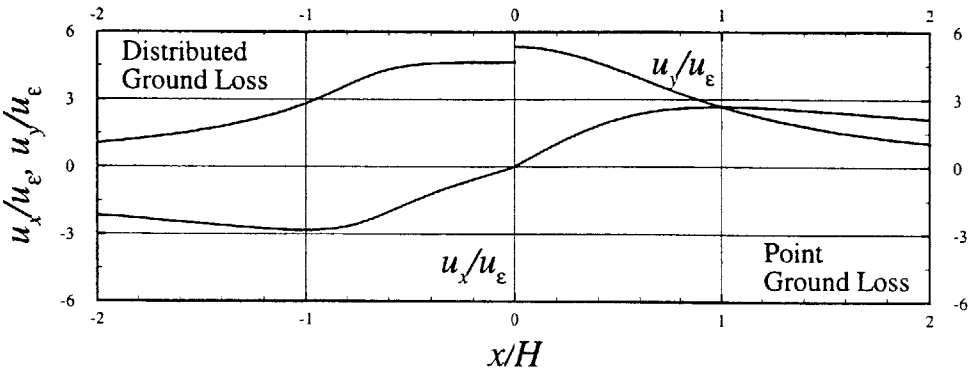

Figure 4.7. Surface displacements due to uniformly distributed ground loss along rectangular tunnel for D/B = 1, $D/2H$=0.7, and ν = 0.25

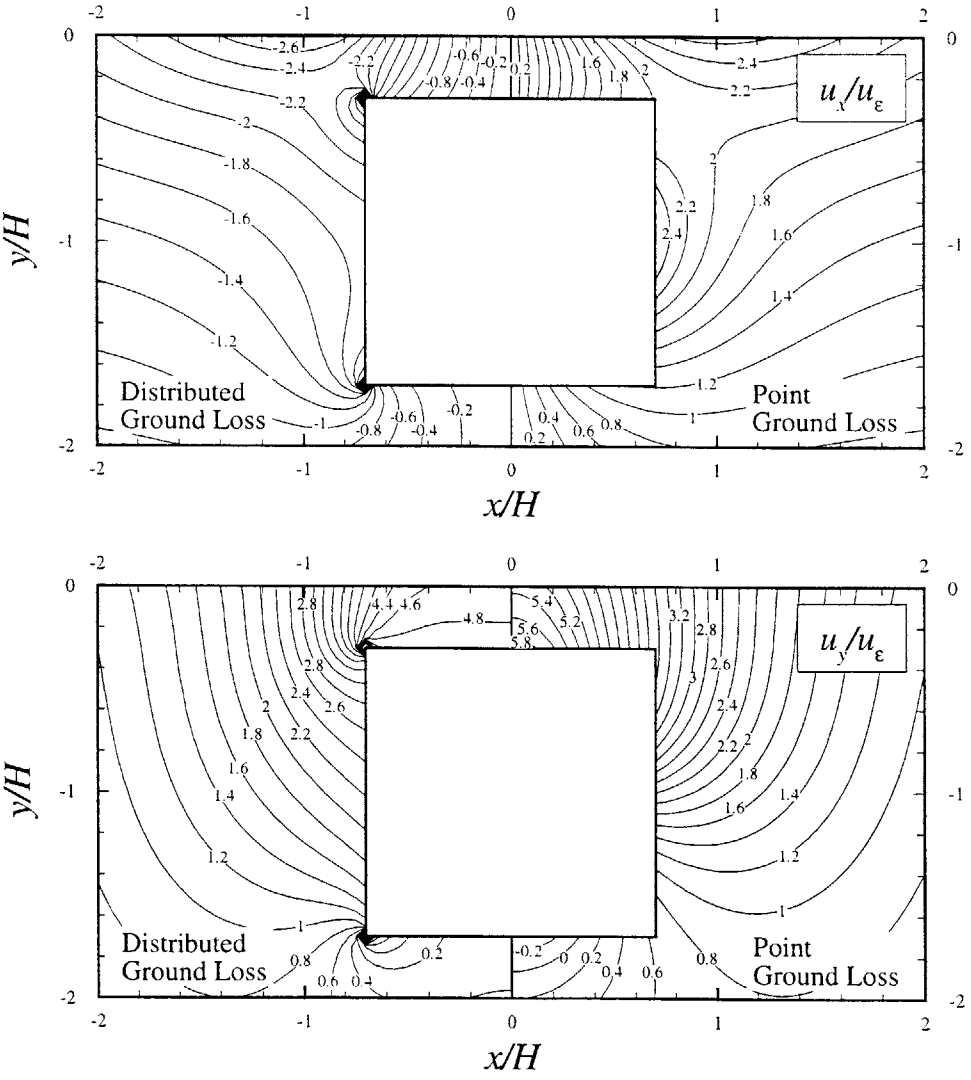

Figure 4.8. Ground displacements due to uniformly distributed ground loss along rectangular tunnel for D/B = 1, $D/2H$=0.7, and ν = 0.25

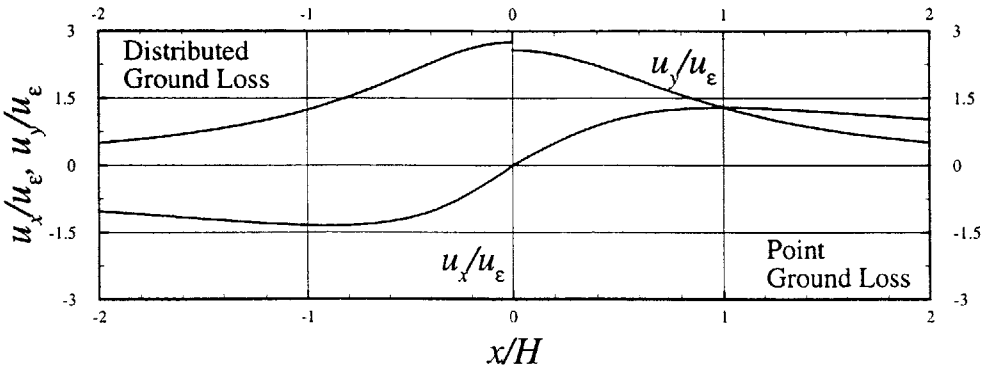

Figure 4.9. Surface displacements due to uniformly distributed ground loss along rectangular tunnel for B/D = 0.5, $D/2H$ = 0.45, and ν = 0.25

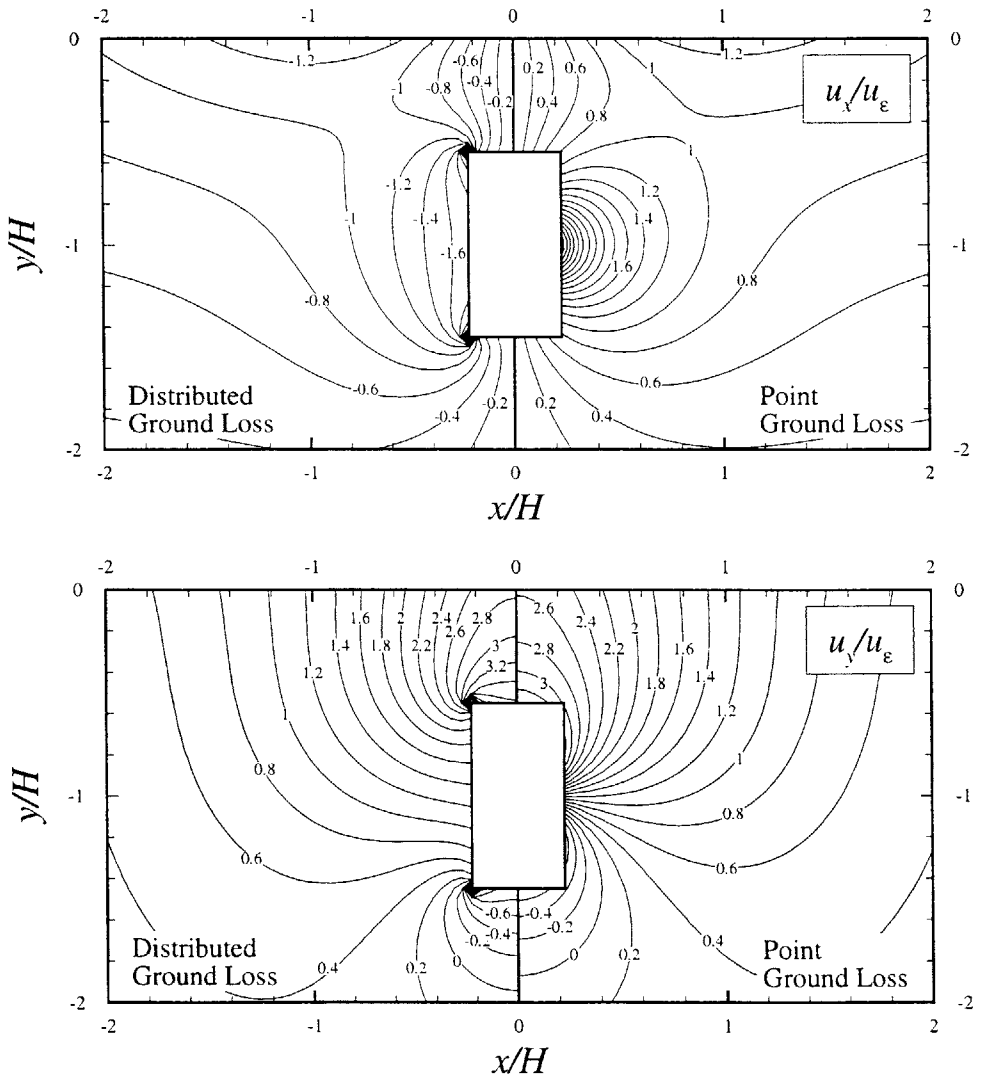

Figure 4.10. Ground displacements due to uniformly distributed ground loss along rectangular tunnel for B/D = 0.5, $D/2H$ = 0.45, and ν =0.25

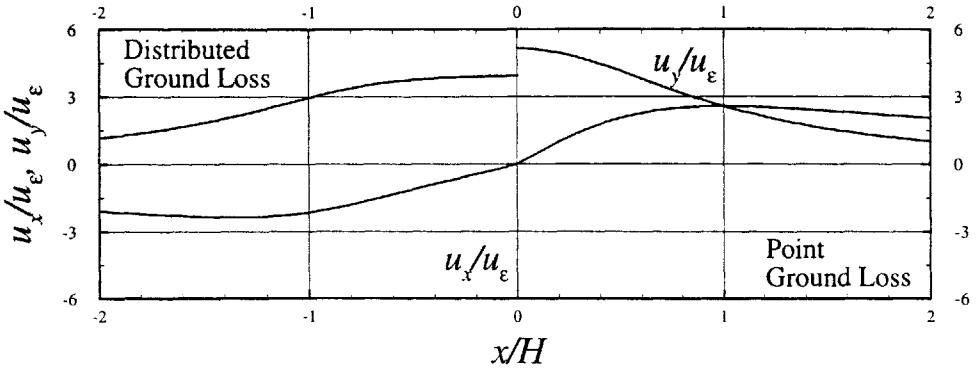

Figure 4.11. Surface displacements due to uniformly distributed ground loss along rectangular tunnel for B/D = 2, $D/2H$ = 0.45, and ν=0.25

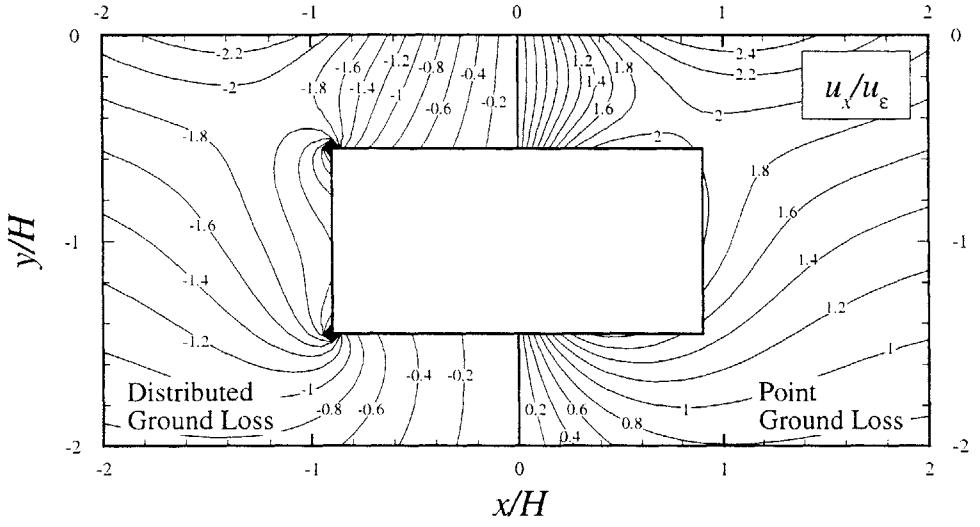

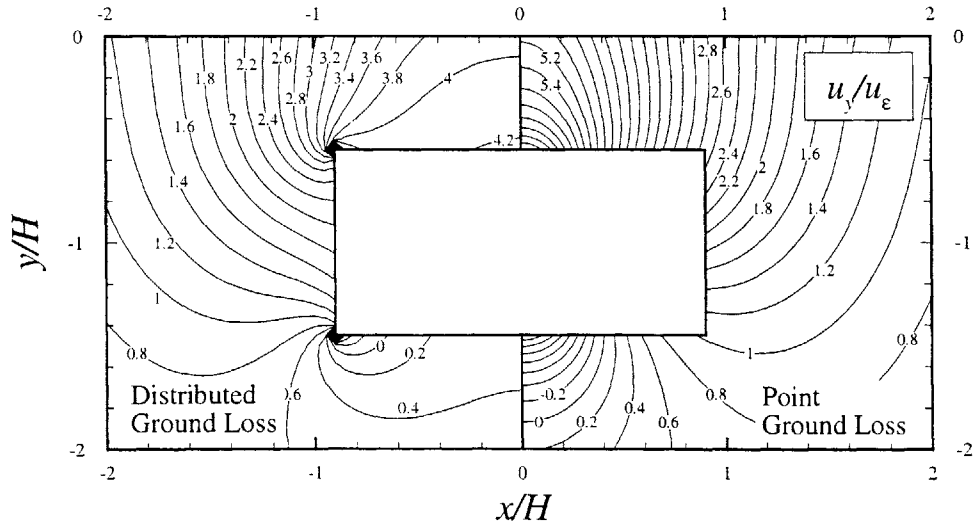

Figure 4.12. Ground displacements due to uniformly distributed ground loss along rectangular tunnel for B/D = 2, $D/2H$ = 0.45, and ν=0.25

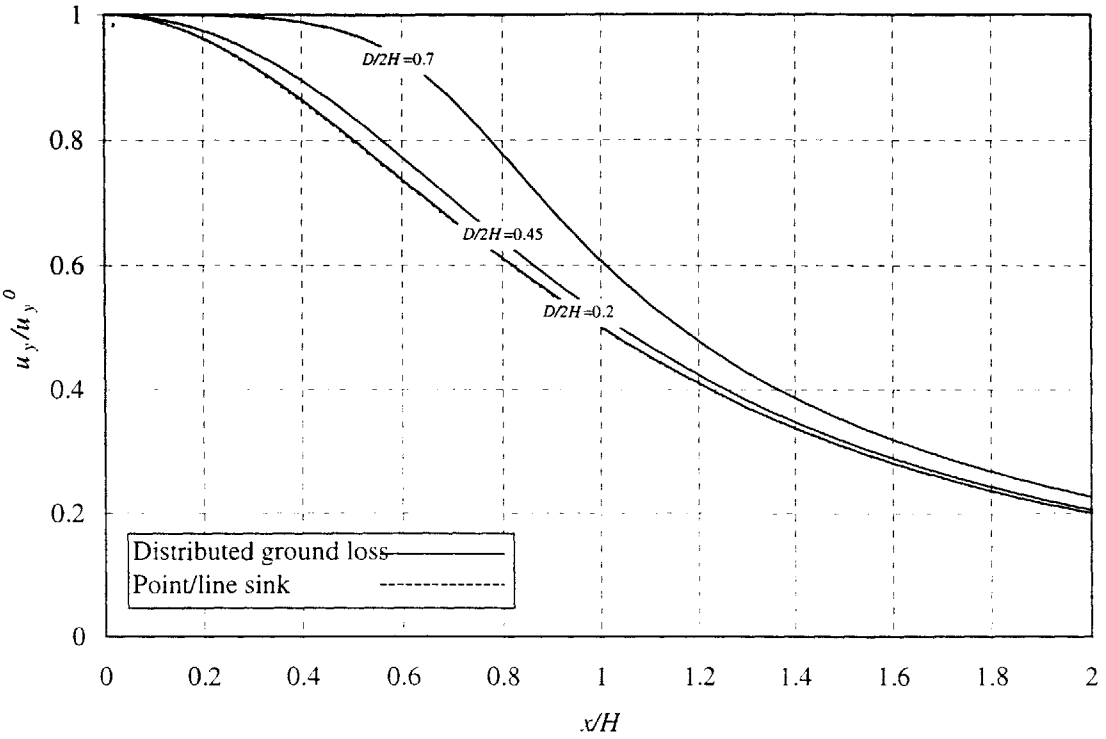

Figure 4.13. Influence of embedment ratio, *D/2H*, on the settlement trough for $\nu = 0.25$, $B/D = 1$

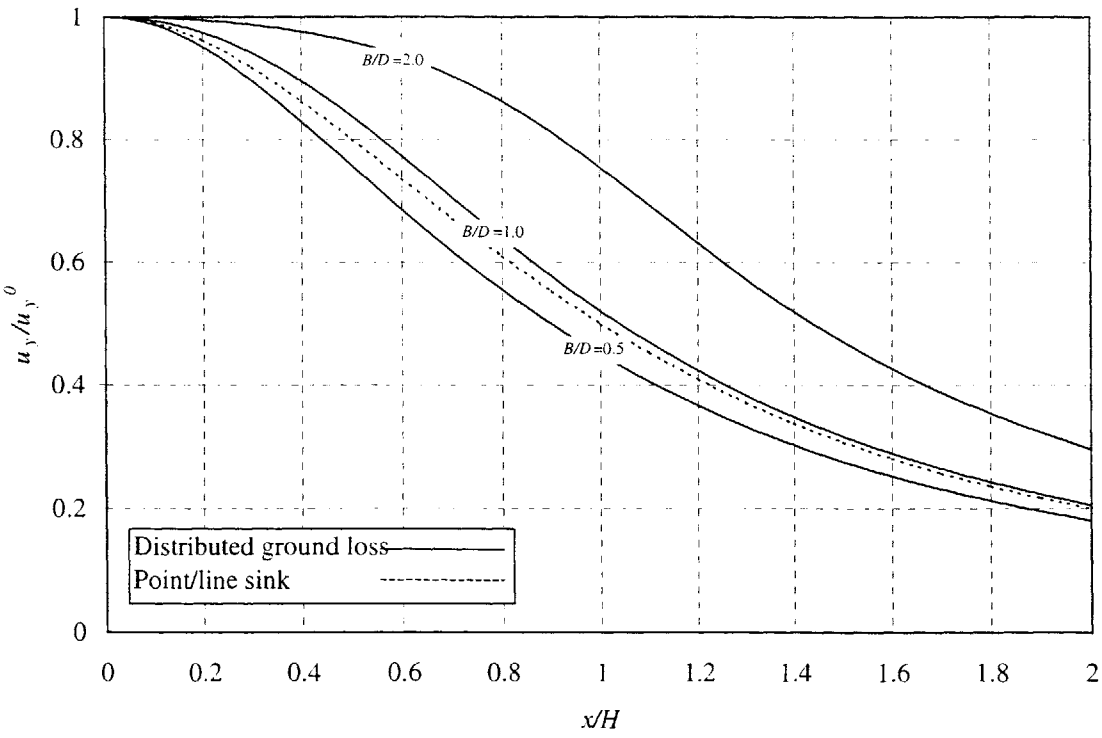

Figure 4.14. Influence of aspect ratio, *B/D*, on the settlement trough for $\nu = 0.25$, $D/2H = 0.45$

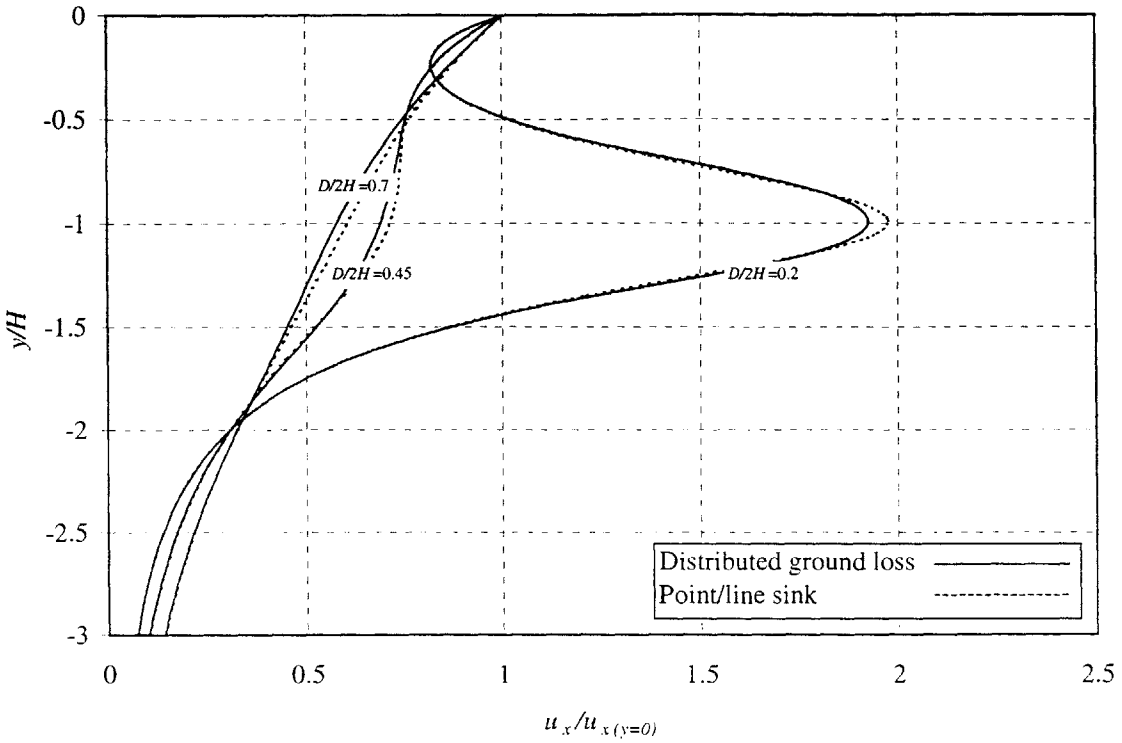

Figure 4.15. Influence of the embedment ratio, *D/2H*, on the horizontal displacements at $x = 2R_{eq}$ for $\nu = 0.25$, $B/D = 1$

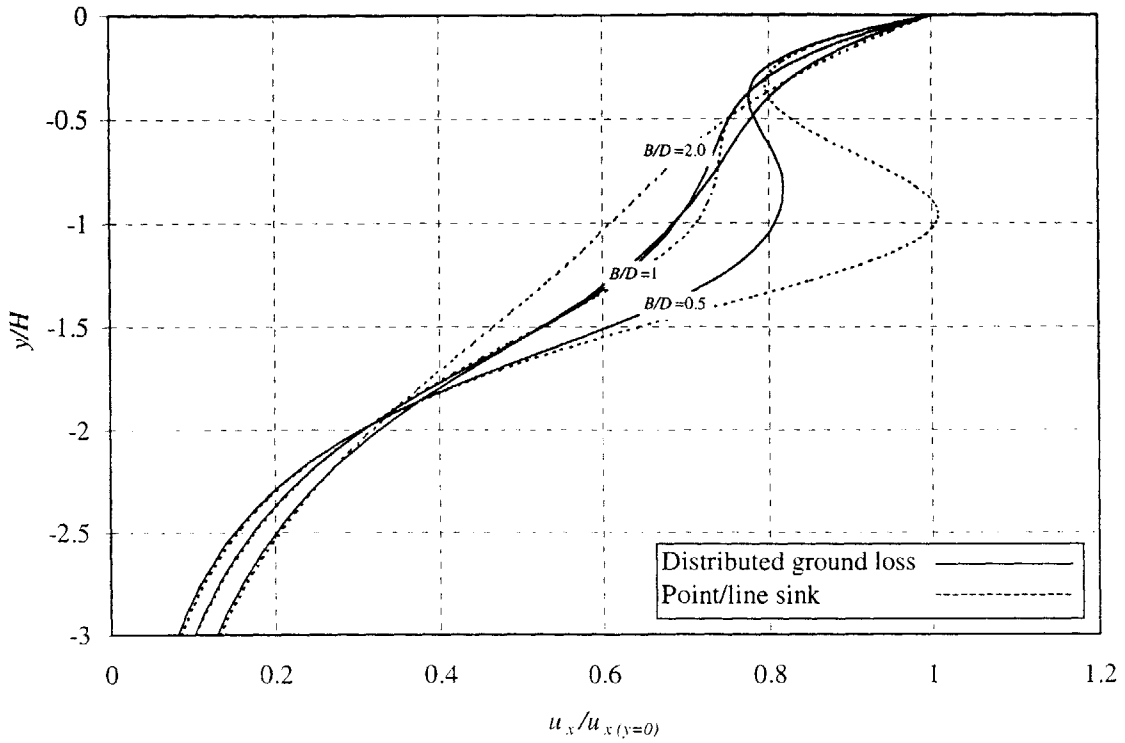

Figure 4.16. Influence of the aspect ratio, *B/D*, on the horizontal displacements at $x = 2R_{eq}$ for $\nu = 0.25$, $B/D = 1$

5. Influence of Soil Plasticity

This Chapter focuses on the effects of plastic behavior on the displacements around a cylindrical cavity in a half-plane. Section 5.1 discusses an exact analytical plastic solution obtained by Yu and Rowe (1998) for the case of a cylindrical cavity in an isotropically (i.e., $K_0 = 1$) pre-stressed infinite plane. By comparing predictions for elastic and elasto-plastic displacementsit is possible to modify the elastic solutions in order to account for a local zone of plastic failure near the tunnel wall. Section 5.2 discusses an approximate solution given by Gonzales (1999) in order to include the effects of plastic behavior for the case of shallow tunnels in an anisotropically (i.e., $K_0 \neq 1$) pre-stressed half-plane.

5.1. 2D Deformation Analyses for a Deep Circular Tunnel in an Infinite Soil

Yu and Rowe (1998) obtained closed-form solutions for the soil stresses and displacements by considering a cylindrical cavity unloading from a $K_0 = 1$ initial state. Both drained and undrained solutions were obtained. The analyses for the drained case model the soil as an elastic-perfectly-plastic Mohr-Coulomb material with a non-associative flow rule and constant dilation angle, ψ. For tunnels causing deformations in clay, the soil was modeled by both the original and modified Cam-Clay models. In order to improve the modeling of highly overconsolidated materials—for which these Cam-Clay models seriously over-predicts the peak shear strength—a Hvorslev envelope was also introduced. In this Section, these solutions are re-arranged in order to account for a displacement (rather than pressure) controlled cavity contraction.

5.1.1. Undrained Plastic Deformations due to a Cylindrical Cavity Contraction

In the undrained case, the displacement field due to a contracting cavity is found by kinematic considerations (i.e., regardless of the constitutive model) provided that material compressibility is neglected (e.g., Sagaseta, 1987). The solution coincides with the elastic solution presented in Section 2.1 (equations {2-15}). Hence, in order to perform undrained deformation analyses, the elastic solution can be used.

5.1.2. Drained Deformations due to a Cylindrical Cavity Contraction

The solution obtained by Yu and Rowe (1998) shows that the displacement field due to a cylindrical cavity contraction is plastic in an annular region defined by a plastic radius, R_p, and elastic elsewhere. Figure 5.1 illustrates the distribution of radial displacements from the elasto-plastic analysis. The parameter u_ε^e corresponds to the equivalent elastic displacement at the tunnel wall.

The critical yield displacement for which the onset of plasticity occurs, u_ε^y, can be written as (see Appendix IV for further details):

$$\frac{u_\varepsilon^{\ y}}{R} = -\frac{\left(N_{\phi'}-1\right)+\overline{Y}}{2\cdot\overline{G}\cdot\left(1+N_{\phi'}\right)} \qquad \{5\text{-}1\}$$

where:

$$N_{\phi'} = \frac{1+sin(\phi')}{1-sin(\phi')} \qquad \{5\text{-}2\}$$

$$\overline{Y} = \frac{2\cdot c'}{p'_0}\cdot\frac{cos(\phi')}{1-sin(\phi')} \qquad \{5\text{-}3\}$$

$$\overline{G} = \frac{G}{p'_0} \qquad \{5\text{-}4\}$$

and c', ϕ' are the Mohr-Coulomb cohesion and friction angle, respectively, G is the average pre-yield elastic shear modulus of the soil, and u_ε^y is always negative, since a cavity contraction (or unloading) is considered.

There will be a plastic region whenever the displacement at the cavity wall, u_ε^p, is such that the following condition is fulfilled:

$$\frac{u_\varepsilon{}^p}{R} \le \frac{u_\varepsilon{}^y}{R} \qquad \{5\text{-}5\}$$

In the foregoing analysis it will be assumed that {5-5} is fulfilled, i.e. plastic behavior takes place. If {5-5} is not fulfilled the solution is purely elastic and coincides with the one given in Section 2.1.

The displacement at the cavity wall can be expressed as:

$$\frac{u_\varepsilon{}^p}{R} = \frac{u_\varepsilon{}^y}{R} \cdot T^{\frac{1+\beta}{1-N_\phi}} \qquad \{5\text{-}6\}$$

where T is a function of the internal pressure (see Appendix IV for full details) and β is a function of the dilation angle (ψ) as follows:

$$\beta = \frac{1+sin(\psi)}{1-sin(\psi)} \qquad \{5\text{-}7\}$$

The plastic displacement at the cavity wall is related to the ground loss, V, as follows:

$$u_\varepsilon{}^p = \frac{V}{2 \cdot \pi \cdot R} \qquad \{5\text{-}8\}$$

Hence, for a prescribed displacement at the tunnel wall, T is given by:

$$T = \left(\frac{u_\varepsilon{}^p}{u_\varepsilon{}^y} \right)^{\frac{1-N_\phi}{1+\beta}} \qquad \{5\text{-}9\}$$

The radius of the plastic zone, R_p, is related to T by the following equation:

$$\frac{R^p}{R} = T^{\frac{1}{1-N_\phi}} \qquad \{5\text{-}10\}$$

By combining {5-10} and {5-6}, the radius of the plastic zone can be related to the displacement at the cavity wall:

$$\frac{R^p}{R} = \left(\frac{u_\varepsilon{}^p}{u_\varepsilon{}^y} \right)^{\frac{1}{1+\beta}} \qquad \{5\text{-}11\}$$

Figures 5.3 to 5.8 show the influence of the displacement at the cavity wall, $u_\varepsilon{}^p$, on the radius of the plastic zone, R^p as functions of the soil properties (G/p'_0, ϕ') for selected values of cohesion (c'/p'_0 = 0.0 to 0.5) and dilation[1] (ψ =0° to 10°). As a first approximation, the normalized cohesion can be related to the overconsolidation ratio of the clay, *OCR*, as proposed by Mesri and Abdel-Ghaffar (1993)[2]:

$$\frac{c'}{p'_0} = 0.1 \cdot OCR \qquad \{5\text{-}12a\}$$

where 0.1 is an average value for several clays in the range $1 < OCR < 5$ (Figure 5.2) or:

$$\frac{c'}{p'_0} = 0.024 \cdot OCR \qquad \{5.12b\}$$

where 0.024 is an average value for the range $10 < OCR < 20$. In any case, the maximum cohesion ratio for the reported *OCR* range is approximately $c'/p'_0 \approx 0.5$. It can be seen parameters that have the stronger influence on the radius of the plastic zone are the shear modulus ratio, G/p'_0, and the dilation angle, ψ. Stiffer materials produce more plasticity for a

[1] The dilation angle, ψ, is given by the difference between the peak friction angle, ϕ'_p, and the critical state friction angle, ϕ'_{cs}. Considering that $\phi'_{cs} \approx 30°$ and $\phi'_p \leq 40°$, the range for the dilation angle is $\psi = 0°$ to 10°.

given cavity contraction, u_ε^p. Increasing the dilation angle, ψ, tends to reduce the plastic zone. Friction angle has little influence on the value of R_p in the range considered herein ($\phi' = 25°$ to 40°). The influence of cohesion is negligible. The magnitude of the cavity contraction, u_ε^p, has a very strong influence on the radius of the plastic zone, especially at low values of u_ε^p (i.e., near the initial yielding, u_ε^y).

The plastic displacement at the tunnel wall, u_ε^p, is mainly a function of the construction method and the final state of stresses supported by the lining. For example., if the NATM excavation method is used, large deformations can be expected. By allowing large (but controlled) deformations to occur, the final pressures acting onto the tunnel lining will be lower, leading to a large radius of the plastic zone. On the other hand, if the tunnel is excavated by means of a TBM and the tail void filled with pressurized grouting, deformations will be smaller and high pressures will occur at the lining, leading to a smaller plastic zone.

For an average material, having the following mechanical properties: $c'/p'_0 = 0.1$; $\phi' = 30°$; $G/p'_0 = 100$; $\psi = 5°$ and a ground loss $V = 2\%$ to 3% (i.e., $u_\varepsilon^p/R \approx -0.015$ to -0.01), the radius of the plastic zone is $R_p \approx 2 \cdot R$. Hence, as a first approximation, the plastic zone extends one radius away from the tunnel wall.

The equivalent elastic displacement at the tunnel wall is related to the radius of the plastic zone as follows:

$$\frac{u_\varepsilon^e}{R} = \frac{u_\varepsilon^y}{R} \cdot \left(\frac{R_p}{R} \right)^2 \qquad \{5\text{-}13\}$$

Combining equations {5-13} and {5-11}, the equivalent elastic displacement, u_ε^e, can be related to the elasto-plastic displacement at the tunnel wall, u_ε^p:

$$\frac{u_\varepsilon^e}{R} = \frac{u_\varepsilon^y}{R} \cdot \left(\frac{u_\varepsilon^p}{u_\varepsilon^y} \right)^{\frac{2}{1+\beta}} \qquad \{5\text{-}14\}$$

A reduction factor, RF, can now be defined as the ratio between the equivalent elastic displacement, u_ε^e, and the plastic displacement at the cavity wall, u_ε^p:

$$RF = \frac{u_\varepsilon^e}{u_\varepsilon^p} \qquad \{5\text{-}15\}$$

Replacing equation {5-14} in {5-13} and rearranging yields:

$$RF = \left(\frac{u_\varepsilon^p}{u_\varepsilon^y} \right)^{\frac{1-\beta}{1+\beta}} \qquad \{5\text{-}16\}$$

It can be seen that if no dilation is assumed (i.e., $\psi = 0°$), the reduction factor, $RF = 1$ (i.e., plasticity has no effect on the predicted displacement field). Hence, it can be noticed that the dilation angle, ψ, has a strong influence on the reduction factor and the displacement patterns in the plastic region.

Figures 5.9 to 5.14 show the influence of the displacement at the cavity wall, u_ε^p, on the reduction factor, RF, as functions of the soil properties (G/p'_0, ϕ') for selected values of cohesion (c'/p'_0 = 0.0 to 0.5) and dilation (ψ=5° to 10°). As for the radius of the plastic zone, it is found that the parameters that have the stronger influence on the reduction factor, RF, are the shear modulus ratio, G/p'_0, and the dilation angle, ψ. Stiffer materials produce lower values of the reduction factor for a given cavity contraction, u_ε^p. Increasing the dilation angle, ψ, tends to reduce the reduction factor. Friction angle has little influence on the value of RF in the range considered herein (ϕ' = 25° to 40°) and the influence of cohesion is negligible. The magnitude of the cavity contraction, u_ε^p, has a very strong influence on the reduction factor, especially at low values of u_ε^p (related to the amount of ground loss by equation {5-8}). Hence, the construction

method has a strong influence on the actual displacement at the tunnel wall, u_ε^p, and the equivalent elastic displacement that would reproduce the far field displacements (i.e., *RF*).

For a typical soil, having the following mechanical properties: $c'/p'_0 = 0.1$; $\phi' = 30°$; $G/p'_0 = 100$; $\psi = 5°$ and a ground loss $V = 2\%$ to 3% (i.e., $u_\varepsilon^p/R \approx -0.015$ to -0.01), the reduction factor is $RF \approx 0.9$. Hence, as a first approximation for drained behavior, the displacements measured at the tunnel wall should be reduced by 10% in order to predict the far field dispalcements by means of elastic solutions. As mentioned before, for the undrained case, both solutions predict the same displacement patterns (i.e., $RF = 1$).

5.2. Approximation of Dilation Effects for a Shallow Tunnel

It has been shown in Section 2.1 that the variation of the displacements in the elastic region for an isotropic cavity contraction is of the form $1/r$:

$$u_x(x, y) = u_\varepsilon \cdot \frac{x \cdot R}{x^2 + y^2} \qquad \{2\text{-}15a\}$$

$$u_y(x, y) = u_\varepsilon \cdot \frac{y \cdot R}{x^2 + y^2} \qquad \{2\text{-}15b\}$$

In the plastic region, the variation of displacements are governed by the flow rule (neglecting the elastic component within the plastic region and vary as $1/r^\beta$, where β is given by equation {5.7}. Hence, the displacement field is given by:

$$u_x(x, y) = u_\varepsilon \cdot \frac{x \cdot R^\beta}{\left(x^2 + y^2\right)^{\frac{\beta+1}{2}}} \qquad \{5\text{-}16a\}$$

$$u_y(x,y) = u_\varepsilon \cdot \frac{y \cdot R^{\beta}}{\left(x^2 + y^2\right)^{\frac{\beta+1}{2}}} \qquad \{5\text{-}16b\}$$

Sagaseta (1988) introduced the α parameter, which is related to β as follows:

$$\alpha = \frac{\beta + 1}{2} \qquad \{5\text{-}17\}$$

and hence, re-writes equations {5.16} as:

$$u_x(x,y) = u_\varepsilon \cdot \frac{x \cdot R^{2\cdot\alpha-1}}{\left(x^2 + y^2\right)^{\alpha}} \qquad \{5\text{-}18a\}$$

$$u_y(x,y) = u_\varepsilon \cdot \frac{y \cdot R^{2\cdot\alpha-1}}{\left(x^2 + y^2\right)^{\alpha}} \qquad \{5\text{-}18b\}$$

It can readily be seen that expressions {5-18} and {2-15} are similar and coincide for the case where $\alpha = 1$ (i.e., $\psi = 0°$). Gonzalez (1999) introduced the α parameter in the elastic solutions for the uniform convergence and distortion by modifying the terms of the form $1/(x^2+y^2)$ to $1/(x^2+y^2)^{\alpha}$ and assuming $\nu = 0.5$. Hence, an approximate solution including dilation due to plastic behavior is obtained. Assuming a maximum dilation of $\psi = 15°$-$20°$, leads to $\alpha = 1.35$-1.50, and corresponds to a practical upper limit for real soil behavior (i.e., elastic-plastic and strain dependence of the dilation angle, ψ). Sagaseta (1999) recommends values for α to be $\alpha = 1.0$ to 2.0 (i.e., $\psi = 0°$-$30°$). The modified displacements for the uniform convergence case considering dilation due to plastic behavior are:

$$u_x(x,y) = u_\varepsilon \cdot R^{2\alpha-1} \cdot \left\{ \begin{array}{l} \dfrac{x}{\left[x^2+(y+H)^2\right]^\alpha} - \dfrac{x}{\left[x^2+(y-H)^2\right]^\alpha} + \ldots \\ \ldots + \dfrac{2\cdot x}{\left[x^2+(y-H)^2\right]^\alpha} - 4\cdot\dfrac{(y-H)\cdot x\cdot y}{\left[x^2+(y-H)^2\right]^{\alpha+1}} \end{array} \right\} \qquad \{5\text{-}19a\}$$

$$u_y(x,y) = u_\varepsilon \cdot R^{2\cdot\alpha-1} \cdot \left\{ \begin{array}{l} \dfrac{(y+H)}{\left[x^2+(y+H)^2\right]^\alpha} - \dfrac{(y-H)}{\left[x^2+(y-H)^2\right]^\alpha} + \ldots \\ \ldots + \dfrac{4\cdot(y-H)\cdot x^2 + 2\cdot H\cdot\left[x^2-(y-H)^2\right]}{\left[x^2+(y-H)^2\right]^{\alpha+1}} - \dfrac{2\cdot(y-H)}{\left[x^2+(y-H)^2\right]^\alpha} \end{array} \right\}$$

{5-19b}

The modified displacements for the pure distortion case are:

$$u_x(x,y) = u_\delta \cdot R^{2\cdot\alpha-1} \cdot x \cdot \left\{ \begin{array}{l} \dfrac{\left[x^2+(y+H)^2\right]^2 - \left[3\cdot(y+H)^2 - x^2\right]\cdot\left[x^2+(y+H)^2 - R^2\right]}{\left[x^2+(y+H)^2\right]^{\alpha+1}} - \ldots \\ \ldots - \dfrac{\left[x^2+(y-H)^2\right]^2 - \left[3\cdot(y-H)^2 - x^2\right]\cdot\left[x^2+(y-H)^2 - R^2\right]}{\left[x^2+(y-H)^2\right]^{\alpha+1}} + \ldots \\ \ldots + 4\cdot\dfrac{x^2+y^2-H^2}{\left[x^2+(y-H)^2\right]^{\alpha+1}} - \ldots \\ \ldots - 8\cdot y\cdot\dfrac{y\cdot(x^2+y^2) + 2\cdot H\cdot(H^2-x^2) - 3\cdot y\cdot H^2}{\left[x^2+(y-H)^2\right]^{\alpha+2}} \end{array} \right\}$$

{5-20a}

$$u_y(x,y) = -u_\delta \cdot R^{2\cdot\alpha-1} \cdot \left\{ \begin{array}{l} (y+H)\cdot\dfrac{\left[x^2+(y+H)^2\right]-\left[3\cdot x^2-(y+H)^2\right]\cdot\left[x^2+(y+H)^2-R^2\right]}{\left[x^2+(y+H)^2\right]^{\alpha+1}}-\ldots \\ \ldots-(y-H)\cdot\dfrac{\left[x^2+(y-H)^2\right]-\left[3\cdot x^2-(y-H)^2\right]\cdot\left[x^2+(y-H)^2-R^2\right]}{\left[x^2+(y-H)^2\right]^{\alpha+1}}-\ldots \\ \ldots-4\cdot\dfrac{x^2\cdot(2\cdot H-y)-y\cdot(y-H)^2}{\left[x^2+(y-H)^2\right]^{\alpha+1}}+\ldots \\ \ldots+8\cdot\dfrac{(y-H)\cdot\left\{H\cdot y\cdot(y-H)^2-x^2\cdot\left[\left(x^2+y^2\right)+H\cdot(y+H)\right]\right\}}{\left[x^2+(y-H)^2\right]^{\alpha+1}} \end{array} \right\} \quad \{5\text{-}20b\}$$

The effect of $\alpha > 1$ is a faster attenuation of the displacements with distance, while the basic features of the elastic solution are kept. Figures 5.15 and 5.16 show the influence of α on the surface settlements distribution. It can be seen that increasing the α value has the effect of reducing the width of the settlement trough. Figures 5.17 and 5.18 show the influence of α on the horizontal displacement distribution at a vertical line inside the ground. It can be seen that increasing α has the effect of a faster attenuation of the displacements with distance.

5.3. Conclusions

It has been shown that elastic solutions can be used in order to model the actual elastic-plastic displacements around infinitely deep tunnels under an initial isotropic state of stress. For the undrained case, the displacements are independent of the constitutive model, provided material compressibility is neglected. For the drained case, elastic solutions can be used in order to predict displacement patterns at points outside the zone of plastic failure around the tunnel wall. The magnitude of the radial displacement, measured at the tunnel wall, is always equal or larger than the equivalent elastic displacement that would be predicted by elastic theory. This chapter proposes a simple reduction factor that can be applied to measured tunnel wall convergence in order to use elastic solutions for computing far field displacements.

For the general case of a shallow tunnel with $K_0 \neq 1$ initial stresses, an approximate solution can be obtained by including the dilation parameter, α, in terms of the form $1/r$ of the elastic solution

for $\nu = 0.5$. If the radius of the plastic zone is such that the plastic zone is likely to extend near the surface, this approximate solution can be used in order to model the soil dilation due to plastic behavior throughout the medium and taking into account the pure distortion component as well. However, dilation is likely to occur only at large strains.

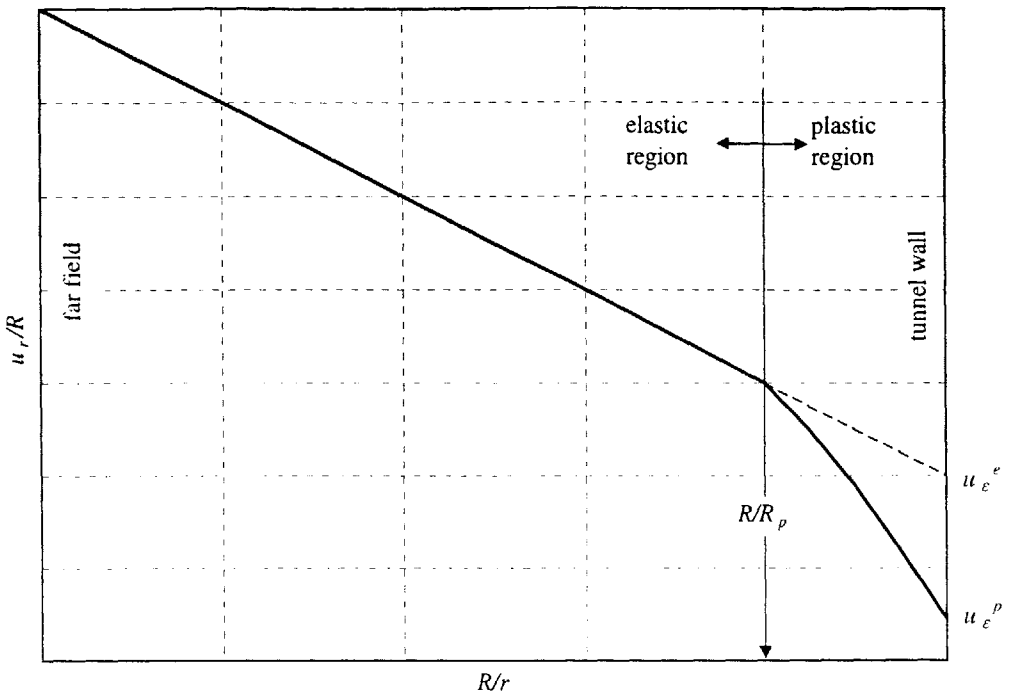

Figure 5.1. Radial displacements due to a cylindrical cavity contraction (after Yu and Rowe, 1998)

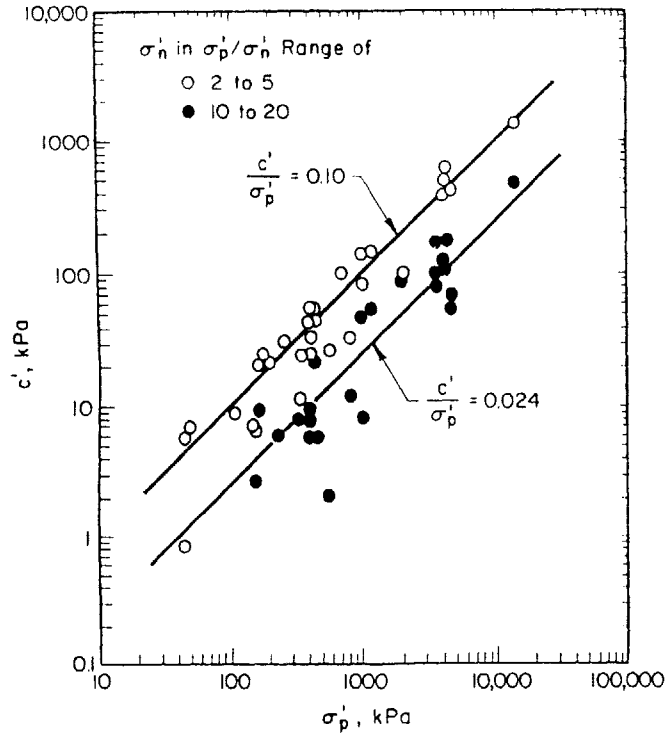

Figure 5.2. Relationship between cohesion intercept, c', and preconsolidation pressure, σ'_p (Mesri and Abdel-Ghaffar, 1993)

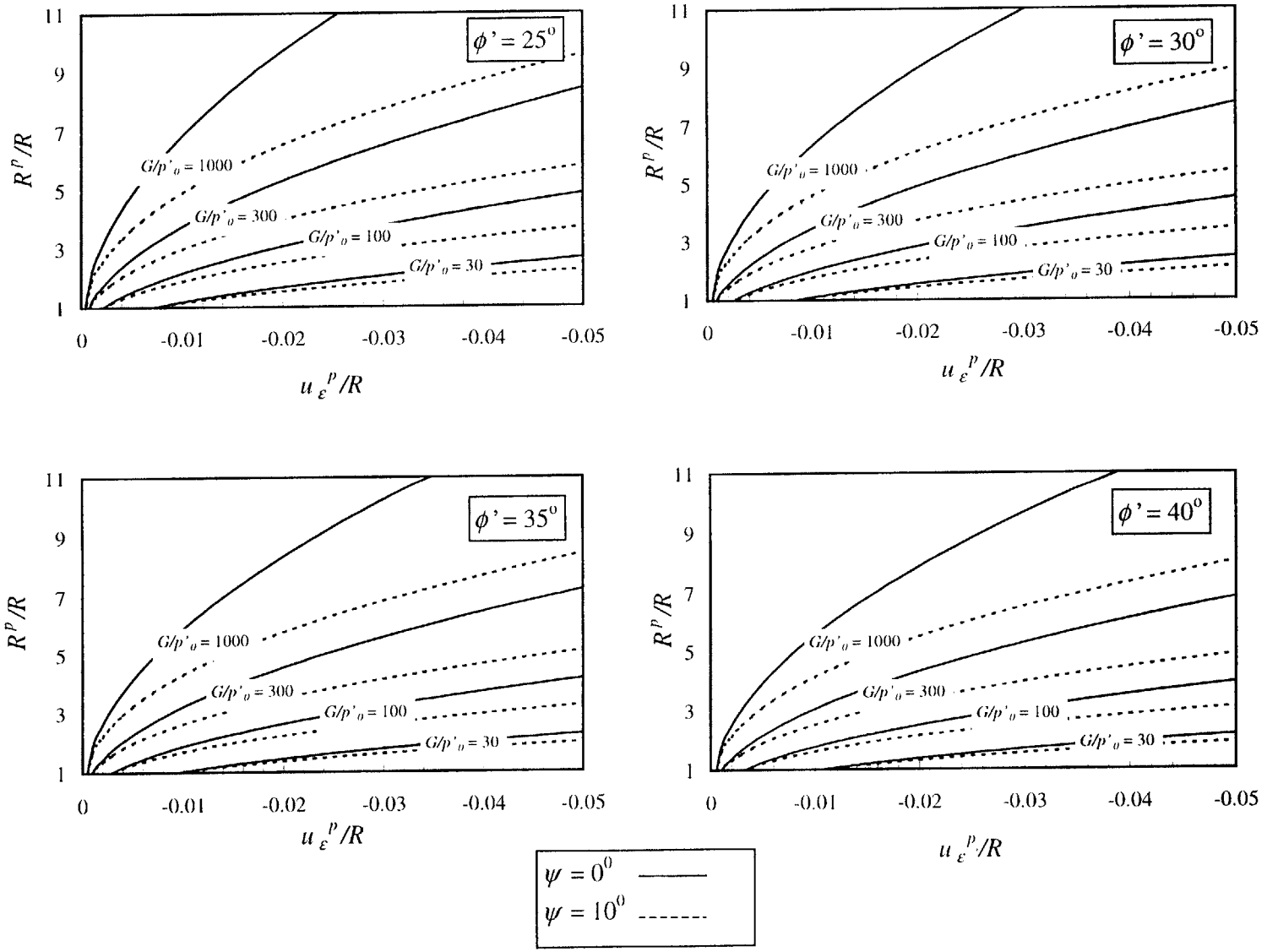

Figure 5.3. Influence of soil properties on the radius of the plastic zone, R_p, for $c'/p'_0 = 0.0$

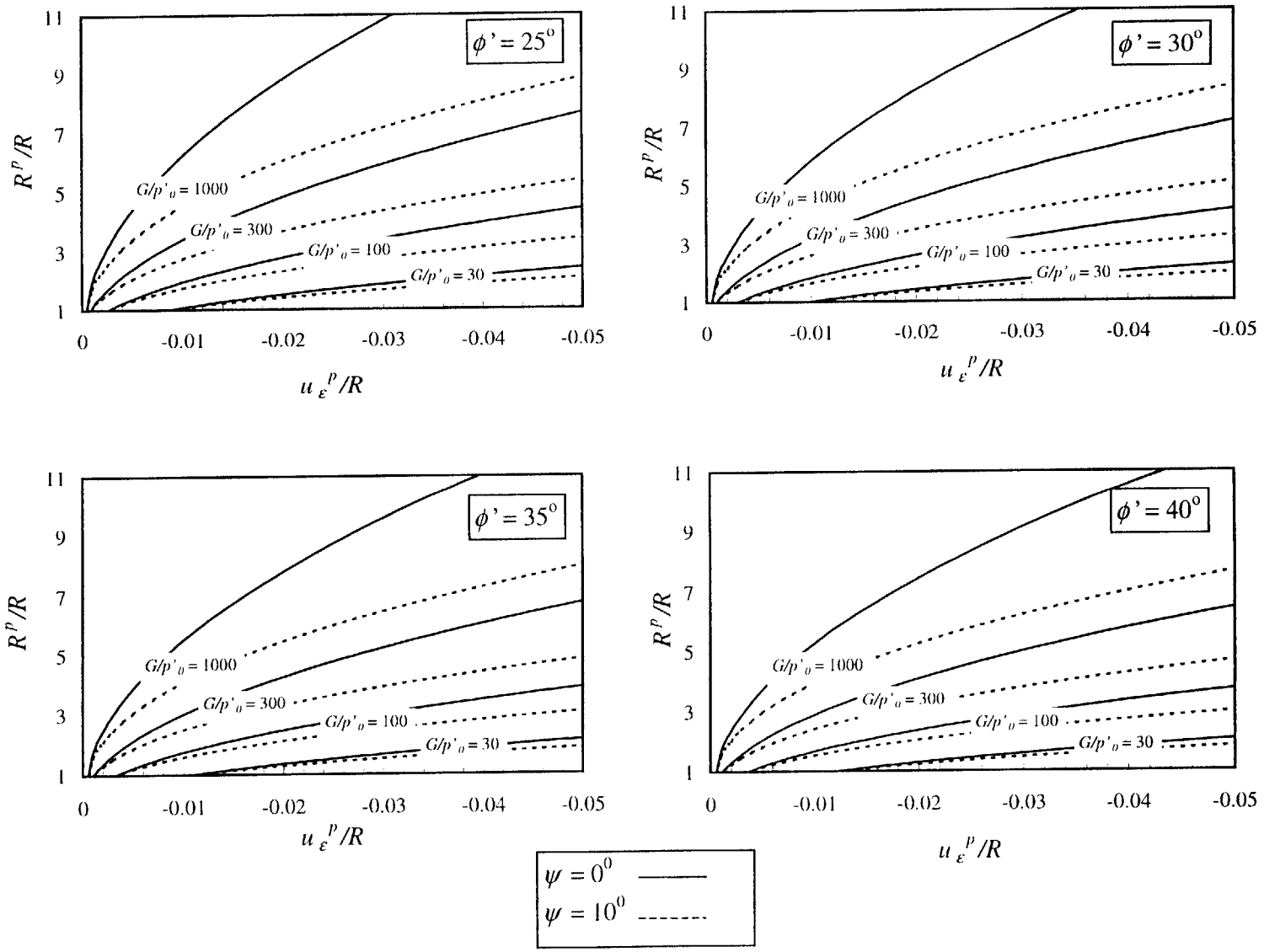

Figure 5.4. Influence of soil properties on the radius of the plastic zone, R_p, for $c'/p'_0 = 0.1$

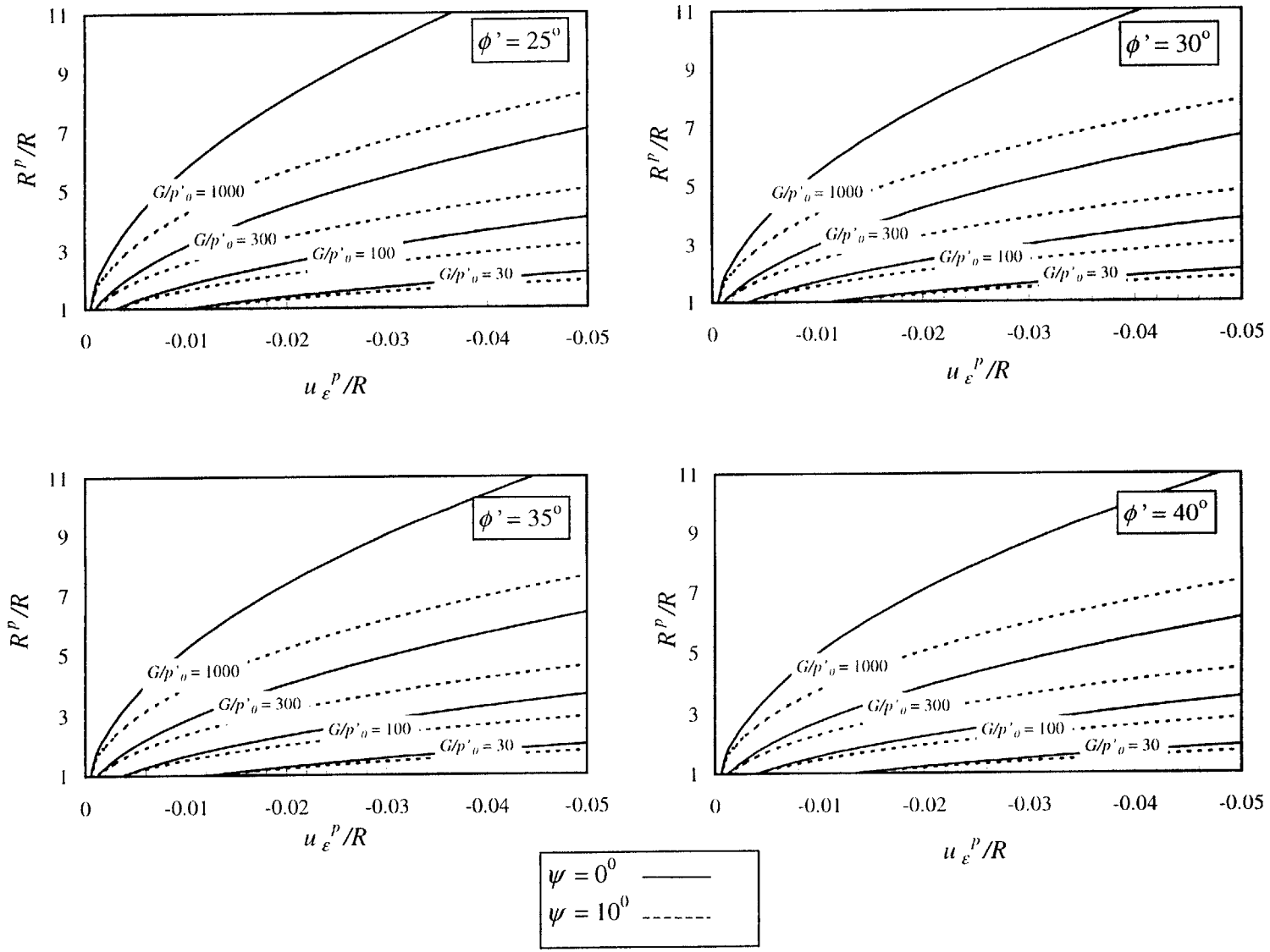

Figure 5.5. Influence of soil properties on the radius of the plastic zone, R_p, for $c'/p'_0 = 0.2$

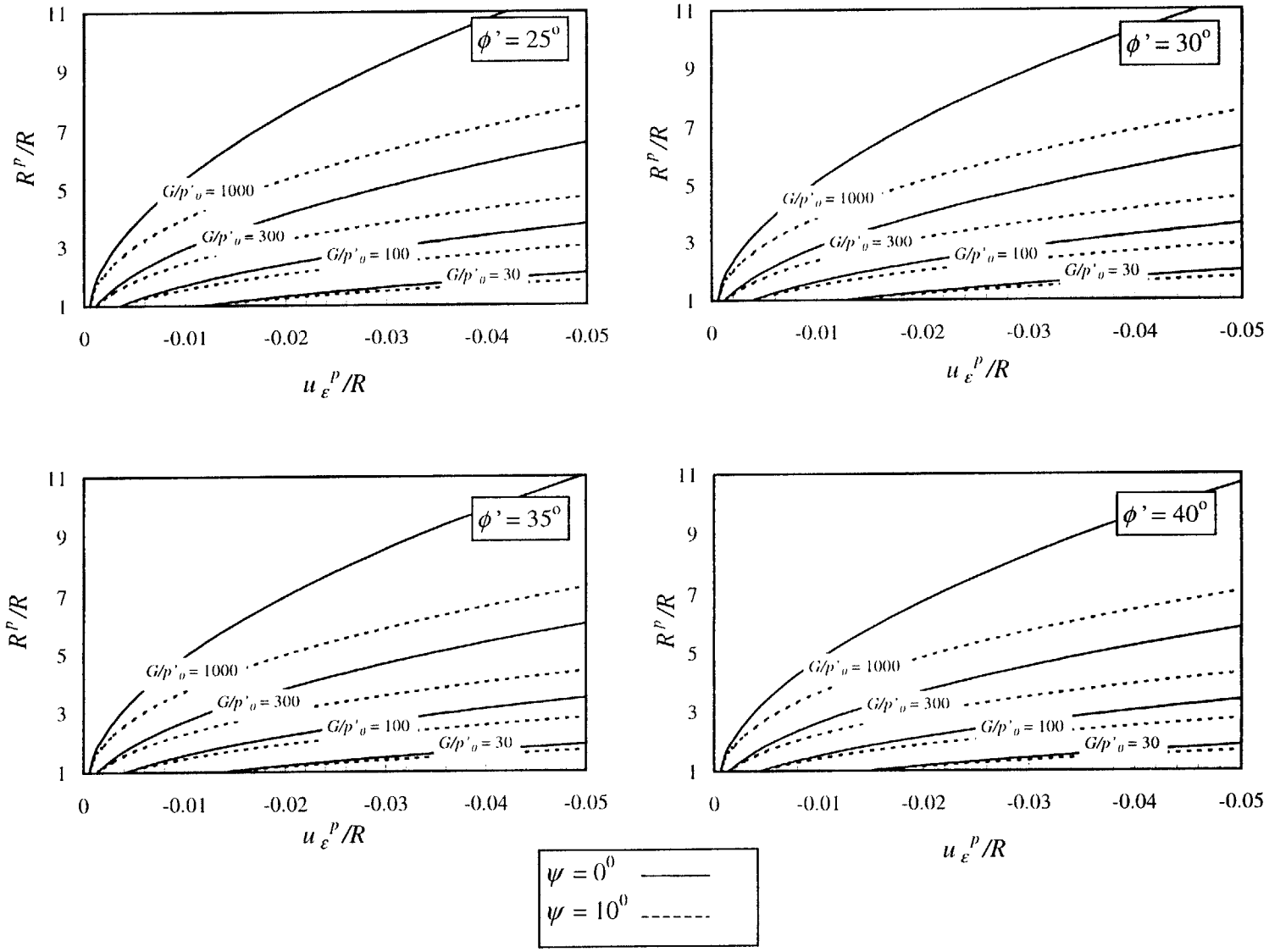

Figure 5.6. Influence of soil properties on the radius of the plastic zone, R_p, for $c'/p'_0 = 0.3$

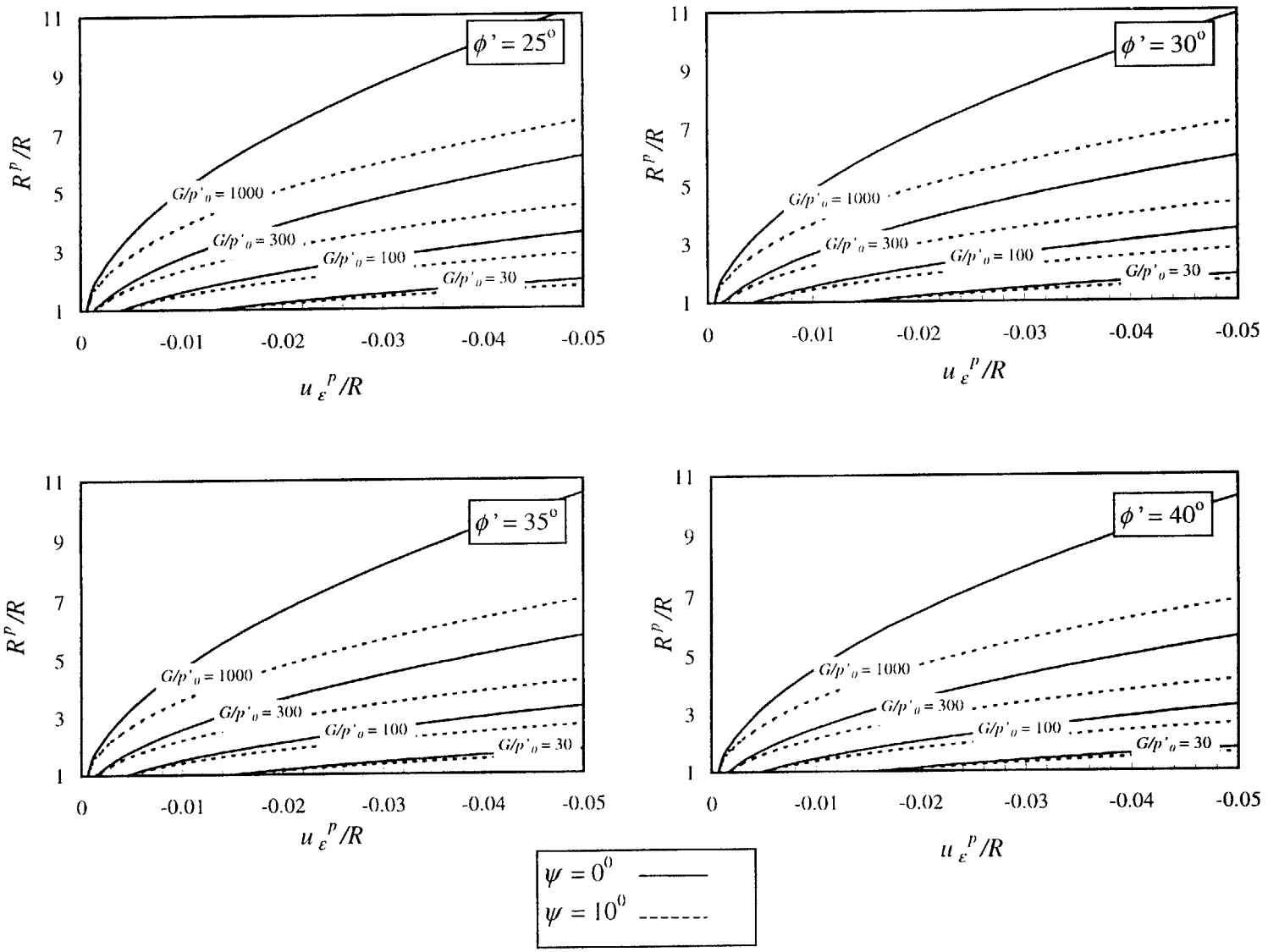

Figure 5.7. Influence of soil properties on the radius of the plastic zone, R_p, for $c'/p'_0 = 0.4$

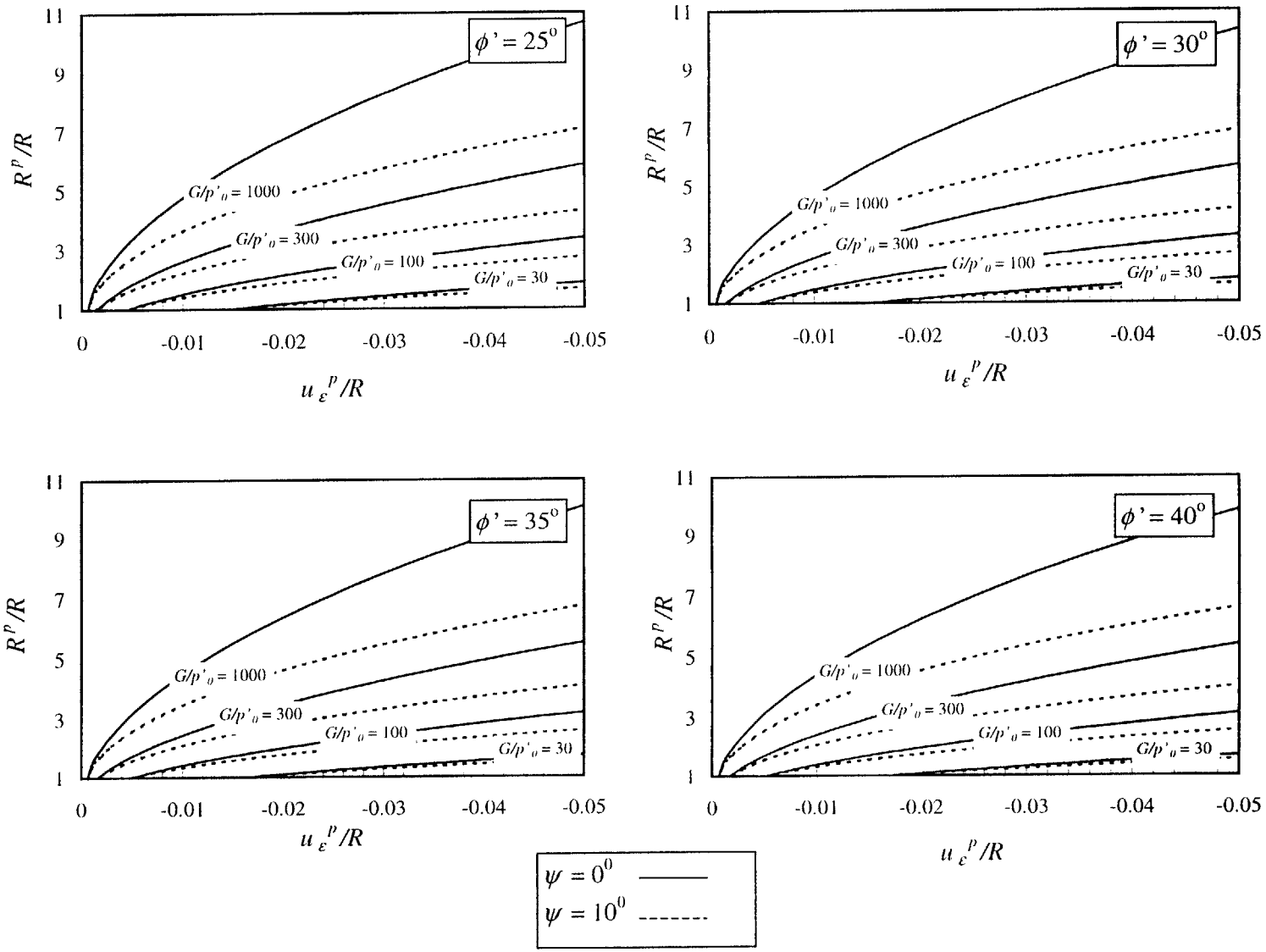

Figure 5.8. Influence of soil properties on the radius of the plastic zone, R_p, for $c'/p'_0 = 0.5$

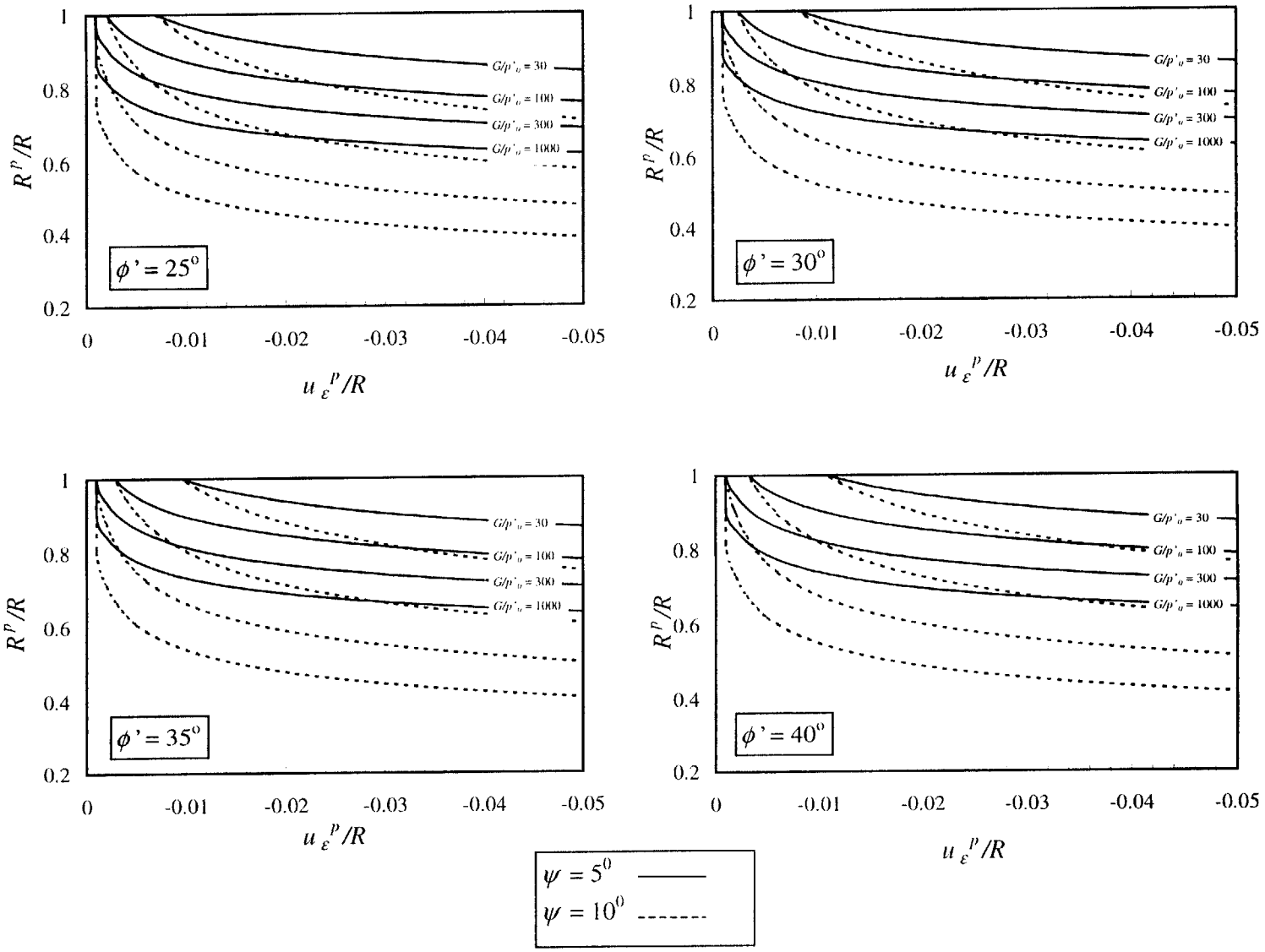

Figure 5.9. Influence of soil properties on the reduction factor, *RF*, for $c'/p'_0 = 0.0$

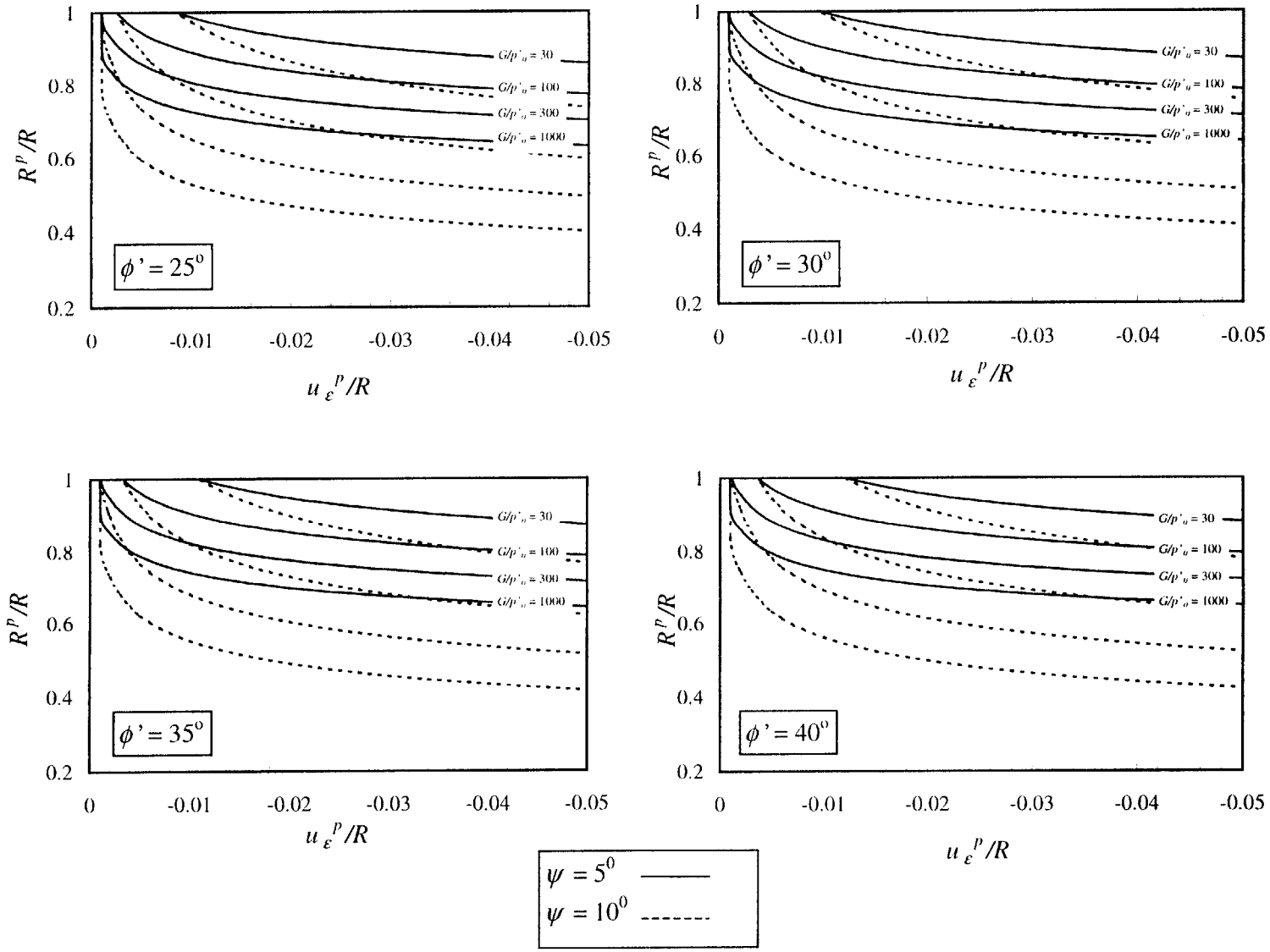

Figure 5.10. Influence of soil properties on the reduction factor, RF, for $c'/p'_0 = 0.1$

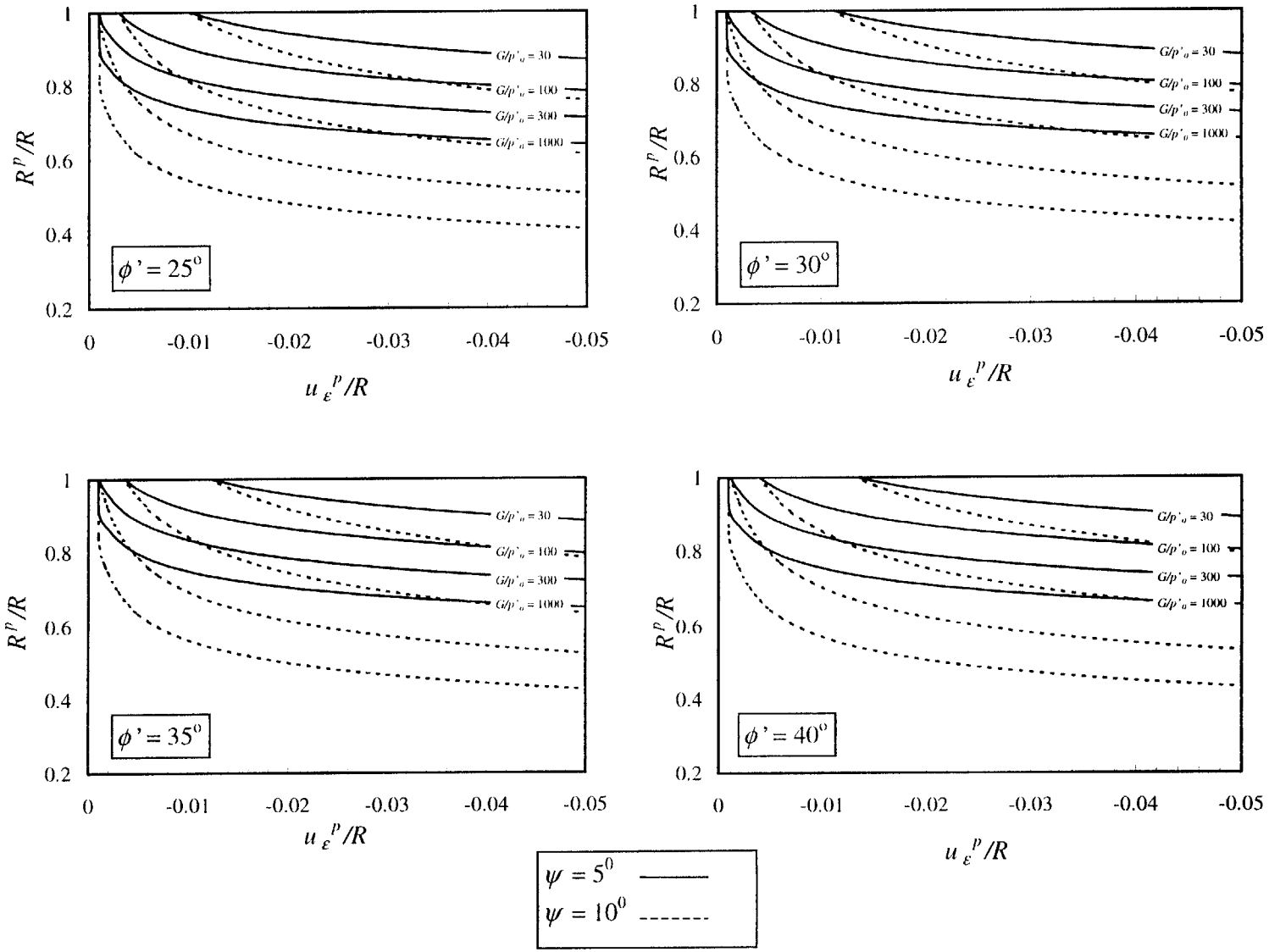

Figure 5.11. Influence of soil properties on the reduction factor, RF, for $c'/p'_0 = 0.2$

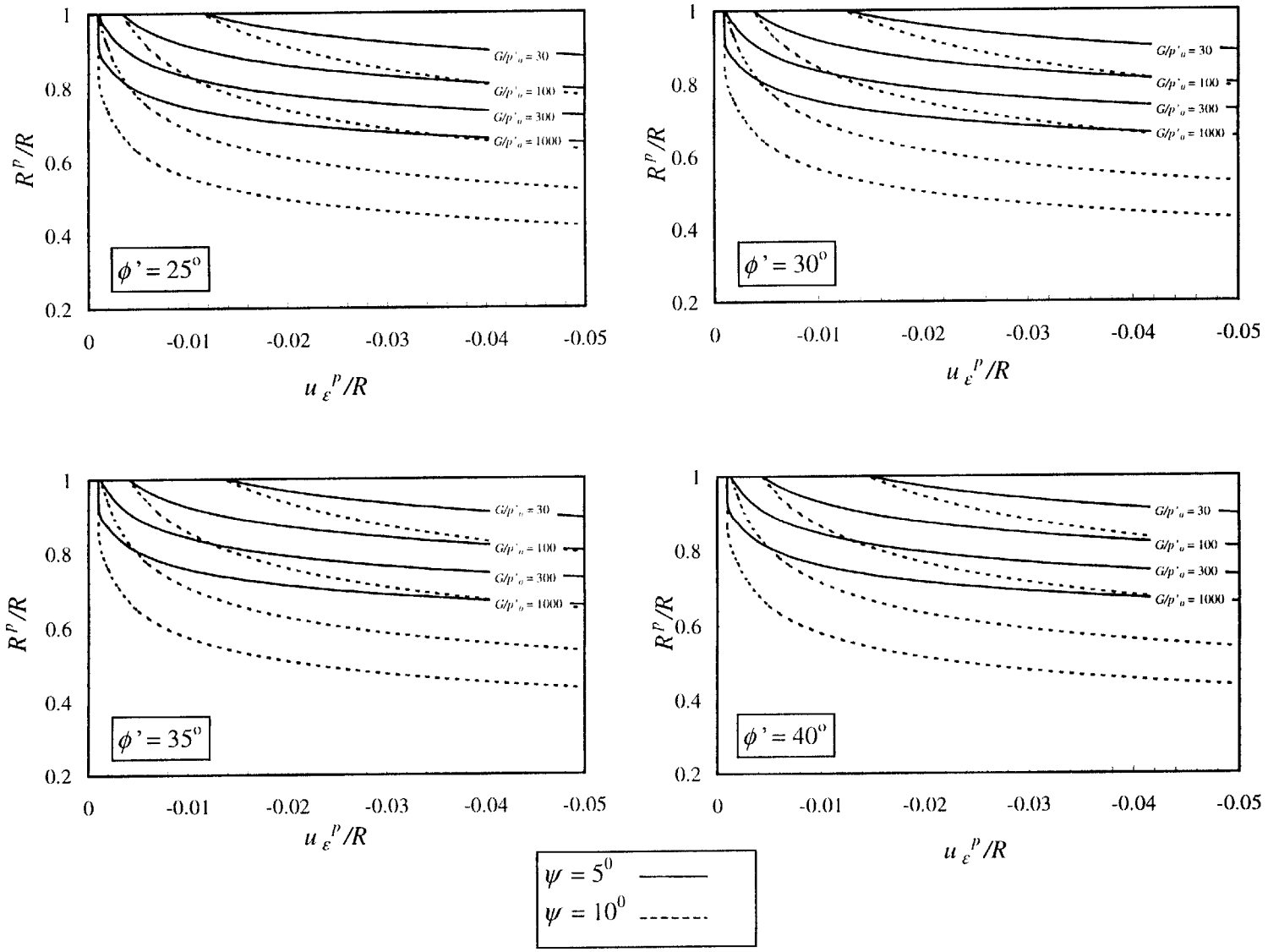

Figure 5.12. Influence of soil properties on the reduction factor, RF, for $c'/p'_0 = 0.3$

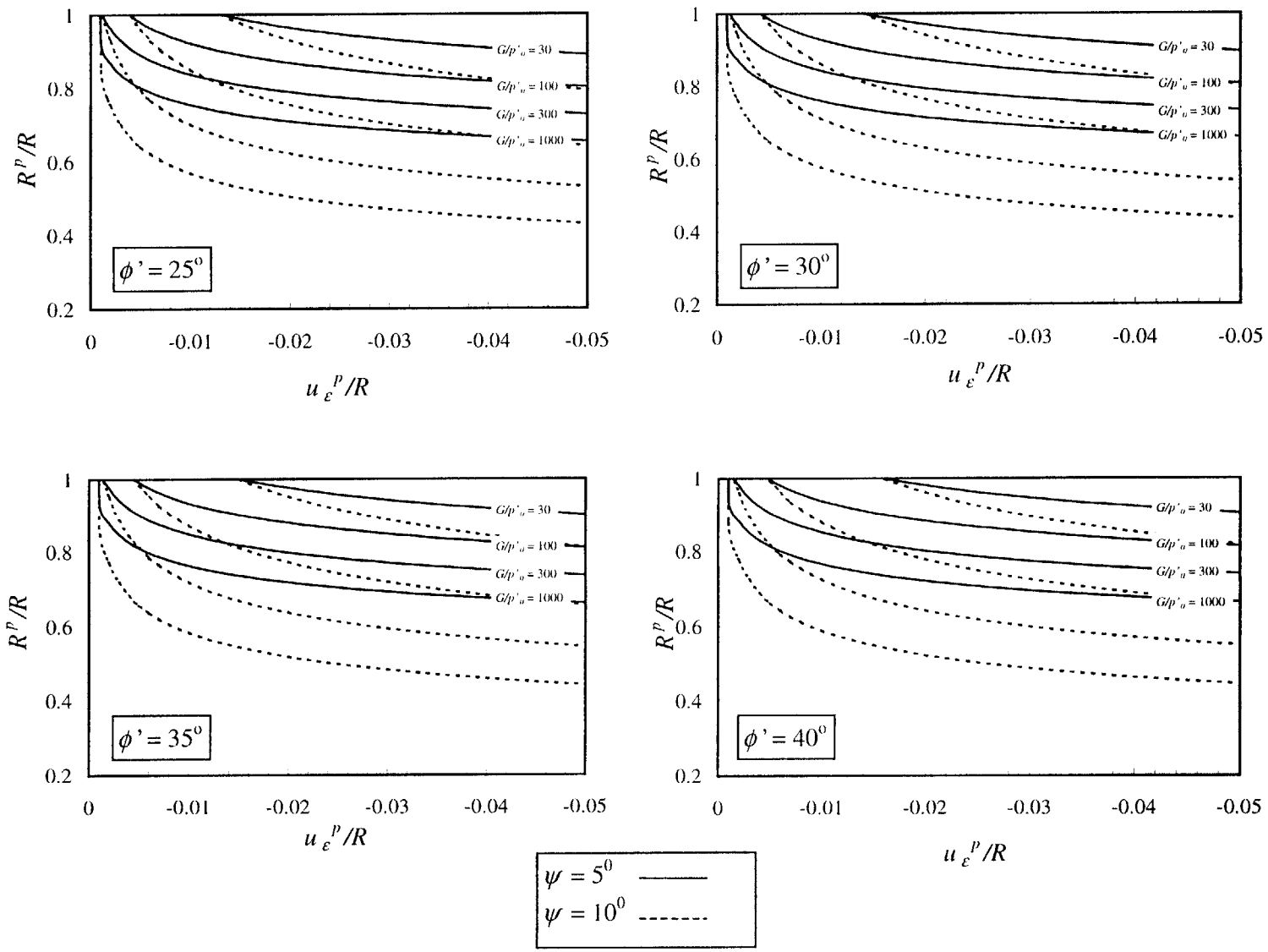

Figure 5.13. Influence of soil properties on the reduction factor, RF, for $c'/p'_0 = 0.4$

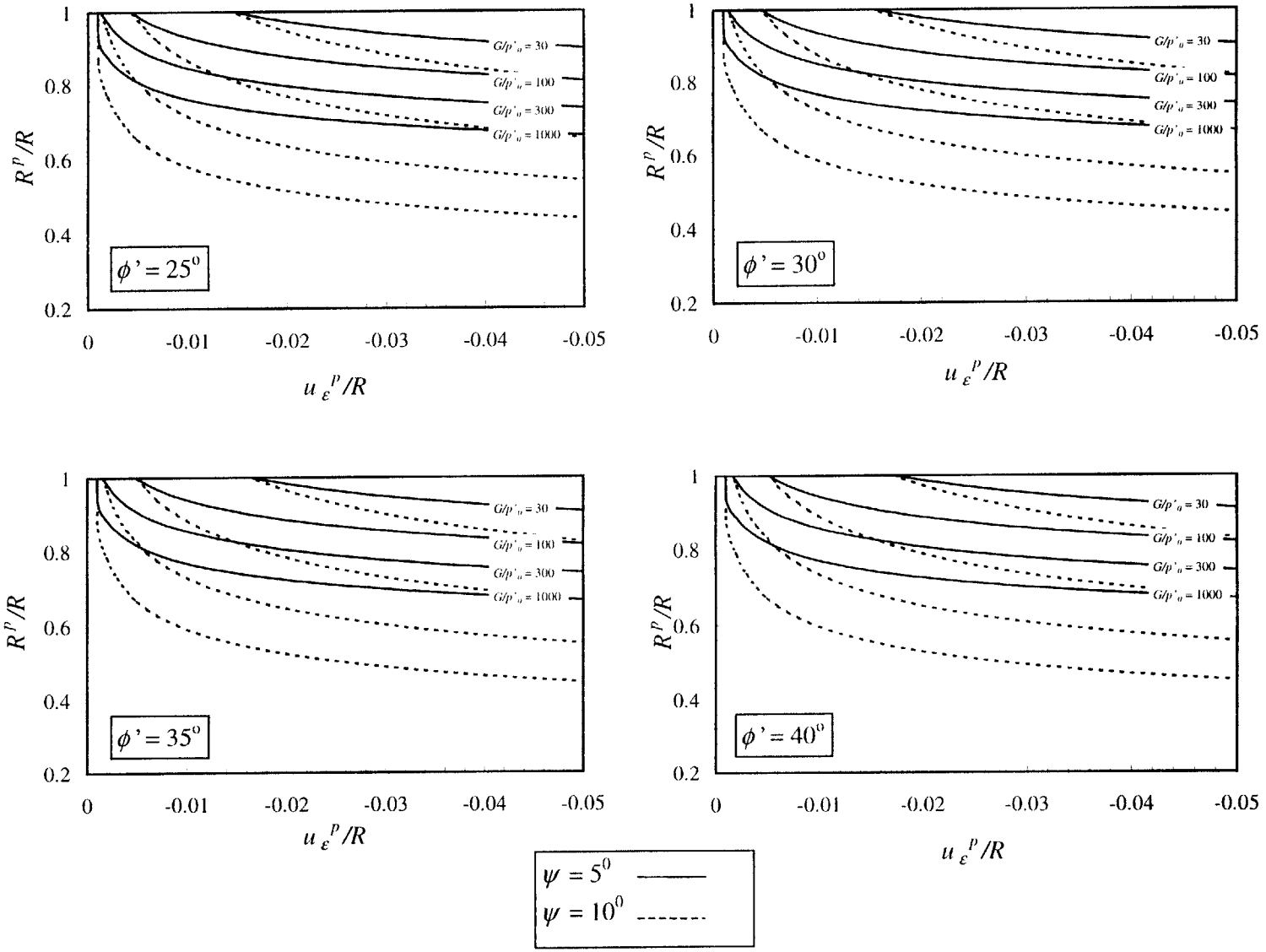

Figure 5.14. Influence of soil properties on the reduction factor, RF, for $c'/p'_0 = 0.5$

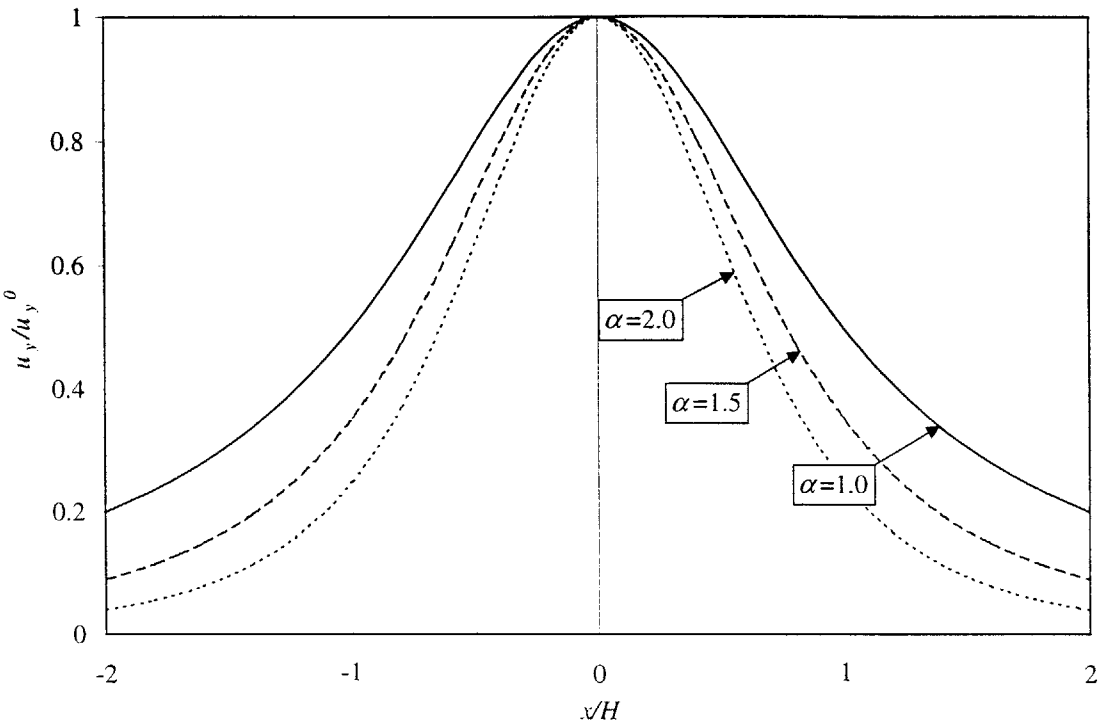

Figure 5.15. Influence of α on surface settlements distribution, $R/H = 0.2$, $\rho = 0$

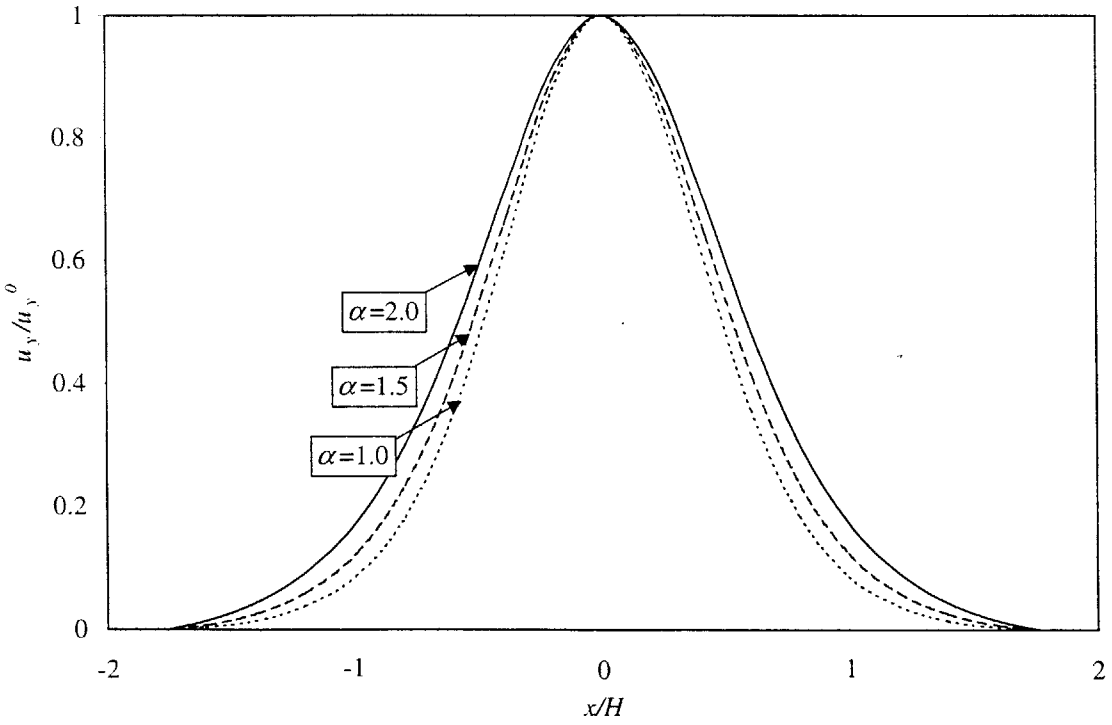

Figure 5.16. Influence of α on surface settlements distribution, $R/H = 0.2$, $\rho = 1$

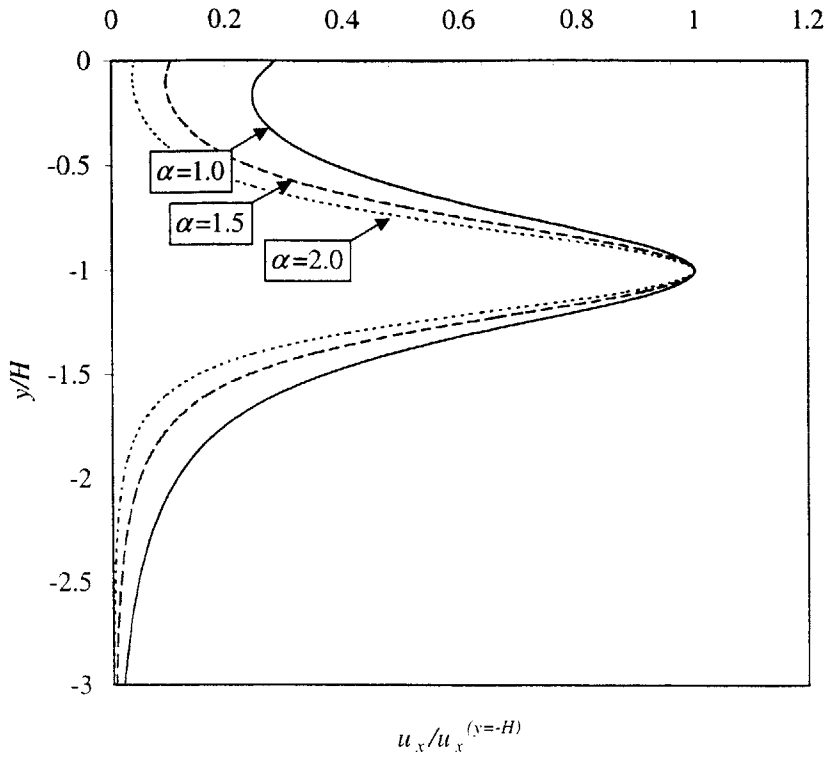

Figure 5.17. Influence of α on horizontal displacements inside the ground, $R/H = 0.2$, $\rho = 0$

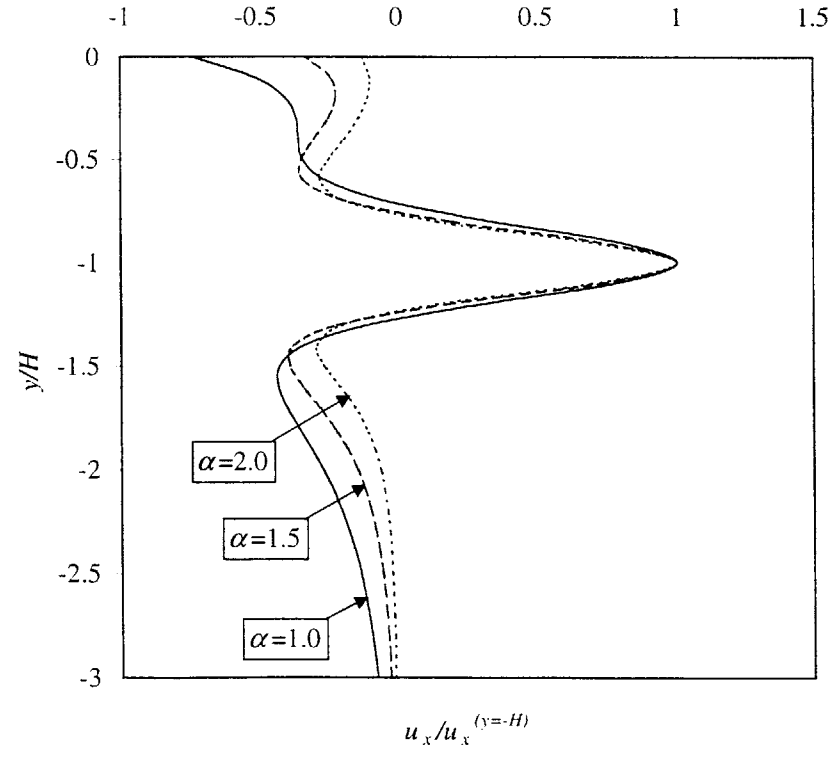

Figure 5.18. Influence of α on horizontal displacements inside the ground, $R/H = 0.2$, $\rho = 1$

6. Comparison with Field Monitoring Data

This Chapter discusses the application of the ground deformation analysis for single tunnels. A simple method is proposed for obtaining the ground deformation parameters, u_ε, ρ, ν or α and its practical application is assessed by considering four case studies. The methodology of analysis is described in Section 6.1 and the case studies are presented in Section 6.2.

6.1. Design Charts for Estimating Model Input Parameters

It has been shown in Chapter 3 that there are three input parameters defining the analytical predictions of ground displacement distribution (but not the magnitude): i) the embedment ratio, *R/H*; ii) the relative distortion, ρ; and iii) the Poisson ratio, ν (if purely elastic), or the α parameter (considering average dilation within the soil mass). Hence, for a given tunnel geometry (i.e., a given *R/H* ratio), the ground displacement distribution is a function of ρ and ν or α. The magnitude of the displacements is defined by the amount of ground loss that takes place, which is related to the convergence parameter, u_ε.

A series of charts have been developed in order to interpret in situ measurements of ground displacements due to tunneling. The purpose of these charts is to provide a practical method for computing values of u_ε, ρ, and ν (or α) parameters from a small number of field measurements. These charts are based on three measured parameters[1]: i) the surface settlement at $x/H = 0$, u_y^0, ii) the surface settlement at $x/H = 1$, u_y^1, and iii) the horizontal displacement at a reference offset, x = $2 \cdot R$ away from the tunnel springline, u_x^0 (Figure 6.1).

[1] Surface settlements are routinely measured at offsets from the tunnel axis in most tunneling projects, while the lateral displacement requires data from an inclinometer installed at (approximately) the reference offset

These parameters have been selected so as to provide maximum information on the effects of ρ and ν or α on the displacement patterns. The surface settlement ratio, u_y^1/u_y^0, is a measure of the width of the settlement trough, which is highly sensitive to variations in ρ and α and somewhat affected by variations in ν (see Sections 3.5.1.4. and 5.2.). The horizontal displacement ratio, u_x^0/u_y^0, is highly sensitive to both variations in ρ and ν (see Sections 3.5.2.). Hence, for a given horizontal and vertical displacement ratios, there is a unique set of ρ, ν or α values that would reproduce the displacement patterns. Once the ρ, ν or α values are obtained, the absolute magnitude of the displacements can be calculated by matching the observed surface settlement at $x/H = 0$, u_y^0, by means of the u_y^0/u_ε ratio, which is a function of ρ, ν or α. Following this reasoning, Appendix V presents a series of design charts for computing the ρ, ν or α values from the displacement ratios u_x^0/u_y^0 and u_y^1/u_y^0 and the u_y^0/u_ε ratio from the selected values for ρ, ν (or α).

In order to obtain the parameters ρ, ν or α, and u_ε from field measurements, the following procedure is proposed:

- Measure u_x^0, u_y^0, and u_y^1
- By means of the horizontal and vertical displacements ratios, obtain ρ and ν (or α) from the proposed design charts.
- Using the selected parameters (ρ, ν, α) obtain u_ε from the proposed design charts.

In the Appendix V charts, plasticity has only been included for $R/H \geq 0.1$, since deeper tunnels are unlikely to produce plastic behavior near the surface. The maximum vertical displacement ratio considered in these charts is 0.5, which would correspond to $\rho = 0$ and $\alpha = 0$. These value was selected in view that most of the published data—if not all—falls in the range where $u_y^1/u_y^0 < 0.5$.

6.2. Case Studies

This Section shows the practical application of the above discussed analysis method for four case studies in a variety of soils and construction methods.

6.1. Case 1: Metro de Madrid (Sagaseta et al., 1999)

The Madrid Metro extension is constructed within tertiary deposits, covered by quaternary sediments. Man-made fills are also frequent in the area. The tertiary soils comprise mainly very stiff, heavily overconsolidated clays. Some sections are excavated by conventional hand-excavation methods (Belgian method) and hence, significant deformations can occur before placing the lining.

The cross section considered in this example was excavated by means of conventional methods and has a horseshoe-shaped cross section of 62 m^2 (equivalent radius R_{eq} = 4.44 m) and a depth to the centerline, H = 15.2 m. Hence, the embedment ratio for this case is R/H = 0.292. Figures 6.2 and 6.3 summarize the measured surface settlements and lateral displacements in an inclinometer located 2 m from the tunnel, respectively. The surface settlement at x/H = 0, u_y^0 = -11.4 mm and the average surface settlement (found by linear interpolation, Figure 6.2) at x/H = 1 is u_y^1 = -4.1 mm. The horizontal displacement measured at the springline is u_x = 4.1 mm (towards the tunnel). However, the inclinometer is located at x/R_{eq} = 1.8, and not at x/R = 2, as defined in the design charts. Nevertheless, it can be shown readily that the elastic horizontal displacements in an infinite medium (due to a combination of distortion and uniform convergence) are given by:

$$\frac{u_x(x, y=-H)}{u_\varepsilon} = \frac{4\cdot(1-\nu)}{3-4\cdot\nu}\cdot(1-\rho)\cdot\frac{R}{x} \qquad \{6\text{-}1a\}$$

while the plastic horizontal displacements in an infinite medium due to a combination of distortion and uniform convergence are given by:

$$\frac{u_x(x, y=-H)}{u_\varepsilon} = 2\cdot(1-\rho)\cdot\frac{R^{2\alpha-1}}{x^\alpha} \qquad \{6\text{-}1b\}$$

Hence, in order to estimate a value for $u_x(2\cdot R,-H) = u_x^0$ from a measured value $u_x(\beta\cdot R,-H)$, the following equations can be used:

Elastic: $$u_x^{\,0} = \frac{\beta}{2} \cdot u_x(\beta \cdot R, -H) \qquad \{6\text{-}2a\}$$

Plastic $$u_x^{\,0} = \left[\frac{\beta}{2}\right]^{\alpha} \cdot u_x(\beta \cdot R, -H) \qquad \{6\text{-}2b\}$$

For this case, β= -1.804 and $u_x(\beta R,-H)$ = 4.1 mm. Therefore, assuming elastic behavior, $u_x^{\,0}$ = -3.7 mm.

Figures 6.4 and 6.5 show the displacement ratios plotted in the design charts for R/H = 0.25 and R/H = 0.30, from which ν and ρ can be estimated by means of linear interpolation[2]. The results lead to estimated values, ν = 0.48 (corresponds to almost undrained conditions), and ρ = 0.22, which is consistent with the expected K_0 conditions and a low inner pressure at the lining. The uniform convergence displacement, u_ε, is obtained from Figures 6.6 and 6.7, in which $u_y^{\,0}/u_\varepsilon$ = 0.84 - 0.85. Hence, the convergence displacement is u_ε = −13.5 mm, and the corresponding ground loss V_L = 0.6 %.

Once the ground deformation parameters ρ, ν, and u_ε, have been obtained, the complete displacement field can be generated reproduced by the analytical model, as shown in Figures 6.8 and 6.9. In this example, the model is in excellent agreement with both the measured settlement trough and inclinometer measurements. Figure 6.10 shows contours of ground displacements predicted by the model.

[2] The results in Figures 6.4 and 6.5 show [ρ = 0.27, ν = 0.39] for R/H = 0.25 and [ρ = 0.21, ν = 0.50] for R/H = 0.30, respectively.

6.2 Case 2: Sewer-Line Tunnel in Mexico City (Romo, 1997)

This tunnel is part of the sewerage system of the Metropolitan area of Mexico City. Construction was carried out by means of a 4 m diameter shield and a pressurized slurry at the tunnel face in order to increase stability. Pre-cast segmental lining was placed behind the shield and the tail void was filled with pressurized grout. The soil profile at the section considered herein is composed of a soft clay deposit underlying some inter-bedded silt and clay strata. Given the construction procedure, it is expected that the ground loss will be rather low and the relative distortion high, as the in-situ K_0 is low (less than 1) and the internal pressure ratio, r_p, high.

The tunnel cross section is circular with a radius, R = 2 m, and embedment depth, H = 12.75 m. Hence, the embedment ratio for this case is R/H = 0.157. Figures 6.11 and 6.12 summarize the surface settlements and lateral deflections (in an inclinometer located at x = 4.5 m from the center of the tunnel). The reference surface settlements are u_y^0 = -28.6 mm (at x/H = 0) and u_y^1 = -7.2 mm (at x/H = 1). The horizontal displacement measured at the springline (Figure 6.12) is u_x = 9.4 mm (outwards the tunnel), at x/R = 2.25. Hence, using equations {6-2}, the reference displacement at x/R = 2 is found to be u_x^0 = 9.4·(2.25/2.0) = 10.6 mm (assuming elastic behavior).

Figures 6.13 and 6.14 show the displacement ratios plotted in the design charts for R/H = 0.15 and R/H = 0.20, from where the Poisson ratio, ν, and relative distortion, ρ, can be estimated by linear interpolation. These charts generate a Poisson ratio, ν = 0.0, which seems unrealistic, and a relative distortion, ρ = 1.53, which is also unrealistically high. The uniform convergence displacement, u_ε, is obtained by means of the design chart shown in Figures 6.15 and 6.16, from which u_ε = –22.2 mm, corresponding to a ground loss V_L = 1.1 %. A careful review of the measured data suggests that the estimation of input parameters may be strongly biased by the inclinometer data (i.e., by u_x^0). Figure 6.12 shows that the inclinometer data are reported over a depth range from y = -3 to -17.5 m. The source reference gives no details of the methods used to benchmark (i.e., set the zero position) for this device. As a result, the data show no well defined zero position, raising the strong possibility that there is a zero shift in the measurements, given the lack of bearing strata at this site. Figure 6.10 considers the effects of a 3 mm shift in the zero

position of the inclinometer (leading to a rigid body translation of the reported data). Considering this adjustment of the inclinometer data (see Figure 6.12), the model input parameters can be re-computed using u_x^0 (corr.) = 6.2 mm (Figures 6.13 to 6.16). The revised parameter set is found ρ = 1.16, ν = 0.12 and u_ε = -26.5 mm (ground loss, V_L = 2.7 %). These parameters are much more consistent with expected behavior, but are difficult to justify without further information to explain the assumed rigid body inclinometer correction.

Figure 6.17 summarizes comparisons between model prediction and vertical displacement measurements at three elevations (y = 0, -5, and −10.15 m) within the overlying clay. The proposed adjustment of the inclinometer has minimal effect on the predicted settlements at these three depths. The results show excellent agreement between computed and measured settlements at the surface. The models tends to overestimate measured movements above the crown of the tunnel at y = -5 m (by 10-20%), and gives a substantial overestimate (up to 70-100%) at y = -10.15 m. This latter result can be largely discounted due to the very close proximity of the measurements to the tunnel lining, where the proposed method is unlikely to replicate accurately the soil behavior or construction process.

Figure 6.18 compares the computed and measured lateral displacements for the inclinometer (both the reported data and adjusted values are shown). Both the measurements and model predictions show outward movements (i.e., away from tunnel) at the tunnel elevation. Both sets of analyses show inward movements for depths less than 8-10 m, while the original measurements show small outward movements even close to the surface. There is a definite improvement in the agreement between predictions and measurements after adjusting the data for a probable zero shift in the reference location of the inclinometer.

6.3. Case 3: Heathrow Express Trial Tunnel (Deane and Basset, 1995)

The soil deposit, outlined in Figure 6.21, comprises a made ground 0.5 m thick, terrace gravel 1-4 m thick, and London Clay at least 45 m thick. The range of moisture content is between 24% and 32% (Atzl and Mayr, 1994). This tunnel was excavated using three different NATM-types of excavation sequences. For the section considered herein, *Type 3* sequence of excavation was used. This sequence consists on a top heading and bench sequence with the bottom of the shotcrete arch of the heading supported on inverted shotcrete arches (Figure 6.22). Reported K_0 values for this site are in the range of 1.5 (Longanathan and Poulos, 1998). Hence a very low value of relative distortion (even negative if evaluated by means of equation {2-53}) and a considerable ground loss volume can be anticipated.

The section considered in the analysis has an average diameter of 8.5 m and a depth to centerline, H = 19.1 m. Hence, the R/H ratio for this case is R/H = 0.22. Figures 6.23 and 6.24 show the observed surface settlements and lateral (inclinometer) movements at x = -9 m at three stages of the construction, together with the interpretation of the pertinent model parameters. The three stages correspond to; i) face of the tunnel on instrument line (19-May-92), ii) completion of face (25-May-92), and iii) completion of invert (28-May-92). Figures 6.25 and 6.26 show the displacement ratios plotted in the design charts for R/H = 0.20 and R/H = 0.25. It can be seen that the points fall outside the region spanned by the elastic solutions. It can also be noticed that the last two stages coincide and will be analyzed together. Two criteria are followed in order to estimate model input parameters from the design charts; 1) consider that the clay is in an undrained condition with no dilation (i.e., α = 1 or ν = 0.5) assuming that the horizontal displacement ratio is reliable, but the settlement trough is unreliable (i.e., errors in measured u_y^I), and 2) consider dilation using the average dilation model. Results obtained by both criteria are given in Table 6.1 (after linear interpolation).

It can be seen that criterion 2 (assuming that all measurements are consistent and accurate) estimates totally unrealistic ground losses, while the values obtained by means of criterion 1 are within the expected range. Using the parameters obtained following criterion 1, ground displacements are evaluated and compared with the measured values in Figures 6.31 and 6.32. It

can be seen that the inclinometer readings are well reproduced (particularly for the 19-May-92 readings), while the settlement troughs given by the model are wider than the measured values. Figures 6.33 and 6.34 show the comparison between the model prediction following criterion 2 and the measurements. In this case, the settlement troughs are very well characterized (at all three stages of construction), while the lateral deflections at stages II and III are poorly predicted above and below the tunnel elevation. Figures 6.35 to 6.37 show contours of ground displacements predicted by criterion 1 for the three stages of construction.

	Criteria 1				Criteria 2			
	ρ	ν	u_ε [mm]	Ground Loss [%]	ρ	α	u_ε [mm]	Ground Loss [%]
19-May-92	0.18	0.5	-15.9	0.8	0.43	1.80	-129.9	6.1
25-May-92	0.26	0.5	-46.7	2.2	0.50	2.00	-701.8	33.0
28-May-92	0.26	0.5	-58.5	2.8	0.50	2.00	-879.4	41.4

Table 6.1. Ground deformation parameters

The lack of agreement between the model predictions and measurements is primarily due to the fact that the narrowness of the measured settlement trough and the measured inward horizontal displacements at the tunnel springline are inconsistent with the elastic solutions. The elastic solution shows that the effect of increasing relative distortion leads to a narrower settlement trough and lower inward movements at the tunnel springline (even outward movements if relative distortion is high). Given the fact that $K_0 \approx 1.5$ for this case, it is expected that the relative distortion would be low, thus leading to wide settlement troughs and inward movements at the tunnel springline. The monitoring data do show inward movements at the tunnel springline, however, the settlement trough is quite narrow. Hence, there is an inconsistency in the predicted vertical displacements. This may be either due to limitations of the model for this type of soils (heavily overconsolidated and fissured) or due to errors in the measurement of the vertical displacements (unlikely). For example, it is well known that London Clay exhibits quite strong elastic anisotropy with E_h/E_v = 1.3 – 1.4 (Bishop et al., 1960; Wroth, 1971; Simpson, 1999), while recent studies have focused on small strain non-linearity of clay (e.g., Stallebrass, 1990).

In order to assess the consistency of the data from the Heathrow Express Trial tunnel, other reported cases in London Clay are considered. Mair and Taylor (1992) compiled measurements of sub-surface vertical and horizontal movements from several tunnels in London Clay. Most of the reported data corresponds to the Green Park and Regents Park tunnels. These tunnels have an embedment ratio, $R/H \approx 0.07$-0.10 (i.e., deep tunnels) and reported ground losses, $V_L \approx 1.3$-1.4 % (Macklin, 1999). It was found that the vertical and horizontal displacements normalized by the tunnel radius, R, follow a linear trend when plotted against R/r (see Figure 6.38). Figure 6.38 shows the data from the Heathrow Express trial tunnel (corresponding to the completion of the invert, 29-May-92) and the prediction of the analytical model (criteria 1) plotted together with the linear regression by Mair and Taylor (1992). It can be seen that there is a remarkable agreement in the normalized horizontal displacements (both measured and predicted) by the model, while the vertical displacements (both measured and predicted values) are larger than the linear regression. Hence, the horizontal displacements at the Heathrow Express Trial tunnel are consistent with other data, while the vertical displacements are 100% larger. This might serve to explain the discrepancy of the model predictions and monitoring data at the Heathrow Express Trial tunnel. However, most of the reported data for tunnels in London Clay (e.g., Attewell and Farmer, 1974) show very narrow settlement troughs and inward movements at the tunnel springline, which is inconsistent with the elastic solutions.

6.4. Case 4: N-2 Contract for the San Francisco Clean Water Project (Clough et al., 1983)

This tunnel was the first constructed in the U.S. with an Earth Pressure Balance machine (EPB). The soil profile at the site consists of an average 6.6 m thick of rubble fill underlain by 7.1 m of soft sediment (known as Recent Bay Mud) followed by a stratum of colluvial and residual sandy clay (Figure 6.39). The tunnel was driven entirely trough the soft sediments, which are normally consolidated except near the top of the stratum, where they have been lightly overconsolidated by desiccation. Given the fact that the soil is normally consolidated, a high value of relative distortion, ρ, is to be expected. The tail void was around 7.6 cm thick (assuming no pitching of the TBM) and was filled with pressurized grouting. However, during construction, it was noticed that the soil tended to fill the gap before grouting was injected (Clough et al., 1983). Hence, the expected displacement at the tunnel crown, $u_c = u_\varepsilon - u_\delta + \Delta u_z$ (see Figure 3.2) is in the range of 7 cm. The depth to centerline is $H \approx 10$ m and the radius, $R = 1.78$ m, hence, the embedment ratio is, $R/H = 0.178$.

Figures 6.40 and 6.41 show the observed surface settlements and lateral deflections measured by an inclinometer located at an offset of $x/R = 2.02$ ($\approx$2.0). It can be seen that surface settlements were only measured in the range where -5 m $< x <$ 5 m, for which u_x^I cannot be obtained. However, the analysis method can still be applied if a Poisson ratio is assumed. Given that the soil is a soft clay, a Poisson ratio of $\nu = 0.5$ (i.e., undrained behavior) will be used. The horizontal displacement $2 \cdot R$ away from the tunnel springline is found to be $u_x^0 = 20.8$ mm and the surface settlement at $x = 0$, $u_y^0 = -30.6$ mm. Figures 6.42 and 6.43 show the horizontal displacement ratio plotted in the design charts for $R/H = 0.15$ and $R/H = 0.20$, respectively. By assuming $\nu = 0.5$, the relative distortion is found to be (after linear interpolation) $\rho = 1.66$, which is consistent with a low value of K_0. Figures 6.44 and 6.45 show the value obtained for the relative distortion and the assumed Poisson ratio plotted in the design charts, from where the uniform convergence displacement is obtained as $u_\varepsilon = -20$ mm, with a corresponding ground loss, $V_L = 2.2\%$.

It is interesting to see the value of the crown displacement predicted by the model and compare its value with the estimated tail void thickness. The uniform convergence displacement, $u_\varepsilon = -20$

mm, which implies a downward movement of $\Delta u_{z\,(\varepsilon)}$ = -3.5 mm (see Figure 3.20). The pure distortion displacement, u_δ = 33.2 mm, which implies a downward movement of $\Delta u_{z\,(\delta)}$ = -5.6 mm (see Figure 3.26). Hence, the displacement at the tunnel crown is u_c = 6.2 cm, which is comparable to the tail void thickness.

Figures 6.46 and 6.47 show comparisons between model predictions and measurements, where it can be seen that there is excellent agreement with the measured surface settlements and inclinometer deflections. Figure 6.48 shows contours of ground displacements predicted by the model.

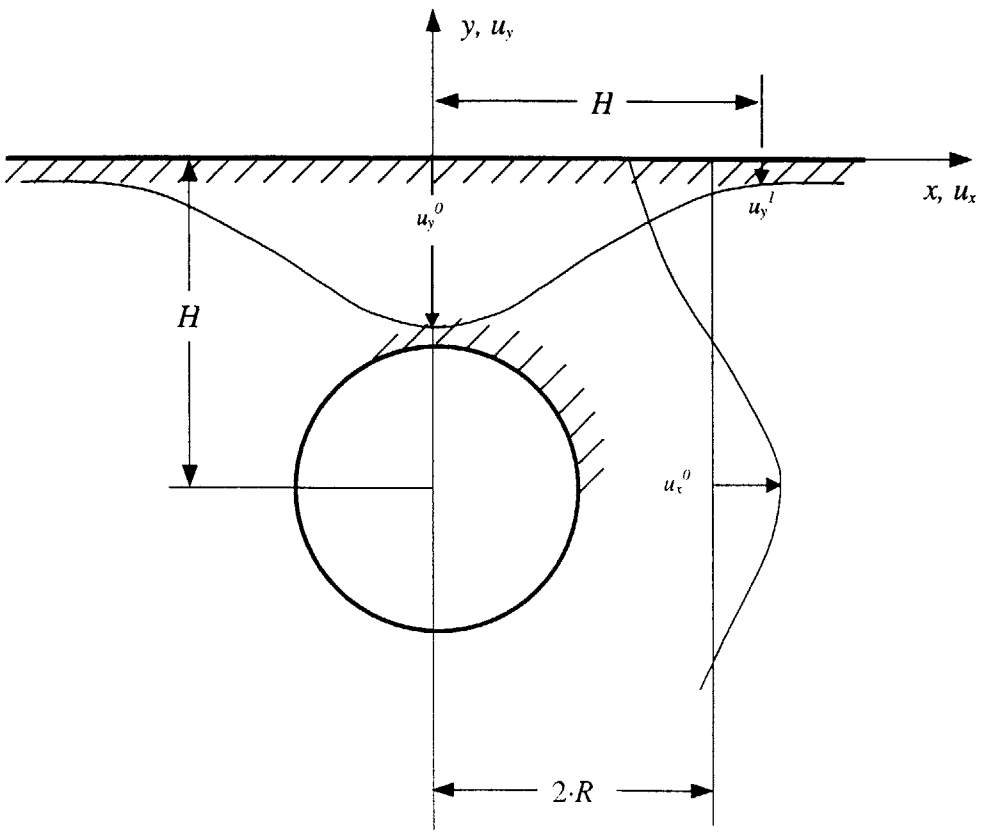

Figure 6.1. Definition of the input parameters for the proposed design charts

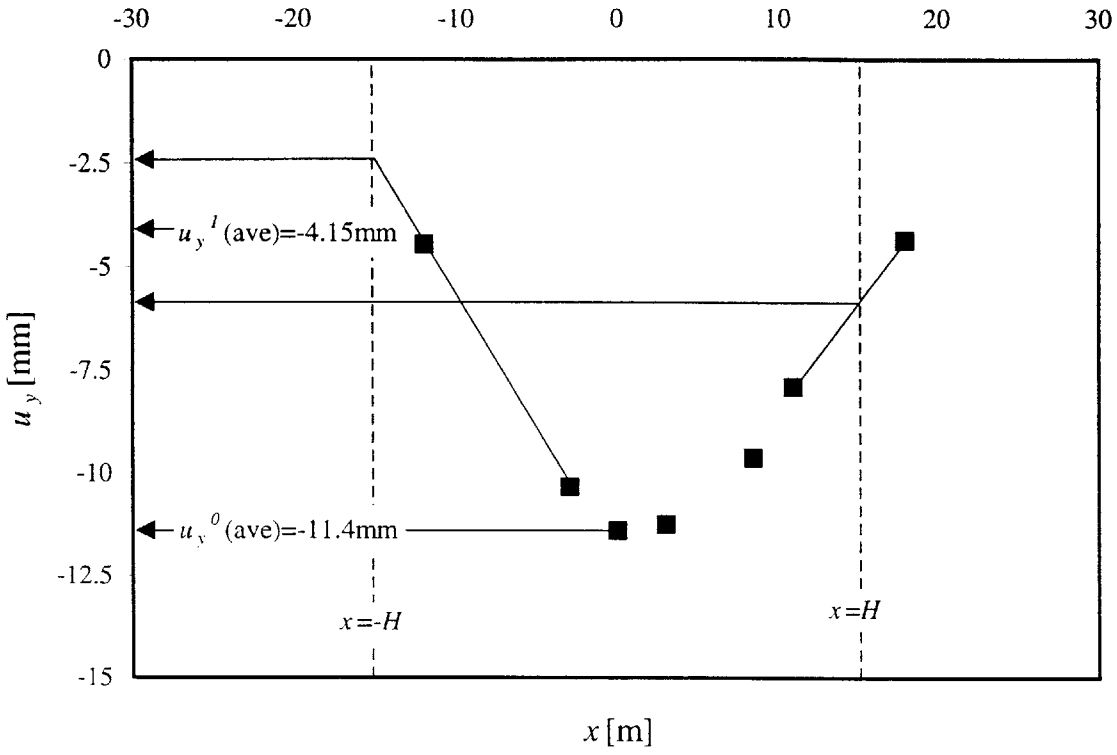

Figure 6.2. Case 1: Madrid Metro - Measured surface settlements

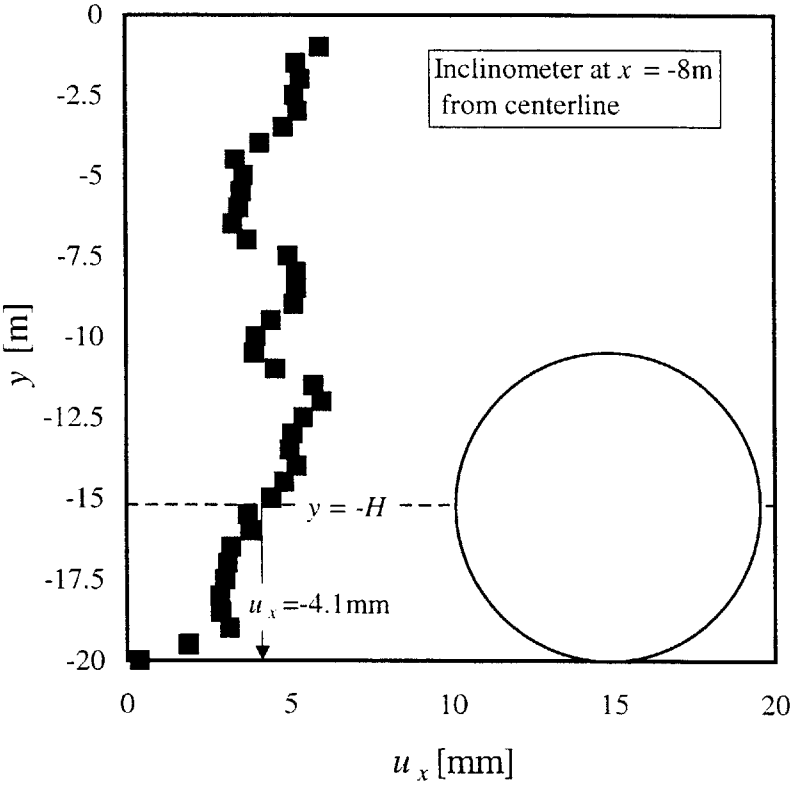

Figure 6.3. Case 1: Madrid Metro - Measured horizontal displacements at x = -8 m

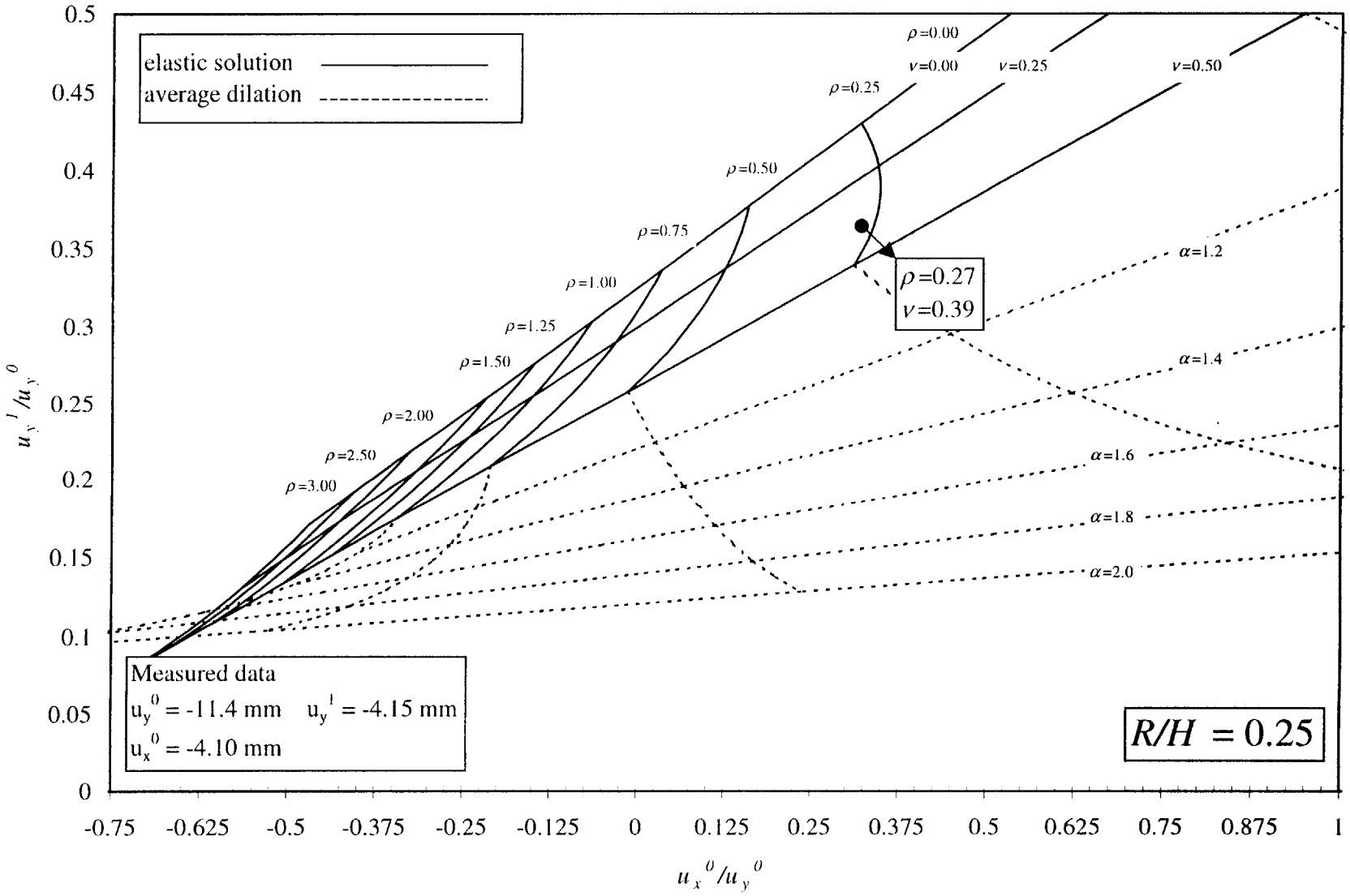

Figure 6.4. Case 1: Madrid Metro - Derivation of parameters ρ, ν

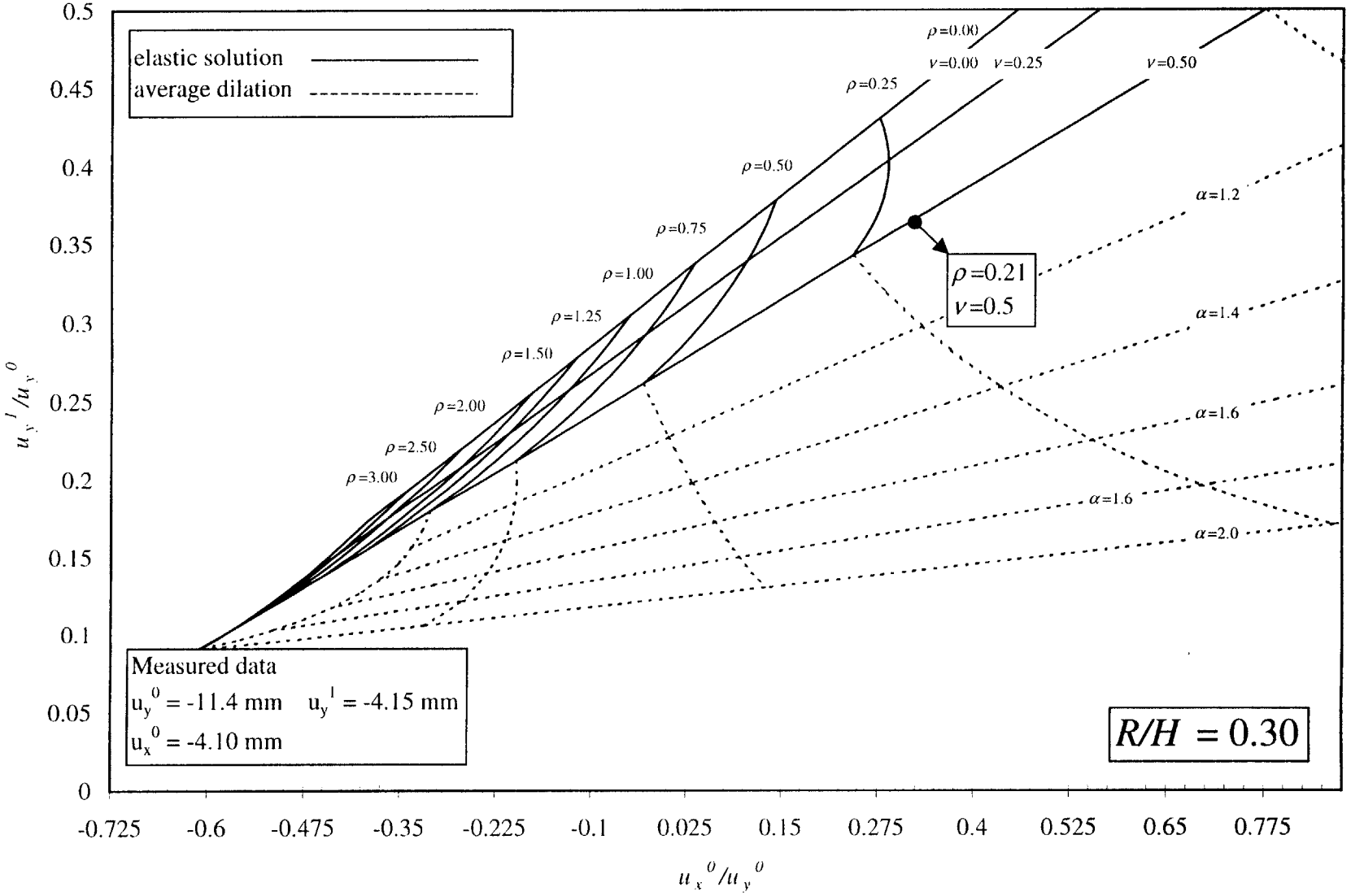

Figure 6.5. Case 1: Madrid Metro - Derivation of parameters ρ, ν

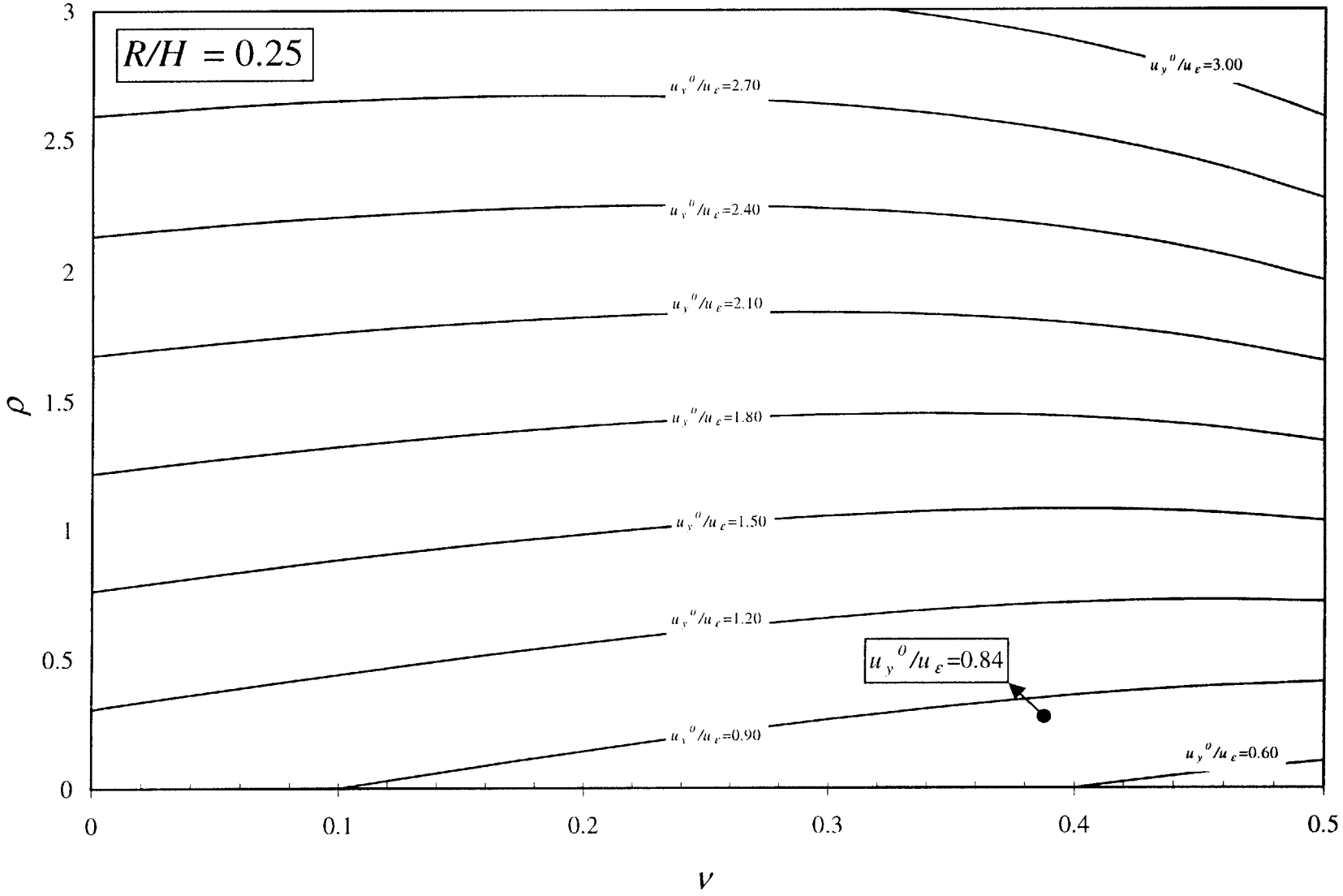

Figure 6.6. Case 1: Madrid Metro - Derivation of parameter u_y^0/u_ε

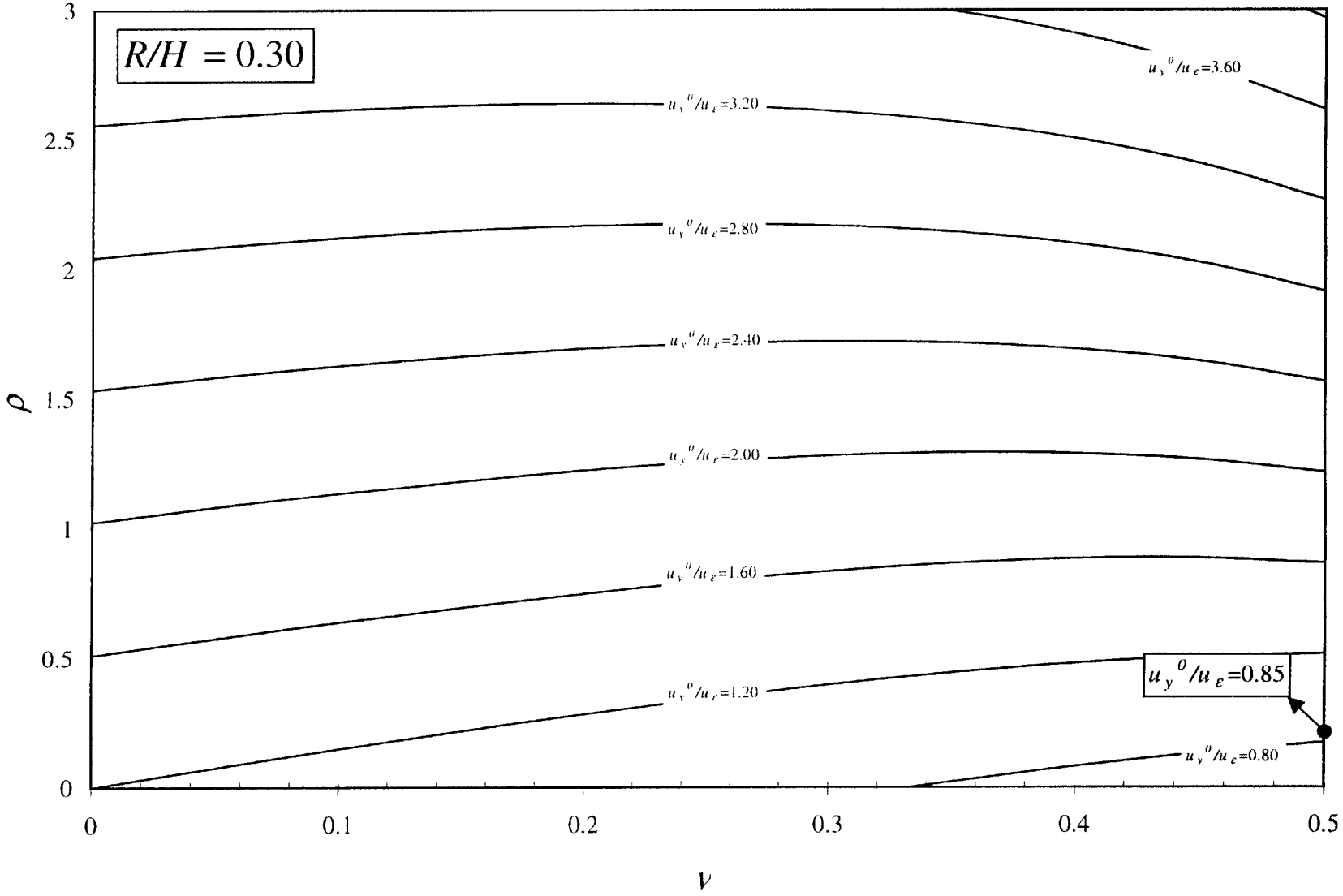

Figure 6.7. Case 1: Madrid Metro - Derivation of parameter u_y^0/u_ε

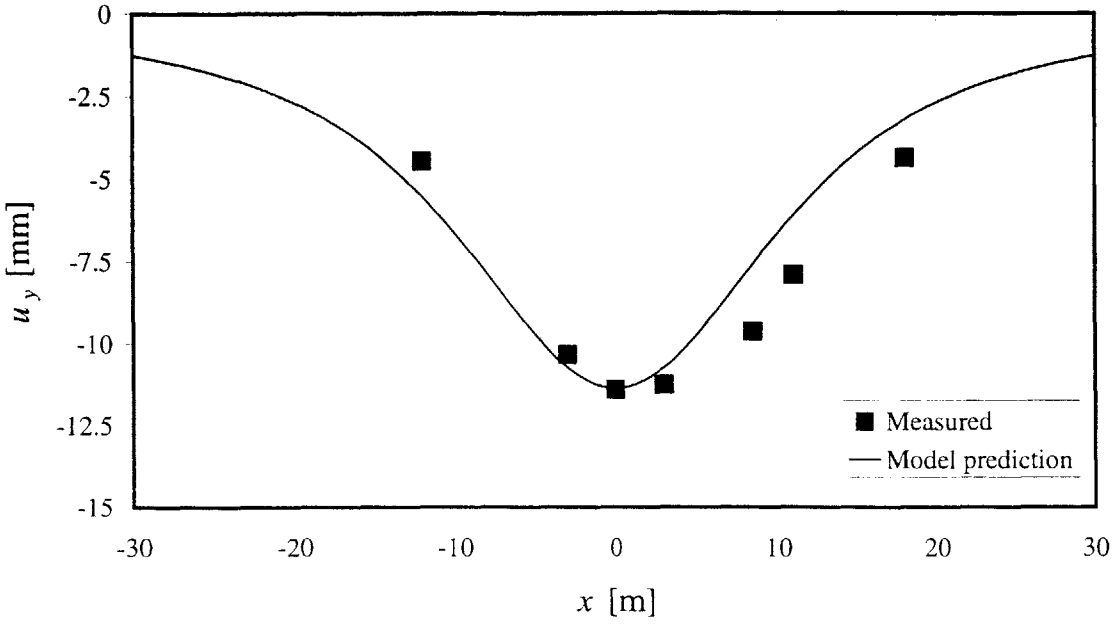

Figure 6.8. Case 1: Madrid Metro - Surface settlements

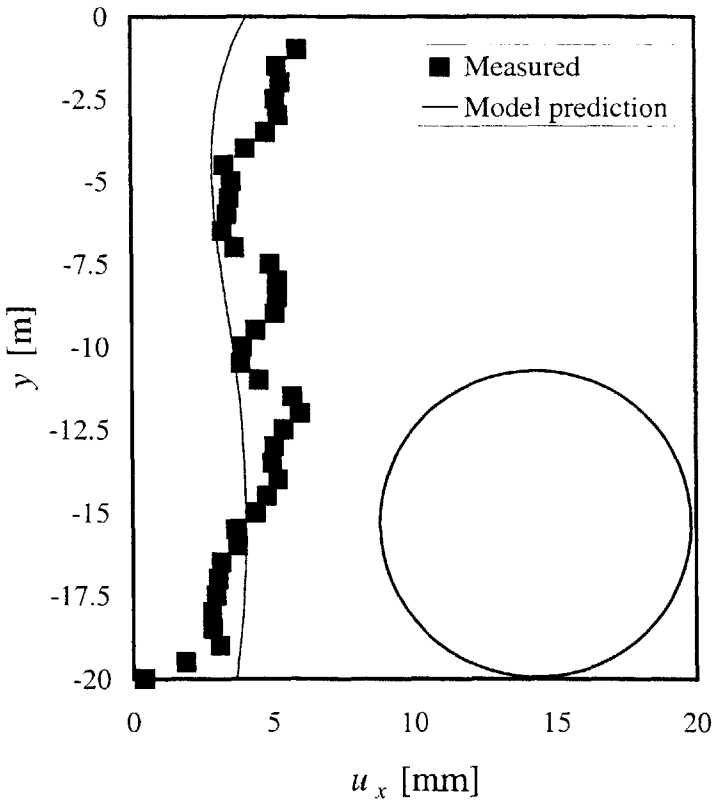

Figure 6.9. Case 1: Madrid Metro - Horizontal displacements

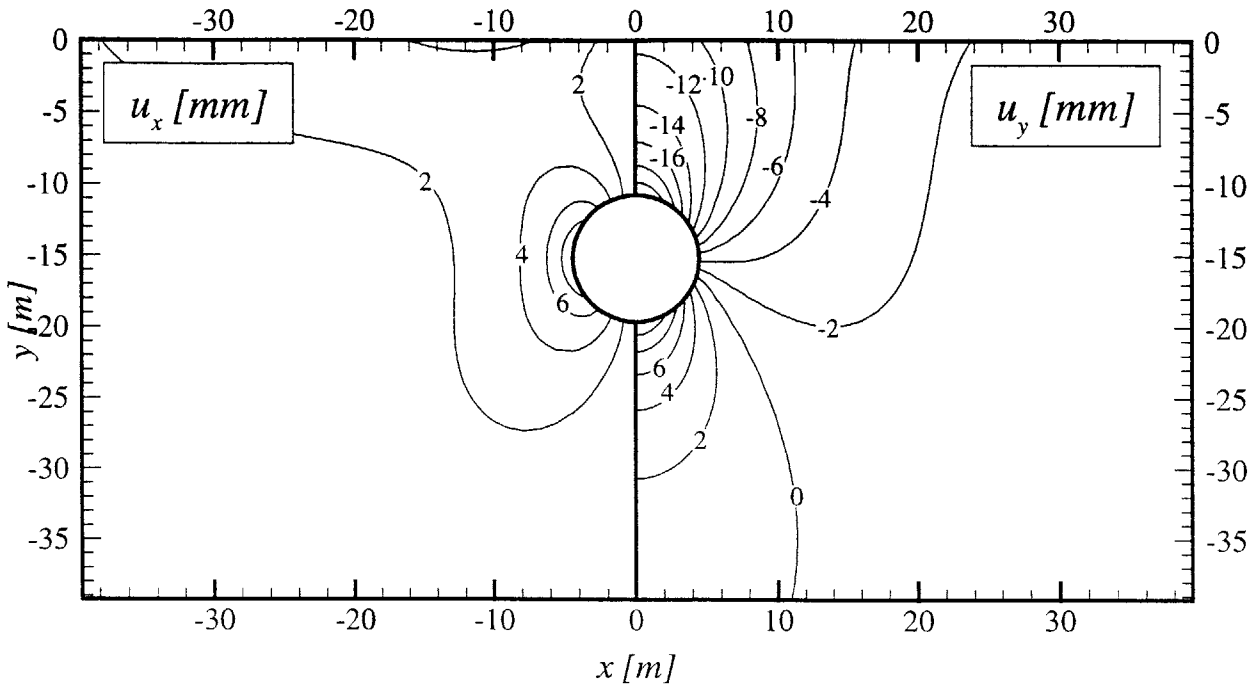

Figure 6.10. Case 1: Madrid Metro - Contours of predicted ground displacements

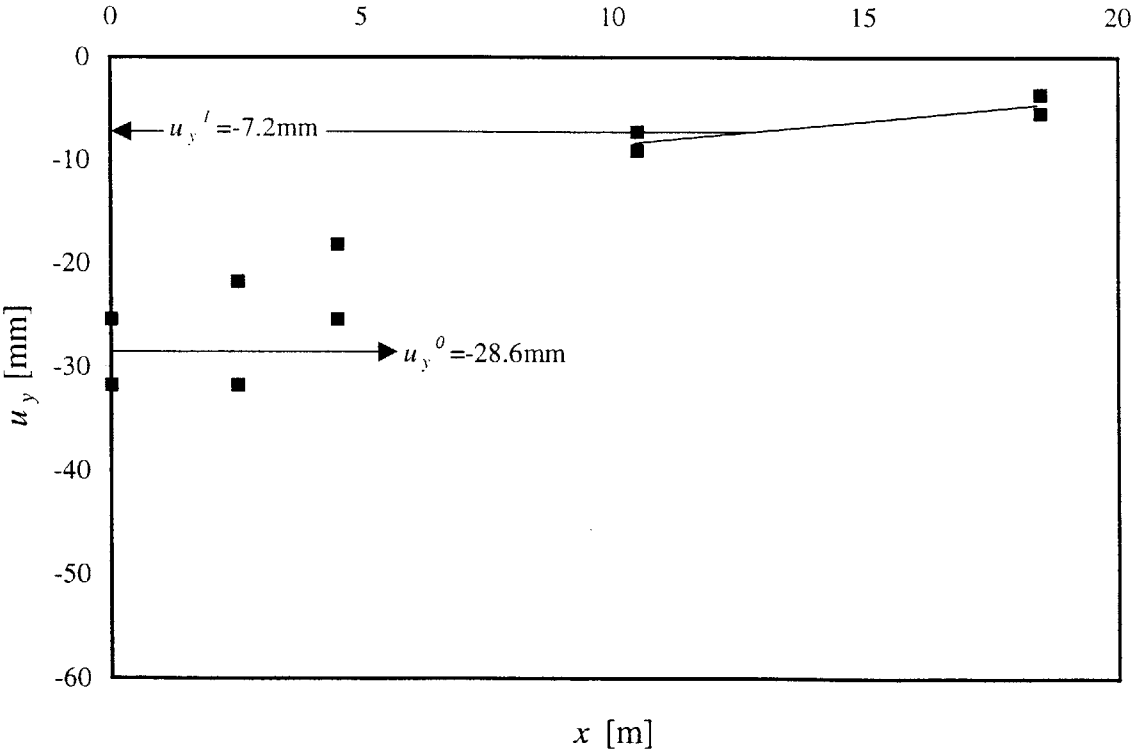

Figure 6.11. Case 2: Sewer-line tunnel in Mexico City - Measured surface settlements

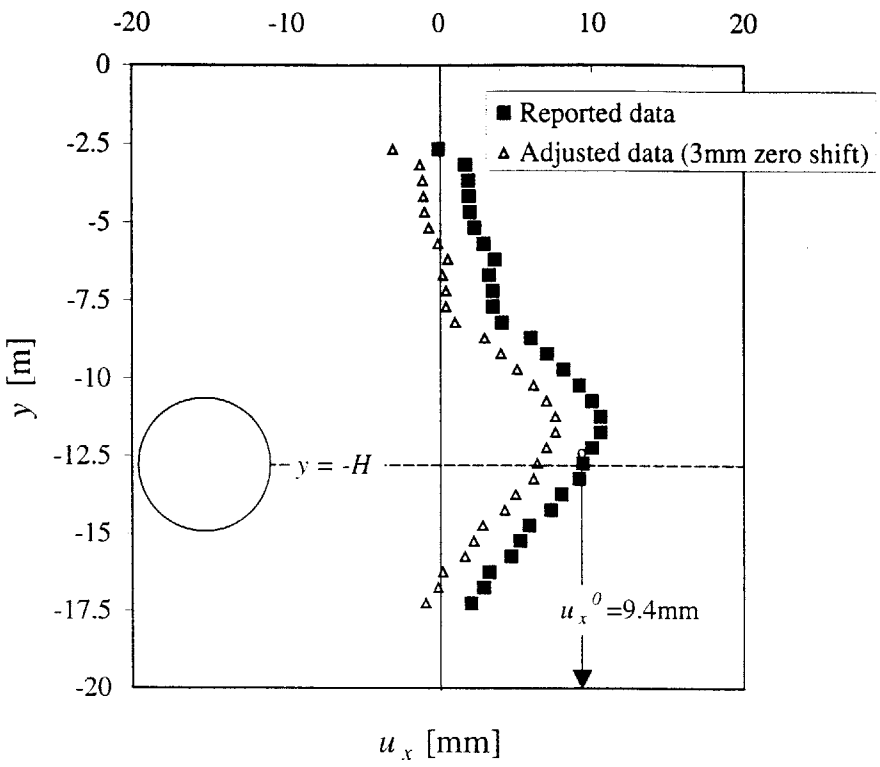

Figure 6.12. Case 2: Sewer-line tunnel in Mexico City - Measured horizontal displacements at $x = 4.5$ m

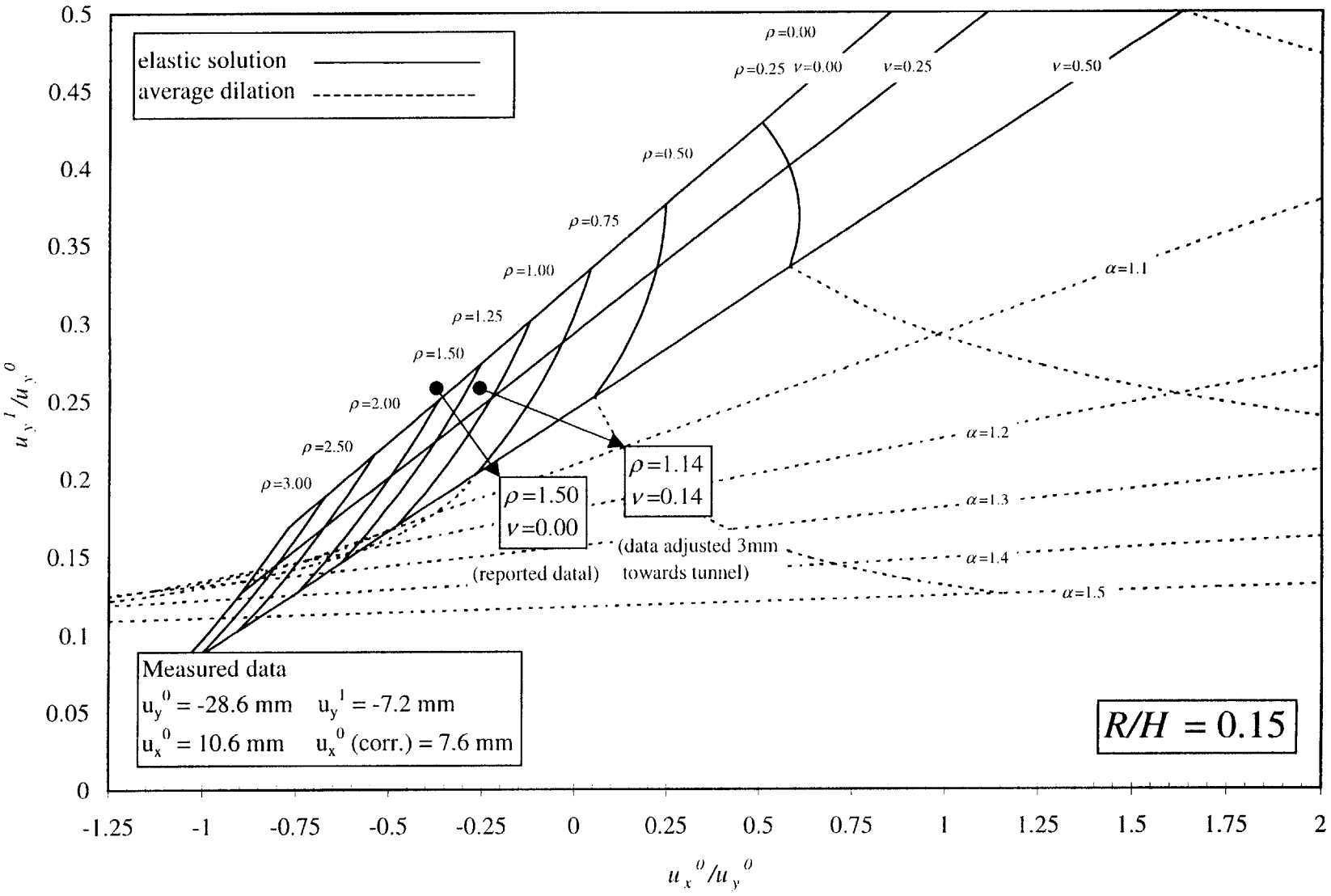

Figure 6.13. Case 2: Sewer-line tunnel in Mexico City – Derivation of parameters ρ, ν

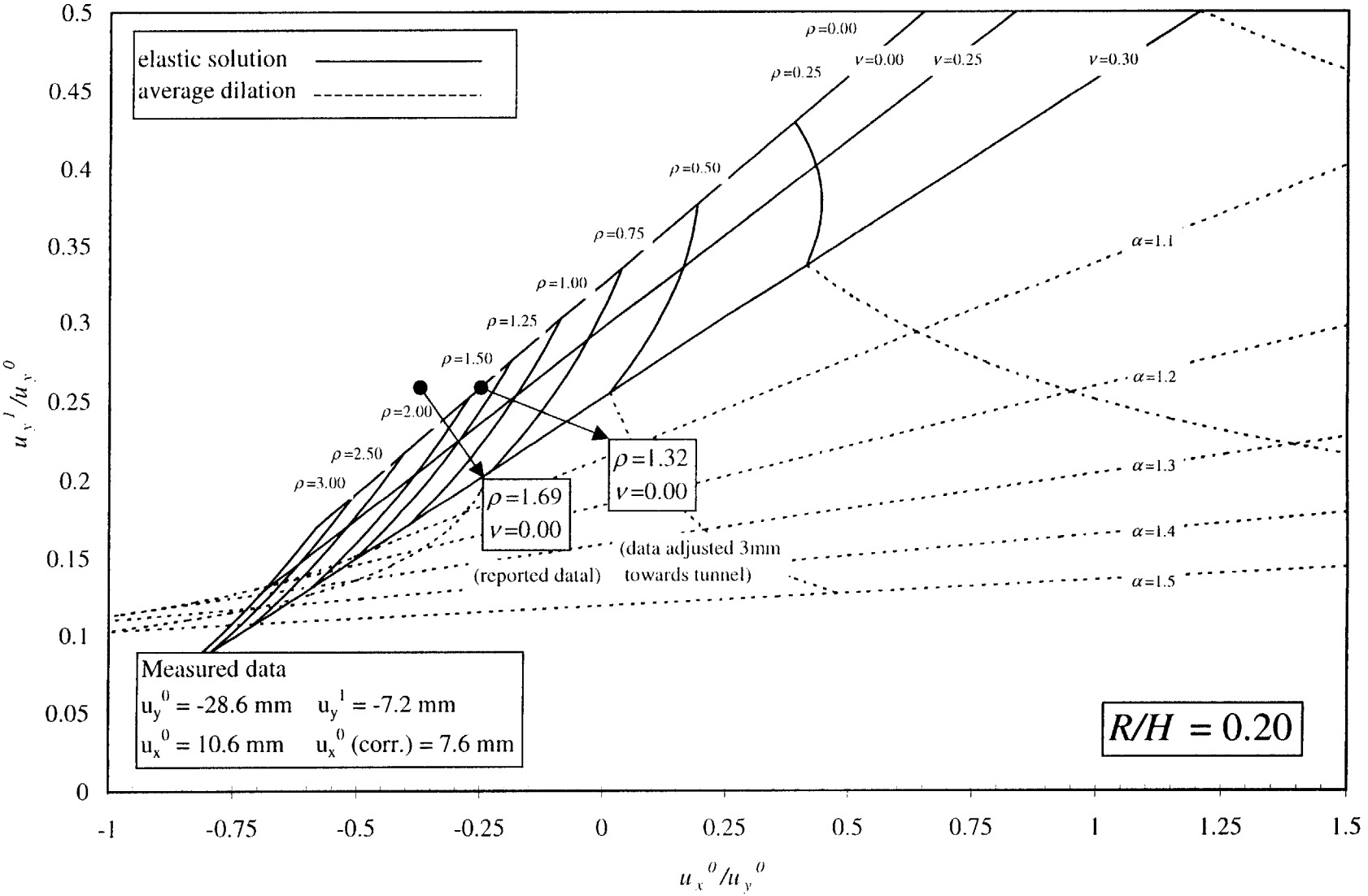

Figure 6.14. Case 2: Sewer-line tunnel in Mexico City – Derivation of parameters ρ, ν

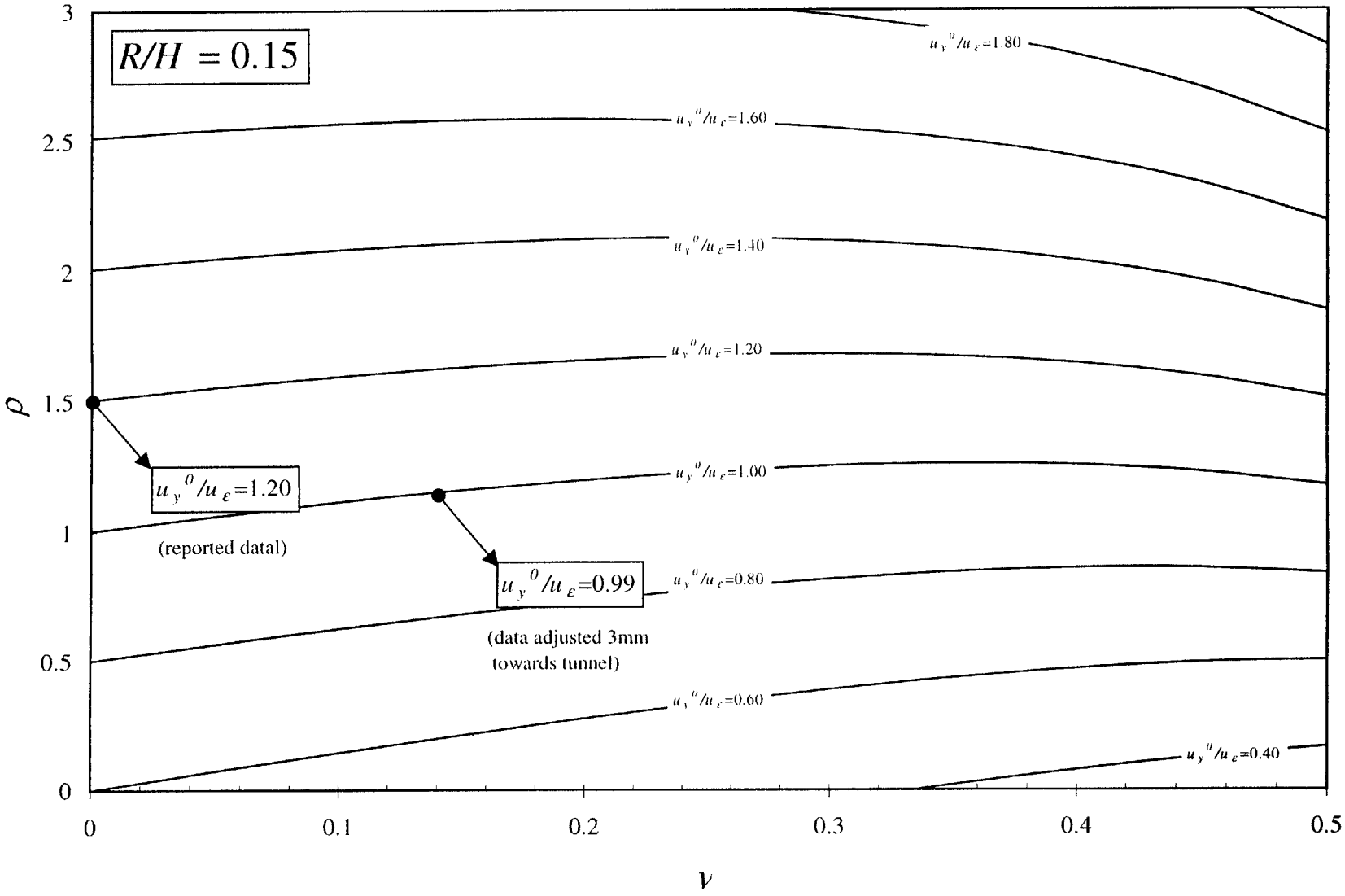

Figure 6.15. Case 2: Sewer-line tunnel in Mexico City – Derivation of parameter u_y^0/u_ε

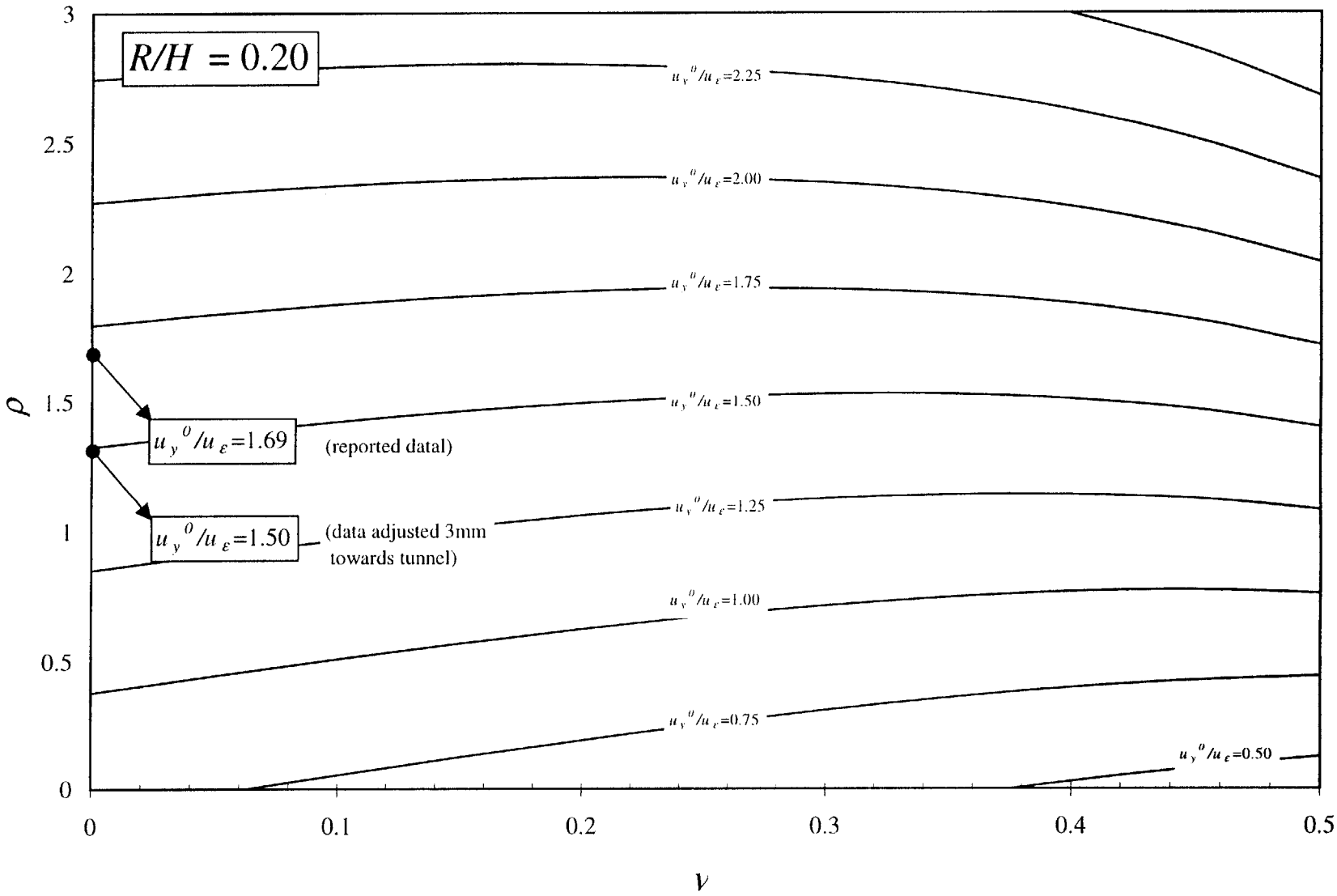

Figure 6.16. Case 2: Sewer-line tunnel in Mexico City – Derivation of parameter u_y^0/u_ε

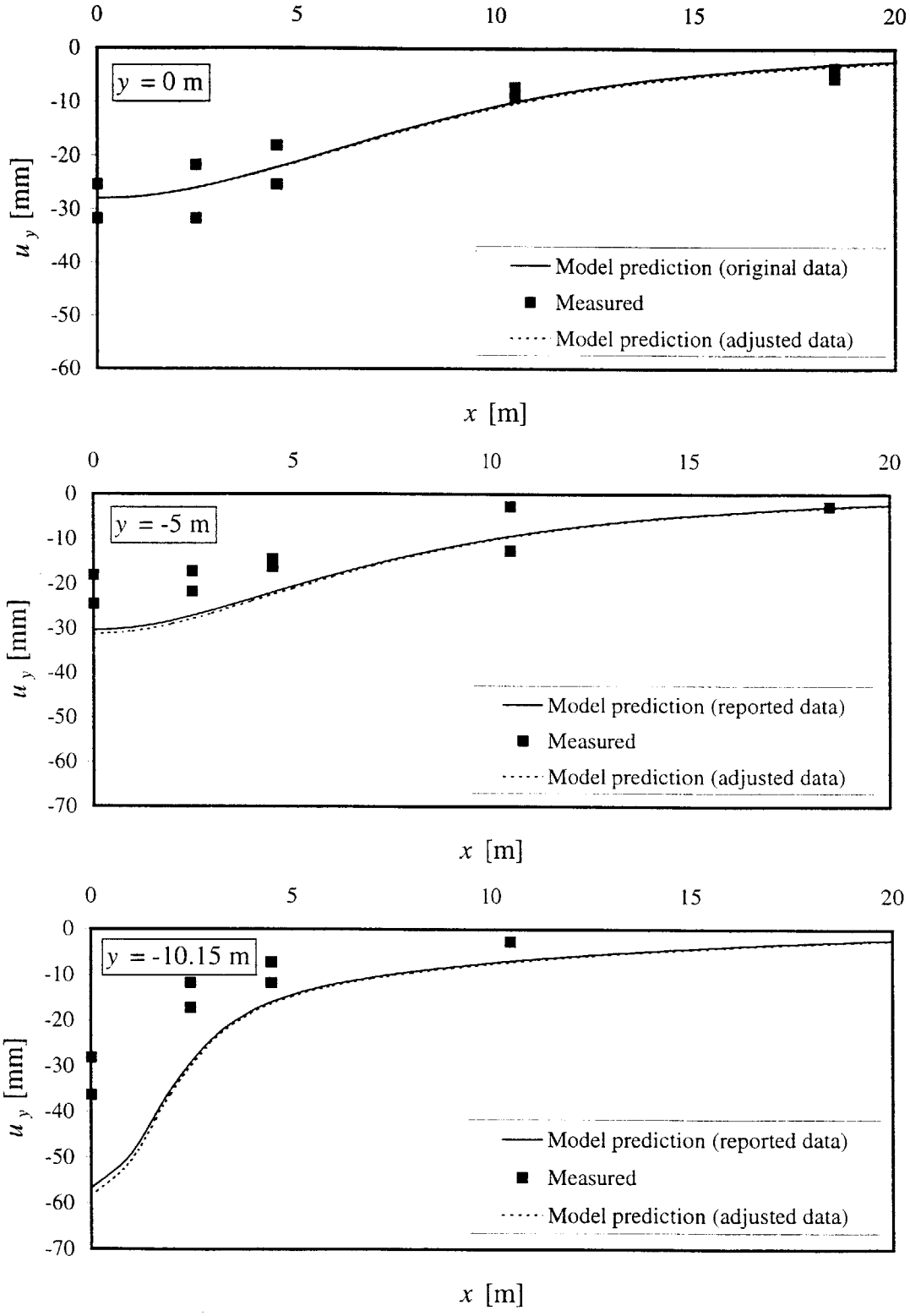

Figure 6.17. Case 2: Sewer-line tunnel in Mexico City – Vertical displacements

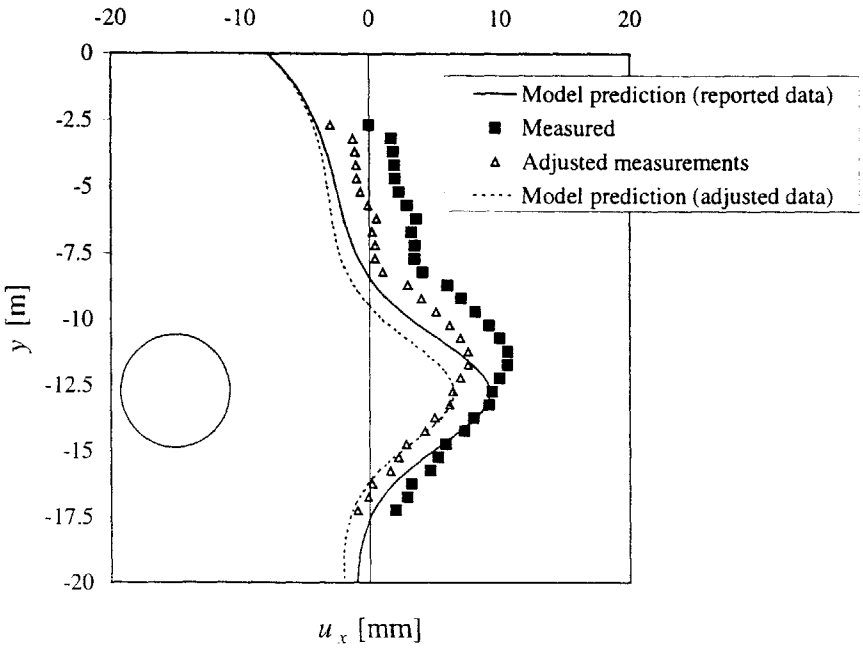

Figure 6.18. Case 2: Sewer-line tunnel in Mexico City – Horizontal displacements

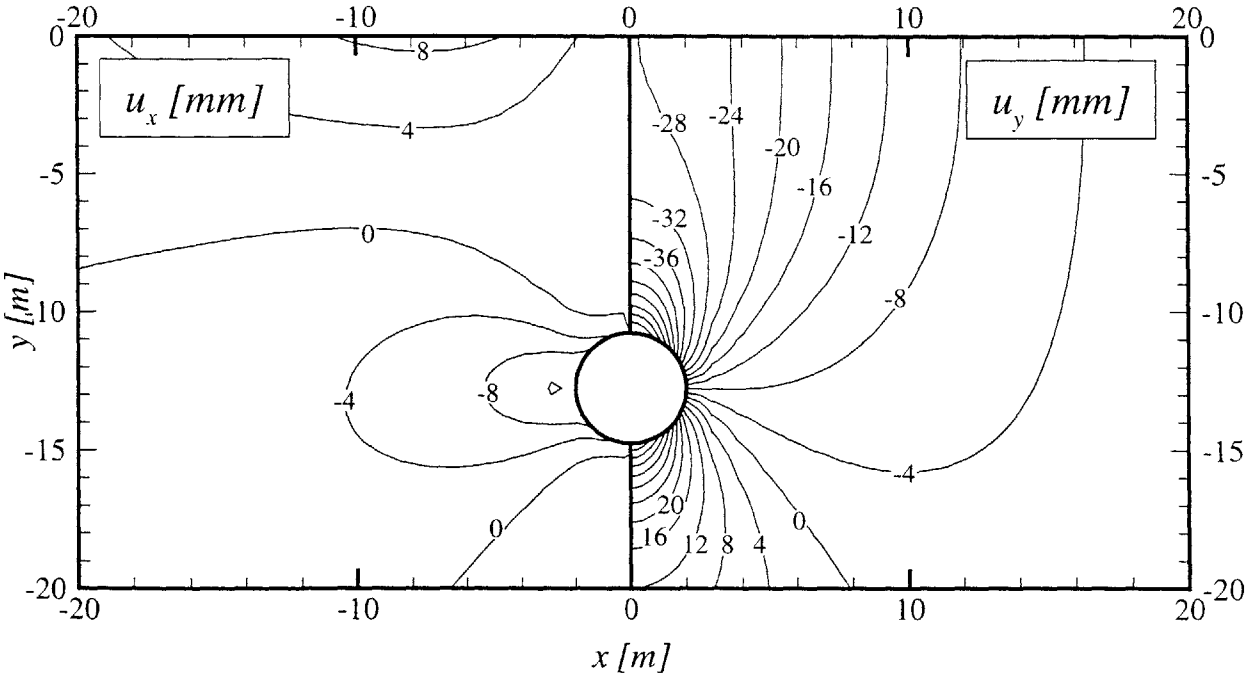

Figure 6.19. Case 2: Sewer-line tunnel in Mexico City – Contours of predicted ground displacements (based on fit to reported data)

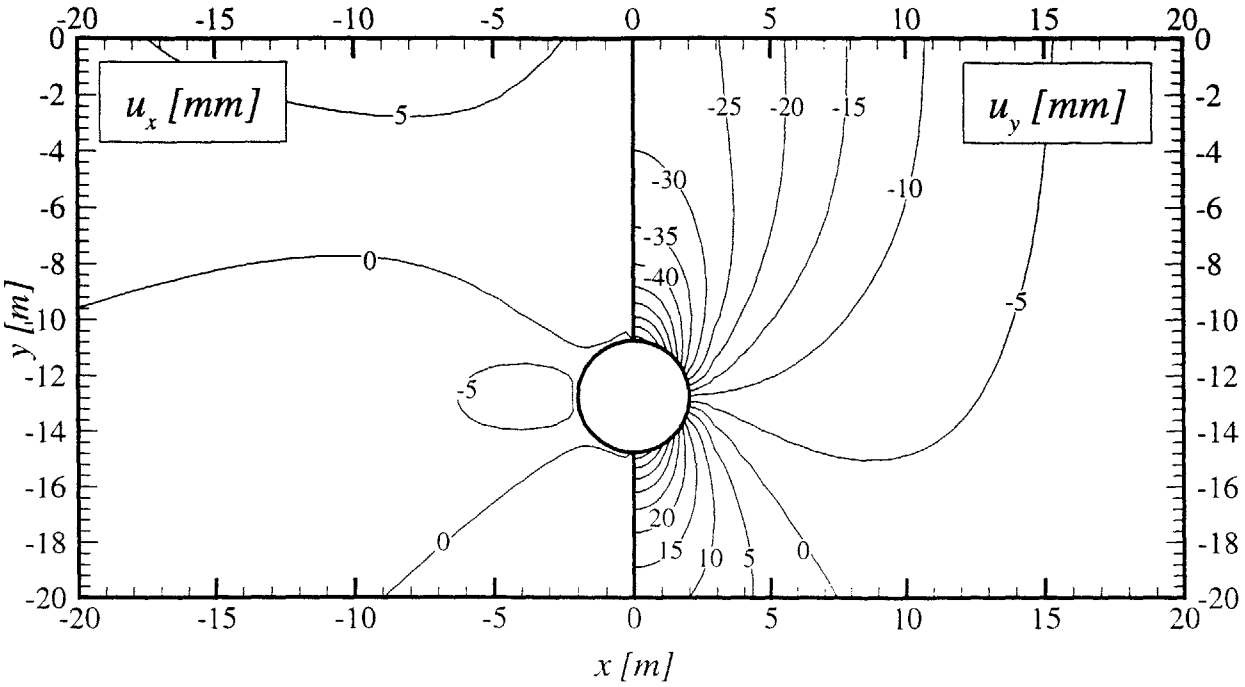

Figure 6.20. Case 2: Sewer-line tunnel in Mexico City – Contours of predicted ground displacements (based on fit to adjusted data)

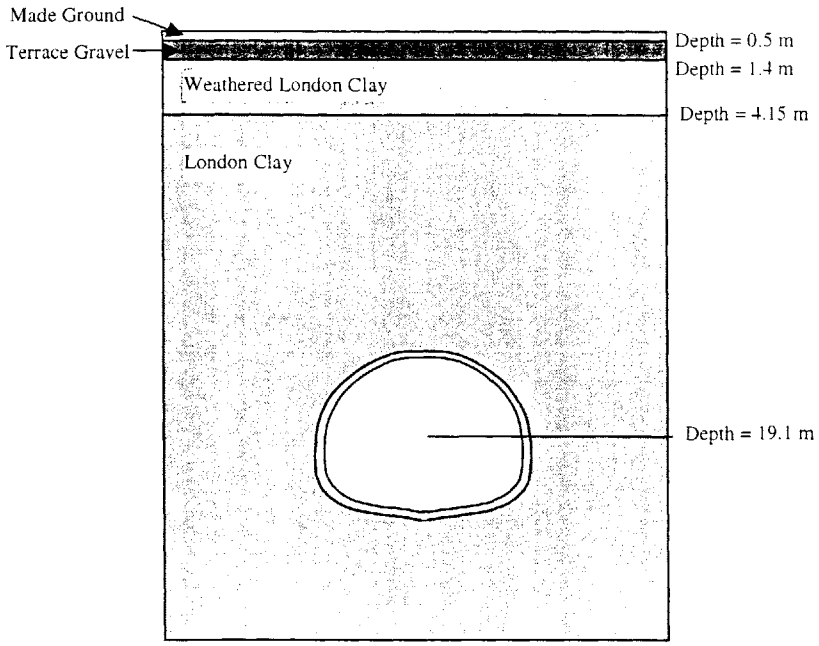

Figure 6.21. Case 2: Heathrow Express Trial Tunnel– Soil Profile

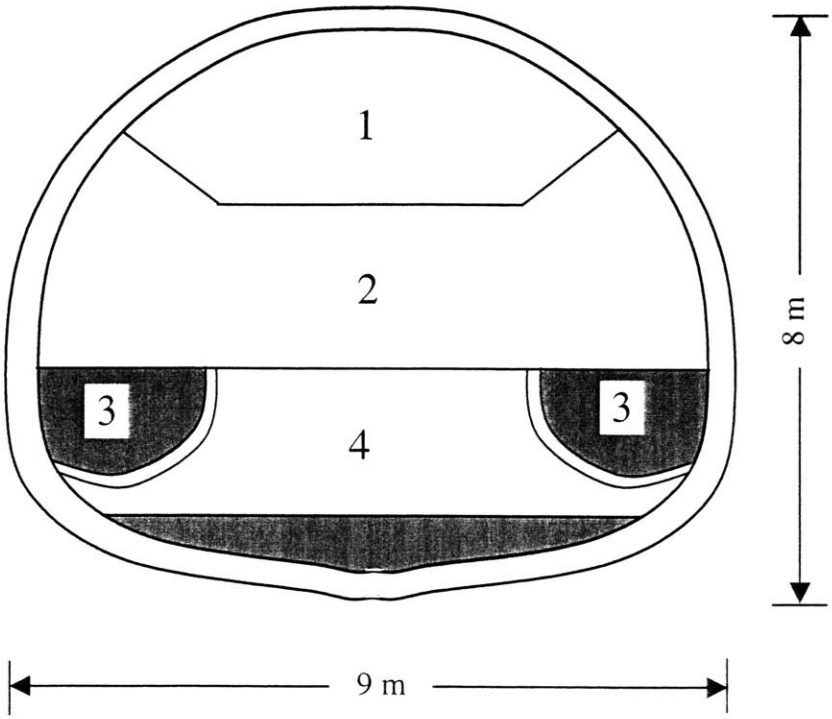

Figure 6.22. Case 2: Heathrow Express Trial Tunnel– Cross section and excavation sequence (*Type three*)

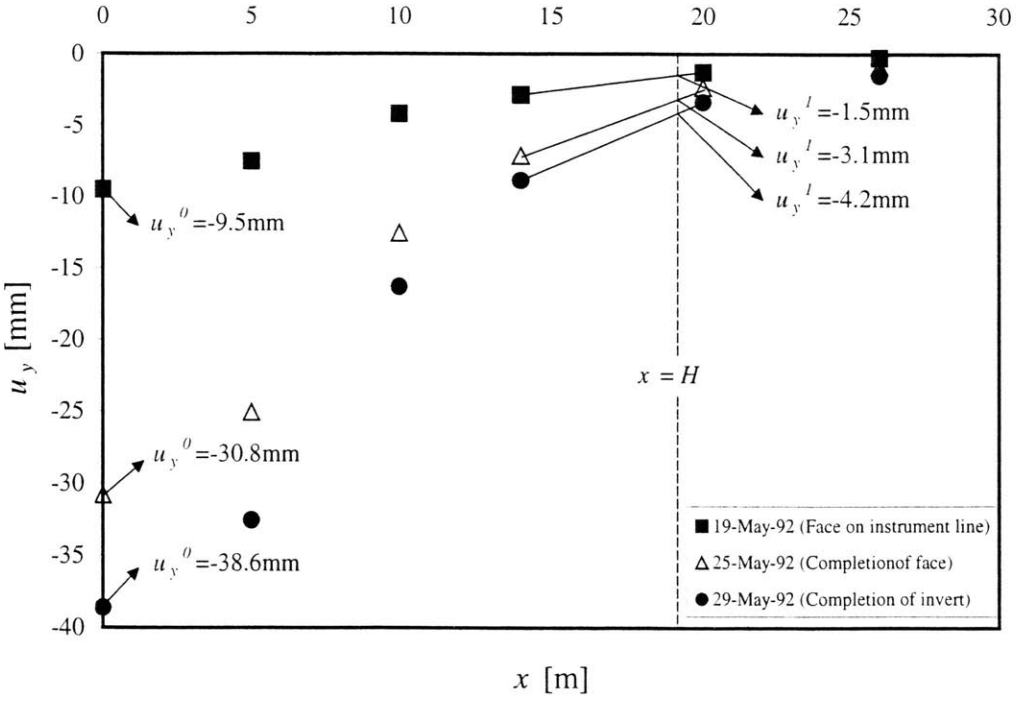

Figure 6.23. Case 3: Heathrow Express Trial Tunnel - Measured surface settlements

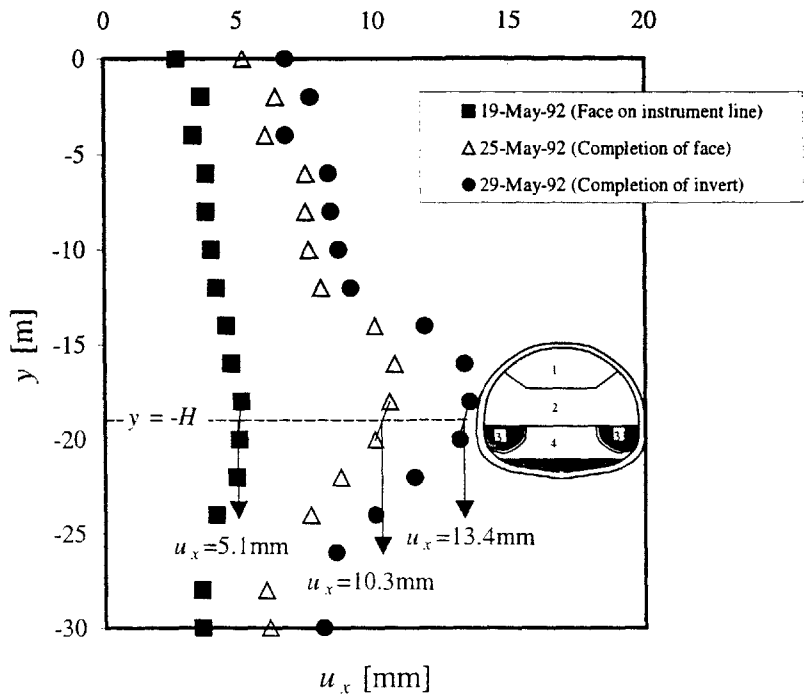

Figure 6.24. Case 3: Heathrow Express Trial Tunnel - Measured horizontal displacements at x = -9 m

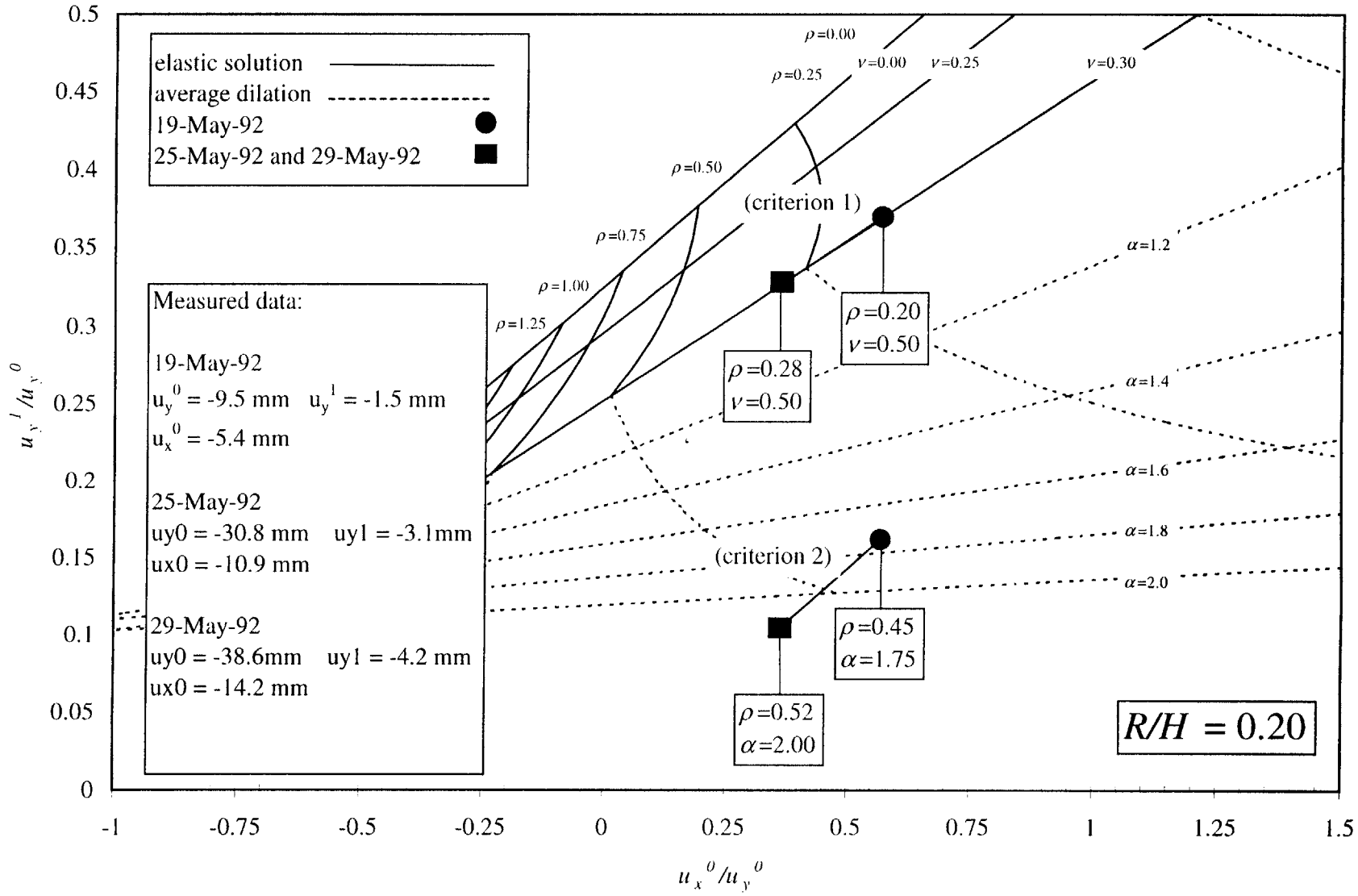

Figure 6.25. Case 3: Heathrow Express Trial Tunnel – Derivation of parameters ρ, ν

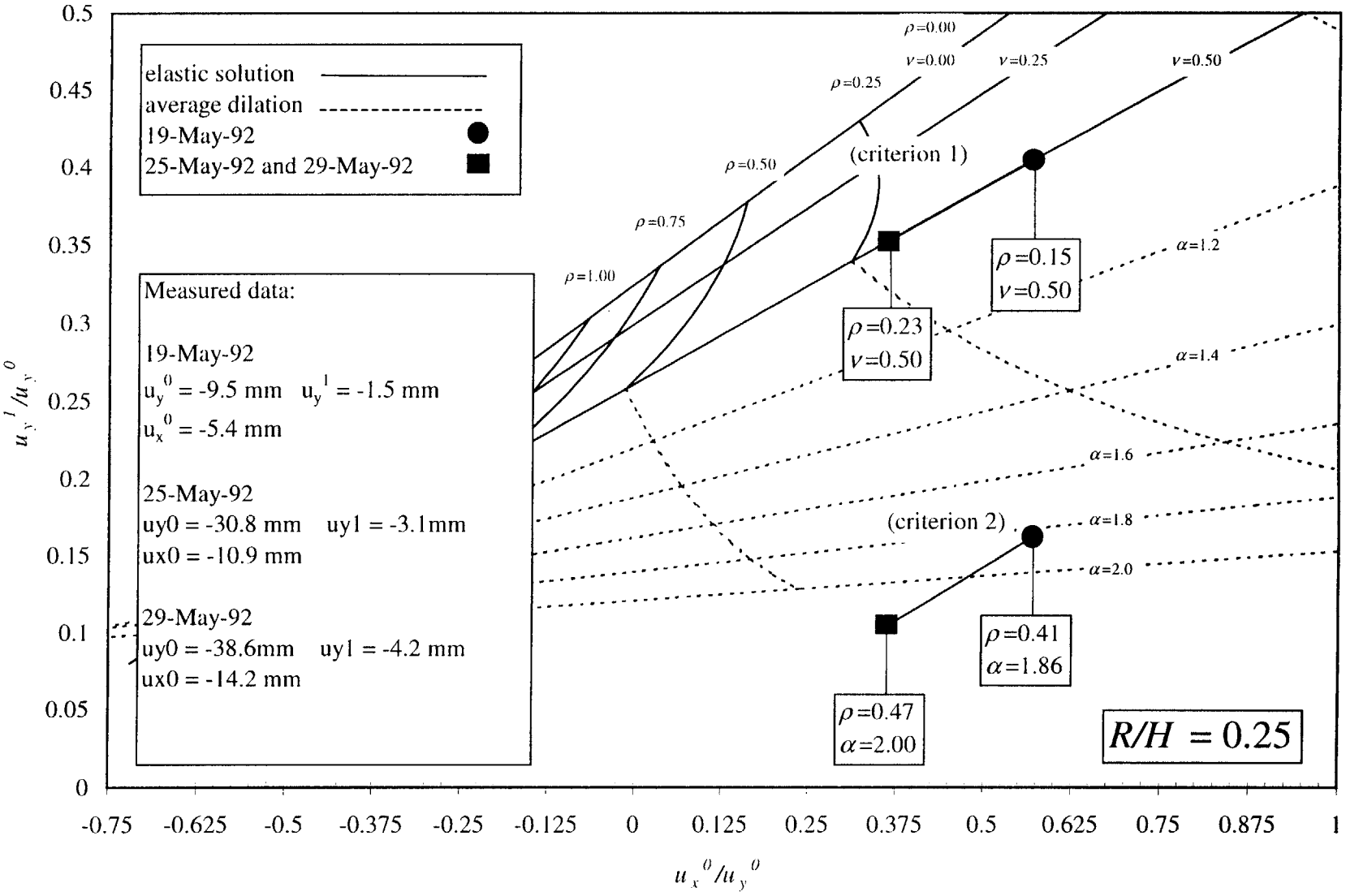

Figure 6.26. Case 3: Heathrow Express Trial Tunnel – Derivation of parameters ρ, ν

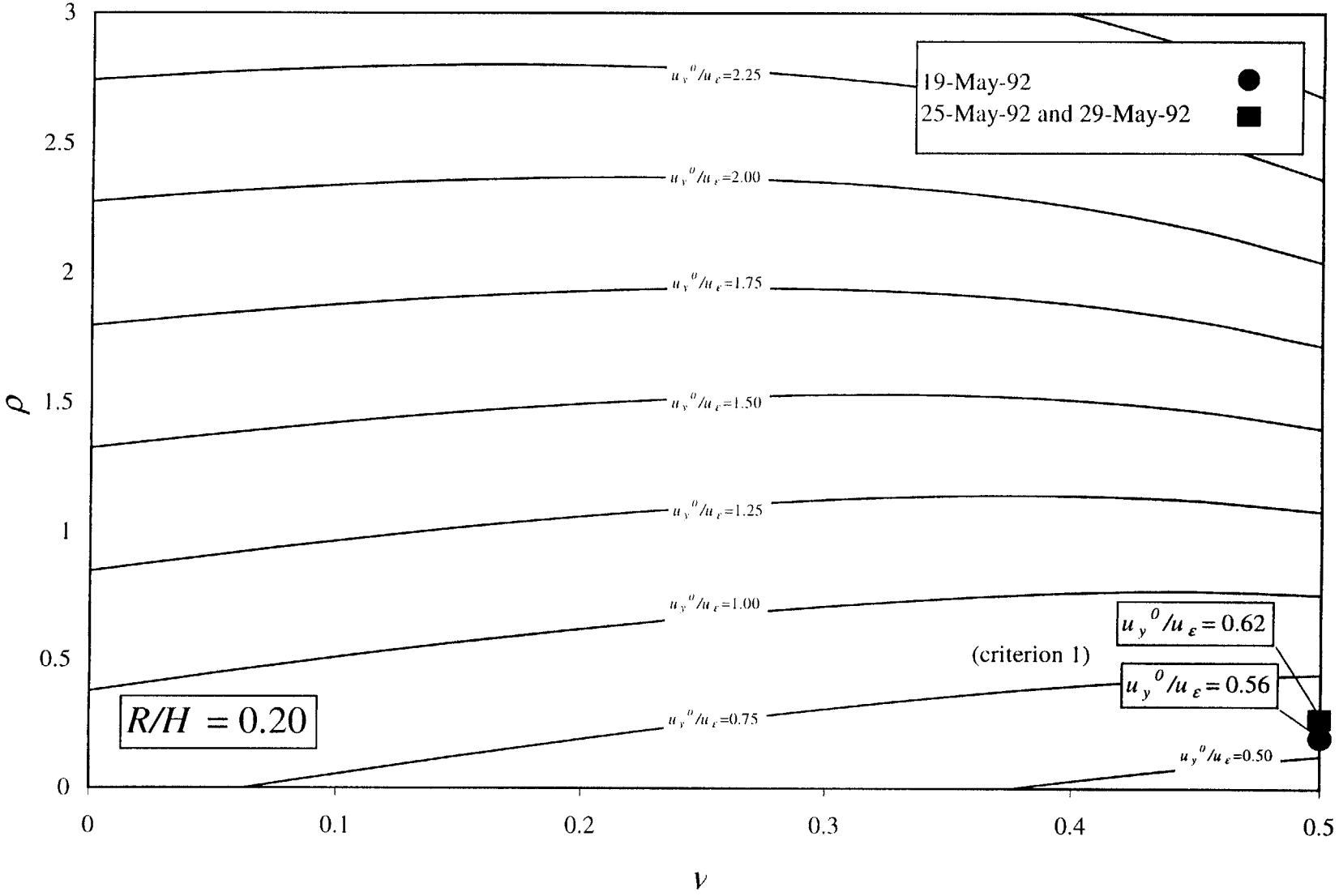

Figure 6.27. Case 3: Heathrow Express Trial Tunnel – Derivation of parameter u_y^0/u_ε (criterion 1)

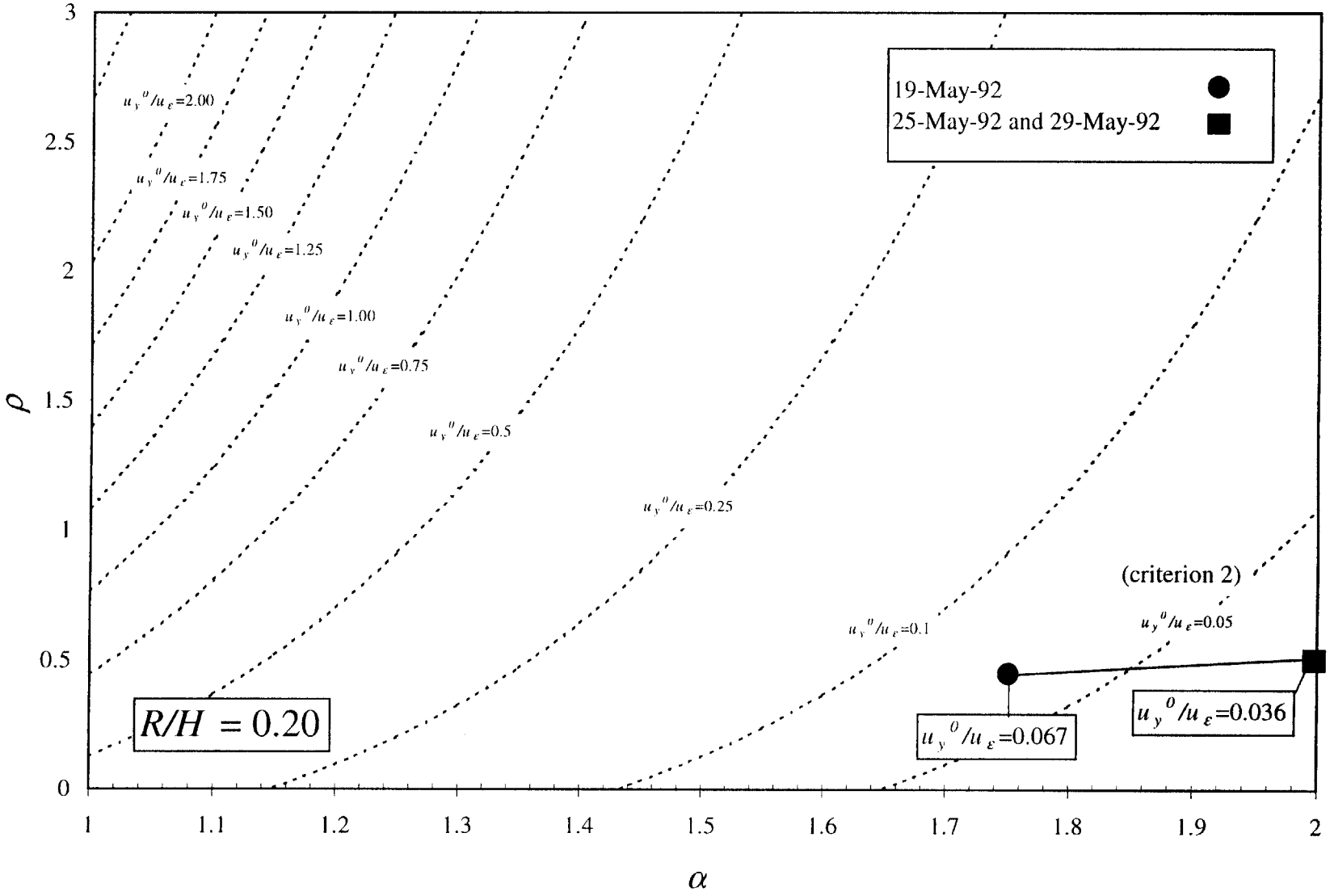

Figure 6.28. Case 3: Heathrow Express Trial Tunnel – Derivation of parameter u_y^0/u_ε (criterion 2)

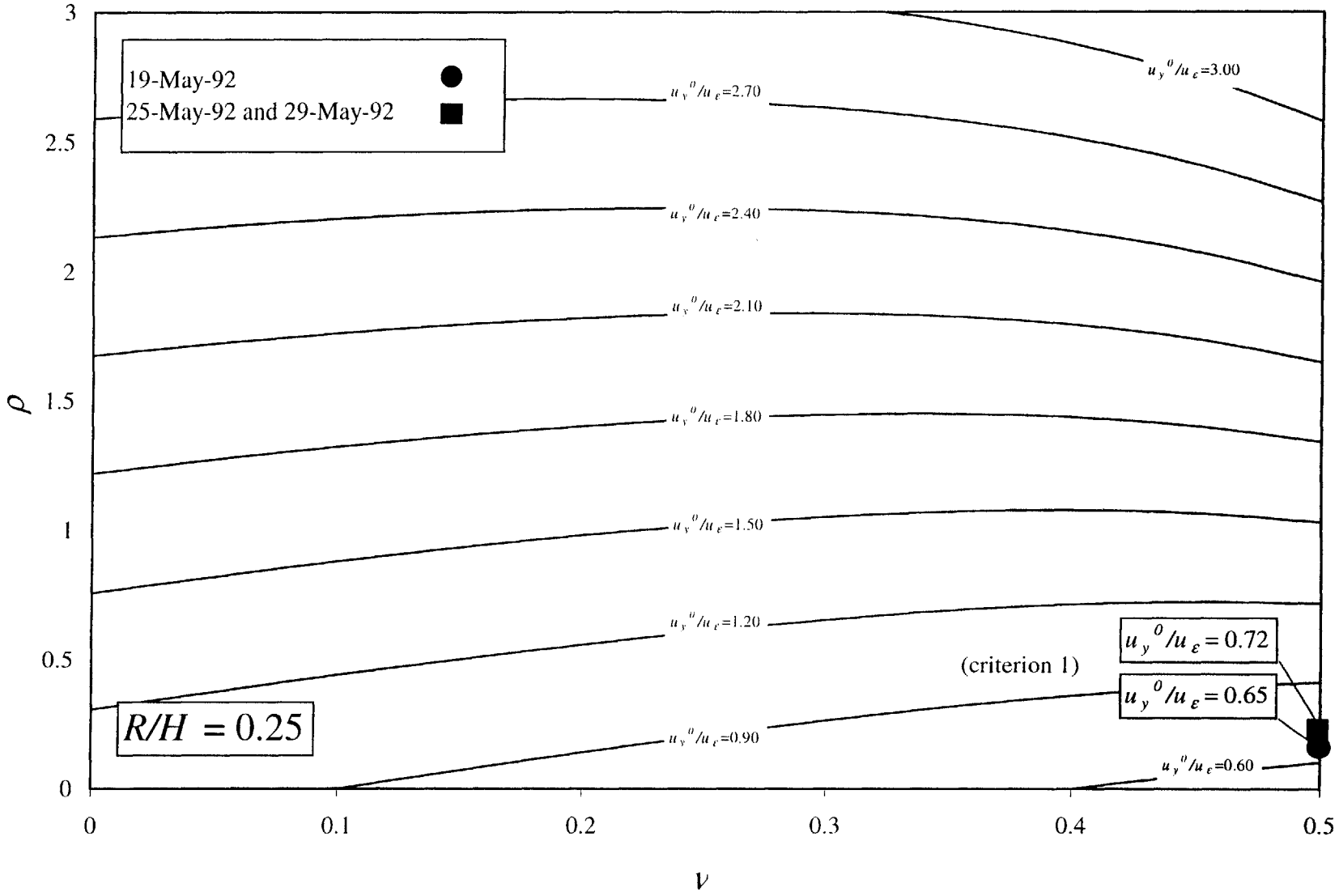

Figure 6.29. Case 3: Heathrow Express Trial Tunnel – Derivation of parameter u_y^0/u_ε (criterion 1)

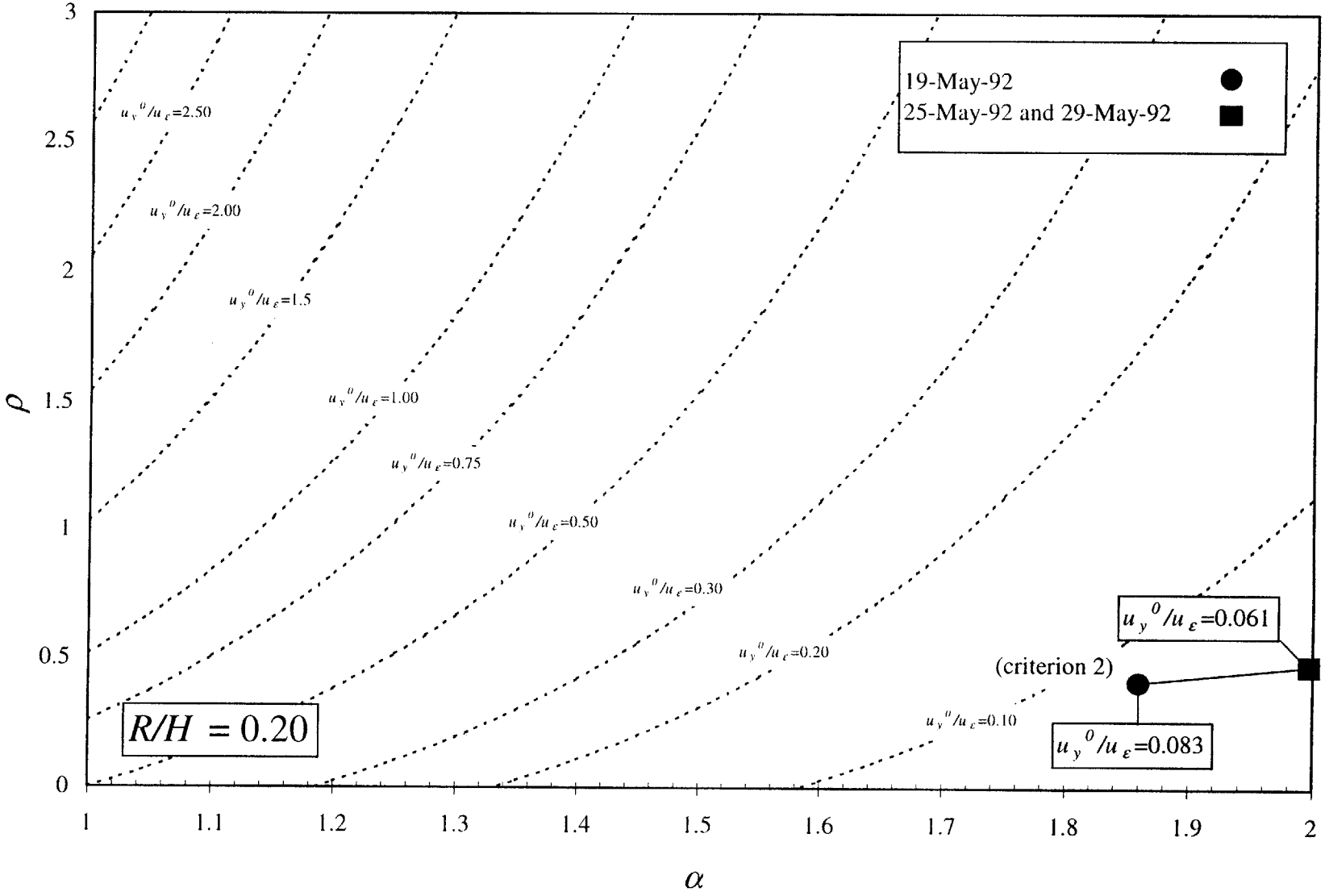

Figure 6.30. Case 3: Heathrow Express Trial Tunnel – Derivation of parameter u_y^0/u_ε (criterion 2)

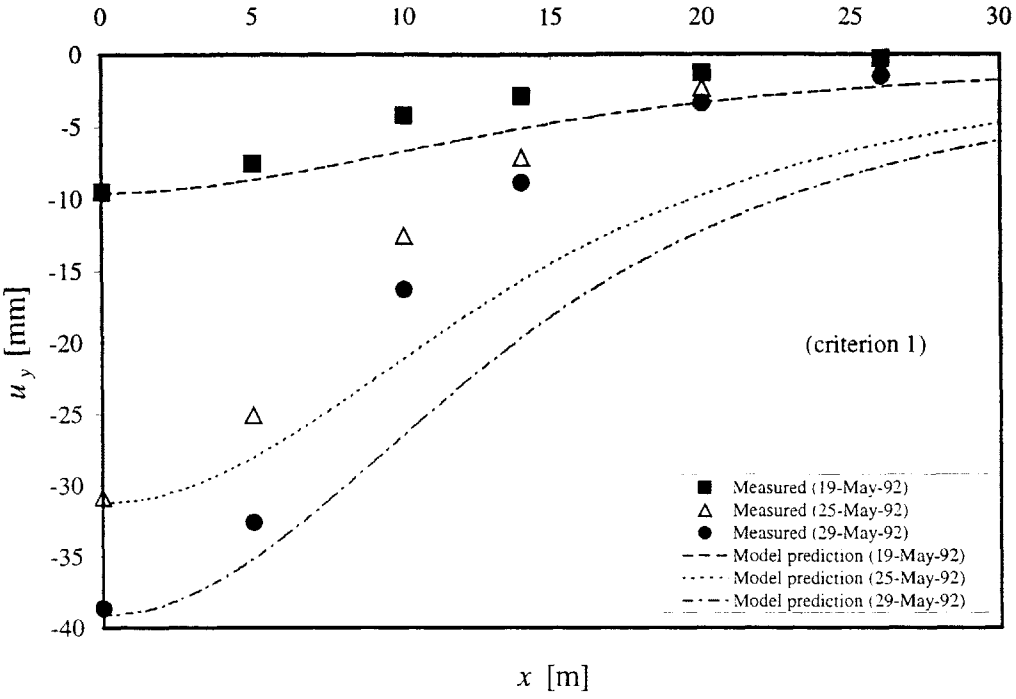

Figure 6.31. Case 3: Heathrow Express Trial Tunnel – Surface settlements, criterion 1

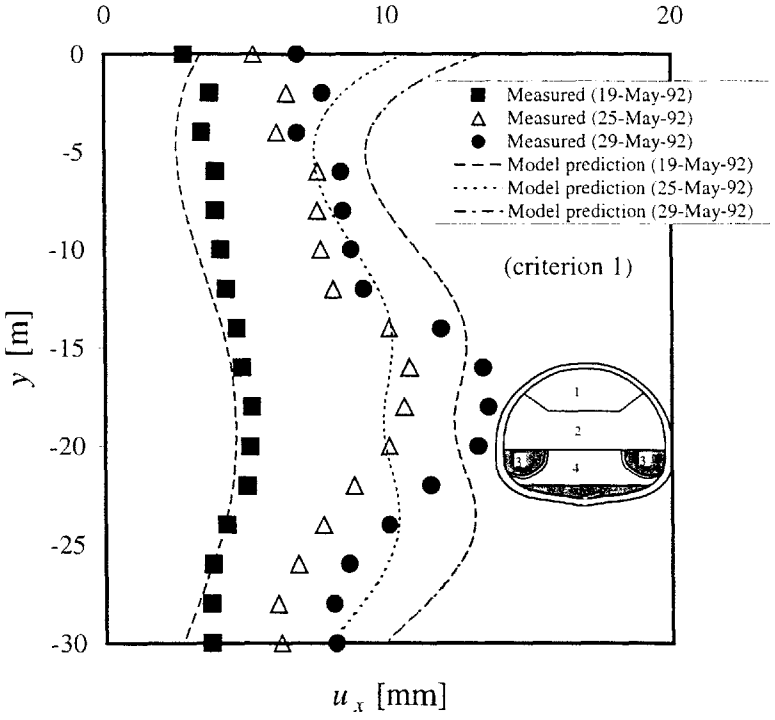

Figure 6.32. Case 3: Heathrow Express Trial Tunnel – Horizontal displacements at x = -9 m, criterion 1

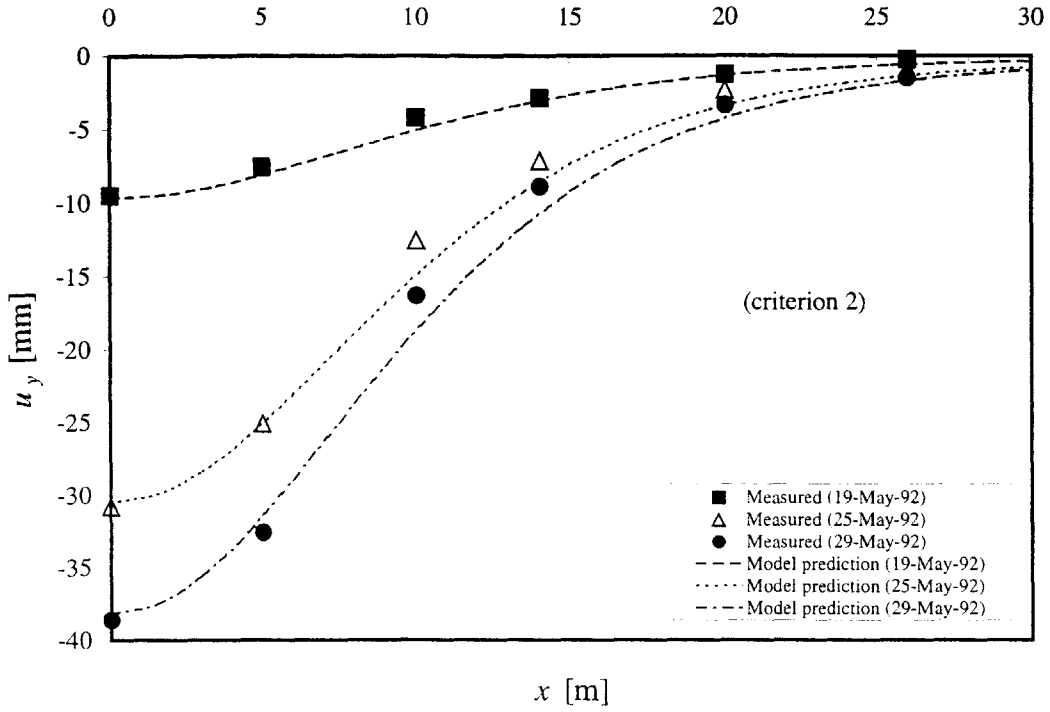

Figure 6.33. Case 3: Heathrow Express Trial Tunnel – Surface settlements, criterion 2

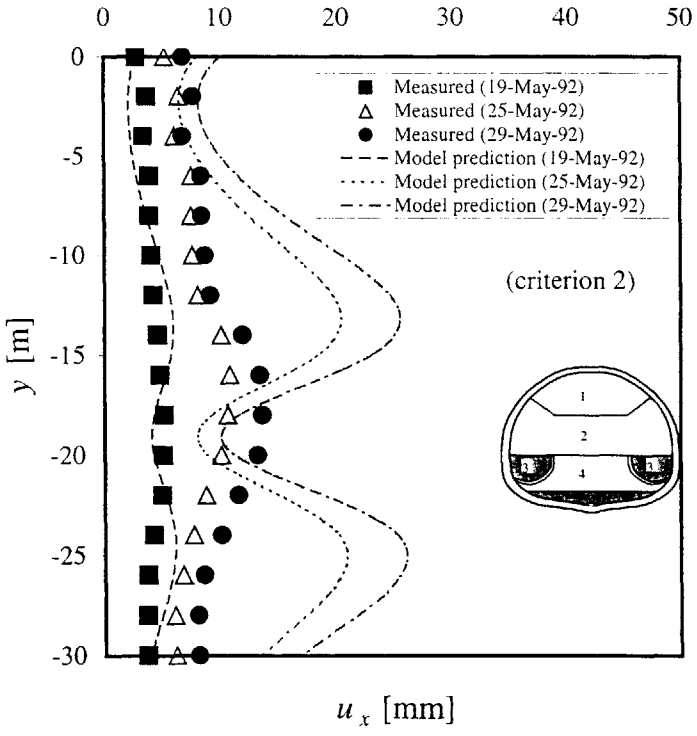

Figure 6.34. Case 3: Heathrow Express Trial Tunnel – Horizontal displacements at x = -9 m, criterion 2

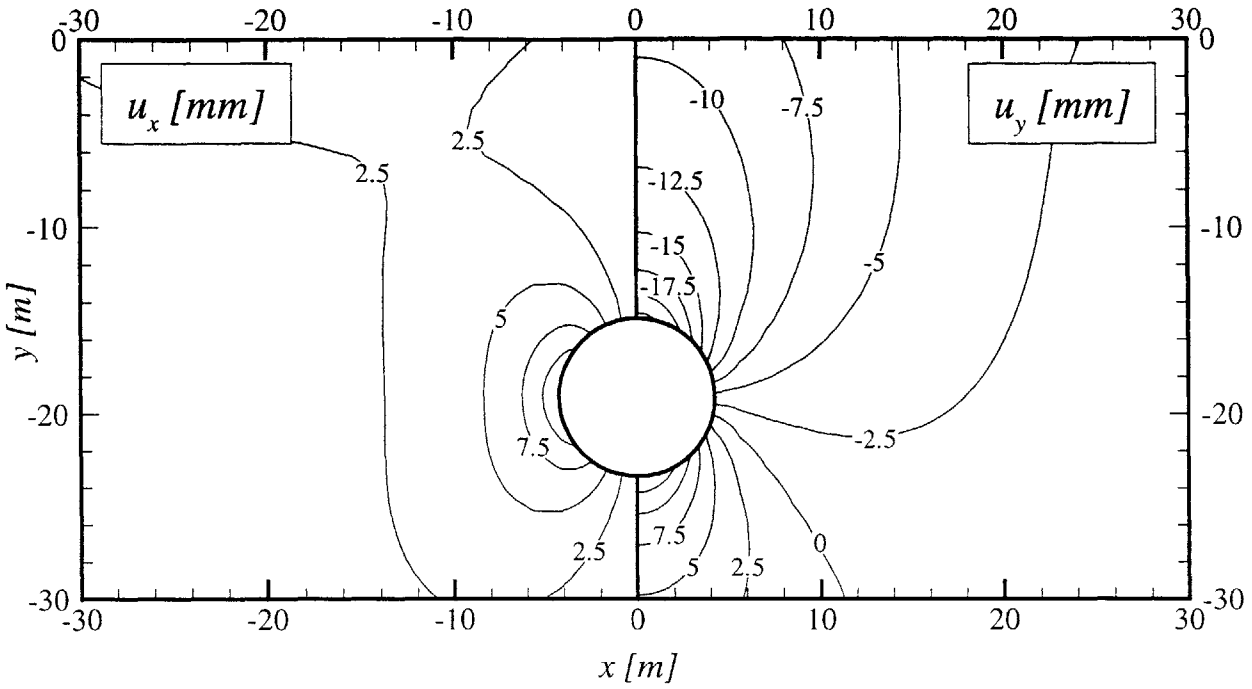

Figure 6.35. Case 3: Heathrow Express Trial Tunnel – Contours of ground displacements predicted by criteria 1, 19-May-92

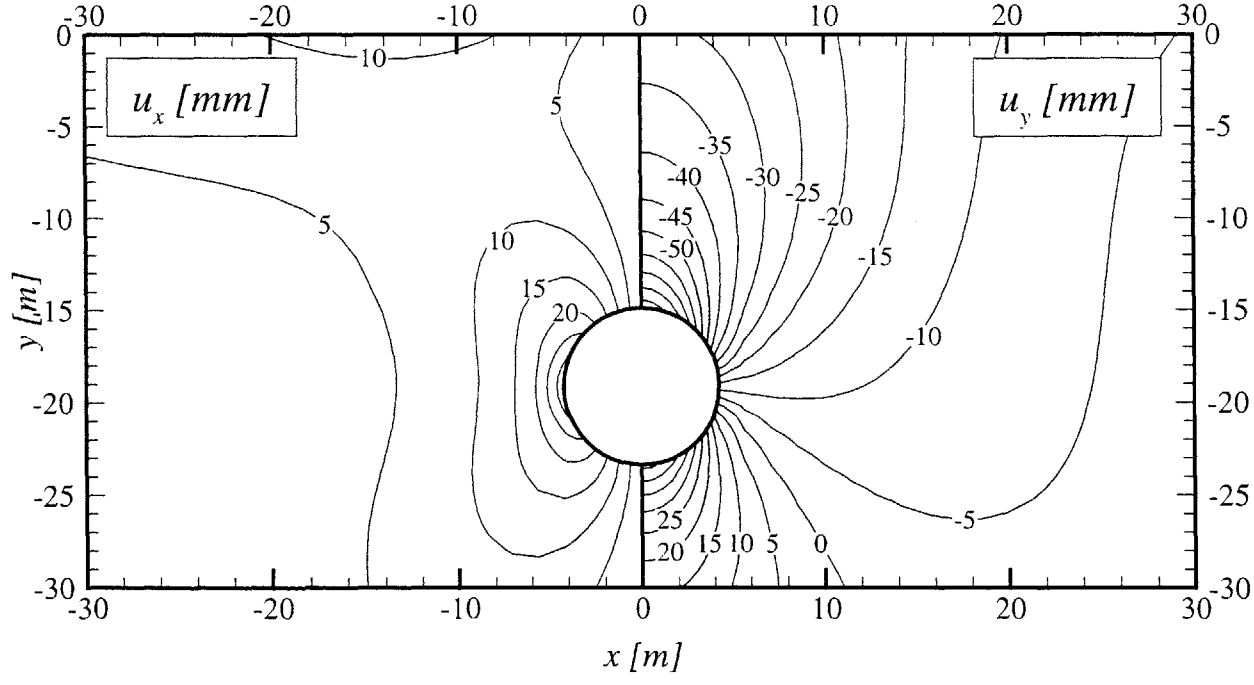

Figure 6.36. Case 3: Heathrow Express Trial Tunnel – Contours of ground displacements predicted by criteria 1, 25-May-92

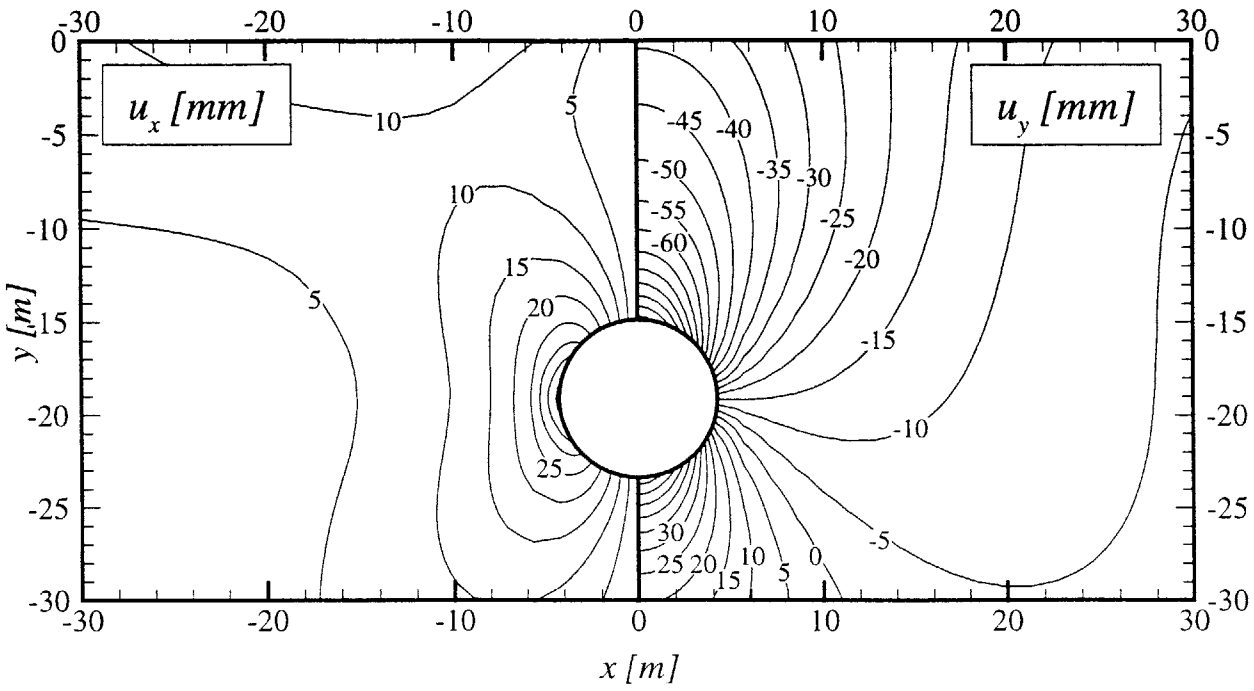

Figure 6.37. Case 3: Heathrow Express Trial Tunnel – Contours of ground displacements predicted by criteria 1, 29-May-92

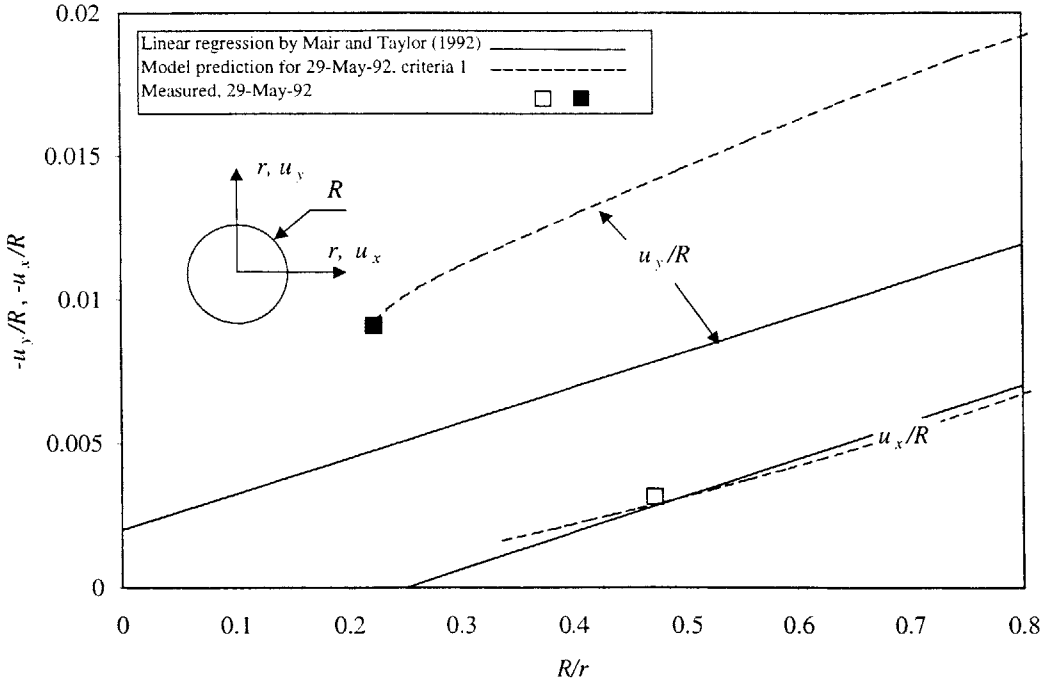

Figure 6.38. Vertical and horizontal sub-surface displacements in the vicinity of tunnels in London Clay (after Mair and Taylor, 1992)

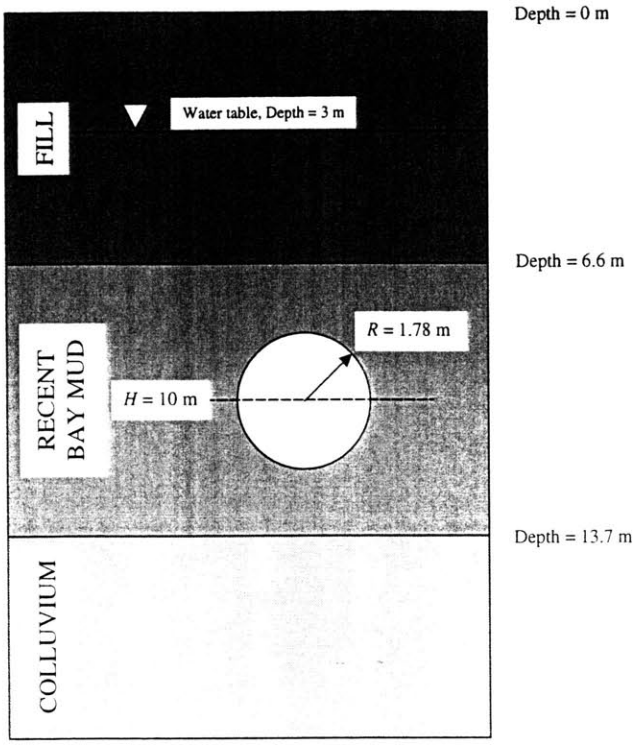

Figure 6.39. Case 4: N-2 Contract tunnel – Cross section

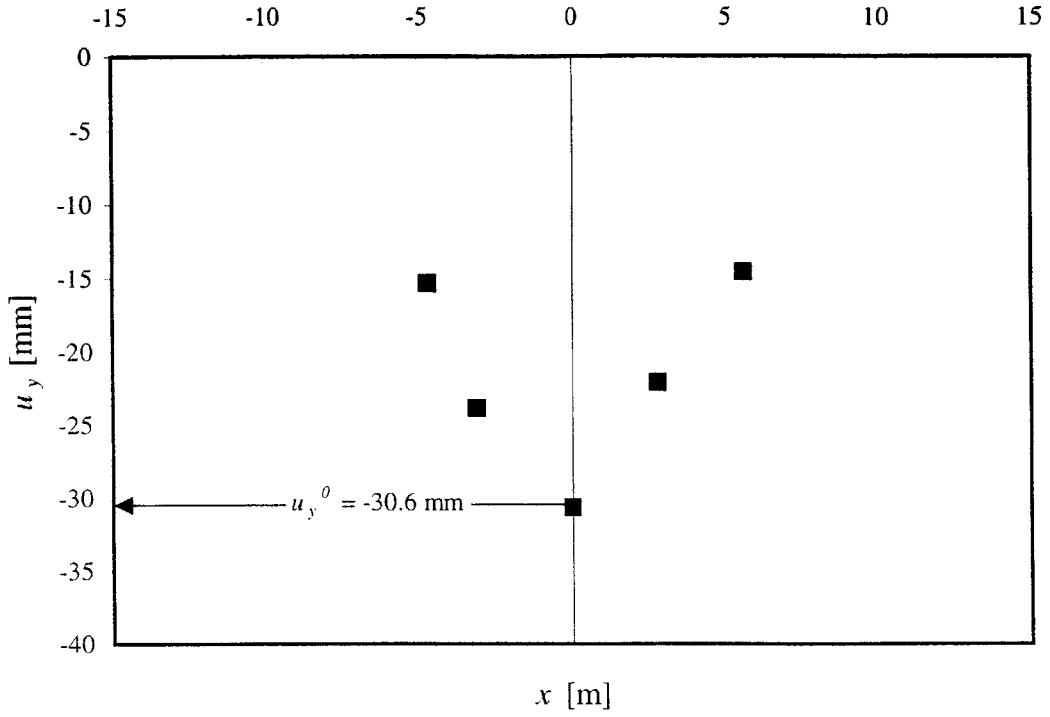

Figure 6.40. Case 4: N-2 Contract tunnel - Measured surface settlements

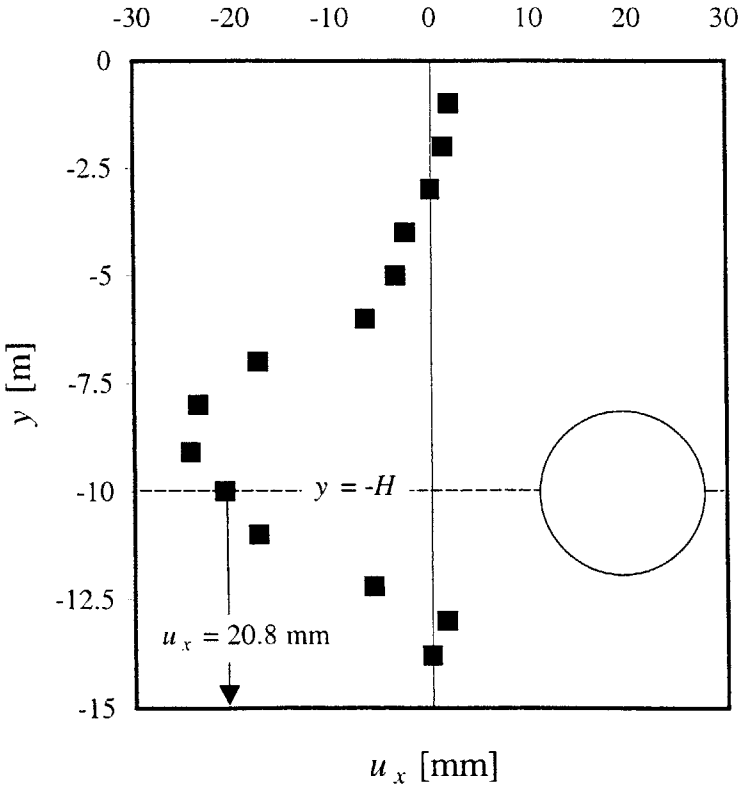

Figure 6.41. Case 4: N-2 Contract tunnel - Horizontal displacements at x = -3.6 m

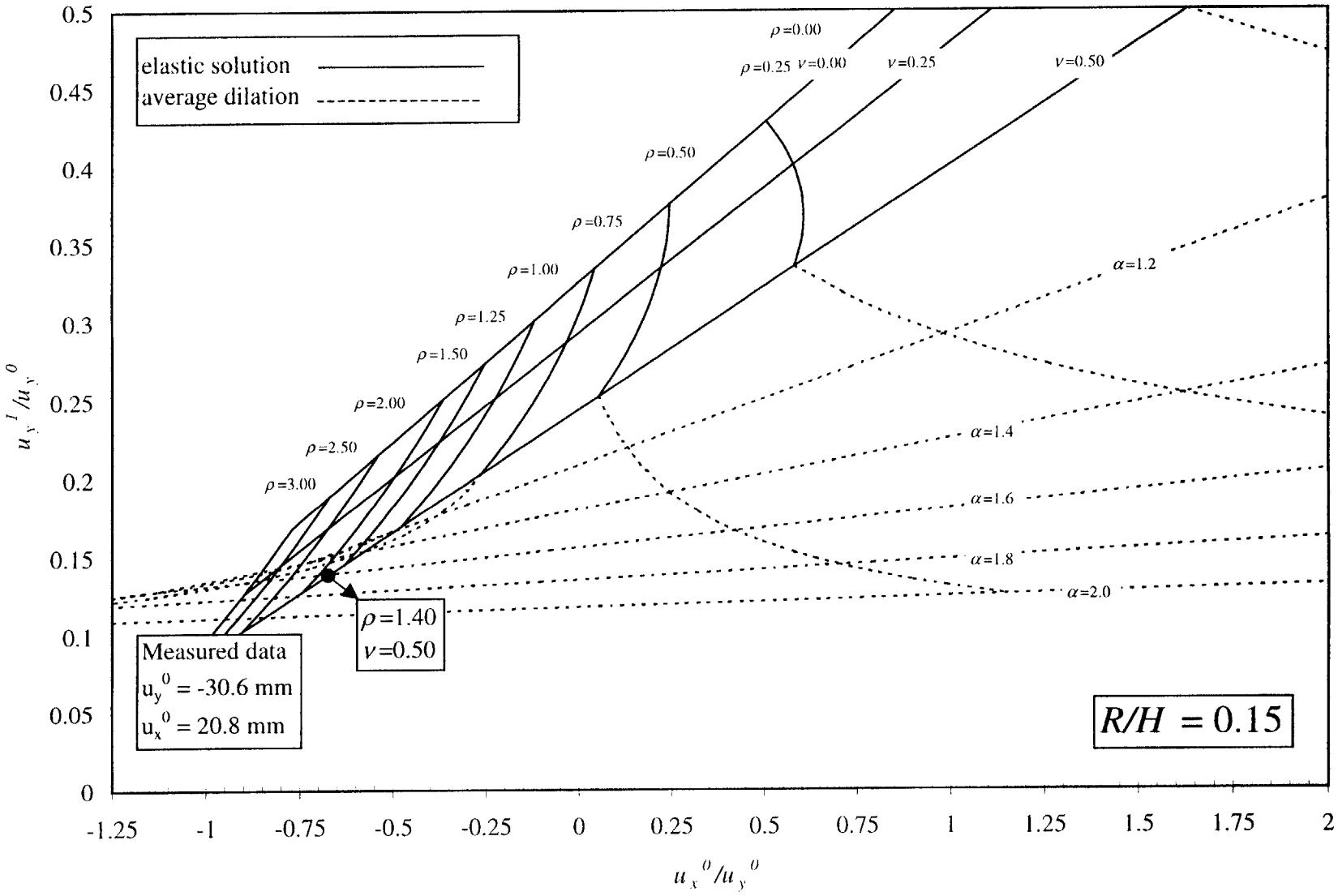

Figure 6.42. Case 4: N-2 Contract tunnel – Derivation of the parameters ρ, ν

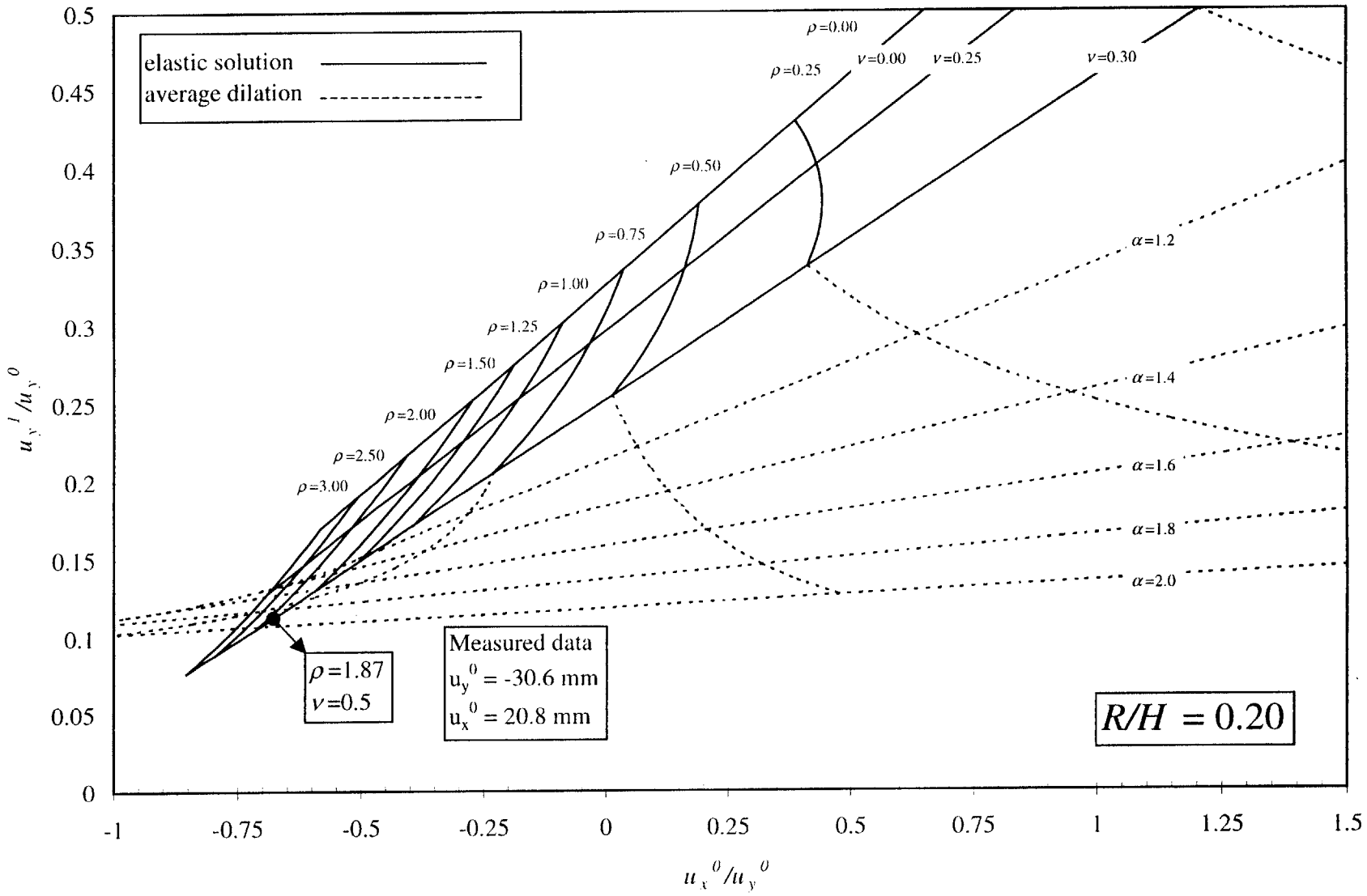

Figure 6.43. Case 4: N-2 Contract tunnel – Derivation of the parameters ρ, ν

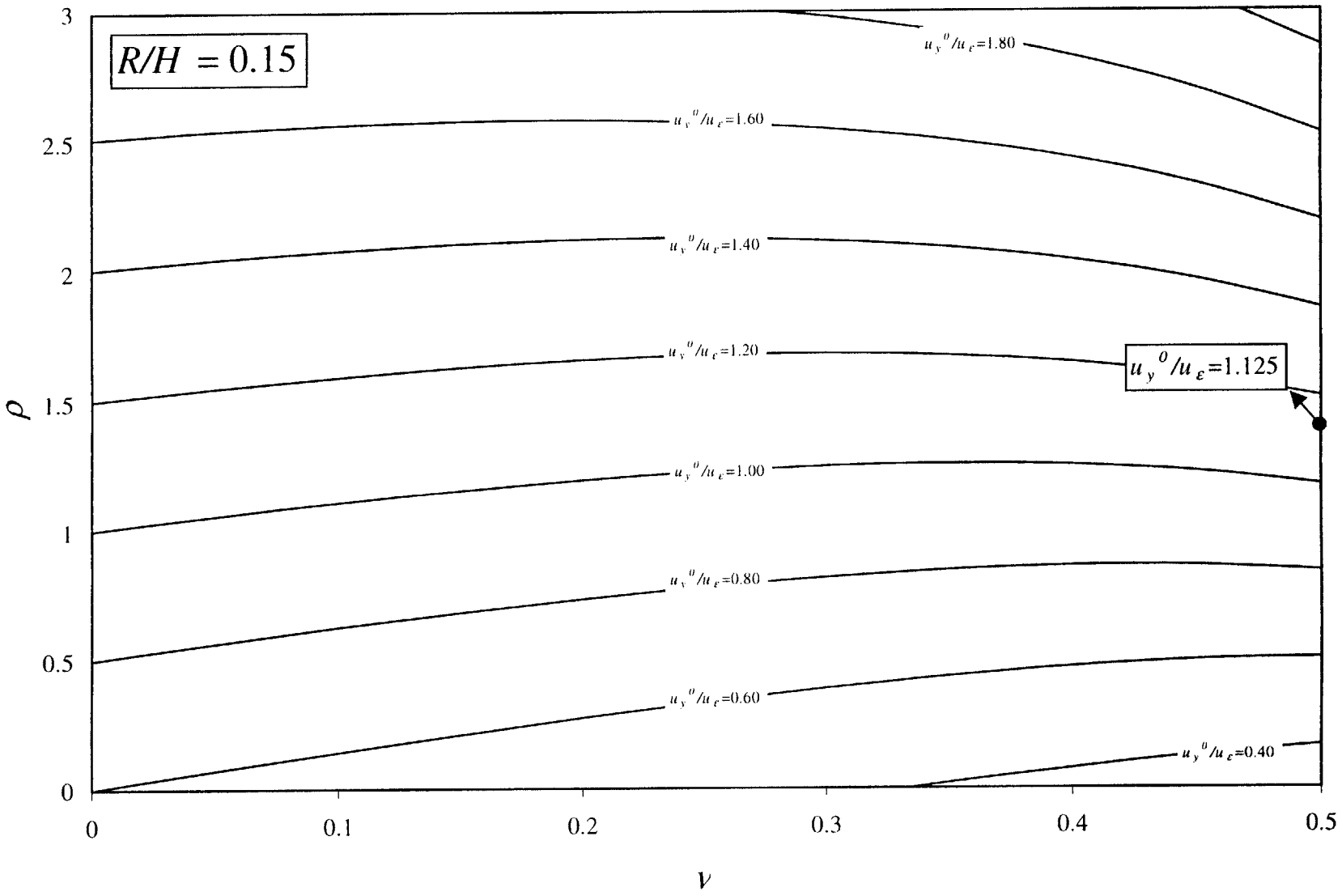

Figure 6.44. Case 4: N-2 Contract tunnel – Derivation of the parameter u_y^0/u_ε

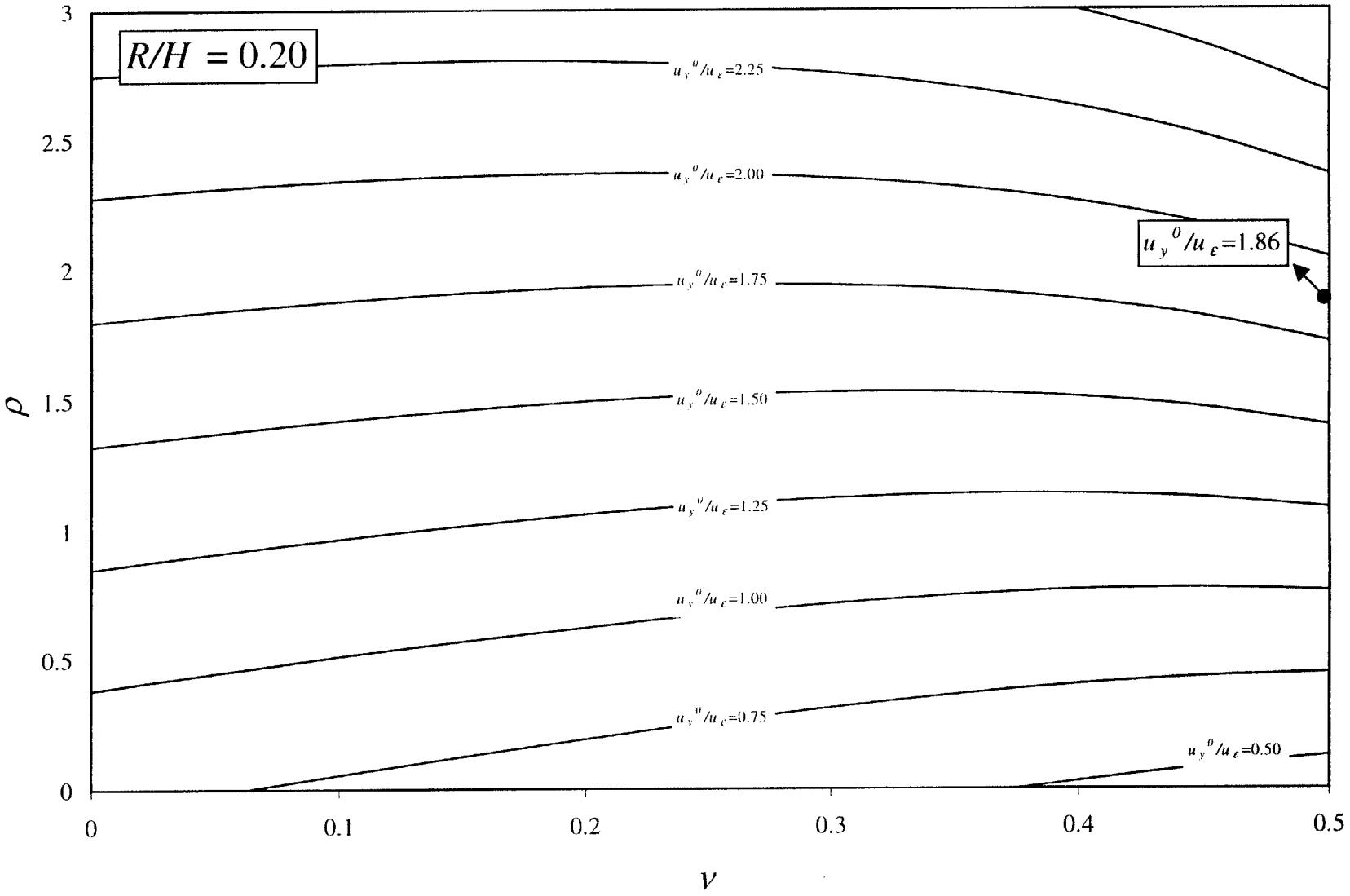

Figure 6.45. Case 4: N-2 Contract tunnel – Derivation of the parameter u_y^0/u_ε

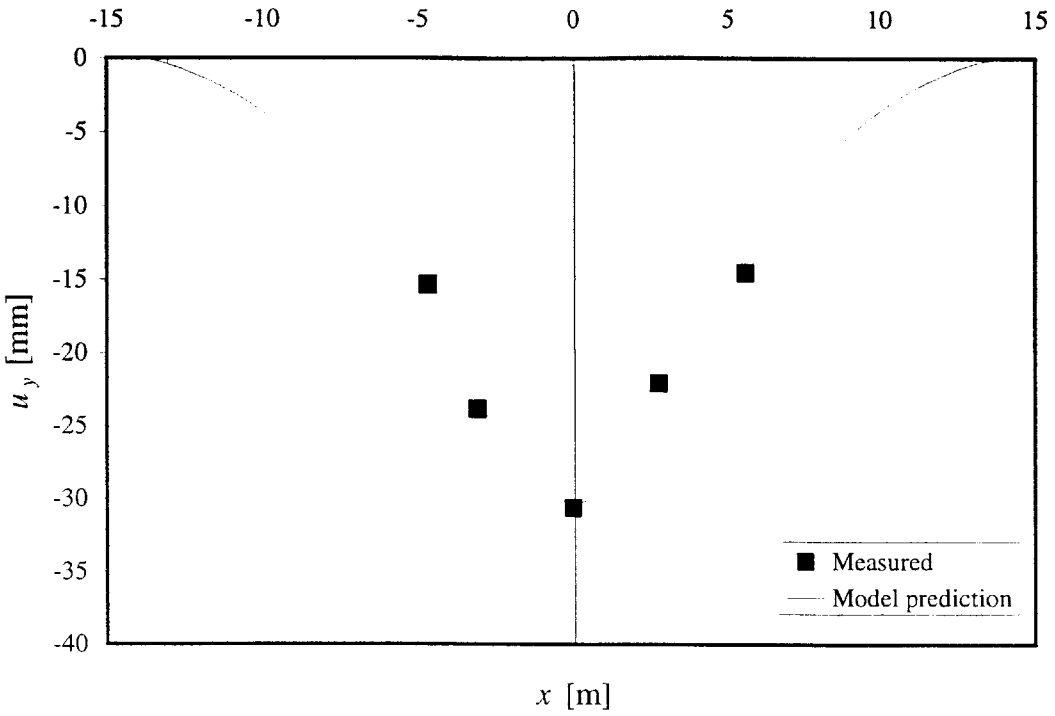

Figure 6.46. Case 4: N-2 Contract tunnel - Surface settlements

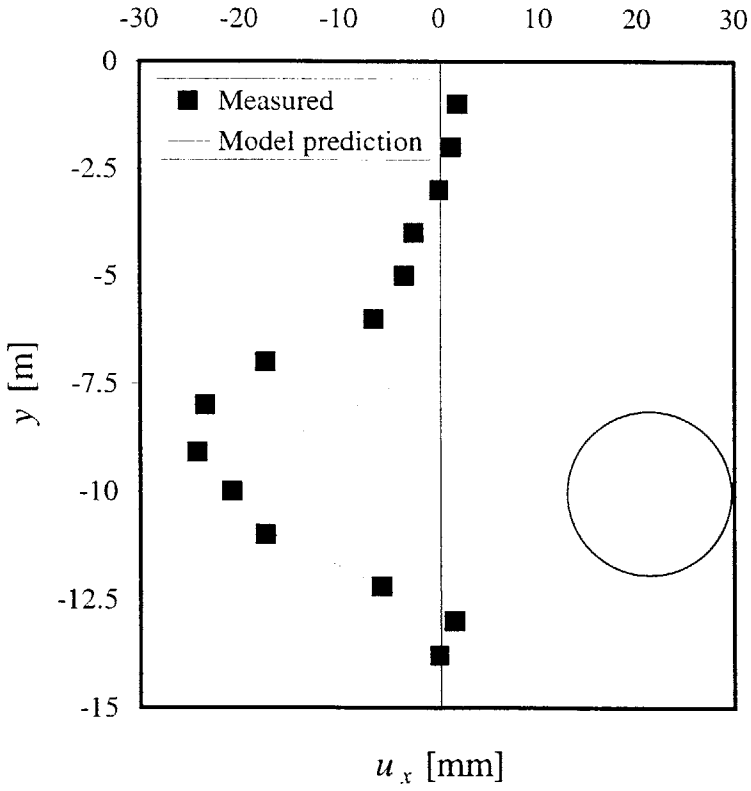

Figure 6.47. Case 4: N-2 Contract tunnel - Horizontal displacements at x = -3.6 m

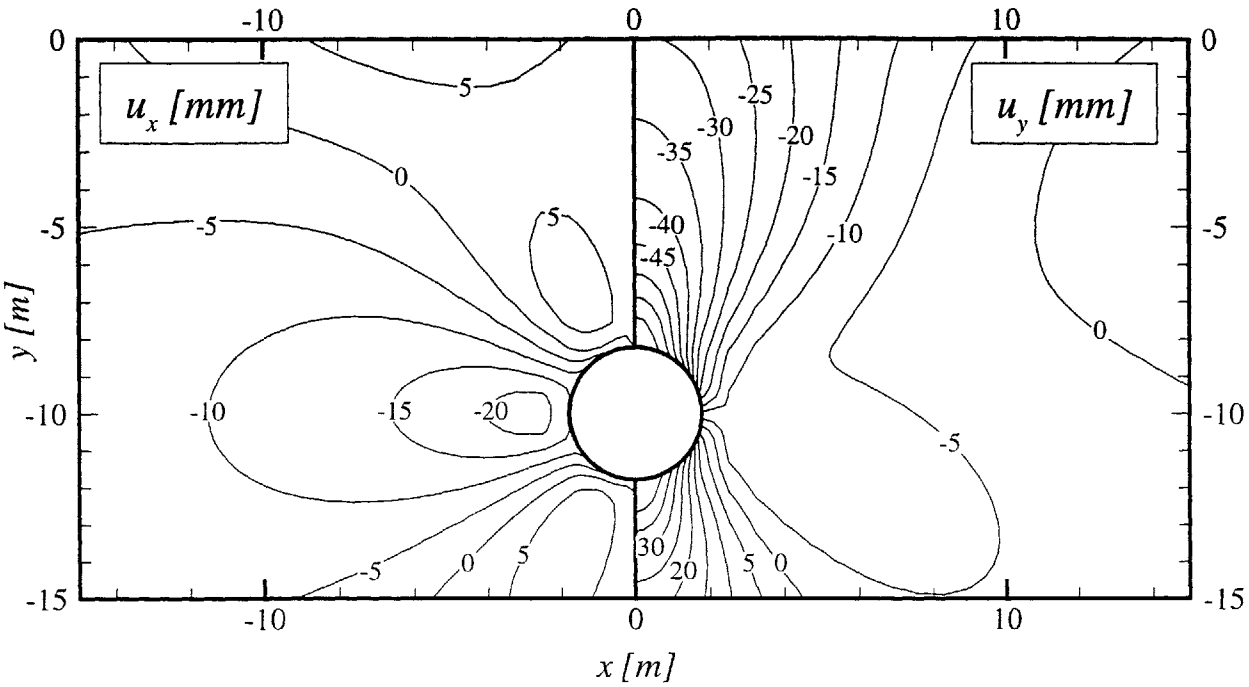

Figure 6.48. Case 4: N-2 Contract tunnel. Contours of predicted ground displacements

7. 3-D Effects. Semi-Infinite Tunnel

This Chapter derives 3D distributions of ground deformations due to a semi-infinite tunnel in elastic half-space. Section 7.1. presents the derivation of the displacement field due to a cavity unloading in an elastic infinite space, while Section 7.2. uses the method of Sen (1950) to obtain the solution for a cavity in an elastic half-space. In Section 7.3., the solution for the displacements due to a cavity in a half-space is used as a Green function in order to obtain an analytical solution for a uniformly distributed ground loss along a semi-infinite tunnel in an elastic half-space. The displacement field due to the semi-infinite tunnel is studied by considering the effects of the proximity of the tunnel heading in the settlement trough and a reference inclinometer located two radii away from the tunnel axis.

7.1 3-D Deformation Analysis due to a Cavity Contraction/Expansion in Elastic Infinite Space

This Section presents the derivation of the displacement field due to a 3-D spherical cavity in an elastic infinite space subjected to an initial hydrostatic state of stresses, p_0. The problem is outlined in Figure 7.1, where R is the initial radius of the cavity. For complete spherical symmetry, the equilibrium equation in spherical coordinates is:

$$\frac{\partial \sigma_r}{\partial r} + 2 \cdot \frac{\sigma_r - \sigma_\theta}{r} = 0 \qquad \{7\text{-}1\}$$

where σ_r and σ_θ are the radial and hoop stress, respectively. The boundary conditions are:

$$\sigma_r(R) = p_i \qquad \{7\text{-}2a\}$$

$$\sigma_r(\infty) = p_0 \qquad \{7\text{-}2b\}$$

where p_i is the internal pressure of the cavity and p_0 the in-situ stress. After introducing the constitutive and kinematic equations, the radial and hoop stresses are given by:

$$\sigma_r = M \cdot \frac{\partial u_r}{\partial r} + 2 \cdot \lambda \cdot \frac{u_r}{r} \qquad \{7\text{-}3a\}$$

$$\sigma_\theta = \lambda \cdot \frac{\partial u_r}{\partial r} + (M + \lambda) \cdot \frac{u_r}{r} \qquad \{7\text{-}3b\}$$

Introducing equations {7-3} in {7-1}, the following ODE is found:

$$\frac{d^2 u_r}{dr^2} + \frac{2}{r} \cdot \frac{du_r}{dr} - \frac{2}{r^2} \cdot u_r = 0 \qquad \{7\text{-}4\}$$

for which the solution is:

$$u_r = A \cdot r + \frac{B}{r^2} \qquad \{7\text{-}5\}$$

where A and B are integration constants that are found by imposing the boundary conditions:

$$A = -\frac{p_0}{2 \cdot G} \frac{1 - 2 \cdot \nu}{1 + \nu} \qquad \{7\text{-}6\}$$

$$B = -\frac{p_0 - p_i}{4 \cdot G} \cdot R^3 \qquad \{7\text{-}7\}$$

Hence, the displacement field is found:

$$u_r = -\frac{p_0}{2 \cdot G} \frac{1 - 2 \cdot \nu}{1 + \nu} \cdot r - \frac{p_0 - p_i}{4 \cdot G} \cdot \frac{R^3}{r^2} \qquad \{7\text{-}8\}$$

As the displacements due to the cavity are of interest, the displacements due to the initial state of stresses (i.e., $p_i = p_0$) must be subtracted. Hence, the displacement field due to the cavity is found to be:

$$u_r = -\frac{p_0 - p_i}{4 \cdot G} \cdot \frac{R^3}{r^2} \qquad \{7\text{-}9\}$$

The displacement at the cavity wall, u_ε, is:

$$u_\varepsilon = -\frac{p_0 - p_i}{4 \cdot G} \cdot R \qquad \{7\text{-}10\}$$

Introducing u_ε in equation {7-9}:

$$u_r = u_\varepsilon \cdot \left(\frac{R}{r} \right)^2 \qquad \{7\text{-}11\}$$

where u_ε can either be evaluated by means of equation {7-10} or regarded as an input parameter.

7.2. 3-D Deformation Analysis due to a Cavity Contraction/Expansion in Elastic Half Space

This Section shows the derivation of the analytical solution for a 3-D cavity expansion/contraction in elastic half-space. This solution is a classical solution of the theory of elasticity and can be found in Sen (1950) or Mindlin and Cheng (1950). The problem outline is shown in Figure 7.2[1].

Equation {7-11} can be expressed in terms of a potential function, V^0, as follows:

$$\Psi = \int u_r \cdot dr = -u_\varepsilon \frac{R^2}{r} \qquad \{7\text{-}12\}$$

from where it can readily be seen that:

[1] The vertical coordinate for 3-D analysis is z, while for the 2-D analyses presented in previous Chapters the vertical coordinate is given by y.

$$u_x = u_r \cdot \frac{x}{r} = \frac{\partial \Psi}{\partial r} \cdot \frac{dr}{dx} = \frac{\partial \Psi}{\partial x} \qquad \{7\text{-}13\}$$

Equation {7-13} can be generalized for x, y, and z. Hence, the displacements can be obtained as the gradient of the potential Ψ in the direction of interest. By considering a cavity at depth, H, beneath the surface, Ψ is given by:

$$\Psi = -u_\varepsilon \frac{R^2}{\sqrt{x^2 + y^2 + (z+H)^2}} \qquad \{7\text{-}14\}$$

This potential implies the following state of stresses at the surface (where advantage has been taken from the fact that there is no volumetric strain component, i.e., $\sigma_i = 2 \cdot G \cdot \varepsilon_i$ for $i = x, y, z$):

$$\sigma_z = 2 \cdot G \cdot \frac{\partial^2 \Psi}{\partial z^2} = -2 \cdot G \cdot u_\varepsilon \cdot R^2 \cdot \frac{3 \cdot (z+H)^2 - \left[x^2 + y^2 + (z+H)^2\right]}{\left[x^2 + y^2 + (z+H)^2\right]^{\frac{5}{2}}} \qquad \{7\text{-}15a\}$$

$$\tau_{yz} = 2 \cdot G \cdot \frac{\partial^2 \Psi}{\partial y \cdot \partial z} = -6 \cdot G \cdot u_\varepsilon \cdot R^2 \cdot (z+H) \cdot \frac{y}{\left[x^2 + y^2 + (z+H)^2\right]^{\frac{5}{2}}} \qquad \{7\text{-}15b\}$$

$$\tau_{xz} = 2 \cdot G \cdot \frac{\partial^2 \Psi}{\partial x \cdot \partial z} = -6 \cdot G \cdot u_\varepsilon \cdot R^2 \cdot (z+H) \cdot \frac{x}{\left[x^2 + y^2 + (z+H)^2\right]^{\frac{5}{2}}} \qquad \{7\text{-}15c\}$$

In order to model a stress-free surface, corrective stresses equal in magnitude and opposite in sign must be applied at $z = 0$. The corrective stresses are:

$$\sigma_z^c\Big|_{z=0} = 2 \cdot G \cdot u_\varepsilon \cdot R^2 \cdot \frac{3 \cdot H^2 - \left[x^2 + y^2 + H^2\right]}{\left[x^2 + y^2 + H^2\right]^{\frac{5}{2}}} \qquad \{7\text{-}15a\}$$

$$\tau_{yz}^{\ c}\Big|_{z=0} = 6 \cdot G \cdot u_{\varepsilon} \cdot R^2 \cdot H \cdot \frac{y}{\left[x^2 + y^2 + H^2\right]^{\frac{5}{2}}} \qquad \{7\text{-}15b\}$$

$$\tau_{xz}^{\ c}\Big|_{z=0} = 6 \cdot G \cdot u_{\varepsilon} \cdot R^2 \cdot H \cdot \frac{x}{\left[x^2 + y^2 + H^2\right]^{\frac{5}{2}}} \qquad \{7\text{-}15c\}$$

where the overscript "c" stands for "corrective". The stresses inside the ground due to the boundary condition {7-15} must fulfill the following equations derived from the theory of elasticity (e.g., Timoshenko and Goodier, 1970):

$$\nabla^2 \sigma_z^{\ c} + \frac{1}{1+\nu} \cdot \frac{\partial^2 \sigma_{kk}^{\ c}}{\partial z^2} = 0 \qquad \{7\text{-}16a\}$$

$$\nabla^2 \tau_{xz}^{\ c} + \frac{1}{1+\nu} \cdot \frac{\partial^2 \sigma_{kk}^{\ c}}{\partial x \cdot \partial z} = 0 \qquad \{7\text{-}16b\}$$

$$\nabla^2 \tau_{yz}^{\ c} + \frac{1}{1+\nu} \cdot \frac{\partial^2 \sigma_{kk}^{\ c}}{\partial y \cdot \partial z} = 0 \qquad \{7\text{-}16c\}$$

where the volumetric stress, $\sigma_{kk}^{\ c} = \sigma_x^{\ c} + \sigma_y^{\ c} + \sigma_z^{\ c}$, must be a harmonic function. The general solution for equations {7-16} (neglecting the boundary condition at the tunnel wall):

$$\sigma_z^{\ c} = -\frac{1}{2 \cdot (1+\nu)} \cdot z \cdot \frac{\partial \sigma_{kk}^{\ c}}{\partial z} + \phi_z \qquad \{7\text{-}17a\}$$

$$\tau_{xz}^{\ c} = -\frac{1}{2 \cdot (1+\nu)} \cdot z \cdot \frac{\partial \sigma_{kk}^{\ c}}{\partial x} + \phi_x \qquad \{7\text{-}17b\}$$

$$\tau_{yz}^{\ c} = -\frac{1}{2\cdot(1+\nu)}\cdot z\cdot\frac{\partial\sigma_{kk}^{\ c}}{\partial y} + \phi_y \qquad \{7\text{-}17c\}$$

where ϕ_x, ϕ_y, ϕ_z, are harmonic functions. Evaluating equations {7-17} at the surface (i.e., $z = 0$):

$$\sigma_z^{\ c}\Big|_{z=0} = \phi_z\Big|_{z=0} \qquad \{7\text{-}18a\}$$

$$\tau_{xz}^{\ c}\Big|_{z=0} = \phi_x\Big|_{z=0} \qquad \{7\text{-}18b\}$$

$$\tau_{yz}^{\ c}\Big|_{z=0} = \phi_y\Big|_{z=0} \qquad \{7\text{-}18c\}$$

By comparing equations {7-18} and {7-15}, it is found that:

$$\phi_z\Big|_{z=0} = 2\cdot G\cdot u_\varepsilon\cdot R^2\cdot\frac{3\cdot H^2-\left[x^2+y^2+H^2\right]}{\left[x^2+y^2+H^2\right]^{\frac{5}{2}}} \qquad \{7\text{-}19a\}$$

$$\phi_x\Big|_{z=0} = 6\cdot G\cdot u_\varepsilon\cdot R^2\cdot H\cdot\frac{x}{\left[x^2+y^2+H^2\right]^{\frac{5}{2}}} \qquad \{7\text{-}19c\}$$

$$\phi_y\Big|_{z=0} = 6\cdot G\cdot u_\varepsilon\cdot R^2\cdot H\cdot\frac{y}{\left[x^2+y^2+H^2\right]^{\frac{5}{2}}} \qquad \{7\text{-}19b\}$$

By defining the following potential:

$$\Psi^c = -u_\varepsilon\frac{R^2}{\sqrt{x^2+y^2+(z-H)^2}} \qquad \{7\text{-}20\}$$

it can be shown that by defining:

$$\phi_z = -2 \cdot G \cdot \frac{\partial^2 \Psi^c}{\partial z^2} \qquad \{7\text{-}21a\}$$

$$\phi_x = 2 \cdot G \cdot \frac{\partial^2 \Psi^c}{\partial x \cdot \partial z} \qquad \{7\text{-}21b\}$$

$$\phi_y = 2 \cdot G \cdot \frac{\partial^2 \Psi^c}{\partial y \cdot \partial z} \qquad \{7\text{-}21b\}$$

equations {7-18} are fulfilled and the ϕ functions are harmonic. It is interesting to note that the gradient vector of the Ψ^c potential coincides with the displacement vector of a positive mirror image.

The equilibrium equation in the z direction reads:

$$\frac{\partial \tau_{xz}}{\partial x} + \frac{\partial \tau_{yz}}{\partial y} + \frac{\partial \sigma_z}{\partial z} = 0 \qquad \{7\text{-}22\}$$

Replacing equations{7-17} in {7-22} and taking advantage from the fact that θ^c is harmonic:

$$\frac{1}{2 \cdot (1+\nu)} \cdot \frac{\partial \sigma_{kk}{}^c}{\partial z} = \frac{\partial \phi_x}{\partial x} + \frac{\partial \phi_y}{\partial y} + \frac{\partial \phi_z}{\partial z} \qquad \{7\text{-}23\}$$

Introducing equations {7-21} in {7-23} yields the following PDE for θ^c:

$$\frac{\partial \sigma_{kk}{}^c}{\partial z} = 4 \cdot (1+\nu) \cdot G \cdot \left\{ \frac{\partial}{\partial z} \left(\nabla^2 \Psi^c \right) - 2 \cdot \frac{\partial^3 \Psi^c}{\partial z^3} \right\} \qquad \{7\text{-}24\}$$

Considering that Ψ^c is harmonic (i.e., $\nabla^2 \Psi^c = 0$) and integrating one time in z:

$$\sigma_{kk}{}^{c} = \sigma_{x}{}^{c} + \sigma_{y}{}^{c} + \sigma_{z}{}^{c} = -8 \cdot (1+\nu) \cdot G \cdot \frac{\partial^2 \Psi^c}{\partial z^2} \qquad \{7\text{-}25\}$$

The stress field due to the corrective stresses at the surface is found by replacing equations {7-21}, and {7-25} in {7-17}:

$$\sigma_{z}{}^{c} = 4 \cdot G \cdot z \cdot \frac{\partial^3 \Psi^c}{\partial z^3} - 2 \cdot G \cdot \frac{\partial^2 \Psi^c}{\partial z^2} \qquad \{7\text{-}26a\}$$

$$\tau_{xz}{}^{c} = 4 \cdot G \cdot z \cdot \frac{\partial^3 \Psi^c}{\partial x \cdot \partial z^2} + 2 \cdot G \cdot \frac{\partial^2 \Psi^c}{\partial x \cdot \partial z} \qquad \{7\text{-}26b\}$$

$$\tau_{yz}{}^{c} = 4 \cdot G \cdot z \cdot \frac{\partial^3 \Psi^c}{\partial y \cdot \partial z^2} + 2 \cdot G \cdot \frac{\partial^2 \Psi^c}{\partial y \cdot \partial z} \qquad \{7\text{-}26c\}$$

The displacement field due to the corrective stress is henceforth obtained by means of the elastic constitutive equations. The constitutive equation for σ_z is given by:

$$\frac{\partial u_z{}^{c}}{\partial z} = \frac{1}{2 \cdot G} \cdot \left(\sigma^{c}{}_{z} - \frac{\nu}{1+\nu} \cdot \sigma_{kk}{}^{c} \right) = 2 \cdot z \cdot \frac{\partial^3 \Psi^c}{\partial z^3} - \frac{\partial^2 \Psi^c}{\partial z^2} + 4 \cdot \nu \cdot \frac{\partial^2 \Psi^c}{\partial z^2} \qquad \{7\text{-}27\}$$

Integrating with respect to z:

$$u_z{}^{c} = 2 \cdot z \cdot \frac{\partial^2 \Psi^c}{\partial z^2} - (3 - 4 \cdot \nu) \frac{\partial \Psi^c}{\partial z} \qquad \{7\text{-}28\}$$

where it can be verified that for an incompressible material (i.e., $\nu = 0.5$) the corrective vertical displacements at the surface (i.e., $z = 0$) correspond to a negative mirror image. Introducing equation {7-20} in {7-28}:

$$u_z^c = -u_\varepsilon \cdot R^2 \cdot \left\{ 2 \cdot z \cdot \frac{3 \cdot (z-H)^2 - \left[x^2 + y^2 + (z-H)^2\right]}{\left[x^2 + y^2 + (z-H)^2\right]^{\frac{5}{2}}} + \frac{(3-4 \cdot \nu) \cdot (z-H)}{\left[x^2 + y^2 + (z-H)^2\right]^{\frac{3}{2}}} \right\} \qquad \{7\text{-}29\}$$

The constitutive equation for τ_{xz} is:

$$\frac{\partial u_x^c}{\partial z} = \frac{\tau_{xz}^c}{G} - \frac{\partial u_z^c}{\partial x} = 2 \cdot \frac{\partial^2}{\partial z \cdot \partial x} \cdot \left(z \cdot \frac{\partial \Psi^c}{\partial z} \right) + (3-4 \cdot \nu) \frac{\partial^2 \Psi^c}{\partial x \cdot \partial z} \qquad \{7\text{-}30\}$$

Integrating with respect to z yields:

$$u_x^c = 2 \cdot \frac{\partial}{\partial x} \cdot \left(z \cdot \frac{\partial \Psi^c}{\partial z} \right) + (3-4 \cdot \nu) \frac{\partial \Psi^c}{\partial x} \qquad \{7\text{-}31\}$$

where it can be verified that the corrective horizontal displacements for an incompressible material at the surface corresponds to a positive mirror image. Introducing equation {7-20} in {7-31}:

$$u_x^c = u_\varepsilon \cdot R^2 \cdot \left\{ -6 \cdot \frac{(z-H) \cdot z \cdot x}{\left[x^2 + y^2 + (z-H)^2\right]^{\frac{5}{2}}} + \frac{(3-4 \cdot \nu) \cdot x}{\left[x^2 + y^2 + (z-H)^2\right]^{\frac{3}{2}}} \right\} \qquad \{7\text{-}32\}$$

similarly:

$$u_y^c = u_\varepsilon \cdot R^2 \cdot \left\{ -6 \cdot \frac{(z-H) \cdot z \cdot y}{\left[x^2 + y^2 + (z-H)^2\right]^{\frac{5}{2}}} + \frac{(3-4 \cdot \nu) \cdot y}{\left[x^2 + y^2 + (z-H)^2\right]^{\frac{3}{2}}} \right\} \qquad \{7\text{-}33\}$$

Finally, the displacement field due to a cavity contraction/expansion in elastic half-space is obtained by adding equations {7-13} and {7-29}, {7-32} and {7-33}:

$$u_x = u_\varepsilon \cdot R^2 \cdot \left\{ \frac{x}{\left[x^2 + y^2 + (z+H)^2\right]^{\frac{3}{2}}} - 6 \cdot \frac{(z-H) \cdot z \cdot x}{\left[x^2 + y^2 + (z-H)^2\right]^{\frac{5}{2}}} + \frac{(3-4 \cdot \nu) \cdot x}{\left[x^2 + y^2 + (z-H)^2\right]^{\frac{3}{2}}} \right\} \quad \{7\text{-}34a\}$$

$$u_y = u_\varepsilon \cdot R^2 \cdot \left\{ \frac{y}{\left[x^2 + y^2 + (z+H)^2\right]^{\frac{3}{2}}} - 6 \cdot \frac{(z-H) \cdot z \cdot y}{\left[x^2 + y^2 + (z-H)^2\right]^{\frac{5}{2}}} + \frac{(3-4 \cdot \nu) \cdot y}{\left[x^2 + y^2 + (z-H)^2\right]^{\frac{3}{2}}} \right\} \quad \{7\text{-}34b\}$$

$$u_z = u_\varepsilon \cdot R^2 \cdot \left\{ \begin{array}{l} \dfrac{(z+H)}{\left[x^2 + y^2 + (z+H)^2\right]^{\frac{3}{2}}} - 2 \cdot z \cdot \dfrac{3 \cdot (z-H)^2 - \left[x^2 + y^2 + (z-H)^2\right]}{\left[x^2 + y^2 + (z-H)^2\right]^{\frac{5}{2}}} - \ldots \\ \ldots - \dfrac{(3-4 \cdot \nu) \cdot (z-H)}{\left[x^2 + y^2 + (z-H)^2\right]^{\frac{3}{2}}} \end{array} \right\} \quad \{7\text{-}34c\}$$

and u_ε is related to the ground loss volume, V_L, as follows:

$$u_\varepsilon = \frac{V_L}{4 \cdot \pi \cdot R^2} \quad \{7\text{-}35\}$$

7.3. 3-D Deformation Analysis due to a Semi-Infinite Tunnel in Elastic Half-Space

This Section considers the effects of the 3-D deformations produced near the tunnel heading. In order to account for the effects of the tunnel heading, a distributed ground loss approach is followed. The ground loss is uniformly distributed along the tunnel axis (parallel to y) from $y = -\infty$ to $y = 0$. The solution is obtained by means of the Green functions in correspondence to a 3-D spherical cavity contraction/expansion in an elastic half-space (Section 7.2).

The displacement field due to a spherical cavity contraction/expansion embedded at depth, H, in elastic half-space can be written as:

$$u_x = \frac{V_L}{4 \cdot \pi} \cdot f(x,y,z) \qquad \{7\text{-}36a\}$$

$$u_y = \frac{V_L}{4 \cdot \pi} \cdot g(x,y,z) \qquad \{7\text{-}36b\}$$

$$u_z = \frac{V_L}{4 \cdot \pi} \cdot h(x,y,z) \qquad \{7\text{-}36c\}$$

where V_L is the ground loss volume and the patterns obtained from equations {7.34} are given by:

$$f(x,y,z) = \frac{x}{\left[x^2 + y^2 + (z+H)^2\right]^{\frac{3}{2}}} - 6 \cdot \frac{(z-H) \cdot z \cdot x}{\left[x^2 + y^2 + (z-H)^2\right]^{\frac{5}{2}}} + \frac{(3-4 \cdot \nu) \cdot x}{\left[x^2 + y^2 + (z-H)^2\right]^{\frac{3}{2}}} \qquad \{7\text{-}37a\}$$

$$g(x,y,z) = \frac{y}{\left[x^2 + y^2 + (z+H)^2\right]^{\frac{3}{2}}} - 6 \cdot \frac{(z-H) \cdot z \cdot y}{\left[x^2 + y^2 + (z-H)^2\right]^{\frac{5}{2}}} + \frac{(3-4 \cdot \nu) \cdot y}{\left[x^2 + y^2 + (z-H)^2\right]^{\frac{3}{2}}} \qquad \{7\text{-}37b\}$$

$$h(x,y,z) = \left\{ \begin{array}{l} \dfrac{(z+H)}{\left[x^2 + y^2 + (z+H)^2\right]^{\frac{3}{2}}} - 2 \cdot z \cdot \dfrac{3 \cdot (z-H)^2 - \left[x^2 + y^2 + (z-H)^2\right]}{\left[x^2 + y^2 + (z-H)^2\right]^{\frac{5}{2}}} - \ldots \\ \ldots - \dfrac{(3-4 \cdot \nu) \cdot (z-H)}{\left[x^2 + y^2 + (z-H)^2\right]^{\frac{3}{2}}} \end{array} \right\} \qquad \{7\text{-}37c\}$$

If the cavity is located in an arbitrary position along the tunnel axis, $y = \zeta$ (see Figure 7.3), equations {7-36} become:

$$u_x = \frac{V_L}{4 \cdot \pi} \cdot f(x, y-\zeta, z) \qquad \{7\text{-}38a\}$$

$$u_y = \frac{V_L}{4 \cdot \pi} \cdot g(x, y-\zeta, z) \qquad \{7\text{-}38b\}$$

$$u_z = \frac{V_L}{4 \cdot \pi} \cdot h(x, y-\zeta, z) \qquad \{7\text{-}38c\}$$

The Green functions are defined as the displacement field due to a unit ground loss (i.e., $V = 1$) occurring at a cavity with coordinates $(x, y, z) = (0, \zeta, -H)$:

$$\Gamma_x(x, y, z, \zeta) = \frac{1}{4 \cdot \pi} \cdot f(x, y-\zeta, z) \qquad \{7\text{-}39a\}$$

$$\Gamma_y(x, y, z, \zeta) = \frac{1}{4 \cdot \pi} \cdot g(x, y-\zeta, z) \qquad \{7\text{-}39b\}$$

$$\Gamma_z(x, y, z, \zeta) = \frac{1}{4 \cdot \pi} \cdot h(x, y-\zeta, z) \qquad \{7\text{-}39c\}$$

Hence, the displacements due to a ground loss distributed along the tunnel axis from $y = -\infty$ to $y = 0$ is given by (see Figure 7.4):

$$u_x = \int_{-\infty}^{0} \Gamma_x(x, y, z, \zeta) \cdot \Omega(\zeta) \cdot d\zeta \qquad \{7\text{-}40a\}$$

$$u_y = \int_{-\infty}^{0} \Gamma_y(x, y, z, \zeta) \cdot \Omega(\zeta) \cdot d\zeta \qquad \{7\text{-}40b\}$$

$$u_z = \int_{-\infty}^{0} \Gamma_z(x, y, z, \zeta) \cdot \Omega(\zeta) \cdot d\zeta \qquad \{7\text{-}40c\}$$

where $\Omega(\zeta) \cdot d\zeta$ represents the ground loss volume. For a uniformly distributed ground loss, $\Omega(\zeta) = V_{2\text{-}D}$, where $V_{2\text{-}D}$ is the two-dimensional ground loss volume, defined in {3-21}. Hence, the displacement field due to a uniformly distributed ground loss[2] is found to be:

$$u_x = \frac{V_{2-D}}{4 \cdot \pi} \cdot \left\{ \frac{x \cdot (R_1 - y)}{r_1^2 \cdot R_1} + \frac{\kappa \cdot x \cdot (R_2 - y)}{r_2^2 \cdot R_2} + \frac{x \cdot z \cdot (z - H) \cdot \left[2 \cdot y \cdot \left(3 \cdot R_2^2 - y^2 \right) - 4 \cdot R_2^3 \right]}{r_2^4 \cdot R_2^3} \right\} \qquad \{7\text{-}41a\}$$

$$u_y = \frac{V_{2-D}}{4 \cdot \pi} \cdot \left\{ \frac{1}{R_1} + \frac{\kappa}{R_2} - \frac{2 \cdot z \cdot (z - H)}{R_2^3} \right\} \qquad \{7\text{-}41b\}$$

$$u_z = \frac{V_{2-D}}{4 \cdot \pi} \cdot \left\{ \begin{array}{l} \frac{(z + H) \cdot (R_1 - y)}{r_1^2 \cdot R_1} + \frac{2 \cdot z \cdot (z - H)^2 \cdot \left[y \cdot \left(3 \cdot R_2^2 - y^2 \right) - 2 \cdot R_2^3 \right]}{r_2^4 \cdot R_2^3} - \ldots \\ \ldots - \frac{\left[\kappa \cdot (z - H) - 2 \cdot H \right] \cdot (R_2 - y) - 2 \cdot (R_2 - y) \cdot (z - H)}{r_2^2 \cdot R_2} \end{array} \right\} \qquad \{7\text{-}41c\}$$

where:

$$r_1 = \sqrt{x^2 + (z + H)^2} \qquad \{7\text{-}42a\}$$

$$r_2 = \sqrt{x^2 + (z - H)^2} \qquad \{7\text{-}42b\}$$

$$R_1 = \sqrt{x^2 + y^2 + (z + H)^2} \qquad \{7\text{-}42c\}$$

$$R_2 = \sqrt{x^2 + y^2 + (z - H)^2} \qquad \{7\text{-}42d\}$$

$$\kappa = 3 - 4 \cdot \nu \qquad \{7\text{-}42e\}$$

[2] More refined predictions of ground loss at tunnel headings can be specified based on finite element models such as Panèt and Guenot (1982).

It can be shown that this solution tends to the one presented in Section 3.3.1. for $y \rightarrow -\infty$.

The displacements at the surface are:

$$u_x\big|_{z=0} = \frac{V_{2-D}}{\pi} \cdot \frac{(1-\nu)\cdot x}{x^2+H^2} \cdot \frac{\sqrt{x^2+y^2+H^2}-y}{\sqrt{x^2+y^2+H^2}} \qquad \{7\text{-}43a\}$$

$$u_y\big|_{z=0} = \frac{V_{2-D}}{\pi} \cdot \frac{(1-\nu)}{\sqrt{x^2+y^2+H^2}} \qquad \{7\text{-}43b\}$$

$$u_z\big|_{z=0} = \frac{V_{2-D}}{\pi} \cdot \frac{(1-\nu)\cdot H}{x^2+H^2} \cdot \frac{\sqrt{x^2+y^2+H^2}-y}{\sqrt{x^2+y^2+H^2}} \qquad \{7\text{-}43c\}$$

It can be seen that the vertical (z) and lateral (x) displacement at the surface are related as follows:

$$u_x\big|_{z=0} = \frac{x}{H} \cdot u_z\big|_{z=0}$$

where it can readily be seen that horizontal displacements are smaller than vertical in the region where $-H < x < H$ and larger elsewhere. This result coincides with the 2-D analysis discussed in Section 3.5.1.1.

Contours of surface displacements are presented in Figure 7.5. It is found that the lateral displacements, u_x, are essentially two dimensional at the region where $y < -2 \cdot H$, while the 3-D effects are important for $y > -2 \cdot H$. The longitudinal displacements, u_y, decay at the same rate in all directions from the tunnel heading. The vertical displacements, u_z, are essentially two dimensional at the region where $y < -2 \cdot H$, and again the 3-D effects are important for $y > -2 \cdot H$ (as for the case of lateral displacements). Figure 7.6 shows the deformed ground surface for R/H =0.2 and $\nu = 0.25$.

Figure 7.7 shows the effects of the proximity of the tunnel heading (i.e., 3-D effects) on the surface settlements, where it can be seen that the trough is wider ahead the tunnel face and slightly narrower at a distance H behind the heading. The troughs have essentially the same shape for $y < 0$ (i.e., behind the tunnel heading). However, the absolute magnitude of the surface displacements are almost independent of the distance to the tunnel heading, y, only for $y < 2 \cdot H$ (i.e., two embedment depths behind the tunnel heading).

Figure 7.8 shows the 3-D effects on the lateral displacements, u_x, inside the ground at a vertical line two radii away from the tunnel centerline. It can be seen that the shapes are almost the same for $y < 0$ (i.e., behind the tunnel heading). However, as for the surface settlements, the absolute magnitude of the lateral displacements are almost independent of the distance to the tunnel heading, y, only for $y < 2 \cdot H$ (i.e., two embeddment depths behind the tunnel heading). The lateral displacements decrease almost linearly with depth ahead the tunnel heading.

Figure 7.9 shows the 3-D effects of on the longitudinal displacements, u_y, inside the ground at a vertical line two radii away from the tunnel centerline. It can be seen that the displacements decrease almost linearly with depth for $-H < y < H$, and present a maximum value at $z = -H$ elsewhere. By comparing Figures 7.10 and 7.11, it can be seen that the longitudinal displacements are larger than the lateral for $y > -H$, while the lateral displacements are predominant elsewhere (i.e., at a distance larger than H behind the tunnel heading).

7.4. Conclusions

It has been shown that is possible to generalize the 2-D solutions in order to take into account the proximity of the tunnel heading in the displacements field for the uniform convergence mode. This allows the evaluation of out-of-plane movements (i.e., in the longitudinal direction), which are not taken into account by the 2-D solutions. It is found that the 3-D effects are confined to a region $2 \cdot H$ behind from the tunnel heading.

A 3-D solution can be obtained for the pure distortion case following a similar approach than the one used for the uniform convergence case by superimposing Neuber (Neuber, 1946) solutions

for a sphere in an infinite space. In order to correct the surface stresses an approach similar to the one followed in Section 7.2. could be used[3].

[3] Fares (1987) proposed a generalized mirror image technique in order to convert any infinite-space solution in to a half-space solution. This approach is particularly interesting since it also allows to model a layered medium by direct superposition.

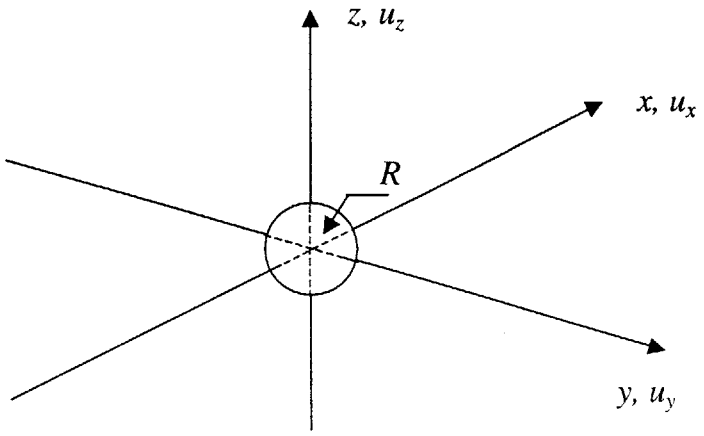

Figure 7.1. Spherical cavity contraction in infinite space - Problem outline

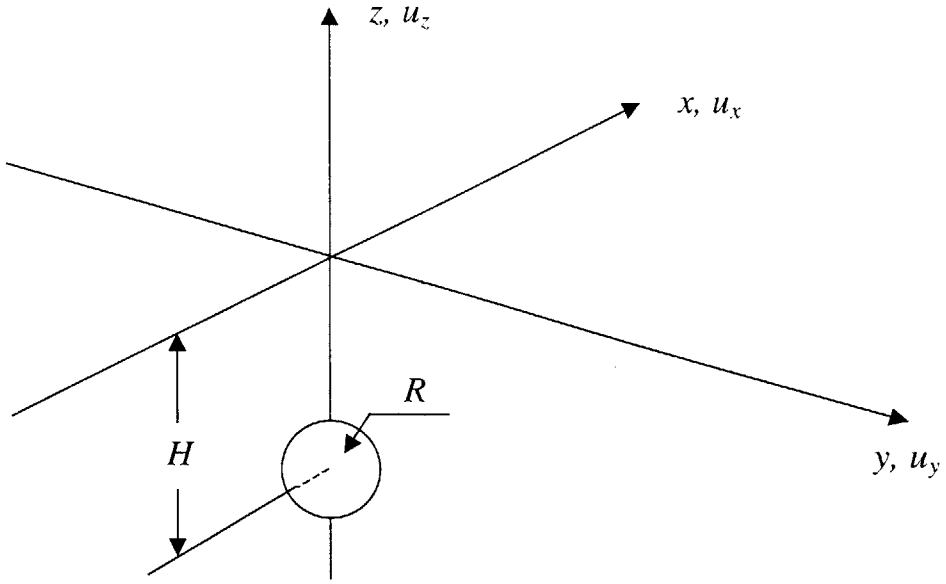

Figure 7.2. Spherical cavity contraction in half space

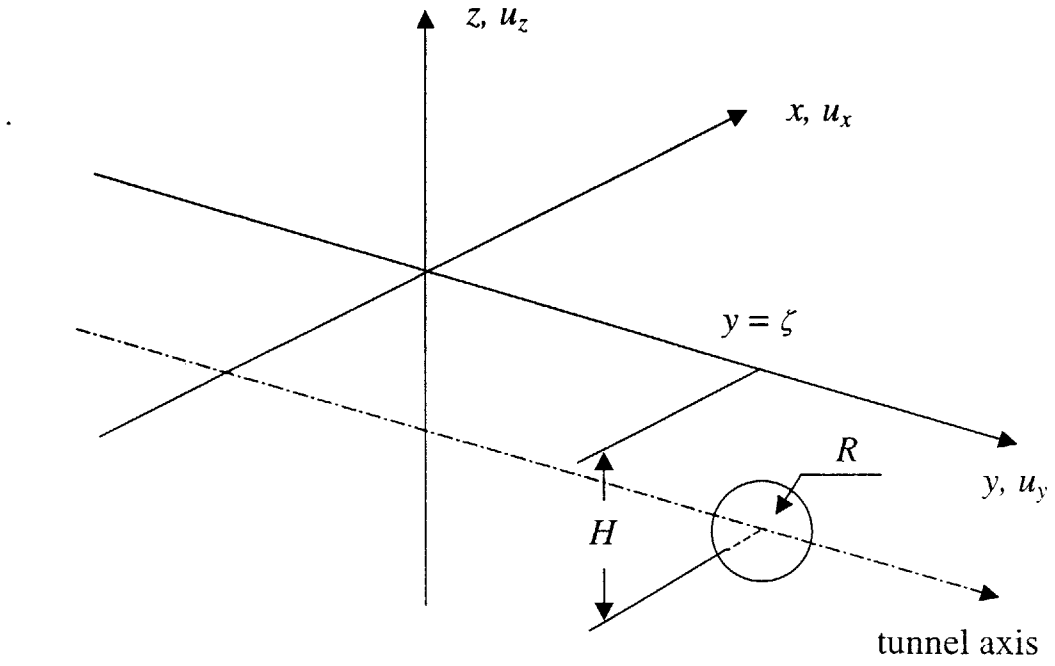

Figure 7.3. Spherical cavity contraction along tunnel axis in half space – Green function

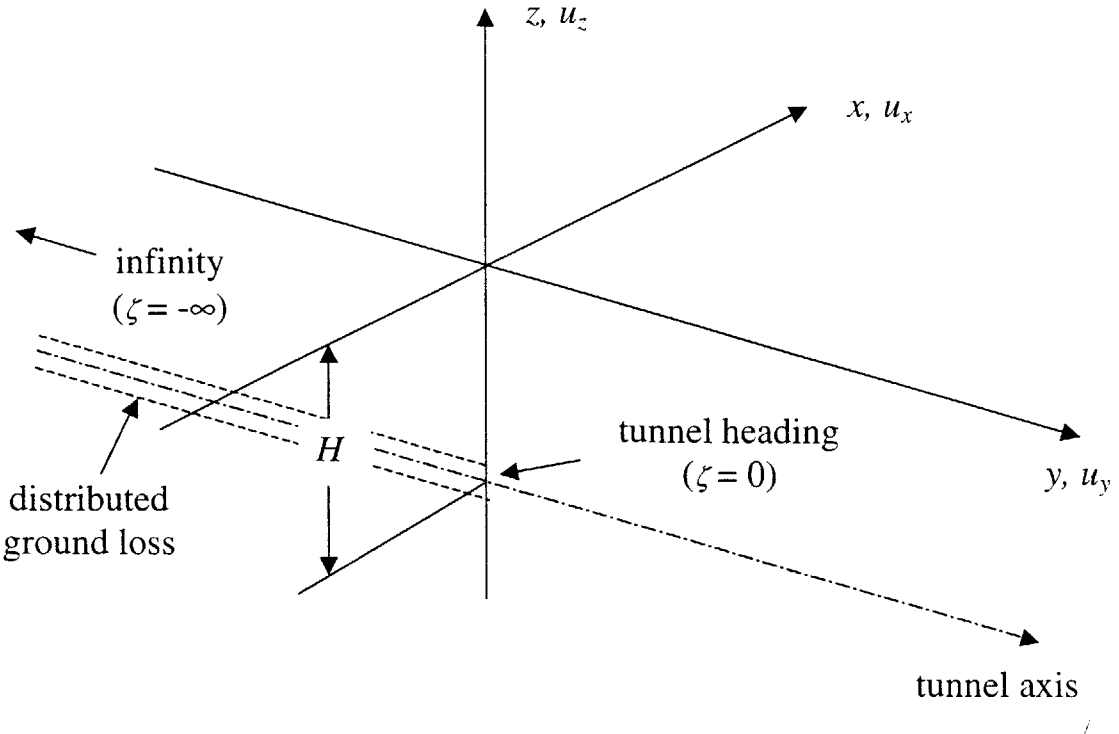

Figure 7.4. Modeling of semi-infinite tunnel – Distributed ground loss

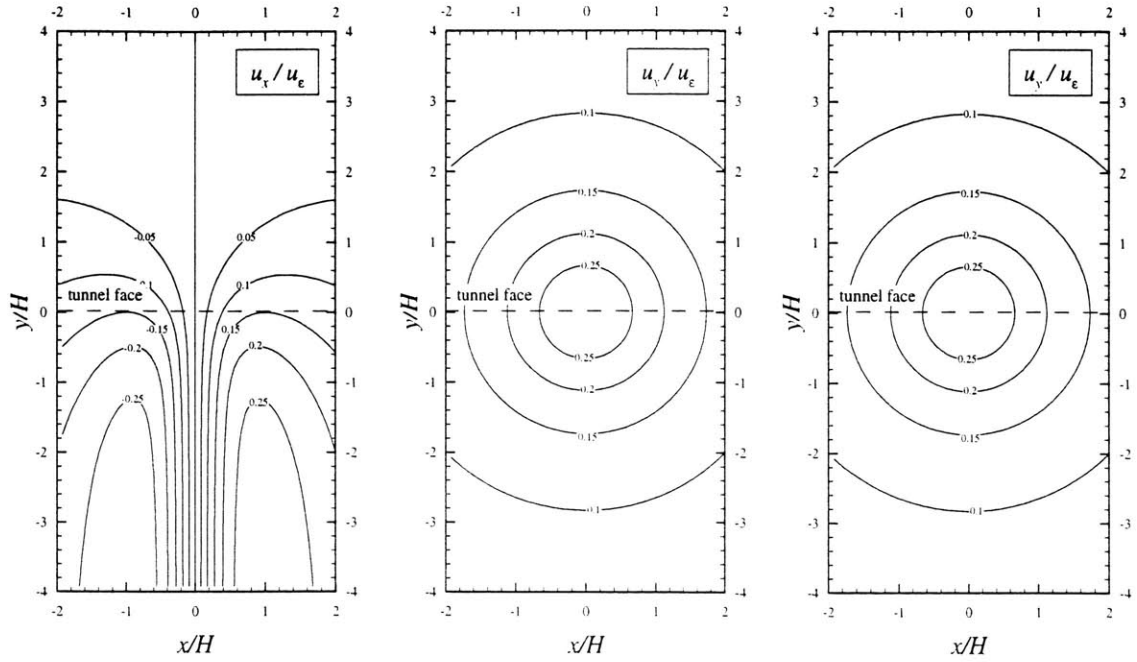

Figure 7.5. Contours of normalized lateral displacement, u_x/u_ε, for $R/H = 0.2$, $\nu = 0.25$

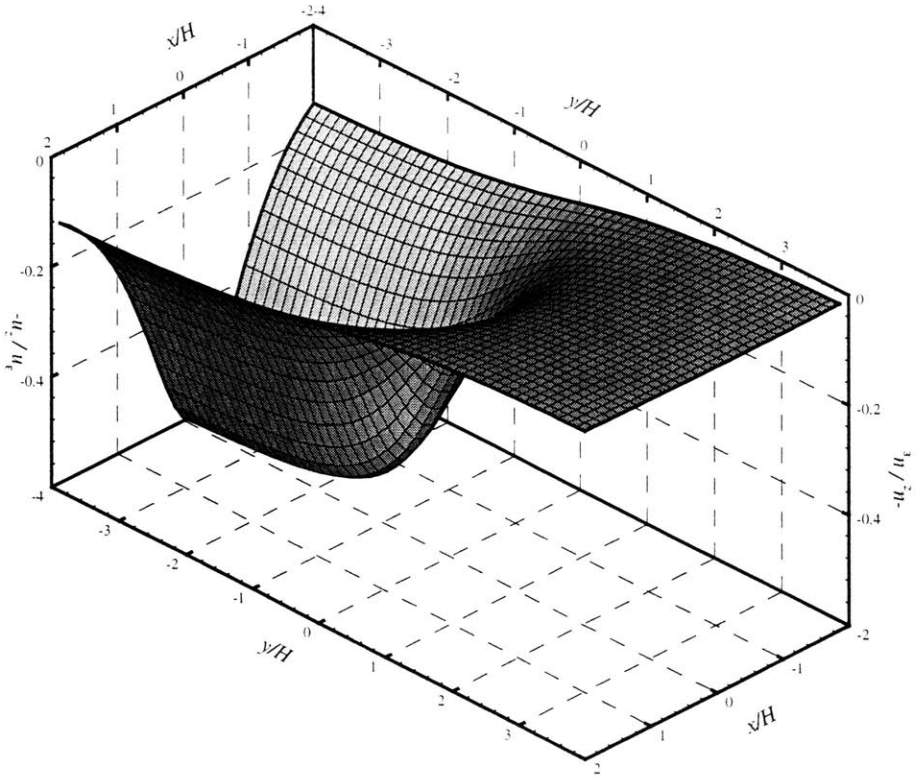

Figure 7.6. Deformed ground surface for $R/H = 0.2$, $\nu = 0.25$

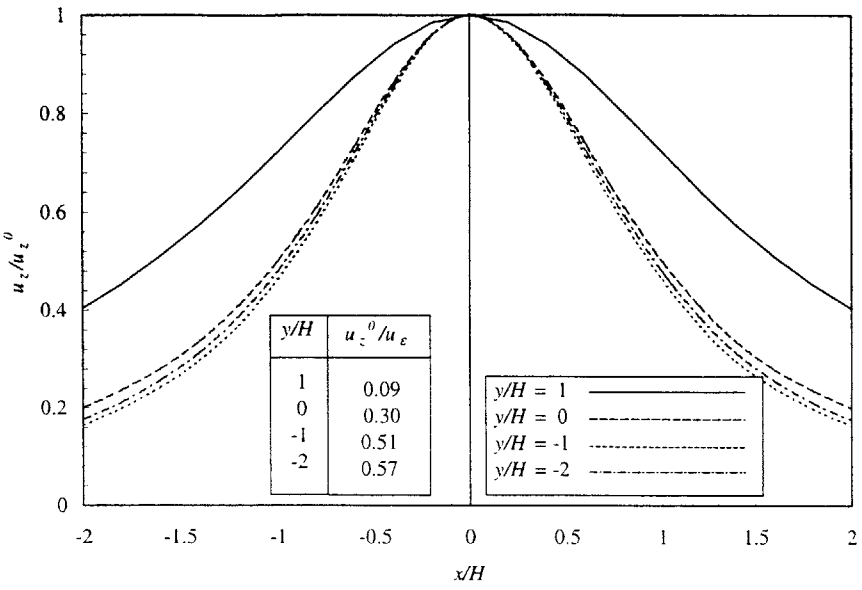

Figure 7.7. Influence of proximity to tunnel heading on surface settlements for

$R/H = 0.2,\ \nu = 0.25$

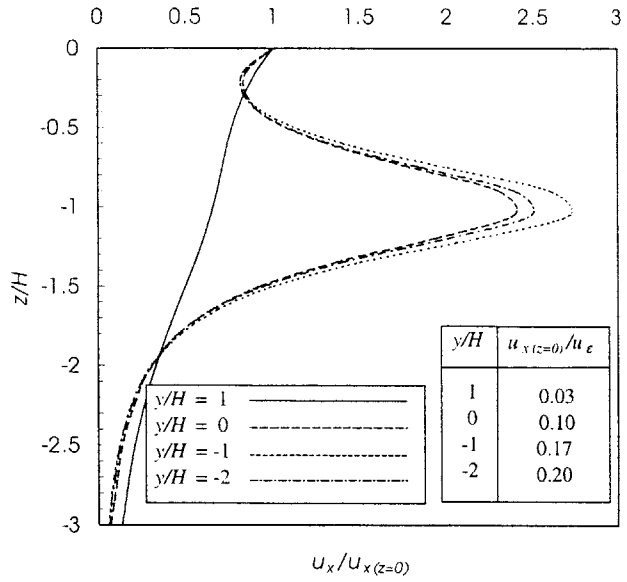

Figure 7.8. Influence of proximity to tunnel heading on lateral displacements at $x = 2 \cdot R$ for

$R/H = 0.2, \nu = 0.25$

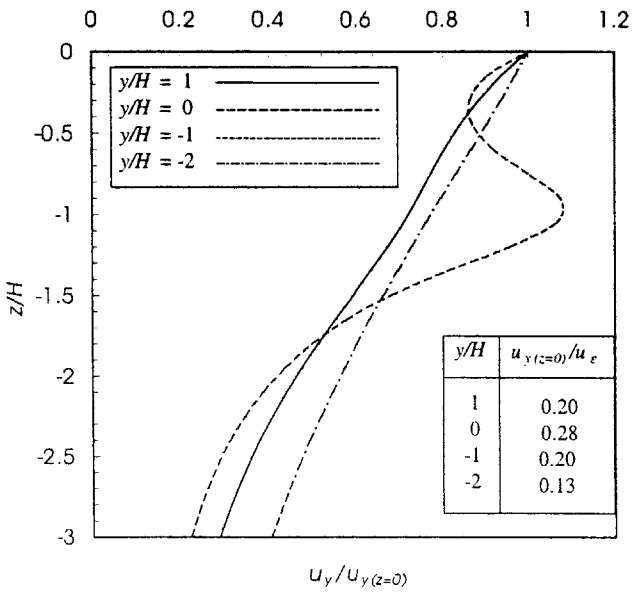

Figure 7.9. Influence of proximity to tunnel heading on longitudinal displacements at $x = 2{\cdot}R$ for $R/H = 0.2, \nu = 0.25$

8. Summary, Conclusions, and Further Recommendations

8.1. Summary

This thesis has re-derived and studied analytical solutions to model ground displacements due to tunneling based on continuum mechanics. Some solutions have been modified and some others have been proposed. Ground deformation patterns, resulting from the deformation of a tunnel have been studied and the factors that affect the distribution of displacements inside the ground have been identified and, in some cases, re-defined in a more consistent form.

- A comparison of exact and approximate solutions for the displacements due to a 2-D circular tunnel in elastic ground has been drawn. It has been found that both solutions yield similar results in the far field for relatively deep tunnels (i.e., $R/H < 0.45$).
- Geometry effects have been investigated by comparing the displacements due to 2-D square vs. circular tunnels in elastic ground. It was found that geometry effects are confined to a region near the tunnel wall, though both solutions predict similar displacement patterns in the far field (one radius away from the tunnel).
- Effects of plasticity have been studied. It was found that a local zone of plasticity is likely to develop around the tunnel wall. However, the displacement patterns in the far field are controlled by the elastic solution. A simple reduction factor that accounts for plastic behavior has been proposed in order to correlate convergence measurements at the tunnel wall with ground loss predicted by elastic solutions.
- Ground displacements predicted by the elastic solutions have been compared with in-situ measurements for a total of four case studies of single tunnels in an variety of soils and excavated by means of different construction methods. A simple set of charts has been proposed in order to obtain the input parameters for the elastic and average dilation models. It was found that the input parameters obtained from the aforementioned case studies are within the range expected for three of these cases. Good agreement between predicted and observed displacements was found, except in the case of a deep NATM tunnel in heavily overconsolidated and fissured London Clay. For this particular case, the measured settlement troughs predicted by the elastic solution are much narrower than those predicted.

- Effects of proximity of the tunnel heading (i.e., 3-D effects) have been studied by considering a semi-infinite tunnel in elastic half-space. It was found that 3-D effects are important in a zone up to $2H$ behind the tunnel heading. 2-D and 3-D solutions predict essentially the same displacement patterns elsewhere.

8.2. Modeling Considerations

The parameters that control the distribution of ground displacements are: i) uniform convergence displacement, u_ε, which is related to the ground loss; ii) relative distortion, ρ, which is related to the ground conditions (K_0), the construction procedure, soil-structure interaction (r_p), and Poisson ratio, ν; and iii) Poisson ratio, ν, if elastic or average dilation parameter, α. The factors that influence the parameters controlling the ground displacements are summarized below:

Influence of Ground Conditions

- Nearly normally consolidated deposits are likely to have more anisotropy of the initial state of stresses (since $K_0 < 1$) than lightly overconsolidated deposits (OCR ≈ 4, $K_0 \approx 1$). This initial stress anisotropy leads to a larger contribution of the pure distortion mode. This results in a narrower settlement trough and smaller inwards horizontal movements (in many cases even outwards) at the tunnel springline.
- Poisson ratio strongly affects the ratio between the relative magnitude of the surface displacements and the displacements inside the ground.
- The friction and dilation angles, cohesion intercept, and shear stiffness control the plastic behavior of the soil. A simple reduction factor has been proposed in order to correlate the ground loss measured at the tunnel wall in order to predict the far field displacements by means of elastic solutions.

Influence of Construction Method

- NATM construction method leads to a larger volume of ground loss, since large deformations at the tunnel head are allowed. Lower values of relative distortion are also expected, due to the fact that the internal pressure ratio, r_p, is close to zero.
- Excavation by means of TBM machines leads to higher values of relative distortion since the internal pressure ratio is likely to be high, especially if the tail void gap is filled with pressurized grouting. If stability is improved at the face either by means of a slurry (Slurry shield machines) or earth pressures (EPB machines), the ground loss is likely to be reduced, which increases even more the contribution of the distortion mode relative to the uniform convergence.

Soil Structure Interaction

- Soil structure interaction effects can only be conceptually taken into account by the relative distortion parameter. It is assumed that the internal pressure arises from the ring effect of the lining while compressed. This pressure is assumed to be distributed uniformly along the tunnel wall, since the lining has a very high axial stiffness in comparison to its bending stiffness. If the lining is placed without allowing large deformations to occur (e.g., pre-cast segmental lining expanded behind the shield), the internal pressure ratio is likely to be high, thus leading to a high relative distortion. On the other hand, if large deformations are allowed before placing the lining (e.g., shotcrete if NATM is used), the internal pressure ratio is likely to be low, thus leading to a lower value of relative distortion.

8.3. Further Recommendations

- An elastic solution for the 3-D distortion problem can be obtained by superimposing Neuber (1946) sources. The solution can be used as a Green function in order to model the 3-D effects of the distortion component by integrating the functions over the tunnel axis. This would serve to complete the set of 3-D solutions needed in order to model ground displacements near the tunnel heading for normally consolidated deposits (likely to have

relatively high contribution of the distortion mode). A technique proposed by Fares (1987) is particularly interesting in this regard, since it provides a straightforward algorithm in order to convert infinite space solutions (e.g., Neuber sources) into half-space solutions.

- 3-D plastic solutions can be introduced in the solutions presented in this thesis by following a similar approach than for the 2-D case.
- In order to model complex 3-D construction procedures, the basic solutions presented throughout this thesis can be directly superimposed. Grouting activities can be introduced in the analysis by means of 2 or 3-D cavity expansions. The stacked drift construction of the main cavern at Río Piedras station can be modeled by superimposing either point or square ground losses and point distortions at each drift and for the cavern as a hole after the excavation of the core material. This direct superposition of solution, straightforward on its own sake, needs to be experimentally validated.
- It is believed that layered media and non-linear soil stress-strain behavior can affect the displacement patterns around tunnels. However, the effect of the aforementioned issues remains uncertain on its quantification.
- Although three of the four examples have shown encouraging results, further experimental validation of these methods is needed from well-documented case studies that include both inclinometer and surface settlement data.

References

Attewell, P. B., and Farmer, I. W. (1974); "Ground Deformations Resulting from Shield Tunneling in London Clay". *Canadian Geotechnical Journal.* Vol. 11, pp. 380-395.

Bernat, S., Cambou, B., and Dubois, P. (1999); "Assessing a Soil Tunneling Numerical Model Using Field Data". *Geotechnique*, 49, No. 4, pp. 427-452.

Boresi, A. P. and Chong, K. P. (1987); "Elasticity in Engineering Mechanics". Elsevier Science Publishing Co., Inc., pp. 394-397.

Bowers, K. H., Hiller, D. M., and New, B. M. (1996); " Ground Movements Over Three Years at the Heathrow Express Trial Tunnel". *Geotechnical Aspects of Underground Construction in Soft Ground*, Mair and Taylor (eds.), Balkema, Rotterdam, pp. 647-652.

Burd, H. J., Houlsby, G. T., Chow, L., Augarde, C. E., and Liu, G. (1994); "Analysis of Settlement Damage to Masonry Structures". *Numerical Methods in Geotechnical Engineering*, Smith (ed.), pp. 203-209.

Clough, G. W., Sweeney, B. P., and Finno, R. J. (1983); "Measured Soil Response to EPB Shield Tunneling". *Journal of Geotechnical Engineering*, Vol. 109, No. 2, pp. 131-149.

Dasari, G. R., Rawlings, and C. G., Bolton, M. D. (1996); "Numerical Modeling of a NATM Tunnel Construction in London Clay". *Geotechnical Aspects of Underground Construction in Soft Ground*, Mair and Taylor (eds.), Balkema, Rotterdam, pp. 491-497.

Deane, A. P. and Basset, R. H. (1995); "The Heathrow Express Trial Tunnel". *Proc. Instn. of Civ. Engrs., Geotech. Engrg.*, 113, pp. 144-156.

Fares, N. (1987); "Green's Functions for Plane-Layered Elastostatic and Viscoelastic Regions with Applications to 3-D Crack Analysis". Ph.D. Thesis, Massachusetts Institute of Technology, Cambridge, Massachusetts.

Kovacevic, N., Edmonds, H. E., Mair, R. J., and Higgings, K.G. (1996); "Numerical Modeling of the NATM and Compensation Grouting Trials at Redcross Way". *Geotechnical Aspects of Underground Construction in Soft Ground*, Mair and Taylor (eds.), Balkema, Rotterdam, pp. 553-559.

Lee, K. M. and Rowe, R. K. (1990); "An Analysis of Three-Dimensional Ground Movements: The Thunder Bay Tunnel". *Canadian Geotechnical Journal*, Vol. 28, pp.25-41.

Longanathan, N. and Poulos, H. G. (1998); "Analytical Prediction for Tunneling-Induced Ground Movements in Clay". *Journal of Geotechnical and Geoenvironmental Engineering*, Vol. 124, No. 9, pp. 846-856.

Macklin, S. R. (1999); "The Prediction of Volume Loss due to Tunneling in Overconsolidated Clay Based on Heading Geometry and Stability Number". *Ground Engineering*, June 1999.

Mesri, G., Abdel-Ghaffar, M. E. M. (1993); "Cohesion Intercept in Effective Stress Stability Analysis". *Journal of Geotechnical Engineering*, Vol. 119, No. 8, pp. 1229-1249.

Mindlin, R. D. (1939); "Stress Distribution Around a Tunnel", *Transactions*, ASCE, pp. 1117-1153.

Mindlin, R. D. and Cheng, D. H. (1950); "Thermoelastic Stress in the Semi-Infinite Solid". *Journal of Applied Physics*, Vol. 21, pp. 931-935.

Muskhelishvili, N. I. (1963); "Some Basic Problems of the Mathematical Theory of Elasticity". P. Noordhoff Ltd., Groningen, The Netherlands.

Neuber, H. (1946); " Theory of Notch Stresses". *Edward Bros.*, Ann Arbor, Michigan.

Oettl, G., Stark, R. F., Hofstetter, G. (1998); "A Comparison of Elastic-Plastic Soil Models for 2D FE Analyses of Tunneling". *Computers and Geotechnics*, Elsevier Science Ltd., 23, pp. 19-38.

Oteo, C. S. and Sagaseta, C. (1996); "Some Spanish Experiences on Measurement and Evaluation of Ground Displacements Around Urban Tunnels". *Geotechnical Aspects of Underground Construction in Soft Ground*, Mair and Taylor (eds.) London, pp. 631-736.

Panet, M. and Guenot, A. (1982); "Analysis of Convergence Behind Face of a Tunnel". Proceedings, Tunneling'82, pp. 197-204.

Peck, R. B. (1969); "Deep Excavations and Tunnels in Soft Ground". *Proceedings of the 7th International Conference on Soil Mechanics and Foundation Engineering*, Mexico City, State of the Art Volume, pp. 225-290.

Romo, M. P. (1997); "Soil Movements Induced by Slurry Shield Tunneling". *Proceedings of the 14th International Conference on Soil Mechanics and Foundation Engineering*, Hamburg, 3, pp. 1473-1481.

Rowe, R. K., and Lee, K. M. (1992); "An Evvaluation of Simplified Techniques for Estimating Three-Dimensional Undrained Ground Movements due to Tunneling in Soft Soils". *Canadian Geotechnical Journal*, 29, pp. 39-52.

Sagaseta, C. (1987); "Analysis of Undrained Soil Deformation due to Ground Loss". *Geotechnique*, London, England, 37, No. 3, pp. 301-320.

Sagaseta, C. (1999); Personal communication.

Schmidt, B. (1988). Discussion, *Geotechnique*, Vol. 38, No. 4, p. 647.

Sen, B. (1950); "Note on the Stresses Produced by Nuclei of Thermo-Elastic Strain in a Semi-Infinite Elastic Solid", *Quarterly Applied Mathematics*, Vol. 8, pp. 365-369.

Simpson, B. (1999); "Engineering Needs". *Proceedings of the Second International Symposium on Prefailure Deformation of Geomaterials*, Torino, Italy, pp. 142-157.

Stallebrass, S. E., Jovi, V. and Taylor, R. N. (1990); "The Influence of Recent Stress History on Ground Movements Around Tunnels". *Proceedings of the International Symposium on Prefailure Deformation of Geomaterials*, Sapporo, Japan. Balkema, Rotterdam.

Terzaghi, K. and Ritchart, F. E. (Jr.) (1952 and 1953); " Stresses in Rock About Cavities". *Geotechnique*, Volume III, pp. 57-90.

Timoshenko, S. P., and Goodier, J. N. (1970); "Theory of Elasticity". Third Edition, McGraw Hill Kogakusha, Ltd.

Verruijt, A. and Booker, J. R. (1996); "Surface Settlements due to Deformation of a Tunnel in an Elastic Half Plane", *Geotechnique*, London, England, 46, No. 4, pp. 753-756.

Verruijt, A. (1997); "A Complex Variable Solution for a Deforming Tunnel in an Elastic Half-Plane". *International Journal for Numerical and Analytical Methods in Geomechanics*, Vol. 21, pp. 77-89.

Wroth, C. P. (1971); "Some Aspects of the Elastic Behaviour of Overconsolodated Clay". *Proceedings of the Roscoe Memorial Symposium*, pp. 347-361.

Yu, H. S. and Rowe, R. K. (1998); " Plasticity Solutions for Soil Behavior Around Contracting Cavities and Tunnels". Research Report No. 165.06.1998, The University of Newcastlle, Asutralia, pp. 1-50.

Appendix I

Complex Variable Solution for a Deforming Circular Tunnel in an Elastic Half-Plane

Complex variable formulation of the theory of planar elasticity

The governing equation of the plane elasticity can be expressed in terms of Airy's stress function as follows:

$$\nabla^2 \cdot \nabla^2 \cdot F = 0 \qquad \{I\text{-}1\}$$

where the ∇^2 operator in Cartesian coordinates is given by:

$$\nabla^2 = \frac{\partial^2}{\partial x^2} + \frac{\partial^2}{\partial y^2} \qquad \{I\text{-}2\}$$

Introducing the following transformation:

$$z = x + i \cdot y \qquad \{I\text{-}3\}$$

the ∇^2 operator can be expressed as follows:

$$\nabla^2 = 4 \cdot \frac{\partial^2}{\partial z \cdot \partial \bar{z}} \qquad \{I\text{-}4\}$$

where the overscript "$\bar{}$" stands for the complex conjugate of the variable.

Introducing {I.4}, the governing equation of plane elasticity yields:

$$\frac{\partial^4 F}{\partial z^2 \cdot \partial \bar{z}^2} = 0 \qquad \{I\text{-}5\}$$

Hence, it can readily be seen that Airy's stress function is given by the following general expression (e.g. Muskhelishvili, 1962):

$$2 \cdot F = \bar{z} \cdot \phi(z) + z \cdot \phi_1(\bar{z}) + \chi(z) + \chi_1(\bar{z}) \qquad \{I\text{-}6\}$$

where ϕ, χ, ϕ_1, and χ_1 are arbitrary functions which are found by imposing the boundary conditions of the problem. In order for Airy's stress function to be real, ϕ, χ, ϕ_1, and χ_1, the following condition must be fulfilled:

$$\left.\begin{aligned} \phi_1(\bar{z}) &= \overline{\phi(z)} \\ \chi_1(\bar{z}) &= \overline{\chi(z)} \end{aligned}\right\} \qquad \{I\text{-}7\}$$

Hence, the general solution for the problem is:

$$2 \cdot F = \bar{z} \cdot \phi(z) + z \cdot \overline{\phi(z)} + \chi(z) + \overline{\chi(z)} \qquad \{I\text{-}8\}$$

The functions ϕ and χ are called Goursat functions. The displacement components are given in terms of the Goursat functions as follows:

$$2 \cdot G \cdot u_z = \kappa \cdot \phi(z) - z \cdot \frac{\overline{d\phi}}{dz} - \bar{\psi} \qquad \{I\text{-}9\}$$

where:

$$\psi = \frac{d\chi}{dz} \qquad \{I\text{-}10\}$$

$$u_z = u_x + i \cdot u_y \qquad \{I\text{-}11\}$$

$$\kappa = 3 - 4 \cdot \nu \qquad \{I\text{-}12\}$$

On the other hand, the stresses can be expressed as derivatives of the Airy stress function:

$$\sigma_x + \sigma_y = 2 \cdot \left(\frac{d\phi}{dz} + \overline{\frac{d\phi}{dz}} \right) \qquad \{I\text{-}13\}$$

$$\sigma_y - \sigma_x + 2 \cdot i \cdot \tau_{xy} = 2 \cdot \left(\bar{z} \cdot \frac{d^2\phi}{dz^2} + \frac{d\psi}{dz} \right) \qquad \{I\text{-}14\}$$

The boundary conditions are usually in terms of either displacements or stresses. In the first case, the boundary conditions are imposed on equation {I-9}. In the second case, it is most convenient to express the boundary condition in terms of the integral of the tractions along the boundary:

$$\Sigma = \Sigma_1 + i \cdot \Sigma_2 = i \cdot \int_0^s \left(t_x + i \cdot t_y \right) \cdot ds \qquad \{I\text{-}15\}$$

where s is a parametric coordinate which describes the position along the boundary and t_x, t_y are the traction boundary conditions. It can be shown that equation {I-15} can be rearranged as:

$$\Sigma = \phi(z) + z \cdot \overline{\frac{d\phi}{dz}} - \overline{\psi(z)} + C \qquad \{I\text{-}16\}$$

where C is an integration constant. For the problem discussed herein (i.e., deforming circular tunnel in a half-plane), the constant C can be omitted (i.e., $C = 0$ since it can be incorporated into a rigid body motion of the entire plane.

Conformal mapping

The problem domain is outlined in Figure I.1, where it can be seen that the domain boundaries cannot be mathematically expressed in one term of the Cartesian variables, x and y. In order to circumvent that problem, the z–plane is mapped onto the ζ-plane by means of the following transformation:

$$\zeta(z)=\frac{i\cdot z\cdot\left(1+\alpha^2\right)-H\cdot\left(1-\alpha^2\right)}{i\cdot z\cdot\left(1+\alpha^2\right)+H\cdot\left(1-\alpha^2\right)} \qquad \{\text{I-17}\}$$

where H is the depth to centerline (Figure I.1) and α is given by:

$$\alpha=\frac{H}{R}-\sqrt{\left(\frac{H}{R}\right)^2-1} \qquad \{\text{I-18}\}$$

where R is the tunnel radius. This conformal transformation has the effect of transforming the problem domain in a much simpler domain, bounded by two concentric circles (Figure I.2) that can be defined by means of only one coordinate (the angle, θ). The horizontal boundary given by y=0 in the z-space is mapped onto a circle of unit radius in the ζ-space and the circular tunnel boundary given by $\left(x^2\right)+\left(H+y\right)^2-R^2=0$ at the z-space onto a circle of radius α in the ζ-space. Because the conformal transformation is an analytic function in the problem domain, the Goursat functions, ϕ and ψ, which must be analytic in the z-plane, can be expressed in terms of the mapped coordinate ζ:

$$\phi(z)=\phi(z(\zeta))=\phi(\zeta) \qquad \{\text{I-19a}\}$$

$$\psi(z)=\psi(z(\zeta))=\psi(\zeta) \qquad \{\text{I-19b}\}$$

As both Goursat functions are analytic in the mapped domain, they can be expanded in Laurent series:

$$\phi(\zeta) = a_0 + \sum_{k=1}^{\infty} a_k \cdot \zeta^k + \sum_{k=1}^{\infty} b_k \cdot \zeta^{-k} \qquad \{\text{I-20a}\}$$

$$\psi(\zeta) = c_0 + \sum_{k=1}^{\infty} c_k \cdot \zeta^k + \sum_{k=1}^{\infty} d_k \cdot \zeta^{-k} \qquad \{\text{I-20b}\}$$

where the coefficients a_k, b_k, c_k, and d_k, must be determined by applying the boundary conditions.

Boundary conditions

The stress free boundary condition at the boundary $y = 0$ (i.e., the stress-free surface) is applied by means of equation {I-16}:

$$\left(\phi(z) + z \cdot \overline{\frac{d\phi}{dz}} - \overline{\psi(z)} \right)_{y=0} = 0 \qquad \{\text{I-21}\}$$

after conformal mapping, equation {I-21} becomes:

$$\left(\phi(\zeta) + \frac{1}{2} \cdot \left(1 - \sigma^{-2}\right) \cdot \overline{\frac{d\phi}{d\zeta}} - \overline{\psi(\zeta)} \right)_{|\zeta|=1} = 0 \qquad \{\text{I-22}\}$$

where $\sigma = e^{i \cdot \theta}$ represents the mapped coordinate at the outer boundary (i.e., stress free surface). Hence, after straightforward algebra, the boudary condition {I-22} can be expressed in terms of the Laurent series coefficients:

$$\sum_{k=1}^{\infty} a_k \cdot \sigma^k + \sum_{k=1}^{\infty} b_k \cdot \sigma^{-k} + \frac{1}{2} \cdot \sum_{k=1}^{\infty} (k+1) \cdot \bar{a}_{k+1} \cdot \sigma^{-k} - \frac{1}{2} \cdot \sum_{k=2}^{\infty} (k-1) \cdot \bar{b}_{k-1} \cdot \sigma^k - \ldots$$

$$\ldots - \frac{1}{2} \cdot \sum_{k=2}^{\infty} (k-1) \cdot \bar{a}_{k-1} \cdot \sigma^{-k} + \frac{1}{2} \cdot \sum_{k=1}^{\infty} (k+1) \cdot \bar{b}_{k+1} \cdot \sigma^k + a_0 + \frac{1}{2} \cdot \bar{a}_1 + \frac{1}{2} \cdot \bar{b}_1 + \bar{c}_0 + \ldots \qquad \{\text{I-23}\}$$

$$\ldots + + \sum_{k=1}^{\infty} \bar{c}_k \cdot \sigma^{-k} + \sum_{k=1}^{\infty} \bar{d}_k \cdot \sigma^k = 0$$

from where the Laurent coefficients c_k and d_k can be obtained by setting the coefficients of all equal powers of σ equal to zero:

$$c_0 = -\bar{a}_0 - \frac{1}{2} \cdot a_1 - \frac{1}{2} \cdot b_1 \qquad \{\text{I-24a}\}$$

$$c_k = -\bar{b}_k + \frac{1}{2} \cdot (k-1) \cdot a_{k-1} - \frac{1}{2} \cdot (k+1) \cdot a_{k+1} \qquad \{\text{I-24b}\}$$

$$d_k = -\bar{a}_k + \frac{1}{2} \cdot (k-1) \cdot b_{k-1} - \frac{1}{2} \cdot (k+1) \cdot b_{k+1} \qquad \{\text{I-24c}\}$$

The prescribed displacement at the tunnel wall boundary condition is applied by means of equation {I-9}, after conformal mapping:

$$2 \cdot G \cdot u_z(\alpha \cdot \sigma) = \left(\kappa \cdot \phi(\alpha \cdot \sigma) - \frac{-\alpha \cdot \sigma - (1 - 2 \cdot \alpha^2) + \alpha \cdot (2 - \alpha^2) \cdot \sigma^{-1} - \alpha^2 \cdot \sigma^{-2}}{2 \cdot (1 - \alpha \cdot \sigma)} \cdot \frac{\overline{d\phi}}{d\zeta} - \overline{\psi(\alpha \cdot \sigma)} \right) \qquad \{\text{I-25}\}$$

where $\alpha \cdot \sigma = \zeta$ at the tunnel boundary and $\sigma = e^{i \cdot \theta}$ (see Figure I.2). It is convenient to rewrite the boundary condition {I-25} as follows:

$$2\cdot G\cdot u_z(\alpha\cdot\sigma)\cdot(1-\alpha\cdot\sigma)=\left(\begin{array}{l}\kappa\cdot\phi(\alpha\cdot\sigma)-\overline{\psi(\alpha\cdot\sigma)}-\ldots\\ \ldots-\dfrac{-\alpha\cdot\sigma-(1-2\cdot\alpha^2)+\alpha\cdot(2-\alpha^2)\cdot\sigma^{-1}-\alpha^2\cdot\sigma^{-2}}{2}\cdot\dfrac{\overline{d\phi}}{d\zeta}\end{array}\right) \qquad \{\text{I-25}\}$$

It can readily be seen that the right-hand side of equation {I-25}, after Laurent series expansion, will be expressed in Fourier series terms, since at that boundary the terms of the Laurent series are of the form $\zeta^k = \alpha\cdot e^{i\cdot k\cdot\theta}$. Hence, it is convenient to expand the displacement boundary condition (left-hand side of equation {I-25}) in Fourier terms:

$$2\cdot G\cdot(1-\alpha\cdot\sigma)\cdot u_z(\sigma)=\sum_{k=-\infty}^{\infty}A_k\cdot\sigma^k \qquad \{\text{I-26}\}$$

where the coefficients A_k are obtained as follows:

$$A_k=\frac{1}{2\cdot\pi}\cdot\int_0^{2\cdot\pi}2\cdot G\cdot(1-\alpha\cdot\sigma)\cdot u_z(\sigma)\cdot\sigma^{-k}\cdot d\theta \qquad \{\text{I-27}\}$$

Introducing equation {I-26} in {I-25} and expanding the right-hand side in Laurent series and introducing equations {I-24} yields a relationship between the Laurent coefficients a_k and b_k and the Fourier expansion coefficients A_k:

$$(1-\alpha^2)\cdot(k+1)\cdot\bar{a}_{k+1}-(\alpha^2+\kappa\cdot\alpha^{-2\cdot k})\cdot b_{k+1}=(1-\alpha^2)\cdot k\cdot\bar{a}_k-(1+\kappa\cdot\alpha^{-2\cdot k})\cdot b_k+A_{-k}\cdot\alpha^{-k} \qquad \{\text{I-28a}\}$$

$$(1+\kappa\cdot\alpha^{2\cdot k+2})\cdot\bar{a}_{k+1}+(1-\alpha^2)\cdot(k+1)\cdot b_{k+1}=(1-\alpha^2)\cdot k\cdot b_k+\alpha^2\cdot(1+\kappa\cdot\alpha^{2\cdot k})\cdot\bar{a}_k+\bar{A}_{k+k}\cdot\alpha^{k+1} \qquad \{\text{I-28b}\}$$

From equations {I-28}, the coefficients ca be calculated recursively. The starting values, a_1 and b_1 can be determined from the coefficients of the powers σ^0 and σ^1:

$$\left(1-\alpha^2\right)\cdot \bar{a}_1 - \left(\kappa+\alpha^2\right)\cdot b_1 = A_0 - (\kappa+1)\cdot a_0 \qquad \{\text{I-29a}\}$$

$$\left(1+\kappa\cdot\alpha^2\right)\cdot \bar{a}_1 + \left(1-\alpha^2\right)\cdot b_1 = \bar{A}_1\cdot\alpha + (\kappa+1)\cdot\alpha^2\cdot \bar{a}_0 \qquad \{\text{I-29b}\}$$

It can be seen that only the a_0 value remains indeterminate and is found by requiring that the Laurent coefficients vanish for $k \rightarrow \infty$.This is done by means of taking advantage of the linearity of the recursive relations (equations {I-28}). Hence, two tentative values of a_0 are used to calculate an approximate value of a_∞ and the value that makes $a_\infty = 0$ is found by linear interpolation.

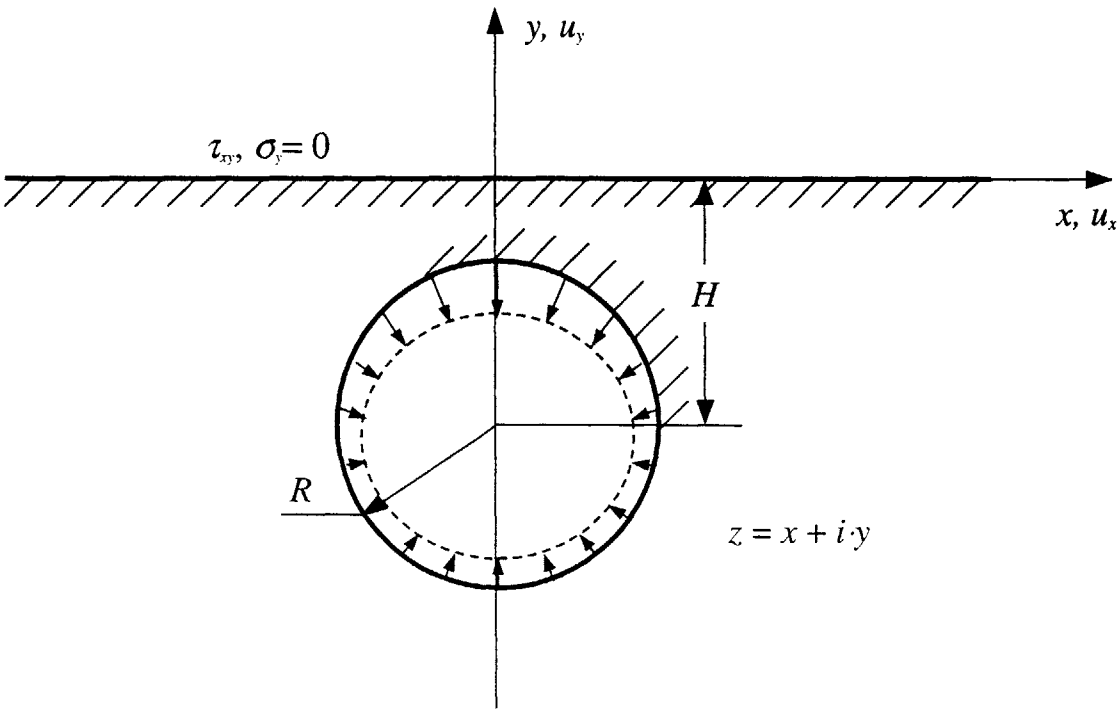

Figure I.1. Problem outline

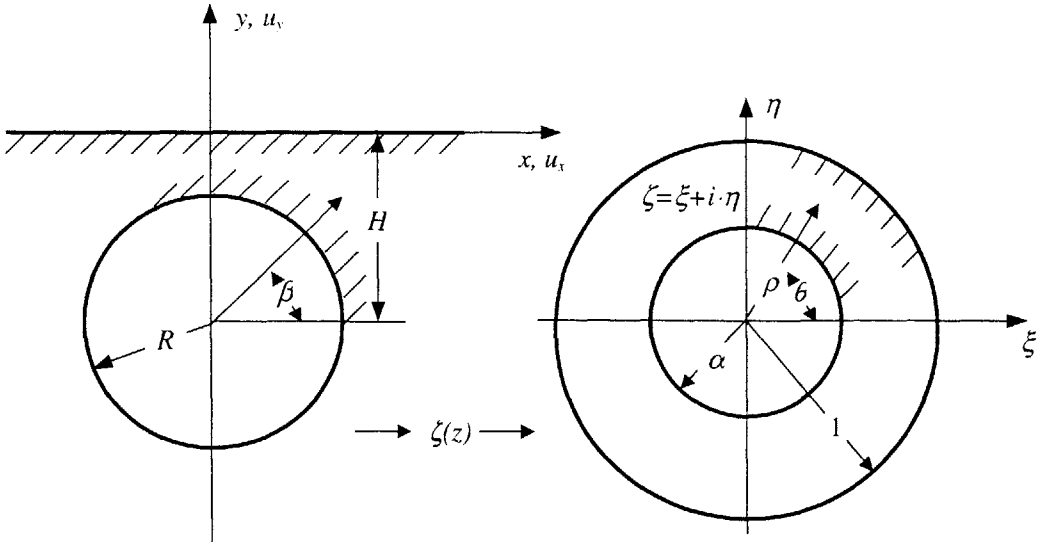

Figure I.2. Conformal mapping (after Verruijt, 1997)

Appendix II

MATLAB Subroutines

File: tunnel.m

```
clear
%
%  2-D TUNNEL
%
%  Generates the ground displacements due to a combination of uniform
%  convergence and distortion at the tunnel wall using the exact and
%  appproximate elastic solutions
%
%  G = shear modulus, nu = Poisson ratio, H = depth to centerline, r = Radius
%  N, NA = number of terms used to obtain the Laurent coefficients for
%  infinite order, NC = number of terms needed for the Laurent series,
%  ud = maximum horizontal displacement at the tunnel wall due to distortion,
%  ue = displacement at the tunnel wall due to uniform convergence,
%  plot.dat = input data file for Techplot
%
%
G=1;
nu=0.25;
H=1;
r=.45;
kg=3-4*nu;
alpha=H/r-((H/r)^2-1)^0.5;
N=150;
NA=150;
NC=ceil(8-11.75*r/H+31.25*(r/H)^2)
ud=1;
ue=-1;
[AP,AN]=gena(NA,alpha,G,ud,ue);
AP(N+1)=0;
AN(N+1)=0;
ai0=0;
```

```
[ai,bi,ci,di]=genl(AP,AN,N,kg,ai0,alpha);
ALi=ai(N+1);
af0=1i;
[af,bf,cf,df]=genl(AP,AN,N,kg,af0,alpha);
ALf=af(N+1);
a0=(af0-ALf/(ALf-ALi)*(af0-ai0));
[a,b,c,d]=genl(AP,AN,N,kg,a0,alpha);
[nx,nnod,nel,con,x,y]=zdom(H,r);
[ux,uy]=calcu(x,y,a,b,c,d,alpha,H,kg,G,NC);
[uxa,uya]=calcua(-x,y,r,H,nu,ue,ud);
X=x(1:nx);
Y=y(1:nx);
UX=ux(1:nx);
UY=uy(1:nx);
UXA=uxa(1:nx);
UYA=uya(1:nx);
fid=fopen('c:\plots\plot.dat','w');
fprintf(fid,'VARIABLES = "x/H", "y/H", "ux/u0", "uy/u0"\nZONE T="EX-MESH",
N=%g, E=%g, F=FEPOINT, ET=QUADRILATERAL\n',nnod,nel);
fprintf(fid,'%g %g %g %g\n',[x; y; ux; uy]);
fprintf(fid,'%g %g %g %g\n',transpose(con));
fprintf(fid,'ZONE T="AP-MESH", N=%g, E=%g, F=FEPOINT,
ET=QUADRILATERAL\n',nnod,nel);
fprintf(fid,'%g %g %g %g\n',[-x; y; uxa; uya]);
fprintf(fid,'%g %g %g %g\n',transpose(con));
fprintf(fid,'ZONE T="EX-SURF", I=%g, F=POINT\n',nx);
fprintf(fid,'%g %g %g %g\n',[X; Y; UX; UY]);
fprintf(fid,'ZONE T="AP-SURF", I=%g, F=POINT\n',nx);
fprintf(fid,'%g %g %g %g\n',[-X; Y; UXA; UYA]);
fclose(fid);
fid=fopen('c:\plots\plotxt.txt','w');
fprintf(fid,'SETTINGS:\n ue=%g ud=%g H=%g r=%g nu=%g\n',ue,ud,H,r,nu);
fclose(fid);
```

File: gena.m

```
function [AP,AN]=gena(N,a,G,ud,ue)
%
```

```
%
% Generates the Fourier coefficients
%
%
A2p(1:N)=0;
for k=2:N;
   A1n(k)=1i*a^(k-1-1)*(1-2*a^2+a^4);
end
A1p(1)=1i*(-2*a+a^3);
A1p(2)=1i*a^2;
%
A2p(1:N)=0;
A2n(1:N)=0;
A2p(1)=1i*a;
A2p(2)=-1i;
%
%
AP=(ud*A1p+ue*A2p)*2*G;
AN=(ud*A1n+ue*A2n)*2*G;
```

File: genl.m

```
function [a,b,c,d]=genl(AP,AN,N,kg,a0,alpha)
%
%
% Generates Laurent Coefficients
%
%
a(1)=a0;
a(2)=conj((1/((1-alpha^2)/(kg+alpha^2)+(1+kg*alpha^2)/(1-
alpha^2)))*(AP(1)/(kg+alpha^2)+conj(AP(2))*alpha/(1-
alpha^2)+conj(a(1))*(kg+1)*alpha^2/(1-alpha^2)-a(1)*(kg+1)/(kg+alpha^2)));
b(2)=(AP(1)-(kg+1)*a(1)-(1-alpha^2)*conj(a(2)))/(-(kg+alpha^2));
for kp=2:N
   k=kp-1;
   Q1(kp)=(1-alpha^2)*(k+1);
   Q2(kp)=-(alpha^2+kg*alpha^(-2*k));
   Q3(kp)=(1-alpha^2)*k;
```

```
    Q4(kp)=-(1+kg*alpha^(-2*k));
    Q5(kp)=AN(kp)*alpha^(-k);
    R1(kp)=(1+kg*alpha^(2*k+2));
    R2(kp)=(1-alpha^2)*(k+1);
    R3(kp)=alpha^2*(1+kg*alpha^(2*k));
    R4(kp)=(1-alpha^2)*k;
    R5(kp)=conj(AP(kp+1))*alpha^(k+1);
    b(kp+1)=1/(Q2(kp)/Q1(kp)-R2(kp)/R1(kp))*(conj(a(kp))*(Q3(kp)/Q1(kp)-
R3(kp)/R1(kp))+b(kp)*(Q4(kp)/Q1(kp)-R4(kp)/R1(kp))+Q5(kp)/Q1(kp)-
R5(kp)/R1(kp));
    a(kp+1)=conj(1/(Q1(kp)/Q2(kp)-R1(kp)/R2(kp))*(conj(a(kp))*(Q3(kp)/Q2(kp)-
R3(kp)/R2(kp))+b(kp)*(Q4(kp)/Q2(kp)-R4(kp)/R2(kp))+Q5(kp)/Q2(kp)-
R5(kp)/R2(kp)));
end
c(1)=-conj(a(1))-1/2*a(2)-1/2*b(2);
for kp=2:N
    k=kp-1;
    d(kp)=-conj(a(kp))+(k-1)/2*(b(kp-1))-(k+1)/2*b(kp+1);
    c(kp)=-conj(b(kp))+(k-1)/2*(a(kp-1))-(k+1)/2*a(kp+1);
end
```

File: zdom.m

```
function [nnx,nnod,nel,con,x,y]=zdom (H,r)
%
%
%  Generates the mesh (and connectivities) at which the displacements are to
%  be evaluated
%
%
Nx1=30;
Nx2=12;
Ny1=12;
Ny2=2*Ny1;
Ny3=Ny1+Ny2;
dx1=(2*H+r)/Nx1;
dy1=(H-r)/Ny1;
dy3=(H+r)/Ny3;
```

```
n=1;
nnx=Nx1+Nx2+1;

for ny=1:Ny1+1;
   for nx=1:Nx1+1;
      x(n)=(nx-1)*dx1-(2*H+2*r);
      y(n)=-(ny-1)*dy1;
      n=n+1;
   end
   for nx=1:Nx2;
      x(n)=Nx1*dx1+r*(1-cos(nx*pi/2/Nx2))-(2*H+2*r);
      y(n)=-(ny-1)*dy1;
      n=n+1;
   end
end
Nxf=Nx2-1;
for ny=1:Nx2;
   for nx=1:Nx1+1;
      x(n)=(nx-1)*dx1-(2*H+2*r);
      y(n)=-H+r*cos(ny*pi/2/Nx2);
      n=n+1;
   end
   for nx=1:Nxf
      x(n)=Nx1*dx1+r*(1-cos(nx*pi/2/Nx2))-(2*H+2*r);
      y(n)=-H+r*cos(ny*pi/2/Nx2);
      n=n+1;
   end
   Nxf=Nxf-1;
end
Nxf=Nxf+2;
for ny=1:Nx2;
   for nx=1:Nx1+1;
      x(n)=(nx-1)*dx1-(2*H+2*r);
      y(n)=-H+r*cos(ny*pi/2/Nx2+pi/2);
      n=n+1;
   end
   for nx=1:Nxf
      x(n)=Nx1*dx1+r*(1-cos(nx*pi/2/Nx2))-(2*H+2*r);
```

```
      y(n)=-H+r*cos(ny*pi/2/Nx2+pi/2);
      n=n+1;
   end
   Nxf=Nxf+1;
end
%
for ny=1:Ny3;
   for nx=1:Nx1+1;
      x(n)=(nx-1)*dx1-(2*H+2*r);
      y(n)=-(ny)*dy3-H-r;
      n=n+1;
   end
   for nx=1:Nx2;
      x(n)=Nx1*dx1+r*(1-cos(nx*pi/2/Nx2))-(2*H+2*r);
      y(n)=-(ny)*dy3-H-r;
      n=n+1;
   end
end
nnod=n-1;
%
% CONNECTIVITY
%
n=1;
for ny=1:Ny1;
   for nx=1:Nx1+Nx2;
      nod1=(ny-1)*(Nx1+Nx2+1)+nx;
      nod2=nod1+1;
      nod3=nod2+Nx1+Nx2;
      nod4=nod3+1;
      con(n,1)=nod1;
      con(n,2)=nod2;
      con(n,3)=nod4;
      con(n,4)=nod3;
      n=n+1;
   end
end
Nxf=Nx1+Nx2-1;
Nxstart1=(Nx1+Nx2+1)*(Ny1)+1;
```

```
for ny=1:Nx2;
   Nxstart2=Nxstart1+Nxf+2;
   for nx=1:Nxf;
      nod1=Nxstart1;
      nod2=Nxstart1+1;
      nod3=Nxstart2+1;
      nod4=Nxstart2;
      con(n,1)=nod1;
      con(n,2)=nod2;
      con(n,3)=nod3;
      con(n,4)=nod4;
      n=n+1;
      Nxstart1=Nxstart1+1;
      Nxstart2=Nxstart2+1;
   end
   nod1=Nxstart1;
   nod2=Nxstart1+1;
   nod3=Nxstart2;
   nod4=Nxstart2;
   con(n,1)=nod1;
   con(n,2)=nod2;
   con(n,3)=nod3;
   con(n,4)=nod4;
   n=n+1;
   Nxf=Nxf-1;
   Nxstart1=Nxstart1+2;
end
%
Nxf=Nxf+1;
for ny=1:Nx2;
   Nxstart2=Nxstart1+Nxf+1;
   for nx=1:Nxf;
      nod1=Nxstart1;
      nod2=Nxstart1+1;
      nod3=Nxstart2+1;
      nod4=Nxstart2;
      con(n,1)=nod1;
      con(n,2)=nod2;
```

```
      con(n,3)=nod3;
      con(n,4)=nod4;
      n=n+1;
      Nxstart1=Nxstart1+1;
      Nxstart2=Nxstart2+1;
   end
   nod1=Nxstart1;
   nod2=Nxstart1;
   nod3=Nxstart2+1;
   nod4=Nxstart2;
   con(n,1)=nod1;
   con(n,2)=nod2;
   con(n,3)=nod3;
   con(n,4)=nod4;
   n=n+1;
   Nxf=Nxf+1;
   Nxstart1=Nxstart1+1;
end
for ny=1:Ny3
   for nx=1:Nx1+Nx2
      nod1=Nxstart1;
      nod2=Nxstart1+1;
      nod3=Nxstart1+Nx1+Nx2+2;
      nod4=nod3-1;
      con(n,1)=nod1;
      con(n,2)=nod2;
      con(n,3)=nod3;
      con(n,4)=nod4;
      n=n+1;
      Nxstart1=Nxstart1+1;
   end
   Nxstart1=Nxstart1+1;
end
nel=n-1;
```

File: calcu.m

```
function [ux,uy]=calcu(x,y,a,b,c,d,alpha,H,kg,G,NC)
%
%
%  Evaluate Laurent Series
%
%
si=size(x);
NX=si(2)-1;
z=1000000000*H;
dz=(1i*z*(1+alpha^2)-H*(1-alpha^2))/(1i*z*(1+alpha^2)+H*(1-alpha^2));
fipc=0;
   fi=a(1);
   psic=conj(c(1));
   for kp=2:NC
      k=kp-1;
      fi=fi+a(kp)*dz^k+b(kp)*dz^(-k);
      fipc=fipc+conj((a(kp))*k*(dz^(k-1))-k*b(kp)*dz^(-k-1));
      psic=psic+conj(c(kp)*dz^k+d(kp)*dz^(-k));
   end
   uf=1/2/G*(kg*fi+1/2*(1+dz)*((-1+conj(dz))^2)/(1-dz)*fipc-psic);
   uyf=imag(uf)
for j=1:(NX+1)
   z=x(j)+1i*y(j);
   dz=(1i*z*(1+alpha^2)-H*(1-alpha^2))/(1i*z*(1+alpha^2)+H*(1-alpha^2));
   fipc=0;
   fi=a(1);
   psic=conj(c(1));
   for kp=2:NC
      k=kp-1;
      fi=fi+a(kp)*dz^k+b(kp)*dz^(-k);
      fipc=fipc+conj((a(kp))*k*(dz^(k-1))-k*b(kp)*dz^(-k-1));
      psic=psic+conj(c(kp)*dz^k+d(kp)*dz^(-k));
   end
   u(j)=1/2/G*(kg*fi+1/2*(1+dz)*((-1+conj(dz))^2)/(1-dz)*fipc-psic);
   ux(j)=real(u(j));
   uy(j)=imag(u(j))-uyf;
end
```

File: calcua.m

```
function [ux,uy]=calcua(X,Y,r,H,nu,ue,ud)
%
%
%  Evaluate displacements using the approximate solution for uniform
%  convergence and distortion
%
%
kg=3-4*nu;
si=size(X);
NX=si(2)-1;
for N=1:NX+1
   x=X(N);
   y=Y(N);
   uxme(N)=ue*x*r/(x^2+(y+H)^2)-ue*(x*r)/(x^2+(y-H)^2);
   uyme(N)=ue*(y+H)*r/(x^2+(y+H)^2)-ue*((y-H)*r)/(x^2+(y-H)^2);
   uxte(N)=4*ue*r*((1-nu)*x/(x^2+(y-H)^2)-(y-H)*x*y/(x^2+(y-H)^2)^2);
   uyte(N)=2*ue*r*((2*(y-H)*x^2+H*(x^2-(y-H)^2))/(x^2+(y-H)^2)^2-2*(1-nu)*(y-
H)/(x^2+(y-H)^2));
   uxmd(N)=ud*r/(3-4*nu)*x*(((3-4*nu)*(x^2+(y+H)^2)^2)-(3*(y+H)^2-
x^2)*(x^2+(y+H)^2-r^2))/(x^2+(y+H)^2)^3-ud*r/(3-4*nu)*x*(((3-4*nu)*(x^2+(y-
H)^2)^2)-(3*(y-H)^2-x^2)*(x^2+(y-H)^2-r^2))/(x^2+(y-H)^2)^3;
   uymd(N)=-ud*r/(3-4*nu)*(y+H)*((3-4*nu)*(x^2+(y+H)^2)^2-(3*x^2-
(y+H)^2)*(x^2+(y+H)^2-r^2))/(x^2+(y+H)^2)^3+ud*r/(3-4*nu)*(y-H)*((3-
4*nu)*(x^2+(y-H)^2)^2-(3*x^2-(y-H)^2)*(x^2+(y-H)^2-r^2))/(x^2+(y-H)^2)^3;
   uxtd(N)=8*ud*r/(3-4*nu)*(x*(1-nu)*(x^2+y^2-H^2)/(x^2+(y-H)^2)^2-
x*y*((y*(x^2+y^2)+2*H*(H^2-x^2)-3*y*H^2)/(x^2+(y-H)^2)^3));
   uytd(N)=8*ud*r/(3-4*nu)*((1-nu)*(x^2*(2*H-y)-y*(y-H)^2)/(x^2+(y-H)^2)^2-
((y-H)*(H*y*(y-H)^2-x^2*(x^2+y^2+H*(y+H))))/(x^2+(y-H)^2)^3);
   ux(N)=uxme(N)+uxte(N)+uxmd(N)+uxtd(N);
   uy(N)=uyme(N)+uyte(N)+uymd(N)+uytd(N);
end
```

Appendix III

Elastic half plane subjected to a shear stress boundary condition at the surface

The problem, outlined in Figure I-1, can be solved by means of the Fourier transform method. This implies that the shear stress distribution at the surface and its first derivative vanish for $x \to \infty$. The boundary conditions are that the normal stresses at the surface are zero, the shear stresses at the surface are prescribed, and that the stresses (or displacements) at infinity must vanish.

The governing equation of the plane elasticity can be expressed in terms of Airy's stress function as follows:

$$\nabla^2 \cdot \nabla^2 \cdot F = 0 \qquad \{I.1\}$$

The solution is sought in terms of the Fourier transform of F, defined as follows:

$$\mathfrak{F} = \int_{-\infty}^{\infty} F(x,y) \cdot e^{-i \cdot \omega \cdot x} \cdot dx \qquad \{I.2\}$$

Hence, the ∇^2 operator can be expressed as:

$$\nabla^2 = \frac{d^2}{dy^2} - \omega^2 \qquad \{I.3\}$$

The Fourier transform of Airy's stress function is assumed to be of the following form:

$$\mathrm{F}(y,\omega) = e^{\delta \cdot y} \qquad \{I.4\}$$

Replacing {I.4} in {I.1} yields the values of the parameter δ:

$$\left(\delta^2 - \omega^2\right)\cdot\left(\delta^2 - \omega^2\right) = 0 \qquad \{I.5\}$$

As can be seen, there are two double roots; ω and $-\omega$. Hence, the Fourier transform of Airy's stress function can be expressed as:

$$\Im(\omega, y) = e^{\omega\cdot y}\cdot(A + B\cdot y) + e^{-\omega\cdot y}\cdot(C + D\cdot y) \qquad \{I.6\}$$

where A, B, C, D are integration constants. Imposing the boundary condition at infinity, $\Im$ can be reduced to:

$$\Im(\omega, y) = e^{-|\omega|\cdot y}\cdot(A + B\cdot y) \qquad \{I.7\}$$

where A and B are integration constants which are found by imposing the boundary conditions at the surface. The Fourier transform of the normal stress at the surface is given by:

$$\Im_y = -\alpha^2\cdot\Im(\omega, 0) \qquad \{I.8\}$$

Introducing {I.7} in {I.8}, it can readily be seen that:

$$A = 0 \qquad \{I.9\}$$

The Fourier transform of the shear stress at the surface is given by:

$$\Im_{xy}(\omega) = i\cdot\omega\cdot B \qquad \{I.10\}$$

Introducing {I.10} and {I.9} in {I.7}, the Fourier transform of Airy's stress function is found to be:

$$\mathfrak{F}(\omega, y) = -i \cdot \frac{\mathfrak{T}_{xy}(\omega)}{\omega} \cdot y \cdot e^{-|\omega| \cdot y} \qquad \{I.11\}$$

Hence, the general solution for Airy's stress function can be found by an inverse Fourier transformation as follows:

$$F(x, y) = \frac{1}{2\pi} \cdot \int_{-\infty}^{\infty} -i \cdot \frac{\mathfrak{T}_{xy}(\omega)}{\omega} \cdot y \cdot e^{-|\omega| \cdot y} \cdot e^{i \cdot \omega \cdot x} \cdot d\omega \qquad \{I.12\}$$

where $\mathfrak{T}_{xy}(\omega)$ is given by:

$$\mathfrak{T}_{xy} = \int_{-\infty}^{\infty} \tau_{xy}(x) \cdot e^{-i \cdot \omega \cdot x} \cdot dx \qquad \{I.13\}$$

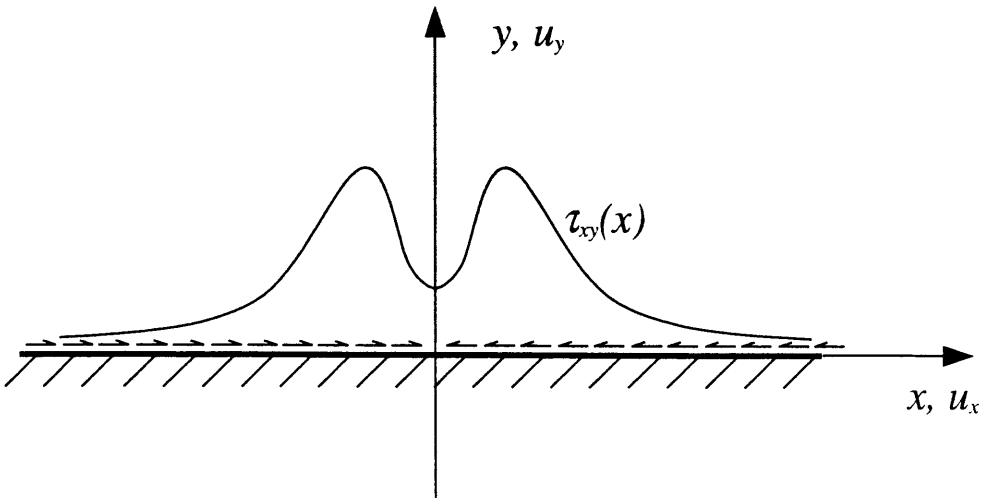

Figure I-1. Problem outline

Appendix IV

Elasto-Plastic Solution for Drained Displacements Around a Contracting Cavity

This Appendix shows the derivation of the analytical solution for the drained (i.e., no excess pore pressures) displacement field around a contracting cavity of radius, R, in an infinite plane subjected to an initial hydrostatic (i.e., $K_0 = 1$) state of stresses. Yu and Rowe (1998) obtained this solution by assuming an elastic-perfectly-plastic material, a Mohr-Coulomb failure criterion and a non-associative flow rule.

Total stress equilibrium in the drained case is fulfilled if:

$$\frac{d\sigma'_r}{dr} + \frac{\sigma'_r - \sigma'_\theta}{r} = 0 \qquad \{\text{IV-1}\}$$

where σ'_r is the radial effective stress, σ'_θ the azimuthal stress, and r is the radial distance from the center of the cavity. The stress boundary conditions are:

$$\sigma'_r(R) = -p'_i \qquad \{\text{IV.2a}\}$$

$$\sigma'_r(\infty) = -p'_0 \qquad \{\text{IV.2b}\}$$

where p'_i is the effective internal pressure (positive if tends to expand the cavity) inside the cavity and p'_0 is the in situ stress in the soil mass (positive if compressive).

Elastic response

Assuming the soil follows linearly elastic behavior, the stresses and displacements fulfill the following relationships derived from elastic theory:

$$\sigma_r' = M \cdot \frac{\partial u_r}{\partial r} + \lambda \cdot \frac{u_r}{r} \qquad \{IV\text{-}3a\}$$

$$\sigma_\theta' = M \cdot \frac{u_r}{r} + \lambda \cdot \frac{\partial u_r}{\partial r} \qquad \{IV\text{-}3b\}$$

where M and λ are the elastic Lame constants, defined in equations {2-3}. Replacing equations {IV-3} in {IV-1} and solving the PDE yields (see Section 2.1):

$$u_r(r) = A \cdot r + \frac{B}{r} \qquad \{IV\text{-}4\}$$

where A and B are integration constants that are found by means of imposing the boundary conditions {IV-2} as follows:

$$A = -\frac{p_0'}{2 \cdot G} \cdot (1 - 2 \cdot \nu) \qquad \{IV\text{-}5a\}$$

$$B = -\frac{p_0' - p_i'}{2 \cdot G} \cdot R^2 \qquad \{IV\text{-}5b\}$$

Hence, the radial displacements and stress components, σ_r' and σ_θ' are:

$$u_r(r) = -\frac{p_0' \cdot (1 - 2 \cdot \nu) + (p_0' - p_0') \cdot \left(\frac{R}{r}\right)^2}{2 \cdot G} \cdot r \qquad \{IV\text{-}6\}$$

$$\sigma_r'(r) = -p_0' + (p_0' - p_i') \cdot \left(\frac{R}{r}\right)^2 \qquad \{IV\text{-}7a\}$$

$$\sigma'_\theta(r) = -p'_0 - (p'_0 - p'_i)\cdot\left(\frac{R}{r}\right)^2 \qquad \{\text{IV-7b}\}$$

It is important to notice that in order to evaluate the displacements due to the presence of the cavity, the displacements due to the initial state of stresses (i.e., $p'_i = p'_0$) must be subtracted, leading to:

$$u_r(r) = -\frac{(p'_0 - p'_i)}{2\cdot G}\cdot\left(\frac{R}{r}\right)^2 \cdot r \qquad \{\text{IV-8}\}$$

Failure criterion

The elastic stresses, given in equations {IV-7}, cannot always be developed by the soil. The Mohr-Coulomb failure criterion can be written:

$$N_{\phi'}\cdot\sigma'_r - \sigma'_\theta = Y \qquad \{\text{IV-9}\}$$

where:

$$N_{\phi'} = \frac{1+\sin(\phi')}{1-\sin(\phi')} \qquad \{\text{IV-10a}\}$$

$$Y = \frac{2\cdot c'\cdot\cos(\phi')}{1-\sin(\phi')} \qquad \{\text{IV-10b}\}$$

and ϕ' and c' are the drained friction angle and cohesion, respectively. It is assumed that after initial yielding, a plastic zone within the region $R < r < R_p$ will develop around the cavity. In the elastic region, equations {IV-3} and {IV-4} are still valid. As the integration constant, A, is evaluated by considering the derivatives of the displacements at infinity (i.e., elastic region), equation {IV-5a} is also still valid. However, the value of B is indeterminate, and must be evaluated by imposing equilibrium in the limit between plastic and elastic regions (i.e., at R_p).

The stresses in the elastic zone are given by:

$$\sigma'_r(r) = -p'_0 + \frac{C}{r^2} \qquad \{\text{IV-11a}\}$$

$$\sigma'_\theta(r) = -p'_0 - \frac{C}{r^2} \qquad \{\text{IV-11b}\}$$

where C is an integration constant related to B as follows:

$$C = -2 \cdot G \cdot B \qquad \{\text{IV-12}\}$$

Plastic response

The stresses in the plastic zone must fulfill both equations {IV-1} (i.e., equilibrium) and {IV-9} (i.e., failure criterion):

$$\sigma'_r(r) = -\frac{Y}{N_{\phi'} - 1} - D \cdot r^{N_{\phi'} - 1} \qquad \{\text{IV-13a}\}$$

$$\sigma'_\theta(r) = -\frac{Y}{N_{\phi'} - 1} - D \cdot N_{\phi'} \cdot r^{N_{\phi'} - 1} \qquad \{\text{IV-13b}\}$$

where D is a constant which is found by imposing the boundary condition at the cavity wall:

$$D = \frac{p'_i \cdot (N_{\phi'} - 1) + Y}{N_{\phi'} - 1} \cdot R^{1 - N_{\phi'}} \qquad \{\text{IV-14}\}$$

The radius of the plastic zone, R_p, and the constant C, are found by imposing continuity of stresses at $r = R_p$:

$$\frac{R_p}{R} = T^{\frac{1}{1-N_{\phi'}}} \qquad \{IV\text{-}15a\}$$

$$T = \frac{1}{2} \cdot \frac{(1+N_{\phi'}) \cdot [(N_{\phi'}-1) \cdot p'_i + Y]}{(N_{\phi'}-1) \cdot p'_0 + Y} \qquad \{IV\text{-}15b\}$$

$$C = \frac{p'_0 \cdot ((N_{\phi'}-1) \cdot p'_0 + Y - 1) + Y}{N_{\phi'}+1} \cdot R_p^{\,2} \qquad \{IV\text{-}15c\}$$

The displacement distribution in the elastic zone due to the cavity unloading (i.e., subtracting the displacements due to the initial state of stresses, p'_0) is given by:

$$u_r = -\frac{p'_0 \cdot (N_{\phi'}-1) + Y}{2 \cdot G \cdot (N_{\phi'}+1)} \cdot \frac{R_p^{\,2}}{r}$$

The determination of the displacements in the plastic region requires the use of a plastic flow rule that define the relative contribution of the plastic strains in different directions. The soil is assumed to dilate plastically at a constant rate with a dilation angle, ψ:

$$\frac{\varepsilon_r^{\,p}}{\varepsilon_\theta^{\,p}} = -\beta \qquad \{IV\text{-}16\}$$

where β is given by:

$$\beta = \frac{1+sin(\psi)}{1-sin(\psi)} \qquad \{IV\text{-}17\}$$

If $\beta = N_\theta$ (i.e., $\phi' = \psi$) the plastic flow is associative to the Mohr-Coulomb yield criterion. By considering that elastic strains are negligible in comparison to plastic strains (i.e., elastic-

perfectly-plastic), equation {IV-16} and introducing the kinematics relations for strains as a function of displacements, the flow rule yields:

$$\frac{du_r}{u_r} = -\beta \cdot \frac{dr}{r} \qquad \{\text{IV-18}\}$$

Solving the ODE yields:

$$u_r = \frac{J}{r^{\beta}} \qquad \{\text{IV-19}\}$$

where J is an integration constant that is found by imposing the continuity of displacement in the limit between the plastic and elastic zones:

$$J = -\frac{p'_0 \cdot (N_{\phi'} - 1) + Y}{2 \cdot G \cdot (N_{\phi'} + 1)} \cdot R_p^{\,1+\beta} \qquad \{\text{IV-20}\}$$

Hence, the displacement in the plastic zone is found to be:

$$u_r = -\frac{p'_0 \cdot (N_{\phi'} - 1) + Y}{2 \cdot G \cdot (N_{\phi'} + 1)} \cdot \frac{R_p^{\,1+\beta}}{r^{\beta}} \qquad \{\text{IV-21}\}$$

As a special case, the displacement at the cavity wall $u_\varepsilon^{\,p}$ is given by:

$$\frac{u_\varepsilon^{\,p}}{R} = -\frac{p'_0 \cdot (N_{\phi'} - 1) + Y}{2 \cdot G \cdot (N_{\phi'} + 1)} \cdot T^{\frac{1+\beta}{1-N_{\phi'}}} \qquad \{\text{IV-21}\}$$

The minimum displacement at the cavity wall that would produce plastic behavior, $u_\varepsilon^{\,y}$, is found for $T = 1$ (i.e., $R_p = R$) as follows:

$$\frac{u_{\varepsilon}{}^{y}}{R} = -\frac{p'_0 \cdot \left(N_{\phi'} - 1\right) + Y}{2 \cdot G \cdot \left(N_{\phi'} + 1\right)} \qquad \{\text{IV-22}\}$$

Appendix V

Design Charts for Ground Deformation Analysis

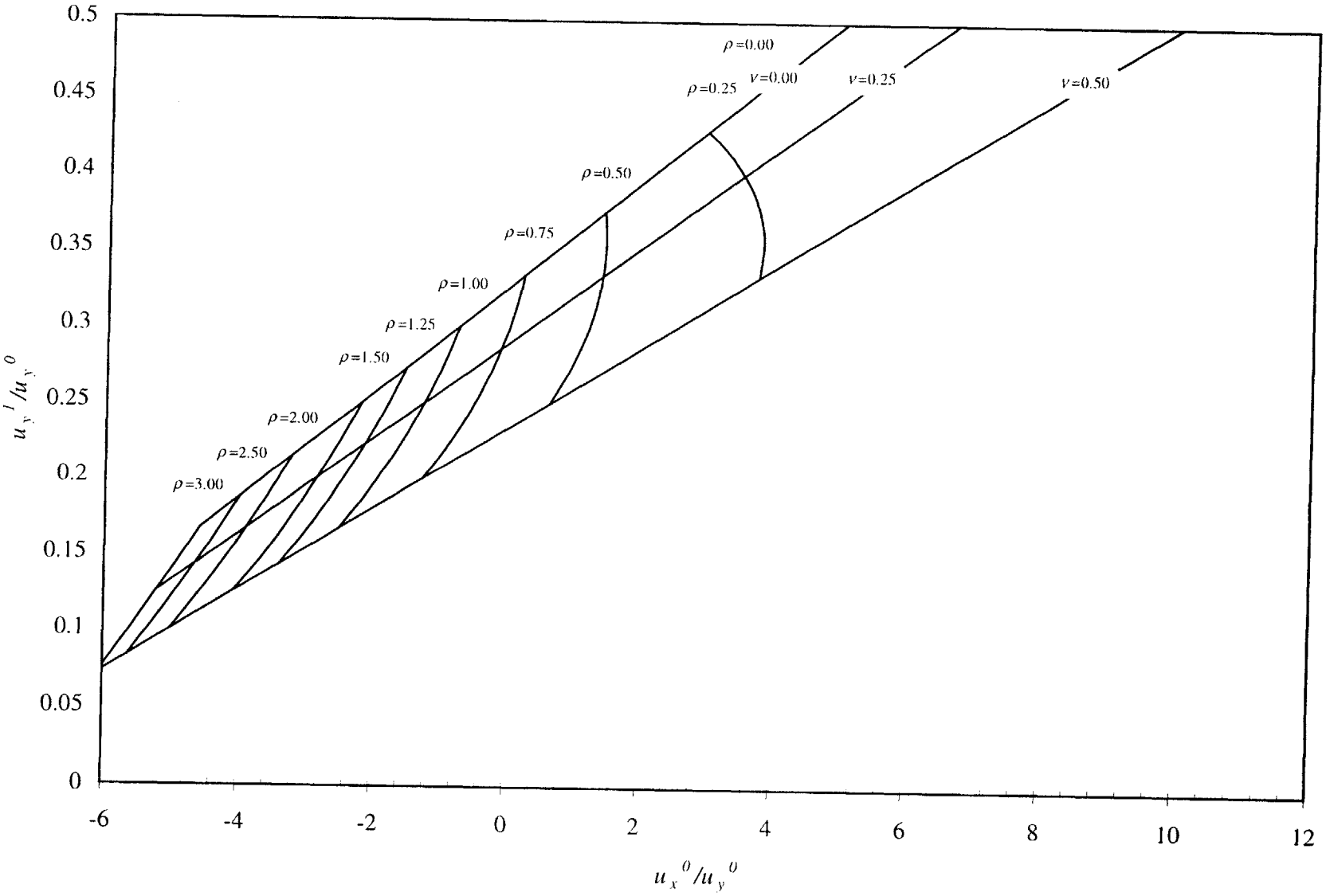

Figure V.1. Design chart for ρ and ν, R/H = 0.025

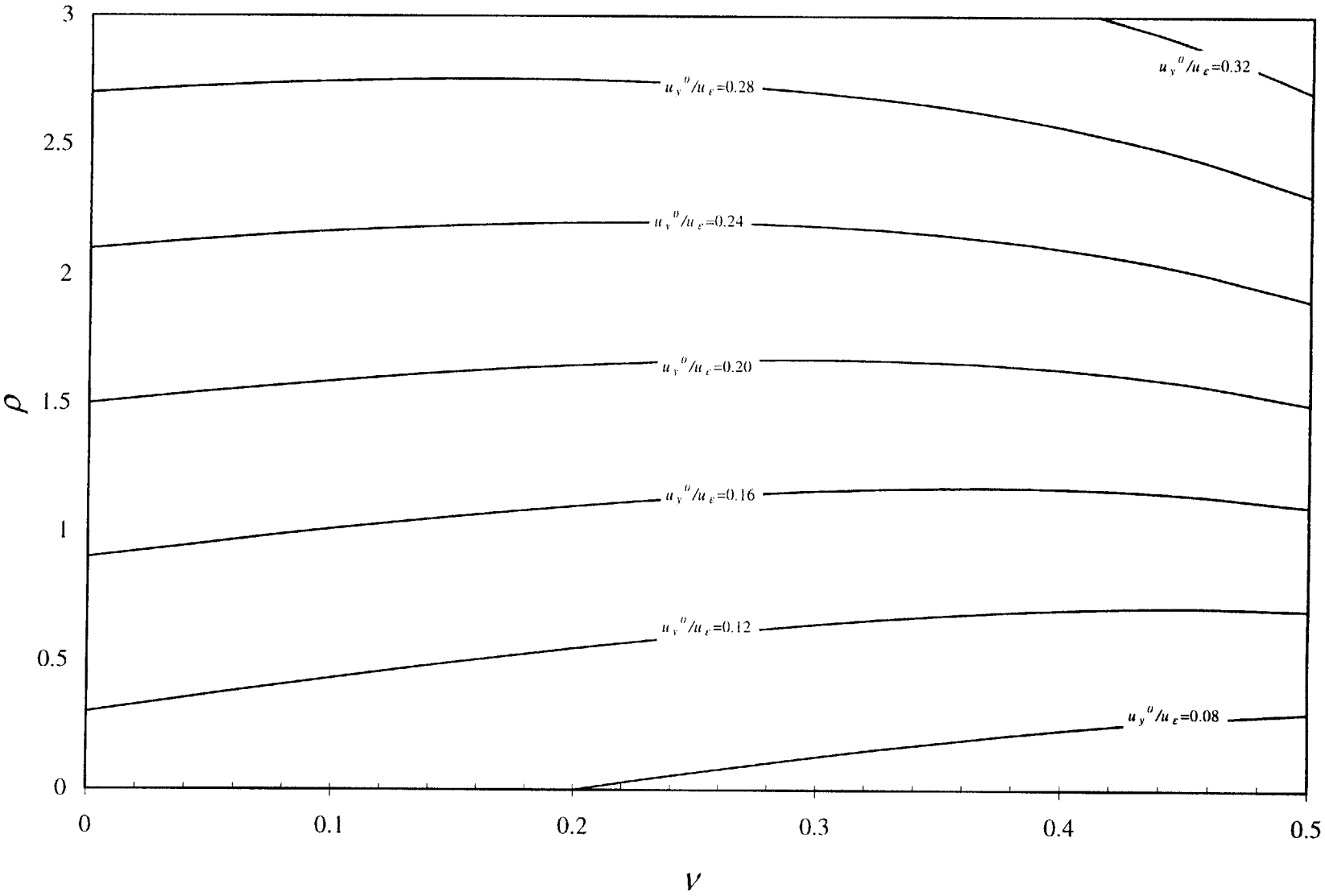

Figure V.2. Design chart for u_y^0/u_ε, R/H = 0.025, no dilation

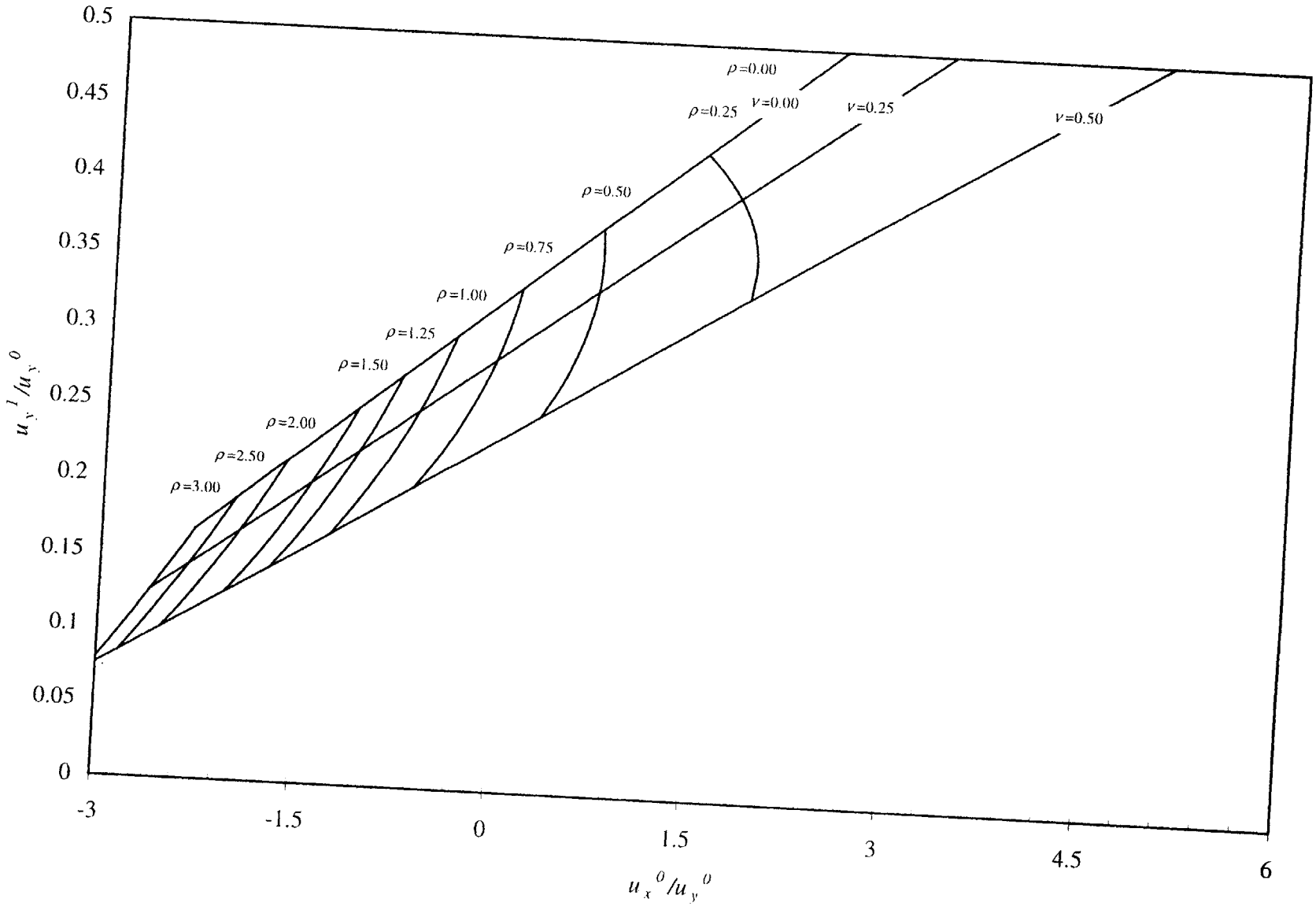

Figure V.3. Design chart for ρ and ν, $R/H = 0.05$

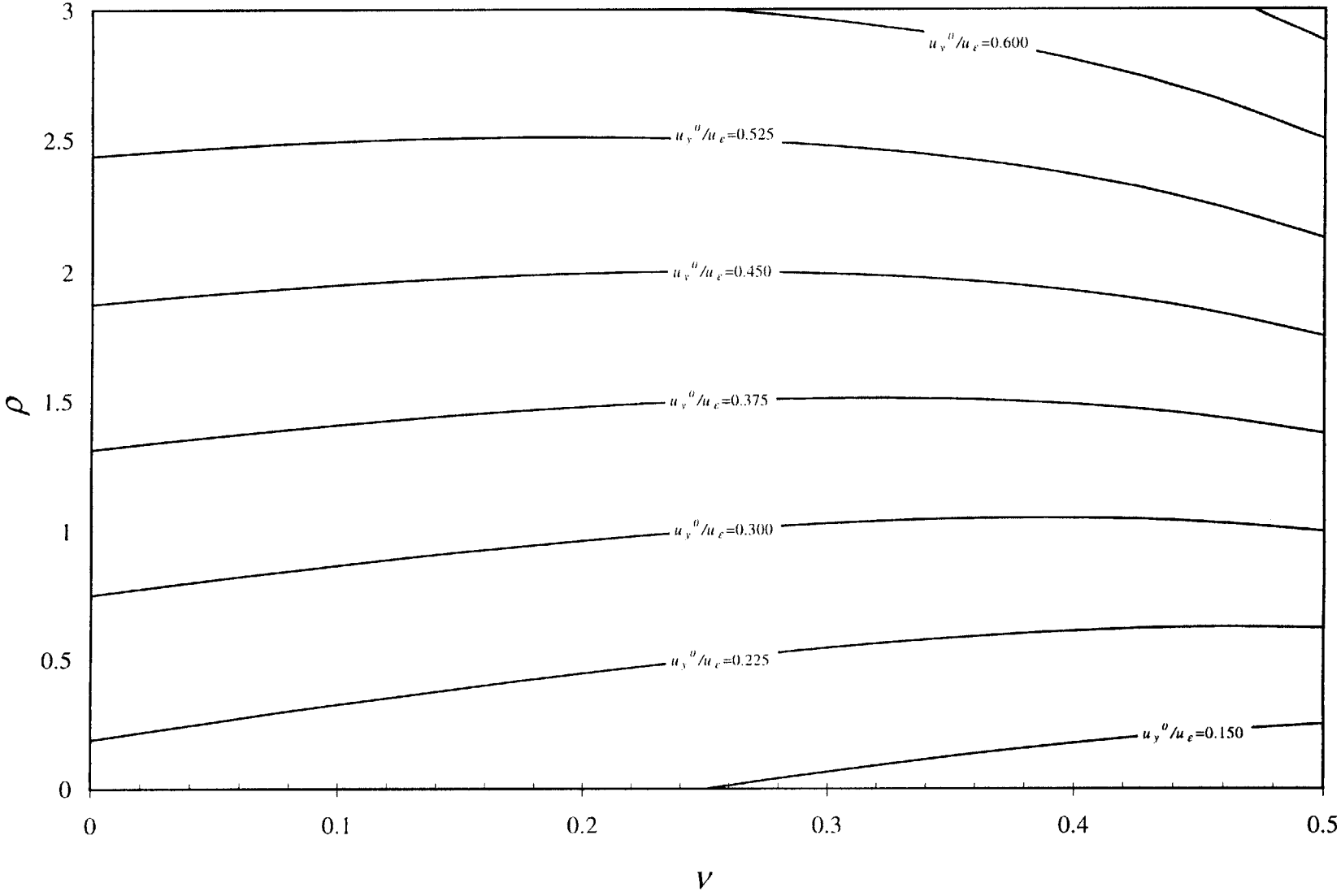

Figure V.4. Design chart for u_y^0/u_ε, R/H = 0.05, no dilation

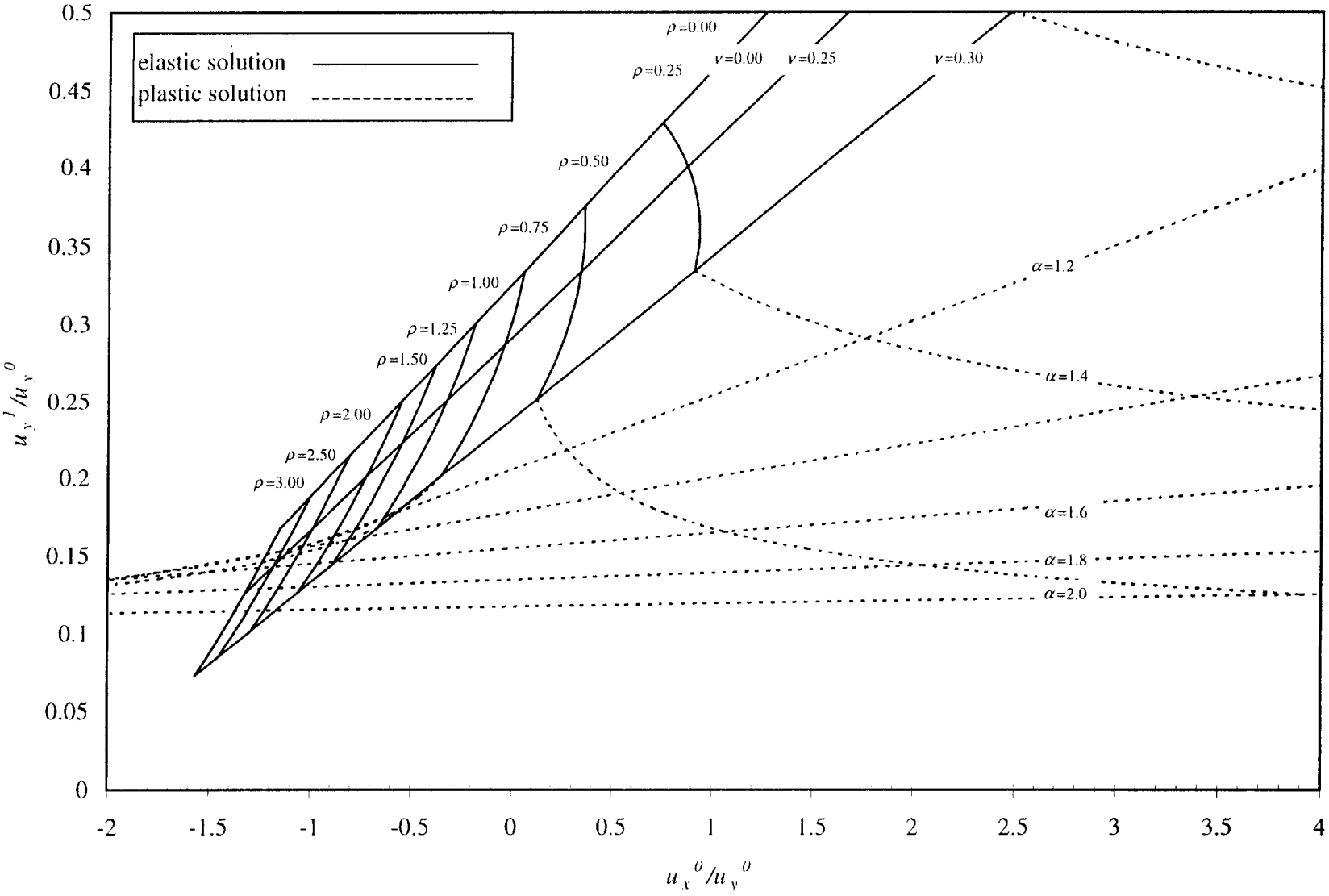

Figure V.5. Design chart for ρ and ν, R/H = 0.1

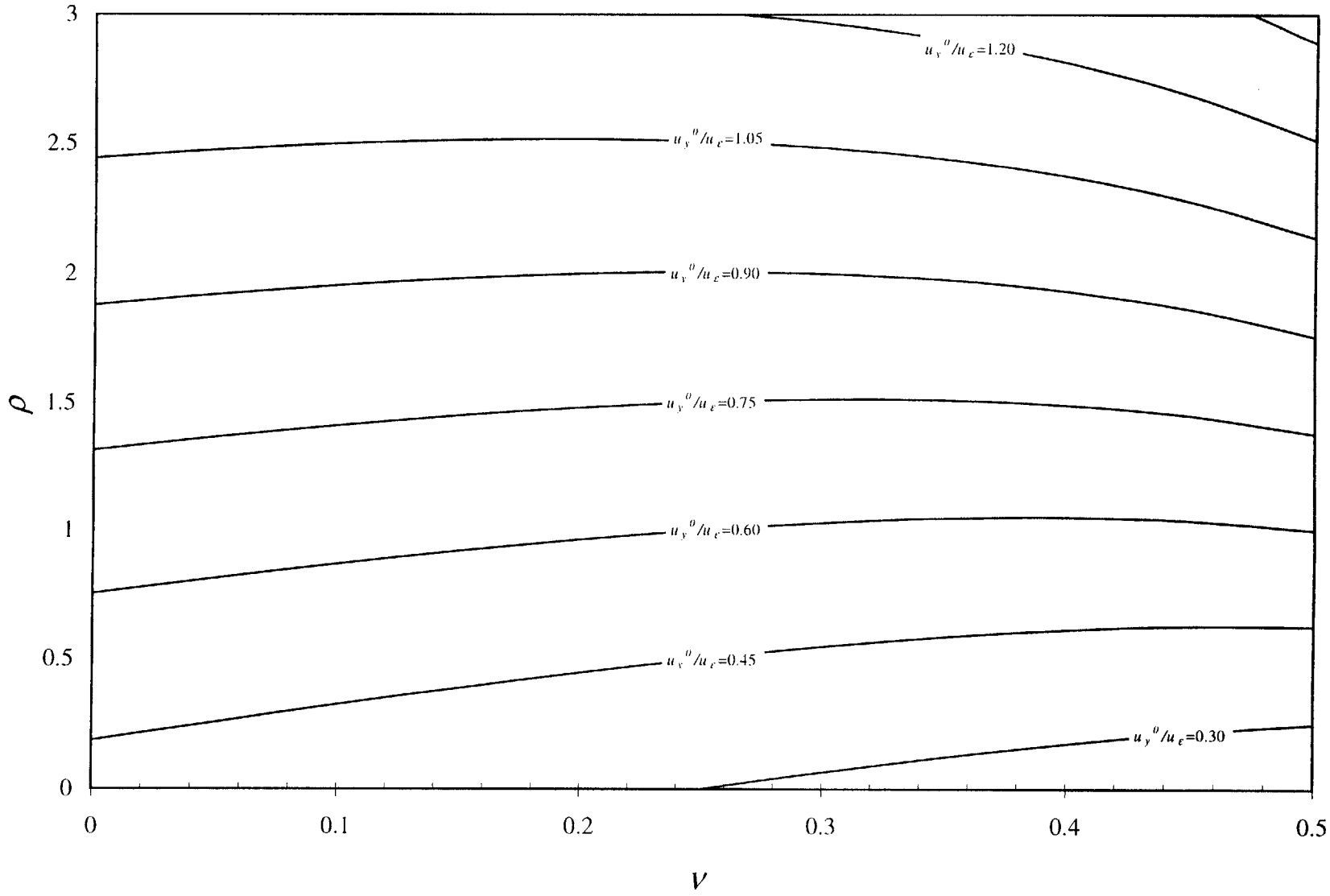

Figure V.6. Design chart for u_y^0/u_ε, $R/H = 0.1$

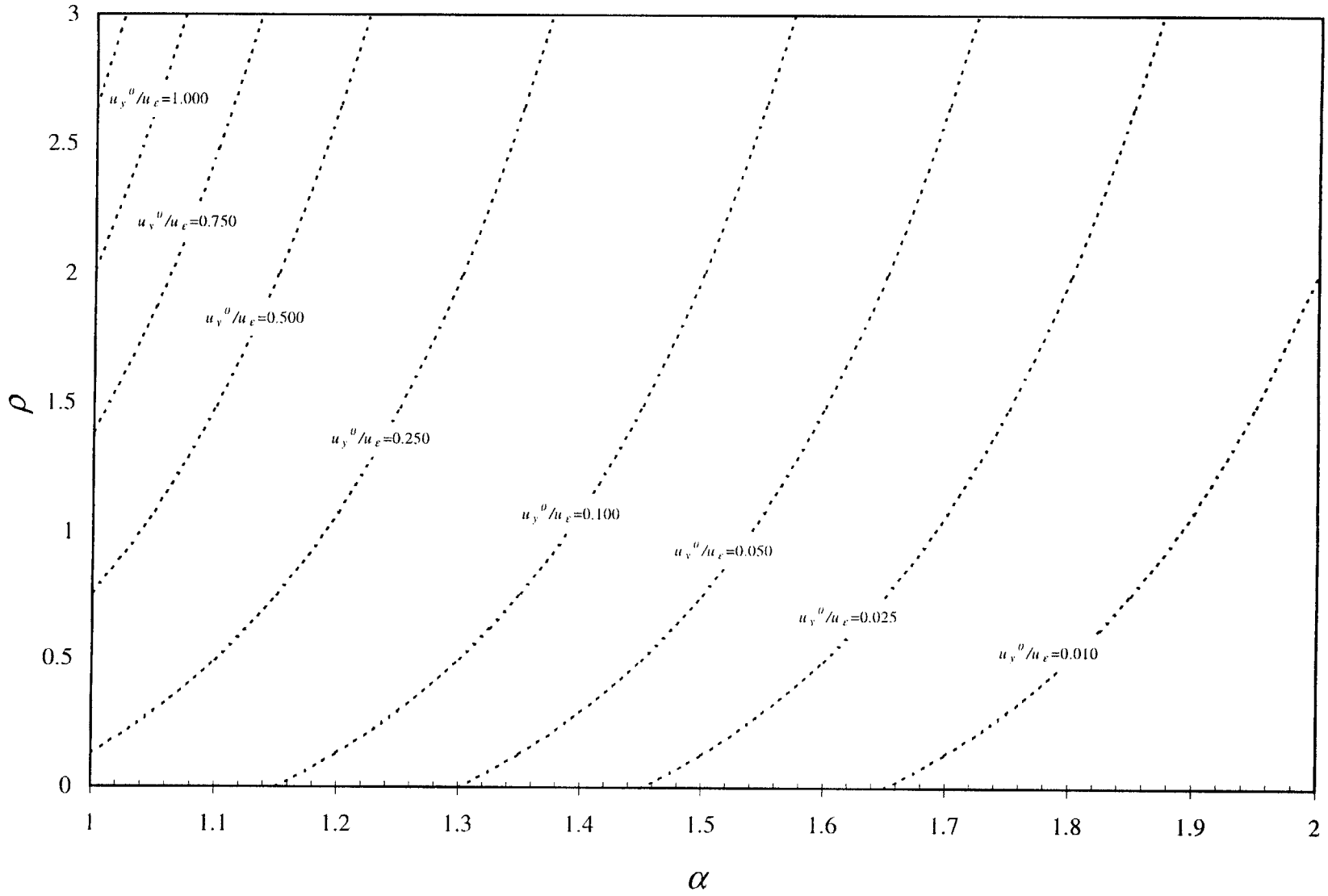

Figure V.7. Design chart for u_y^0/u_ε, R/H = 0.1, dilation

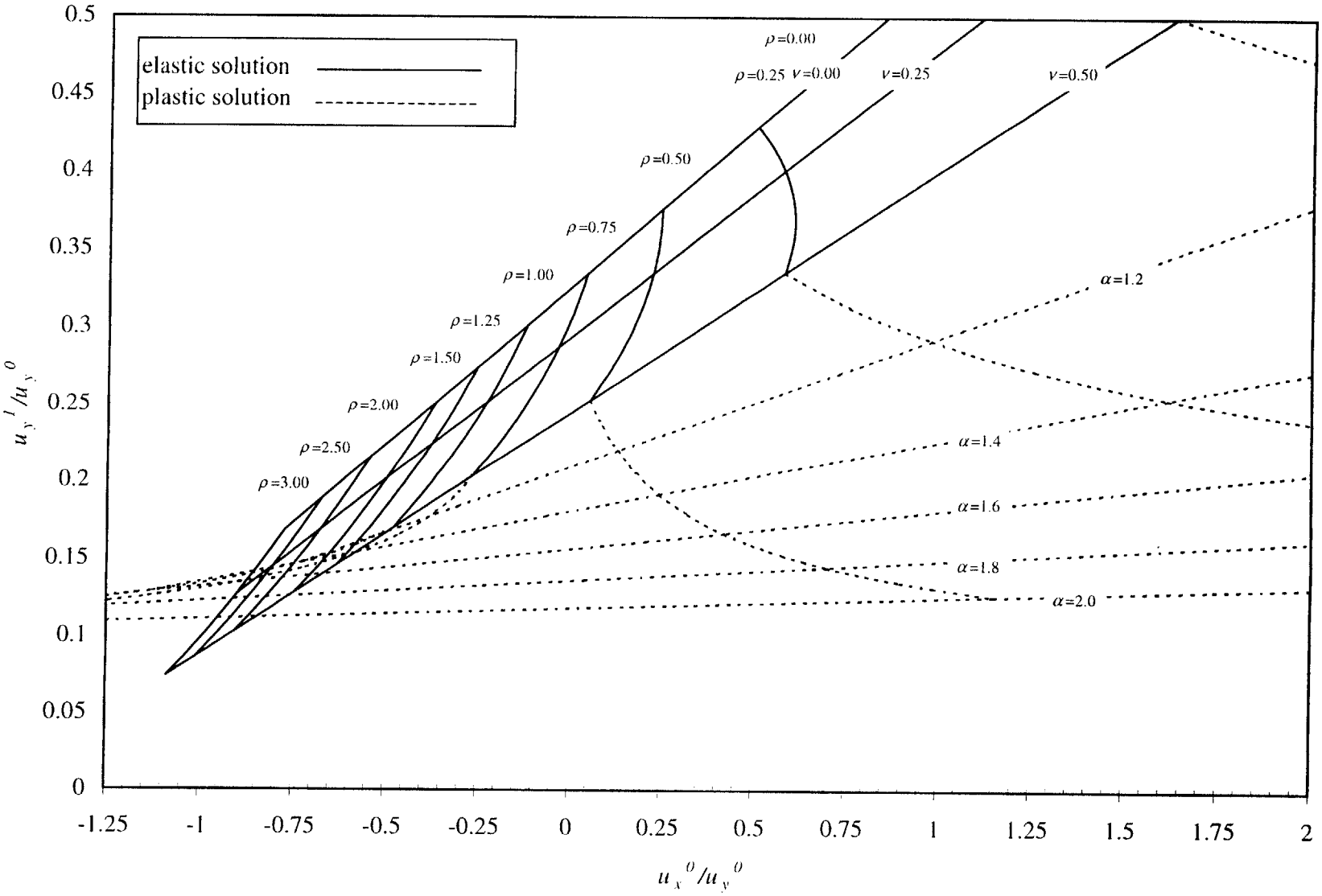

Figure V.8. Design chart for ρ and ν, $R/H = 0.15$

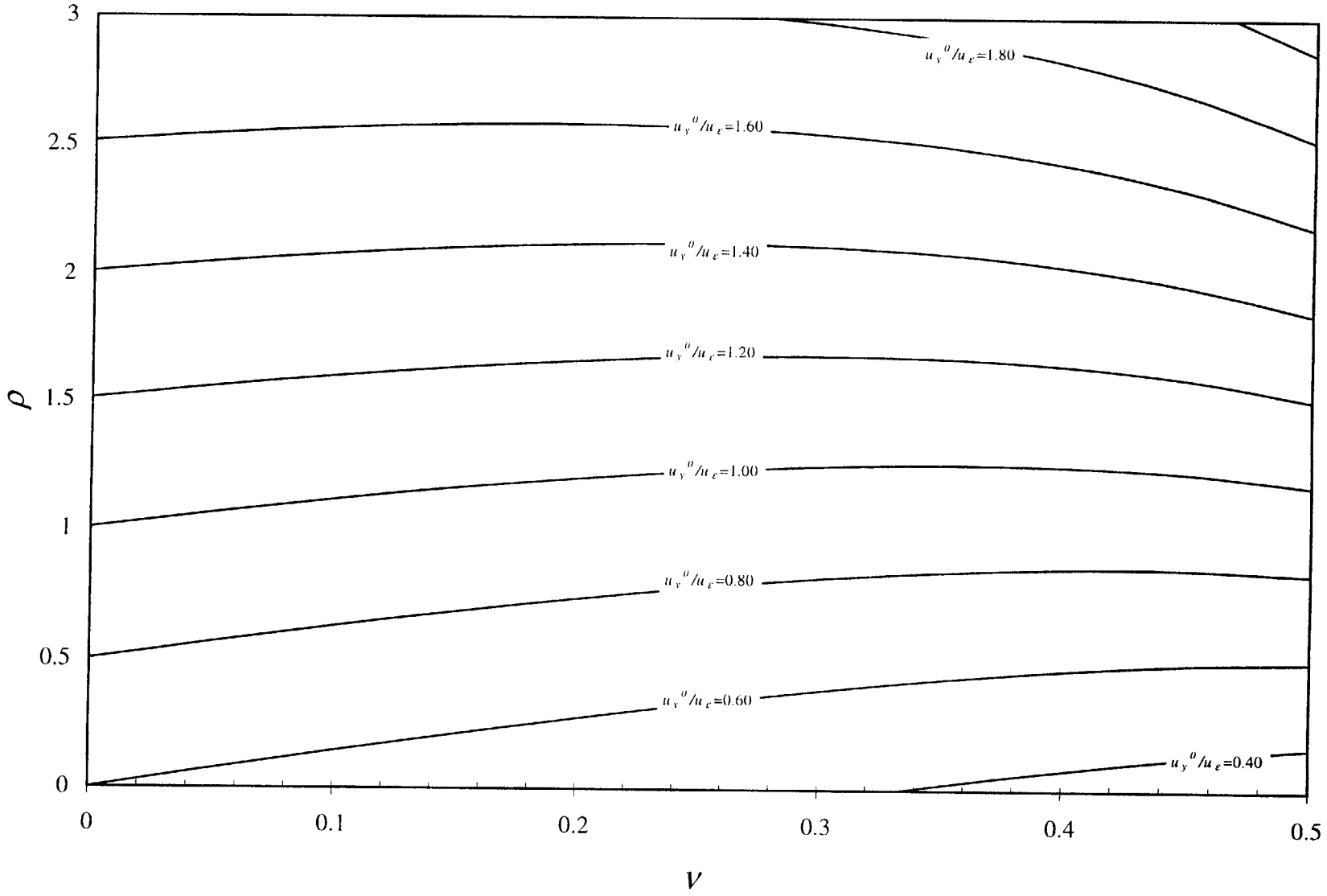

Figure V.9. Design chart for u_y^0/u_ε, R/H = 0.15, no dilation

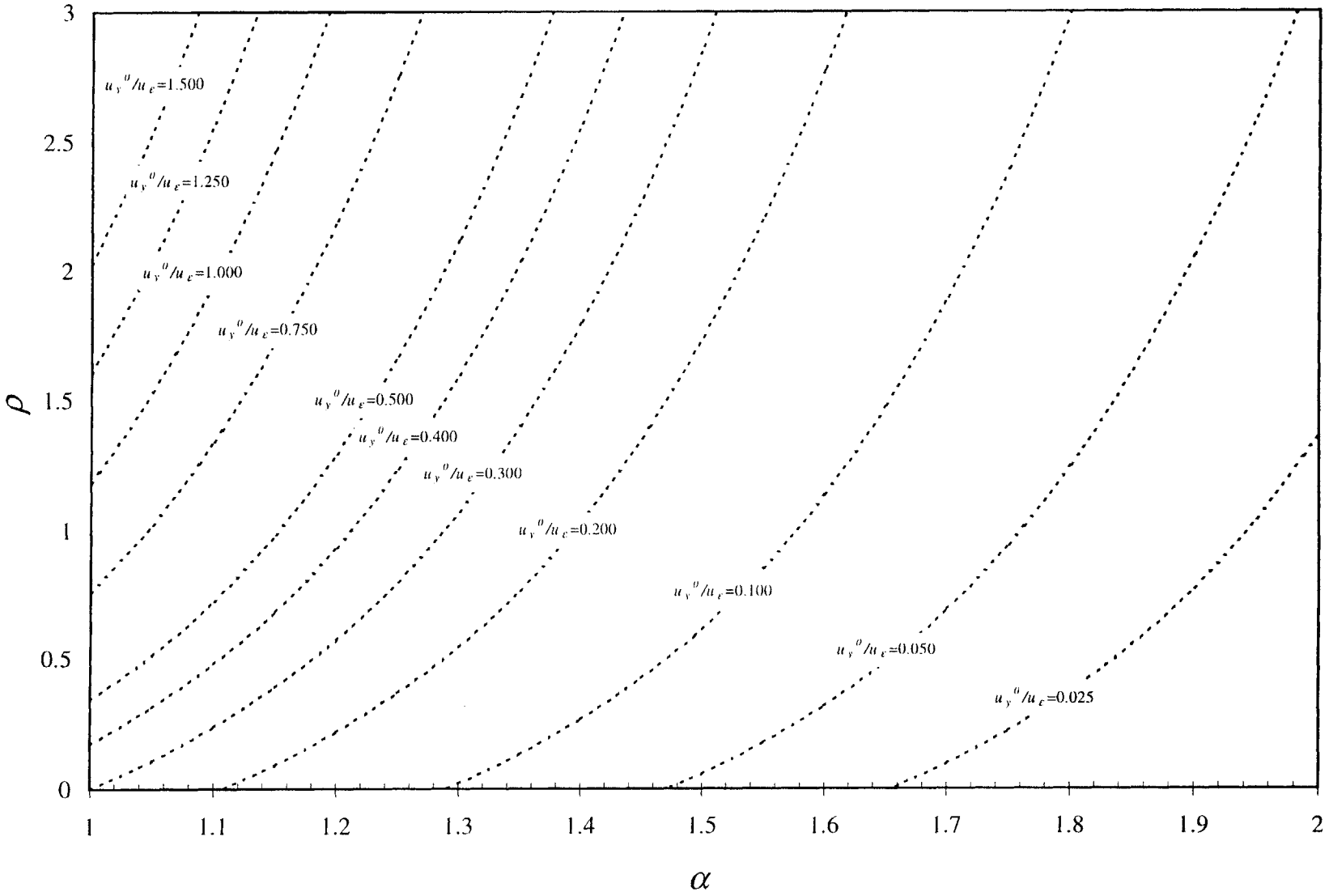

Figure V.10. Design chart for u_y^0/u_ε, R/H = 0.15, dilation

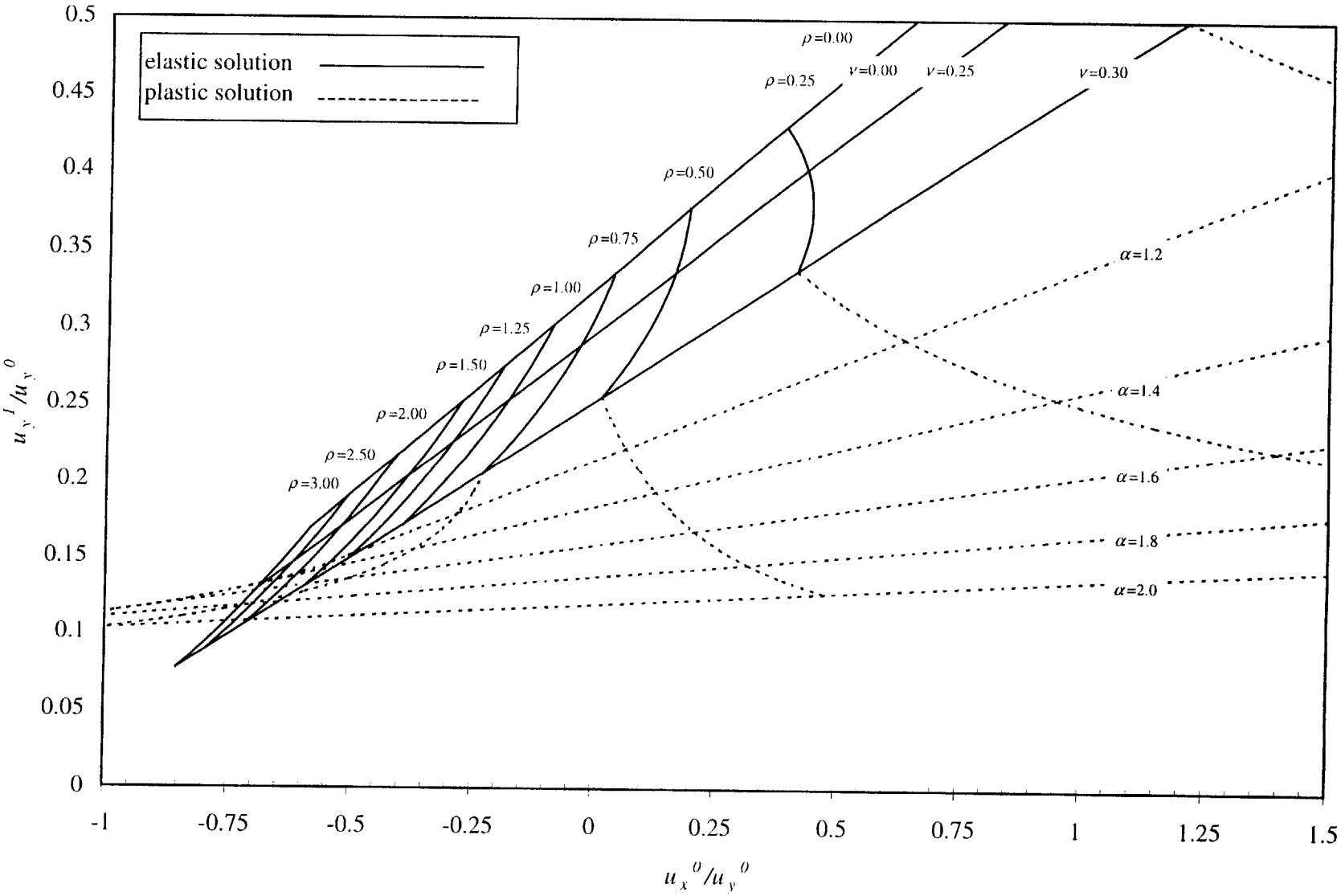

Figure V.11. Design chart for ρ and ν, $R/H = 0.2$

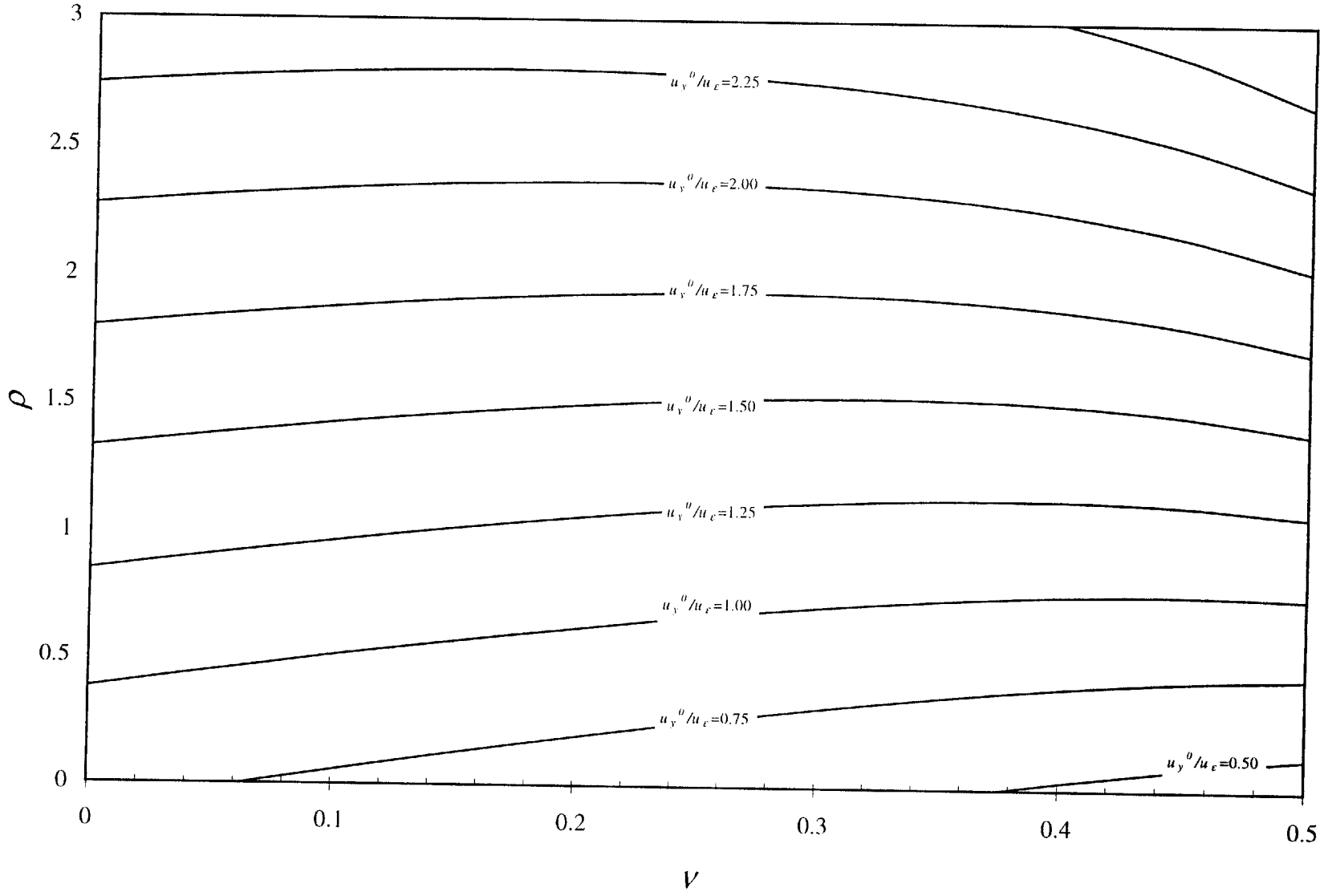

Figure V.12. Design chart for u_y^0/u_ε, R/H = 0.2, no dilation

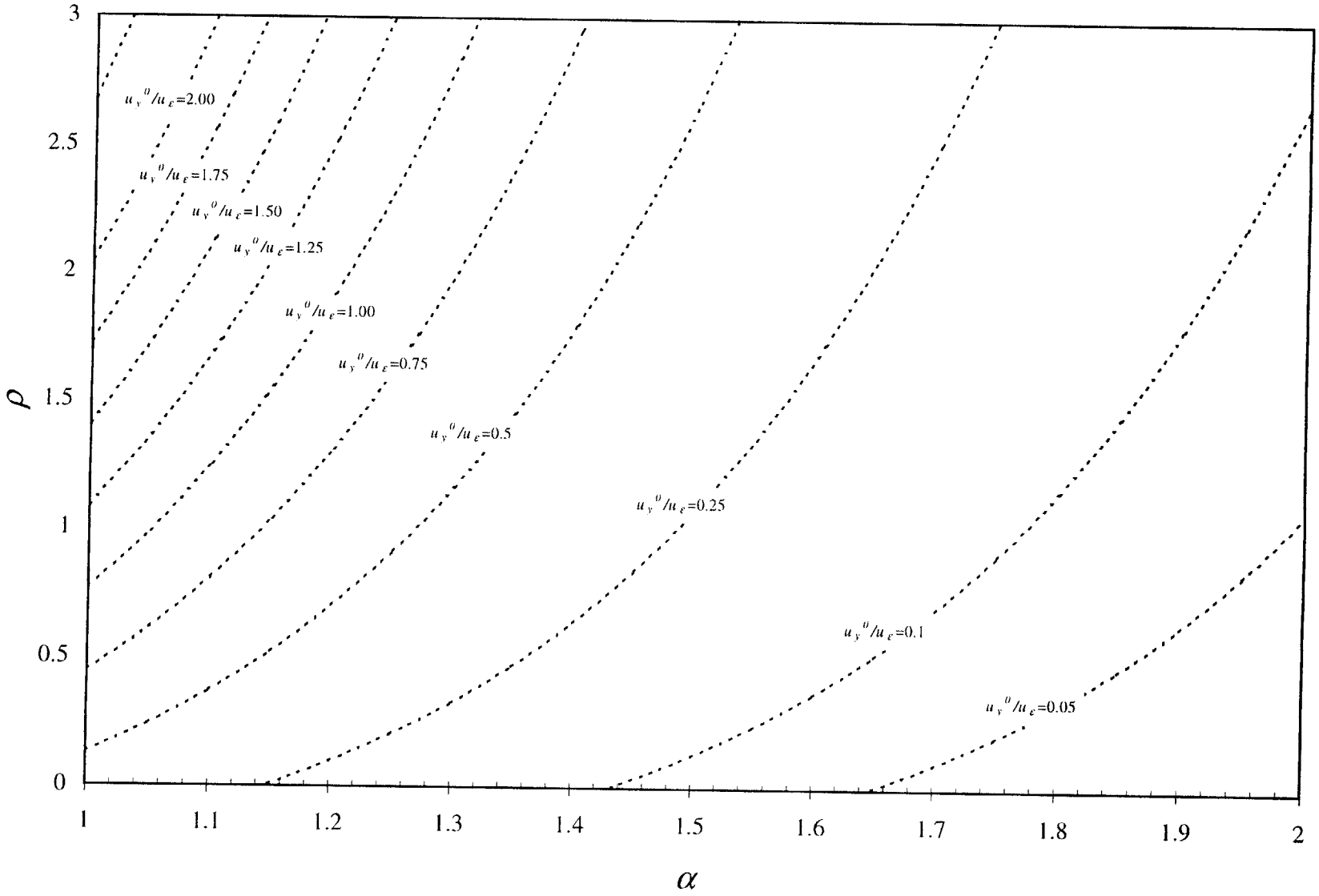

Figure V.13. Design chart for u_y^0/u_ε, R/H = 0.2, dilation

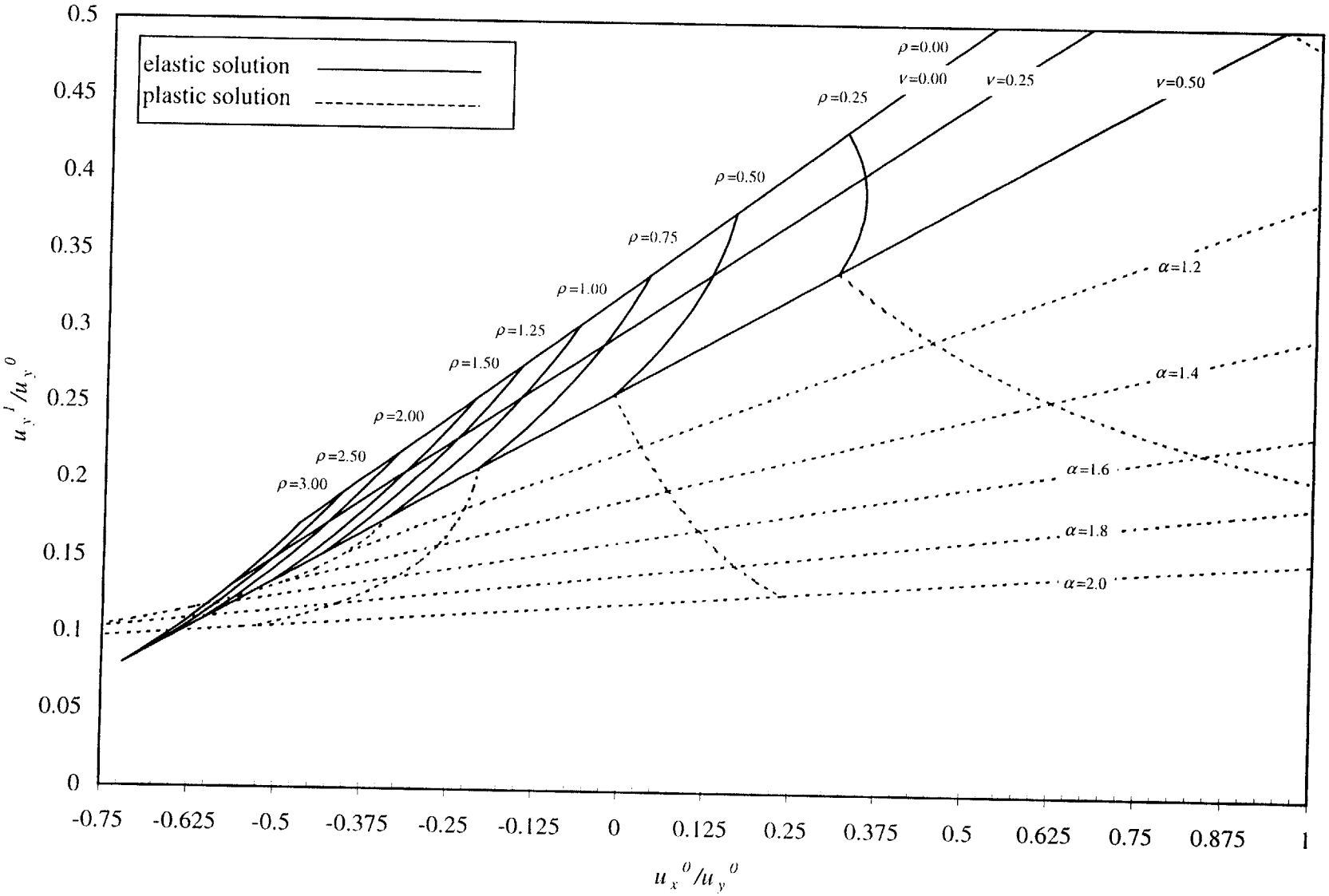

Figure V.14. Design chart for ρ and ν, $R/H = 0.25$

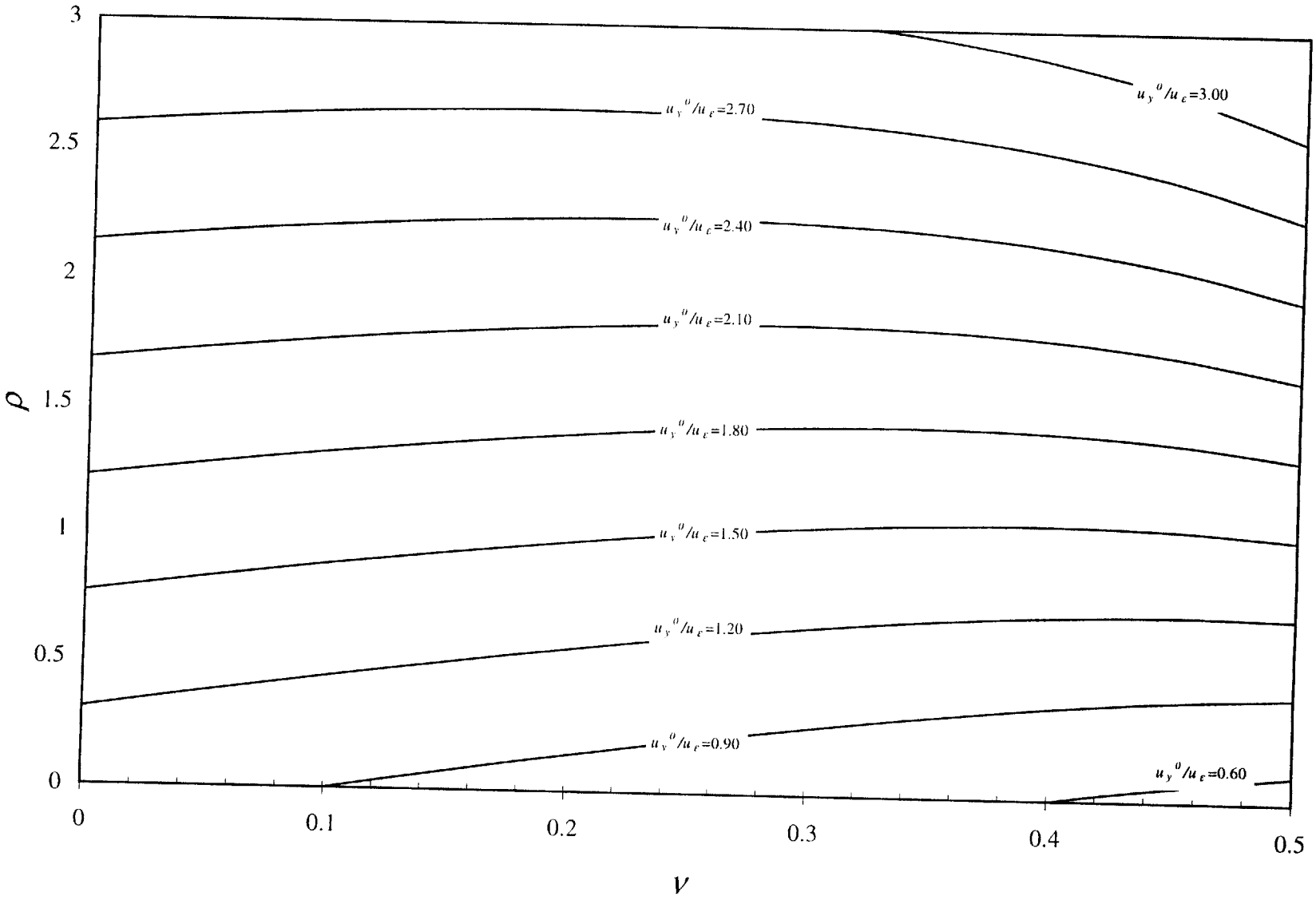

Figure V.15. Design chart for u_y^0/u_ε, R/H = 0.25, no dilation

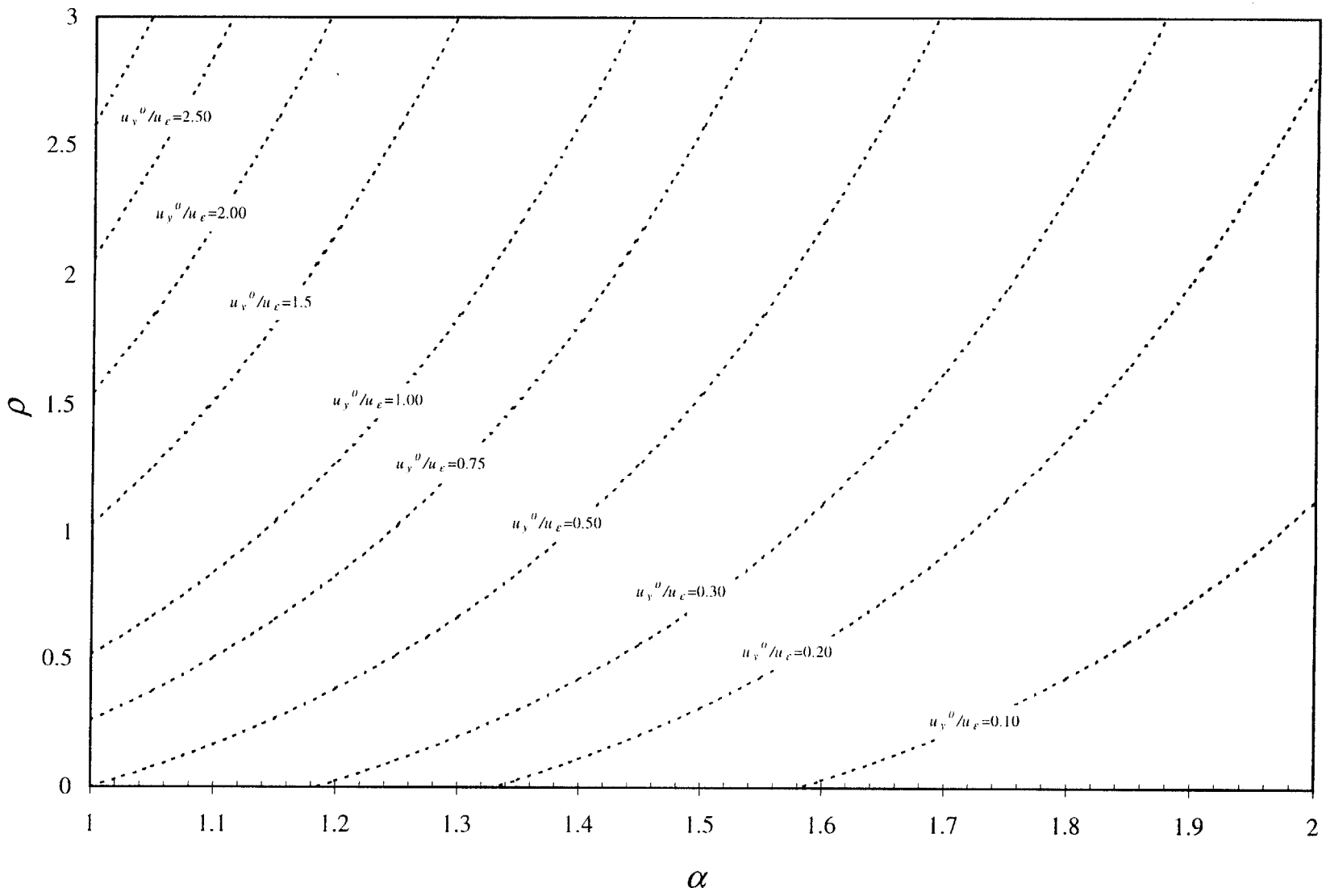

Figure V.16. Design chart for u_y^0/u_ε, R/H = 0.25, dilation

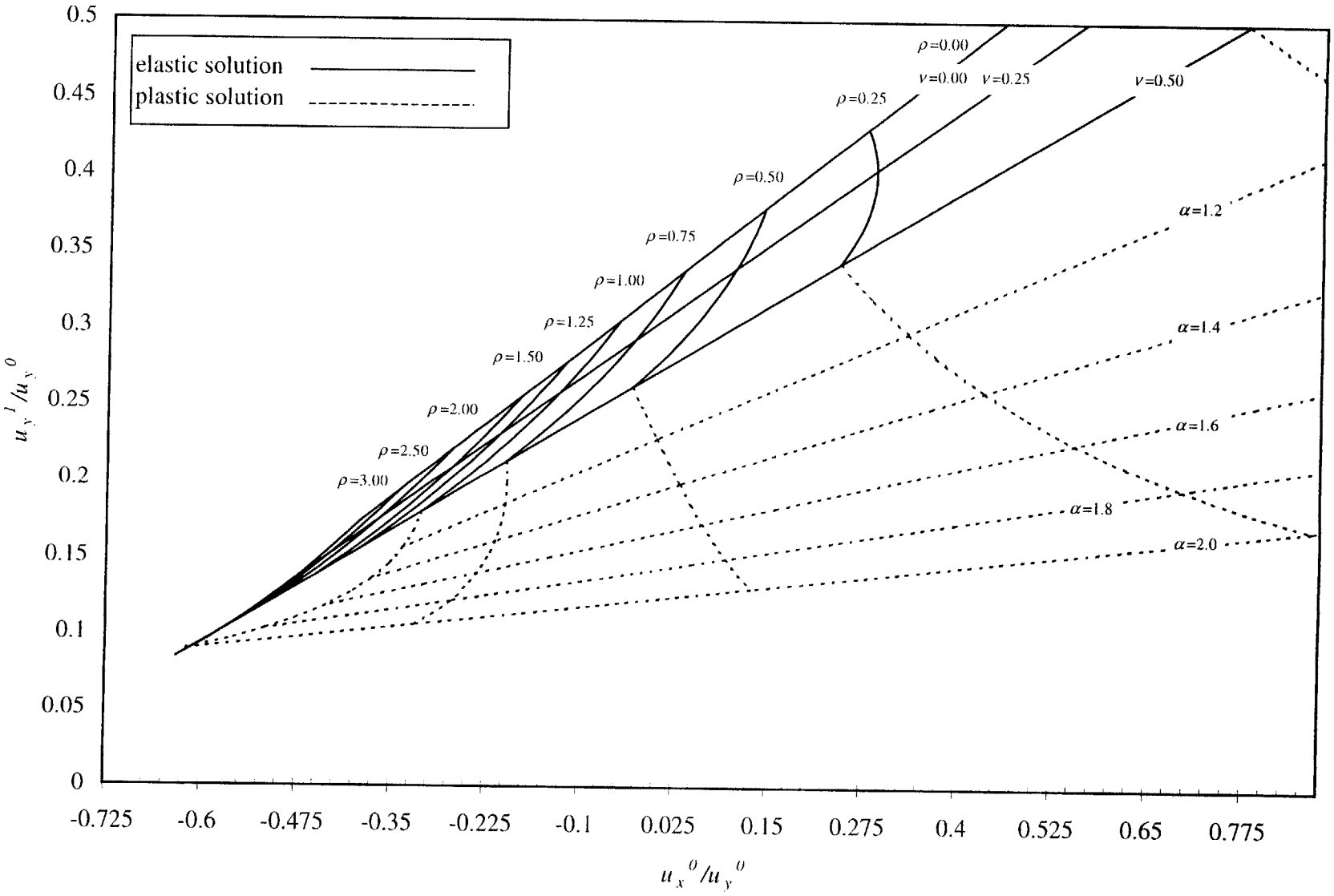

Figure V.17. Design chart for ρ and ν, $R/H = 0.3$

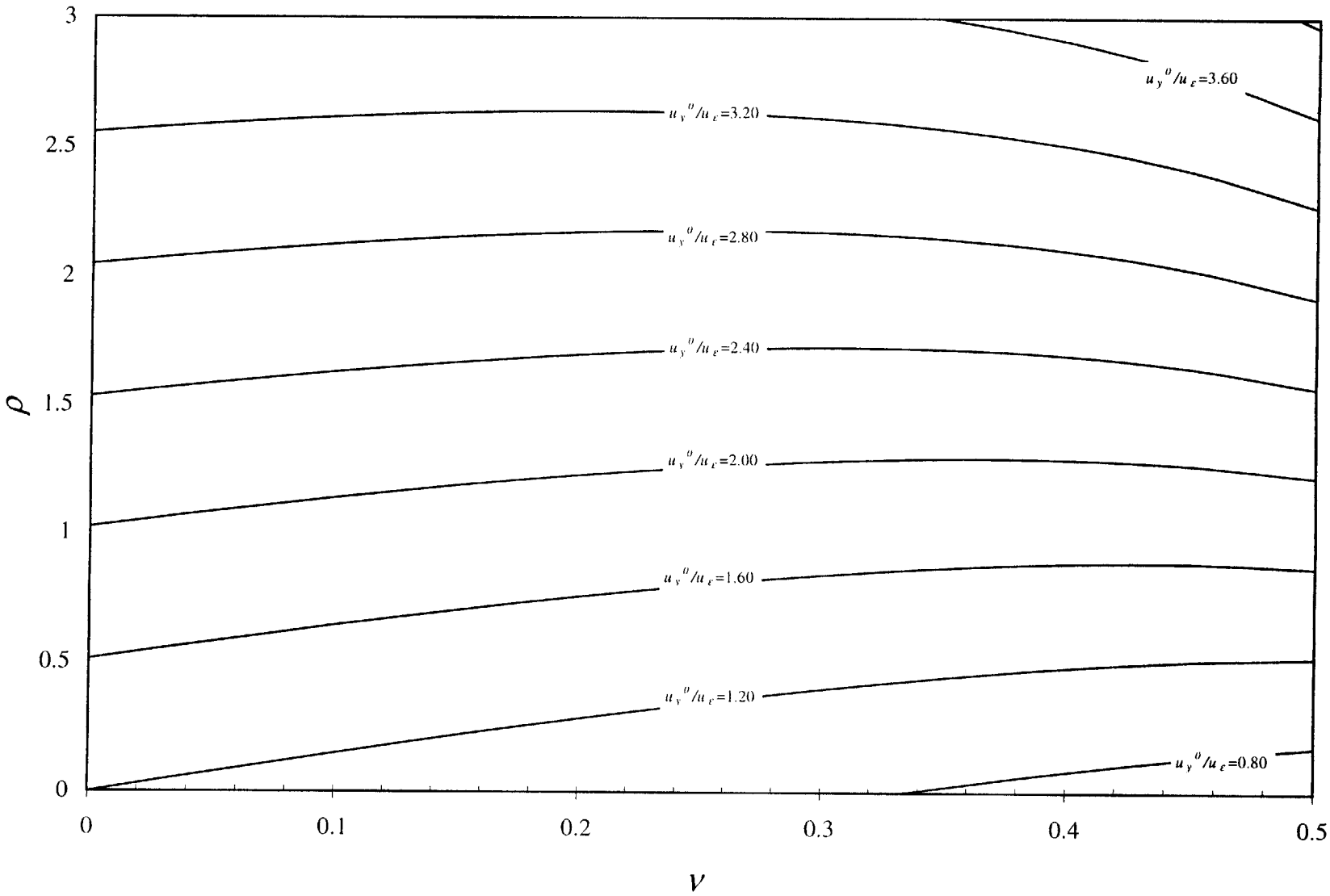

Figure V.18. Design chart for u_y^0/u_ε, R/H = 0.3, no dilation

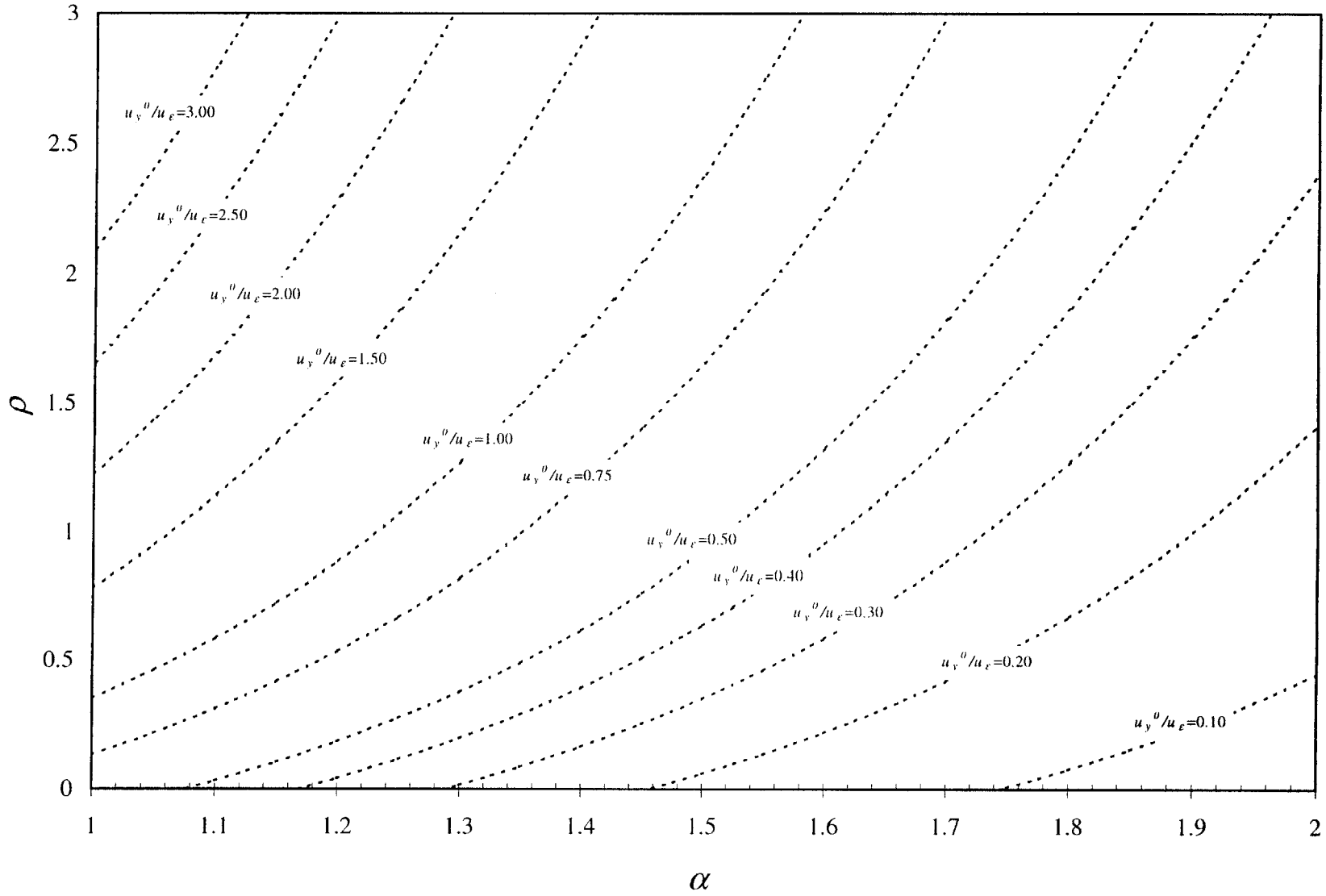

Figure V.19. Design chart for u_y^0/u_ε, R/H = 0.3, dilation

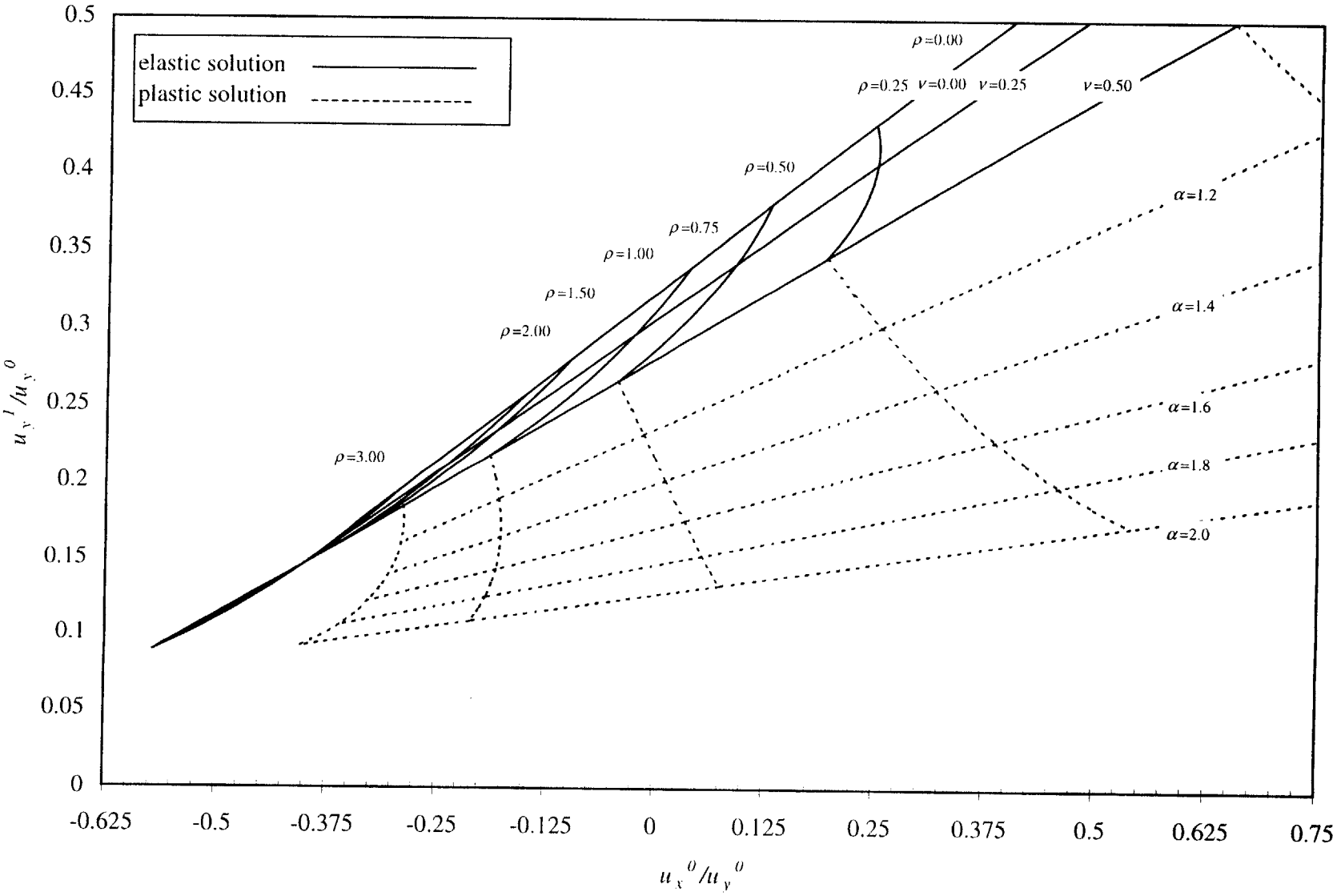

Figure V.20. Design chart for ρ and ν, $R/H = 0.35$

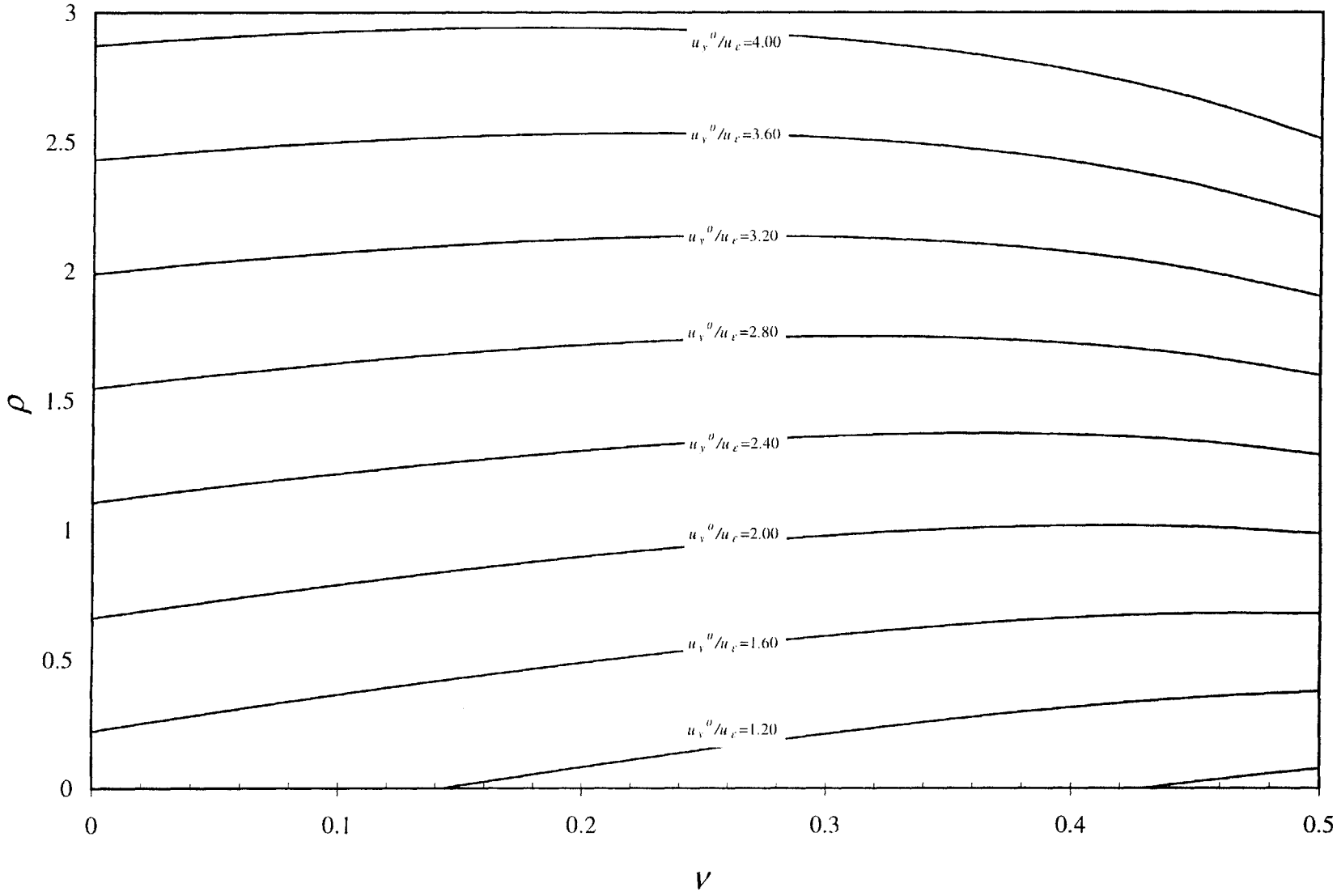

Figure V.21. Design chart for u_y^0/u_ε, R/H = 0.35, no dilation

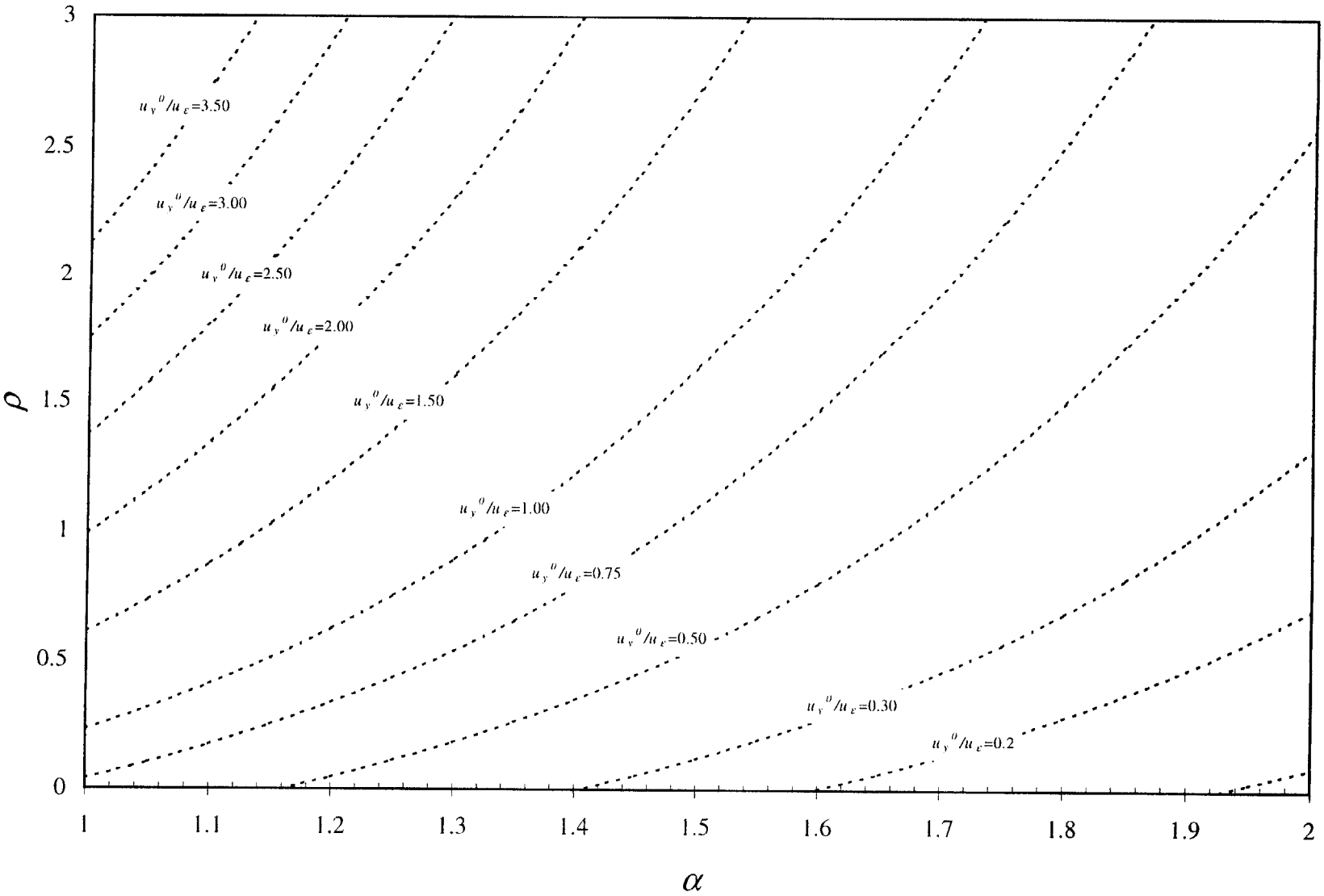

Figure V.22. Design chart for u_y^0/u_ε, R/H = 0.35, dilation

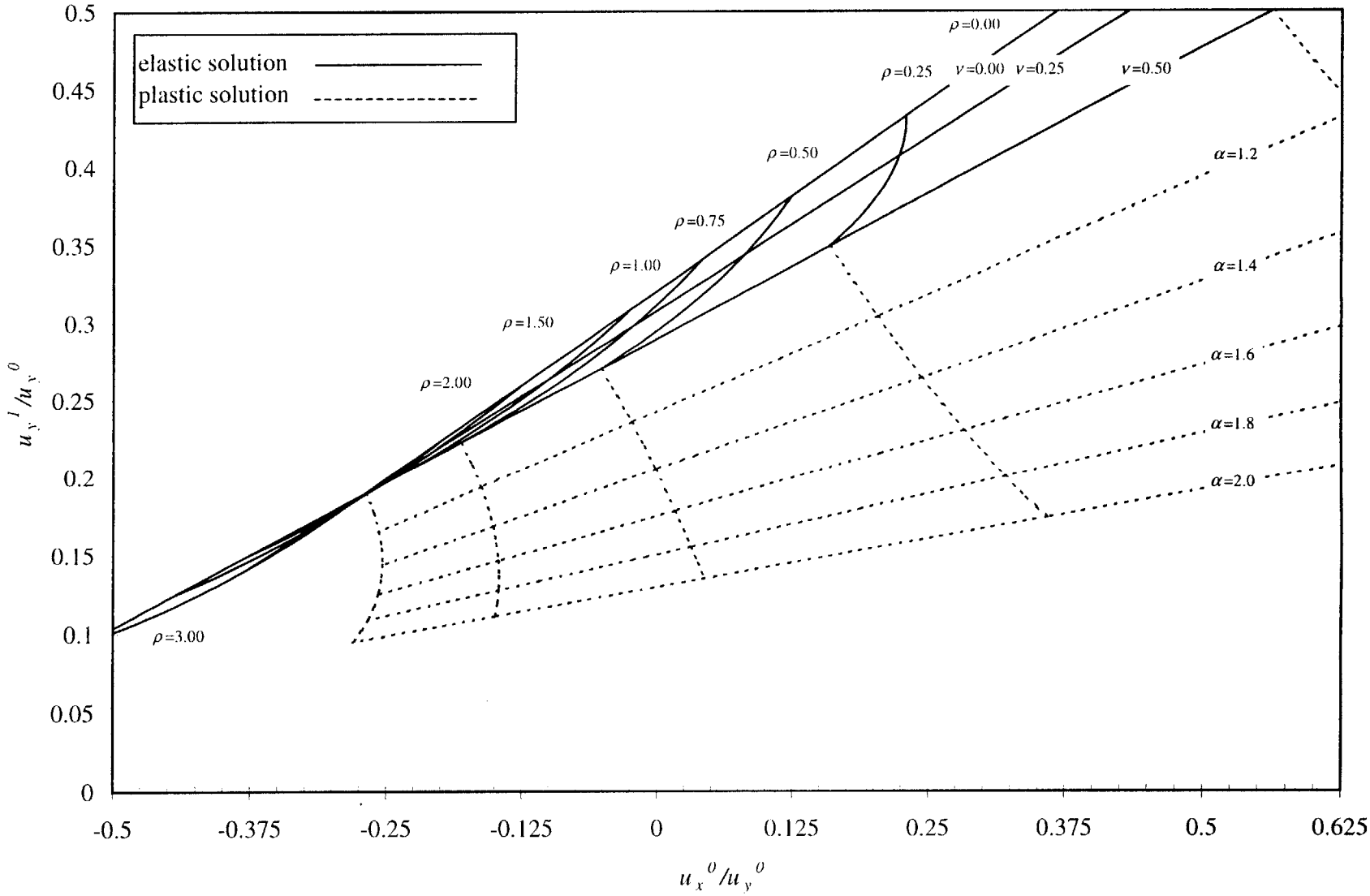

Figure V.23. Design chart for ρ and ν, R/H = 0.4

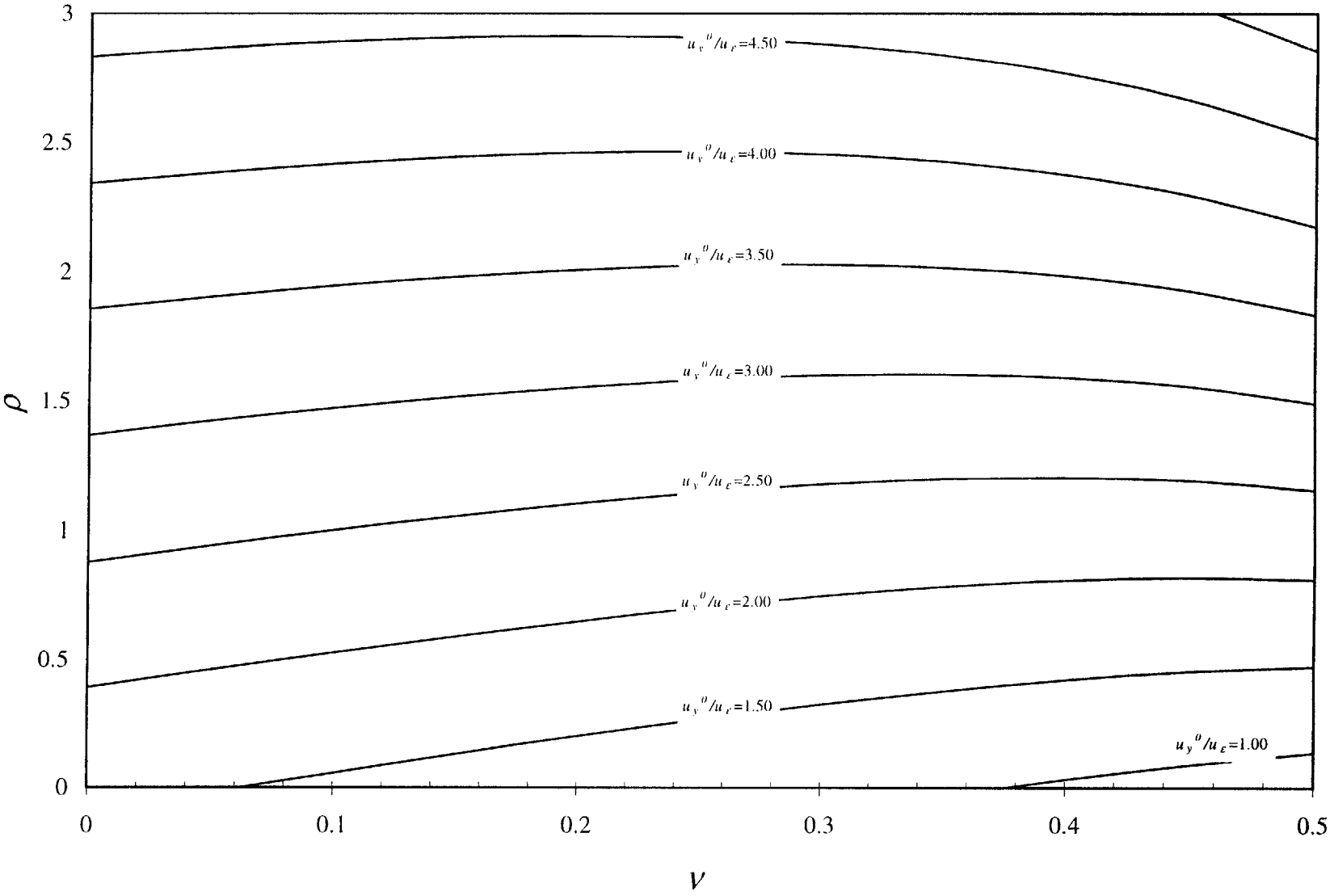

Figure V.24. Design chart for u_y^0/u_ε, R/H = 0.4, no dilation

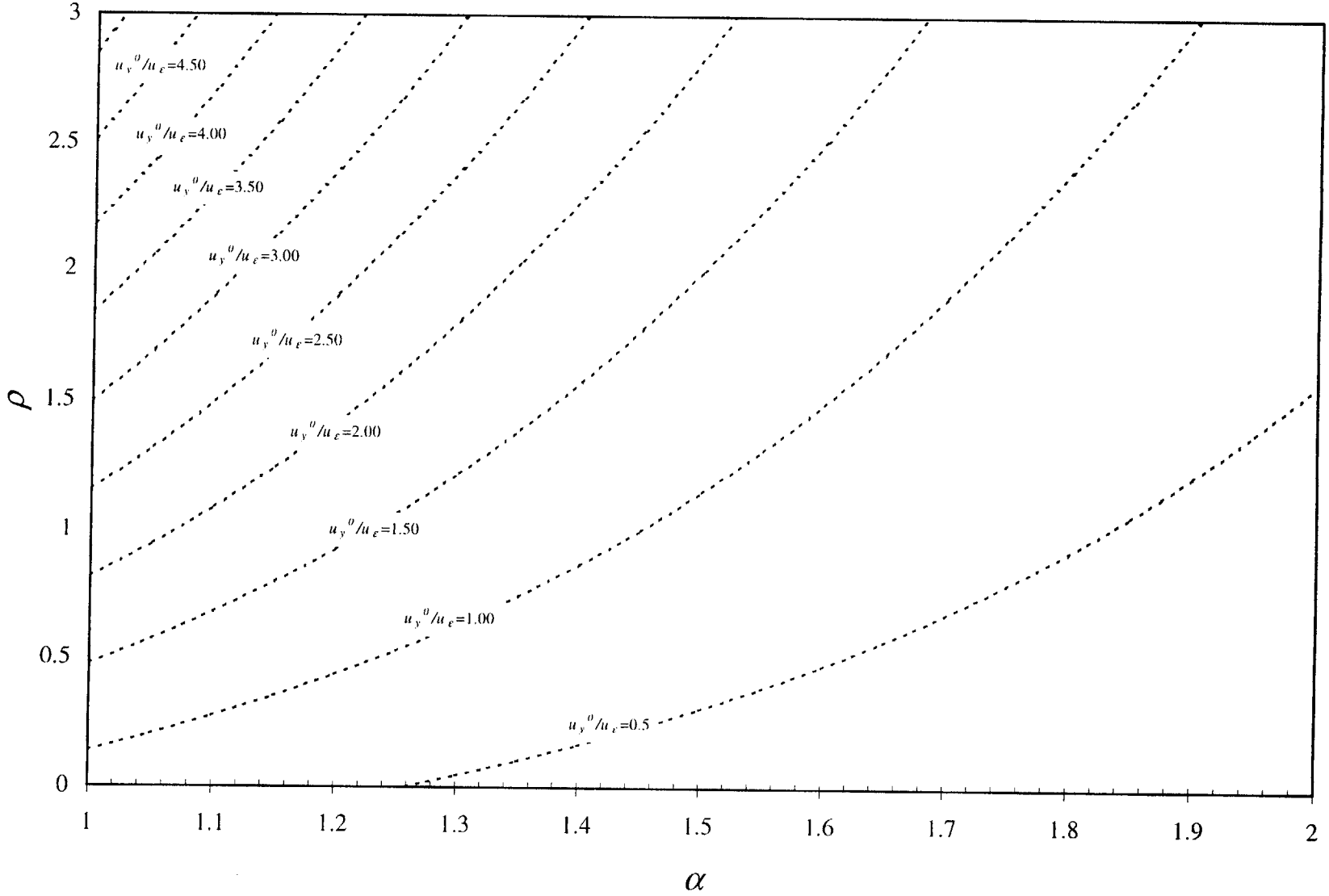

Figure V.25. Design chart for u_y^0/u_ε, R/H = 0.4, dilation

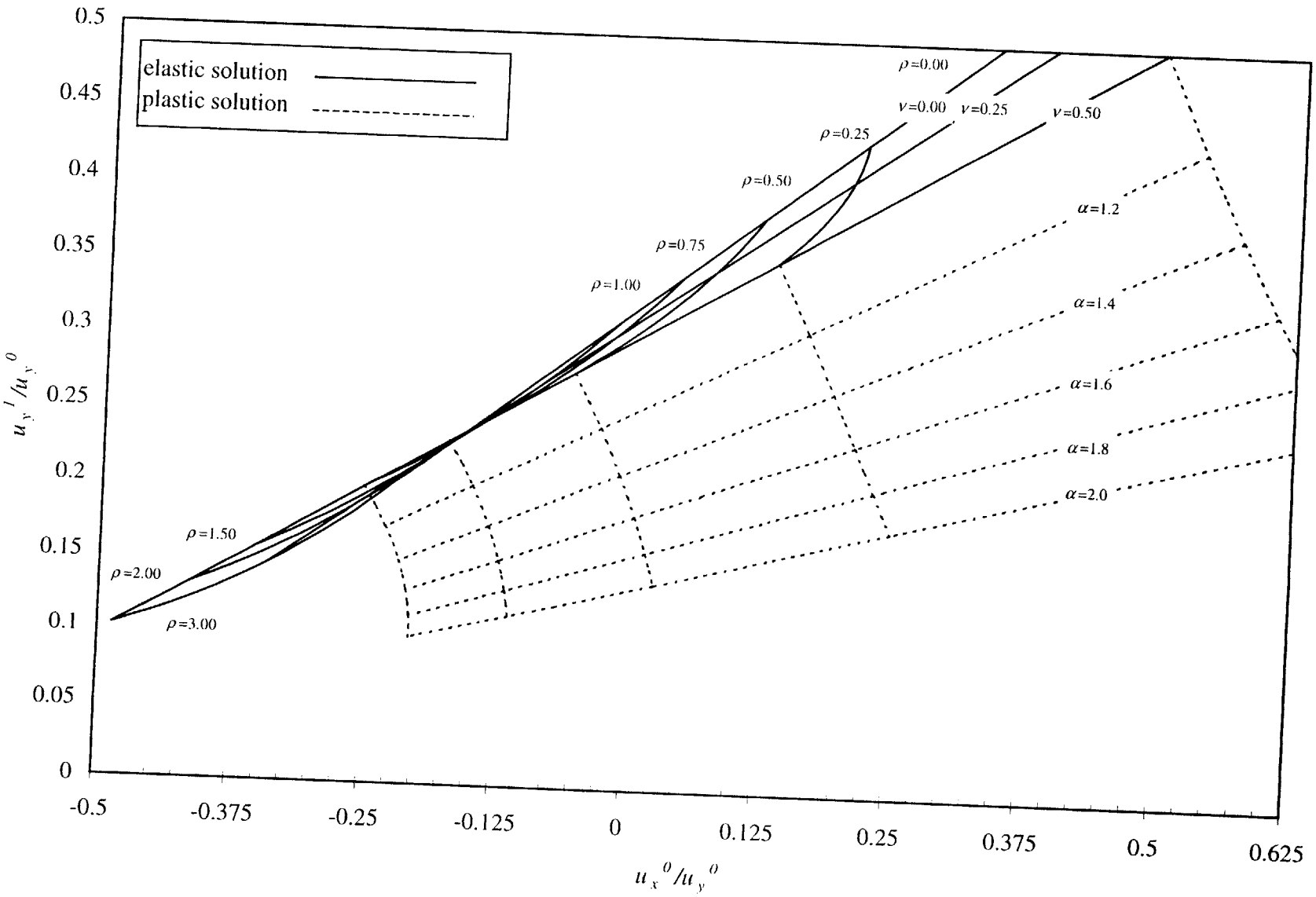

Figure V.26. Design chart for ρ and ν, $R/H = 0.45$

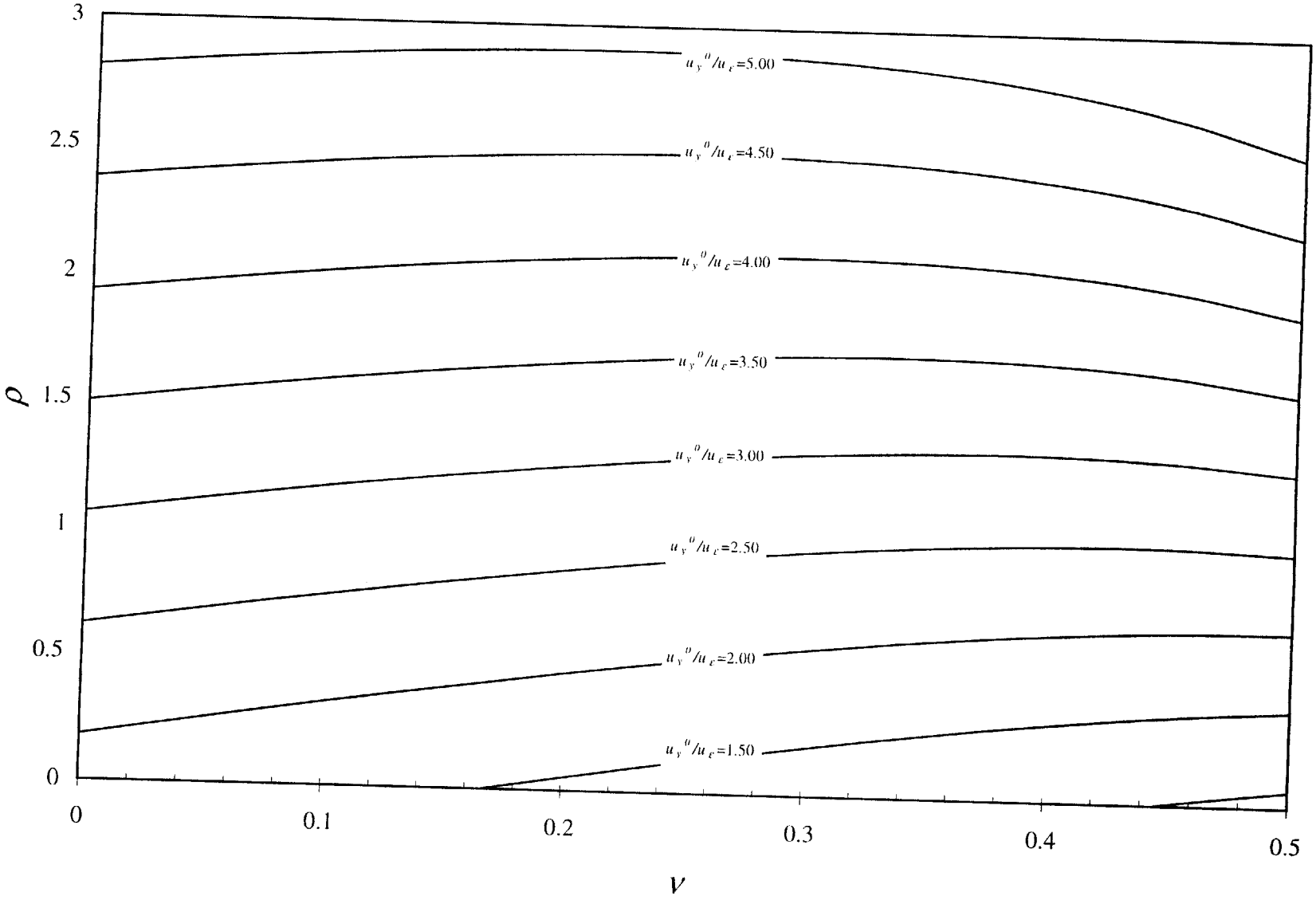

Figure V.27. Design chart for u_y^0/u_ε, R/H = 0.45, no dilation

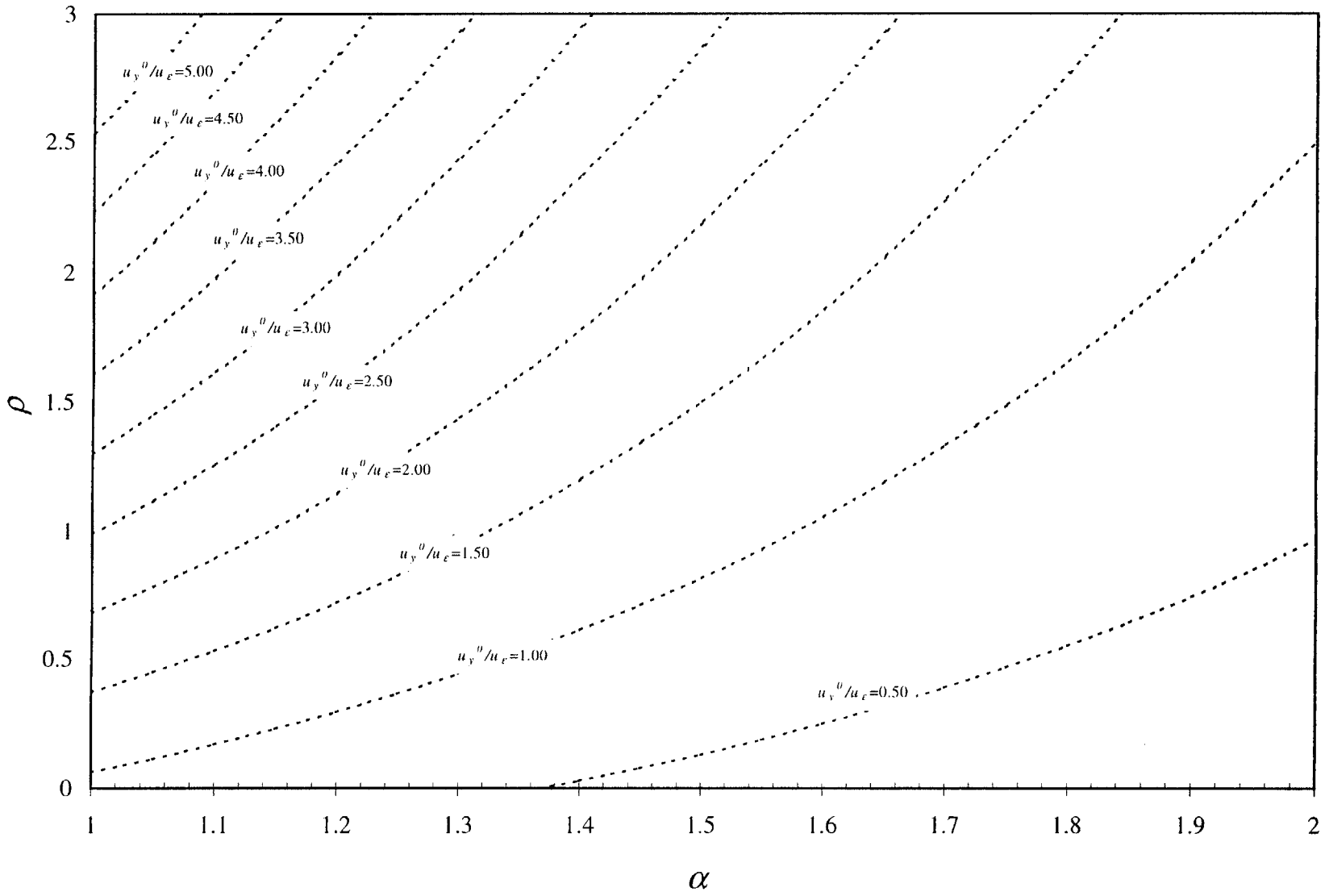

Figure V.28. Design chart for u_y^0/u_ε, R/H = 0.45, dilation